

Automated Oil Spill Detection System Using Spaceborne Synthetic Aperture Radar with Deep Learning-Based Algorithm

Dissertation

zur Erlangung des Doktorgrades
der Mathematisch-Naturwissenschaftlichen Fakultät
der Christian-Albrechts-Universität zu Kiel

vorgelegt von

Yi-Jie Yang

Kiel, 2025

Erster Gutachter: Prof. Dr. Florian Schütte

Zweiter Gutachter: Dr. Suman Singha

Tag der mündlichen Prüfung: 17.11.2025

In memory of Wan-Hsin Yang,

*a colleague from my first research group in Taiwan,
a great support at the beginning of my research voyage,
a friend who was just like an elder sister to me.*

Abstract

Oil spills are one of the major sources of marine pollution. They cause environmental damage and affect marine wildlife. In order to take early action in oil spill incidents, an automated system for the regular monitoring and detection of oil spills can be beneficial. Spaceborne synthetic aperture radar (SAR) is suitable for the first warning of a spill due to its wide coverage and frequent revisits. With increasing computing power and the growing number of publicly available SAR data, deep learning-based methods have been applied to oil slick detection applications. In the frame of this thesis, an automated oil spill detection system has been developed and its potential for integration into an early warning system has been demonstrated. The system identifies oil slicks with a custom trained deep learning-based object detector and provides binary masks of oil as output using a segmentation algorithm. The system has been tested in the Southeastern Mediterranean Sea for a year of acquisitions in 2019. The false discovery rate and false negative rate are 23.3 % and 24.0 %, respectively, demonstrating the ability of using such an automated system in operation to reduce the effort of manual interpretation. Complete records of oil spills, especially those from illegal operations, are often missing or unavailable to the public, so collecting and annotating oil slicks is usually the first task when developing a deep learning-based method for oil slick detection. As a result, different published methods use different datasets, making it difficult to compare the diverse approaches. Therefore, a ready-to-use dataset has been published as part of this thesis, which contains oil slicks and “look-alikes” that originate from other phenomena but may be misinterpreted as oil slicks in SAR data. Images in the dataset were sorted into different groups using the K-means unsupervised clustering algorithm based on image features. These groups provide a general selection of signatures from different phenomena. This dataset includes an *oil* set of 1365 image patches with a total of 3225 oil slicks and a *no-oil* set of 2290 image patches with look-alikes inside. The performance of the object detector used in the developed system was evaluated on image patches from different groups, providing a baseline for other studies to use for comparison. In addition, this thesis provides a comprehensive explanation of how various oceanic and atmospheric phenomena manifest in SAR scenes, thus bridging the knowledge gap between readers with different backgrounds, such as remote sensing, oceanography, and machine learning.

Zusammenfassung

Ölteppiche sind eine der Hauptquellen der Meeresverschmutzung. Sie verursachen Umweltschäden und beeinträchtigen die Meeresfauna. Um bei Ölverschmutzungen frühzeitig eingreifen zu können, kann ein automatisiertes System zur regelmäßigen Überwachung und Erkennung von Ölverschmutzungen von Vorteil sein. Radarsatelliten mit synthetischer Apertur (SAR) eignen sich aufgrund ihrer großen Reichweite und der häufigen Überflüge für die frühe Warnung vor einer Ölpest. Durch die zunehmende Rechenleistung und die steigenden Menge öffentlich verfügbarer SAR-Daten wurden dazu Deep-Learning-Methoden für Anwendungen zur Erkennung von Ölteppichen eingesetzt. Im Rahmen dieser Dissertation wurde ein automatisiertes System zur Erkennung von Ölteppichen entwickelt und dessen Potenzial zur Integration in ein Frühwarnsystem demonstriert. Das System identifiziert Ölteppiche mit einem speziell trainierten, auf Deep Learning basierenden Objektdetektor und generiert mithilfe eines Segmentierungsalgorithmus binäre Masken der Ölverschmutzung. Das System wurde im südöstlichen Mittelmeer mit Satellitendaten des vollständigen Jahres 2019 getestet. Die Falscherkennungsrate und die Falsch-Negativ-Rate liegen bei 23,3 % bzw. 24,0 %. Dies zeigt, dass der Einsatz eines solchen automatisierten Systems im operationellen Betrieb den Aufwand für die manuelle Interpretation der Satellitendaten verringern kann. Vollständige Aufzeichnungen über Ölverschmutzungen, insbesondere durch illegales Verklappen, fehlen oft oder sind nicht öffentlich zugänglich. Deshalb ist das manuelle Zusammenstellen und Markieren von Ölteppichen in der Regel die erste Aufgabe bei der Entwicklung einer auf Deep Learning basierenden Methode zur Erkennung von Ölteppichen. Infolgedessen verwenden verschiedene veröffentlichte Methoden unterschiedliche Datensätze, was einen Vergleich der verschiedenen Ansätze erschwert. Daher wurde im Rahmen dieser Dissertation ein einfach zu verwendender Datensatz veröffentlicht, der Ölteppiche und „Look-Alikes“ enthält, die von anderen Phänomenen herrühren, aber in SAR-Daten fälschlicherweise als Ölteppiche interpretiert werden könnten. Die Bilder des Datensatzes wurden mit Hilfe des unüberwachten K-Means-Clustering von Bildmerkmalen in Gruppen eingeteilt. Diese Gruppen liefern eine generelle Auswahl charakteristischer SAR-Signaturen, die durch verschiedene Phänomene hervorgerufen werden. Der Datensatz enthält einen Öl-Datensatz von 1365 Bildern mit insgesamt 3225 Ölteppichen und einen Datensatz aus 2290 Bildkacheln, die „Look-

Alikes“ und keine Ölverschmutzungen enthalten. Die Ergebnisse des Objektdetektors, der in dem entwickelten System verwendet wird, wurden mit Bildern aus den verschiedenen Gruppen evaluiert, um eine gemeinsame Vergleichsgrundlage für zukünftige Studien zu liefern. Darüber hinaus bietet diese Arbeit eine umfassende Erklärung, wie verschiedene ozeanische und atmosphärische Phänomene in SAR-Szenen zu erkennen sind, und überbrückt so die Wissenslücke zwischen Lesern aus verschiedenen Bereichen wie Fernerkundung, Ozeanographie und maschinelles Lernen. ¹

¹The translation of the German abstract was done by Dr. Christoph G. Schnupfhn from the German Aerospace Center (DLR).

Contents

List of Figures	vii
List of Tables	viii
List of Acronyms and Abbreviations	ix
1 Introduction	1
1.1 Marine oil pollution	2
1.1.1 Properties and fate of oil	4
1.1.2 Clean-up strategies	8
1.1.3 Environmental impact	10
1.2 Oil slick detection with remote sensing	12
1.2.1 Optical sensors for oil slick detection	12
1.2.2 Microwave sensors for oil slick detection	17
1.2.3 Existing oil spill monitoring systems	20
1.3 Oil slick detection using spaceborne SAR	23
1.4 Approach in this thesis	26
1.5 Research questions	28
2 Southeastern Mediterranean Sea	29
2.1 Oil pollution hotspot	29
2.1.1 Shipping	30
2.1.2 Discovery of oil and gas in the Levantine Basin	32
2.2 Environmental factors	32
2.2.1 Oceanographic forcing	35
2.2.2 Vertical mixing and biological factors	37
2.2.3 Mesoscale dynamics	38
2.2.4 Internal waves	39
2.2.5 Atmospheric factors	39
2.3 Relevance for SAR analysis	41

3 SAR Signatures	43
3.1 Dataset of oil slicks, look-alikes, and remarkable SAR signatures	43
3.2 Explanations of ocean SAR signatures	45
4 Development of an Automated Oil Slick Detection System	79
4.1 Custom-trained oil object detector	79
4.2 Automated oil spill detection and early warning system	109
5 Summary	141
5.1 Progress on research questions	141
5.2 Integration of the results into the current level of knowledge	147
5.3 Further improvement on the oil slick detection algorithm	147
5.4 Outlook	148
Bibliography	151
Acknowledgements	173
Declaration	175

List of Figures

1.1	Global oil spill incidents	1
1.2	Different processes over time after the spill of an oil	4
1.3	Schematic illustration of the different processes of oil weathering	7
1.4	Schematic illustration of the different cleaning strategies	9
1.5	Parts of the electromagnetic spectrum on which the sensor operates for oil spill detection	13
1.6	Illustration of the Bragg resonance geometry	19
1.7	Illustration of deep learning-based methods for SAR oil slick detection .	25
1.8	Illustration of the two-step approach proposed in this thesis	27
2.1	Bathymetry map of the Mediterranean Sea	30
2.2	A zoomed-in bathymetry map in the Southeastern Mediterranean Sea .	31
2.3	Ship density in the Levantine Sea	33
2.4	Discovery of gas fields in the Levantine Basin	34
2.5	Vertical distribution of water masses in the Mediterranean Sea	36
2.6	Surface circulation in the Mediterranean Sea	37

List of Tables

1.1	Summary of optical sensors used for oil slick detection	14
1.2	Estimation of oil volume based on oil appearance according to the Bonn Agreement	15

List of Acronyms and Abbreviations

ABL	atmospheric boundary layer	40
AGWs	atmospheric gravity waves	39
AIS	automatic identification system	22
AP	average precision	144
API	American Petroleum Institute	5
ARPEL	Association of Oil, Gas and Renewable Energy Companies of Latin America and the Caribbean	10
CDOM	colored dissolved organic matter	16
chl-<i>a</i>	chlorophyll <i>a</i>	37
CNN	convolutional neural network	24
DLR	German Aerospace Center	146
EEZ	exclusive economic zone	32
e.m.	electromagnetic	12
EMODnet	European Marine Observation and Data Network	143
EMSA	European Maritime Safety Agency	3
ESA	European Space Agency	22
ESI	environmental sensitivity index	9
FDR	false discovery rate	144
FIR	far infrared	13
FNR	false negative rate	144
FOV	field of view	12

GMES Global Monitoring for Environment and Security	22
GSHHG Global Self-consistent, Hierarchical, High-resolution Geography Database	31
IOLR Israel Oceanographic and Limnological Research	26
IPIECA International Petroleum Industry Environmental Conservation Association	10
IR infrared	12
ITOPF International Tanker Owners Pollution Federation Limited	1
KSAT Norwegian Kongsberg Satellite Service	22
LWIR long-wave infrared	13
MARPOL 73/78 International Convention for the Prevention of Pollution from Ships, 1973 as modified by the Protocol of 1978	3
MWIR mid-wave infrared	13
NIR near infrared	12
NOAA National Oceanic and Atmospheric Administration	3
OIWs oceanic internal waves	39
OPRC International Convention on Oil Pollution Preparedness, Response and Co- operation	3
R-CNN region-based convolutional neural network	26
REMPEC Regional Marine Pollution Emergency Response Centre for the Mediter- ranean Sea	3
RFI radio frequency interference	45
SAR sythetic aperture radar	2
SLAR side-looking airborne radar	19
SST sea surface temperature	6
SWIR short-wave infrared	13
UAVs unmanned aerial vehicles	21
UV ultraviolet	12

YODA YOLO-based Oil Detection Algorithm	109
YOLO You Only Look Once	79

1 Introduction

Marine oil pollution can cause environmental damage and affect marine wildlife. Figure 1.1 highlights several oil spill incidents. Blue points indicate tanker spills, while brown points indicate spills from other sources, including platform spills, vessel spills, and deliberate oil spills resulting from war. Tanker spills that occurred in the past ten years are marked yellow. The pink points show four major tanker spills of more than 200 000 tonnes (metric ton), as recorded by the International Tanker Owners Pollution Federation Limited (ITOPF) (ITOPF, 2025). These and other incidents have raised societal awareness of oil pollution due to the serious environmental damage that can be seen in the news and media.

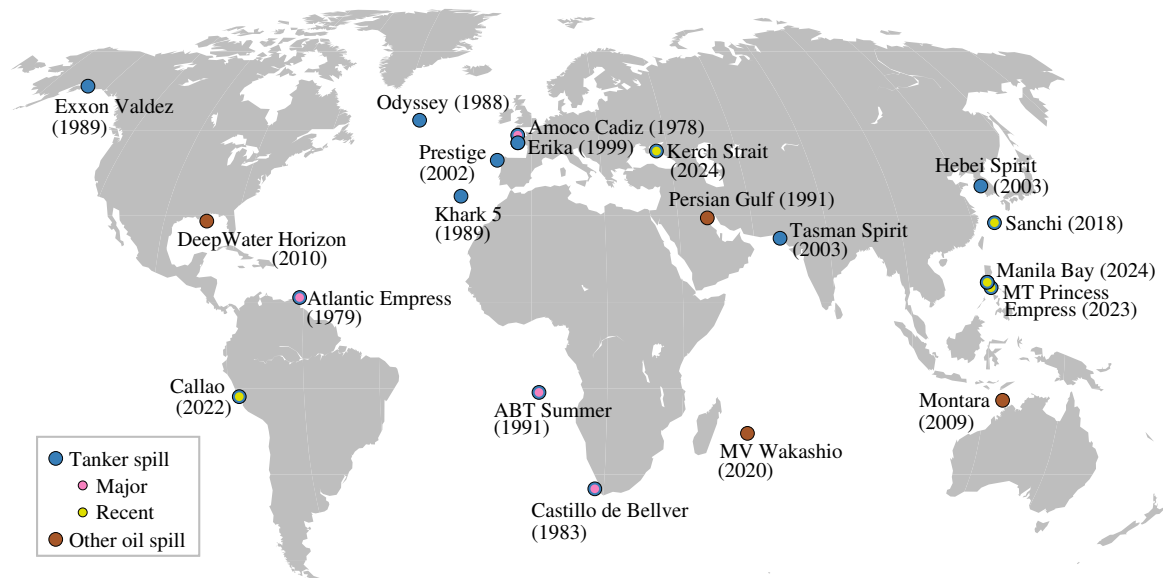


Figure 1.1: Global oil spill incidents collected from reports, news articles, and literature. Blue points indicate tanker spills. The four major tanker spills with spills of more than 200 000 tonnes are marked in pink, while those occurring in the past ten years are marked in yellow. Brown points show oil spills from other sources, such as platforms, vessels, and deliberate spills.

Section 1.1 first provides an overview of marine oil pollution, including the composition and sources of oil, as well as statistics on global oil spills. Before addressing the impact of oil pollution, it is necessary to understand the properties of oil, how it is physically transported on the sea, and how it weathers (see Subsection 1.1.1).

Although the marine environment can recover from oil spills through weathering processes, clean-up operations should still be implemented to mitigate the negative impact of oil, especially for large incidents (see Subsection 1.1.2). However, the impact of oil on organisms, as well as its ecological, environmental, and socio-ecological consequences, cannot be fully mitigated. Their long-term impact can be better understood through examination over the course of several years (see Subsection 1.1.3).

Various remote sensing techniques have been used to detect oil spills. This thesis focuses on using spaceborne synthetic aperture radar (SAR) for the early detection of oil spills. However, SAR sensors alone cannot provide all the information necessary for cleaning up oil. It is therefore important to understand the information that other sensors obtain about oil and how different sensors can be deployed on various platforms to provide a comprehensive view of an oil spill. Section 1.2 first introduces different sensors and explains which oil properties they can detect (see Subsections 1.2.1 and 1.2.2). Then, it describes how these sensors are typically deployed on different platforms, using existing systems or services as examples (see Subsection 1.2.3). After providing an overview of the role of spaceborne SAR in oil spills, Section 1.3 reviews the literature on different oil slick detection methods using SAR and points out research gaps in previous studies. This thesis proposes an approach that fills these research gaps, as shown in Section 1.4. Section 1.5 summarizes the value of this thesis by addressing the research questions it will answer.

1.1 Marine oil pollution

Petroleum is a complex mixture of hydrocarbons, organic compounds, and a trace amount of metals. It naturally exists in gaseous state as natural gas, liquid state as crude oil, and solid state as asphalt (Wang et al., 1964). The proportion of elements in petroleum depends on its type and origin. Crude oil is typically composed of 84.5 % carbon, 13 % hydrogen, and 1–3 % sulfur; the rest consists of nitrogen, oxygen, metals, and salts (Aitani, 2004). Marine oil pollution is primarily attributable to crude oil, refined petroleum products, petroleum by-products, fuels, and oily waste water (Zhang et al., 2019). Such pollution is referred to as “oil slicks”, which are films of oil on the surface of the water, and it is the result of natural seepage or oil spills. The term “oil spill” refers to an incident involving the presence of oil that has been caused by human intervention. Hence, a single oil spill may consist of multiple oil slicks.

Oil spills are commonly caused by discharges from ships and offshore platforms. Operational oil discharges from ships can come from engine room waste, bilge water, oily ballast water from the tanker, and tanker wash residues. These frequent deliberate

spills may continuously pose a threat to the local environment. Monitoring and surveillance of busy shipping lanes can reduce the number of illegal oil discharges by ships in violation of international or regional conventions and agreements, such as the International Convention on Oil Pollution Preparedness, Response and Co-operation (OPRC), the International Convention for the Prevention of Pollution from Ships, 1973 as modified by the Protocol of 1978 (MARPOL 73/78), and the Barcelona Convention for the Mediterranean Sea. On the other hand, monitoring offshore platforms can be relatively practical because they are in fixed locations. The main source of oil pollution from platforms is produced water, a by-product extracted with oil and natural gas; however, other activities, such as well cleaning, well abandonment, and system failure, can also release oil (Ferraro et al., 2009). In those areas with oil and gas exploration and exploitation activities, oil seepages from seabed may also commonly occur. In addition to these sources, the transportation of petroleum involves 10 to 15 transfer points from oil fields to consumers, including tankers, pipelines, trains, and tank trucks; spills can occur at any of them (Fingas, 2012).

A previous study summarized the various sources of oil entering the worldwide marine waters for the years of 1975–1985 and 1990–1999: 47 % from natural seepage, 38 % from petroleum consumption, 12 % from petroleum transportation, and 3 % from petroleum extraction (Polinov et al., 2021). Of all the sources of oil spills, tanker spills have the most complete record. The ITOPF organization publishes annual reports on oil tanker spills, addressing those recorded in the previous year and providing an overview of tanker spills since 1970. These tanker spills may result from collisions, groundings, hull or equipment failure, explosions, or other incidents. According to their latest report for 2024 (ITOPF, 2025), there has been a decrease in the global tanker spill trend. From 1970 to 1979, the average number of accidents per year was 78.8. Four decades later, from 2010 to 2019, this number decreased to an average of 6.3 per year. From 2020 to 2024, the average was 7.4 accidents per year. However, as tanker spills account for only about 8 % of oil pollution (Polinov et al., 2021), it is essential to take into account various sources. Such information may be available from local services. For example, the European Maritime Safety Agency (EMSA) offers maritime surveillance services and incident reports in European waters; the Regional Marine Pollution Emergency Response Centre for the Mediterranean Sea (REMPEC) supports contingency plans for combating marine pollution incidents in the Mediterranean Sea; the Sentinel Asia provides emergency satellite observation before and after major disasters in the Asia-Pacific region; the National Oceanic and Atmospheric Administration (NOAA) maintains a database of oil and chemical spills, with a primary focus on incidents within the U.S.

Although large accidents pose a significant environmental risk, the impact of an oil spill depends not only on its volume, but also on its physical and chemical properties, its weathering conditions, the clean-up strategies employed, and the ecological characteristics of the area. The following subsections address these factors, and the overall impact of oil is explained at the end of this section.

1.1.1 Properties and fate of oil

Once an oil spill has occurred, understanding its trajectory and fate is necessary to best respond to it. The physical transport of an oil slick is mainly controlled by spreading and advection (also known as drift). Over time, oil undergoes several weathering processes, including evaporation, dissolution, dispersion, emulsification, sedimentation, biodegradation, and photo-oxidation; these processes change the physical and chemical properties of the oil (Fingas, 2017). Figure 1.2 illustrates various processes over time following a spill.

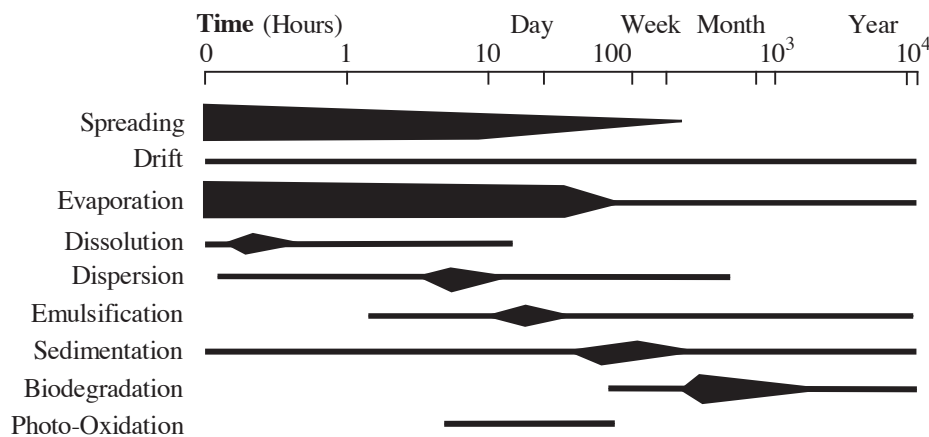


Figure 1.2: Different processes over time after the spill of an oil (ExxonMobil, 2014).
Copyright © 2014 ExxonMobil Research and Engineering Company.

After the spill, the oil begins to spread due to gravity as driving force and inertia as retarding force. Gravity creates an unbalanced pressure distribution between the oil and the surrounding water. This causes the oil to spread sideways, but the inertia of the oil film, which is driven by friction, counterbalances this force. As the oil spreads and becomes thinner, the inertia of the oil film decreases. However, the inertia of the viscous layer of water beneath the oil increases as it grows thicker over time. Therefore, the dominant retarding force transitions gradually from inertia to viscous force. On the other hand, the gravity force-induced spreading diminishes as the oil continues to become thinner. Therefore, the spreading coefficient, which pulls the oil film outward,

becomes more dominant. The spreading coefficient is due to an imbalance in the interfacial tension at the water–air interface compared to the oil–air and oil–water interfaces. The interfacial tension is not related to the oil thickness, but rather to the size of the slick (Fay, 1971; Hollebone, 2017). The above explanation of spreading is based on the three-regime spreading theory proposed by Fay (1971): the gravity-inertia regime, the gravity-viscous regime, and the surface tension-viscous regime; the names of the regimes are specified as the spreading force followed by the retarding force. These spreading and retarding forces indicate that the tendency to spread persists despite the presence of wind and surface currents. Wind and surface currents both contribute to the advection of an oil slick. For an oil slick close to land when the wind speed is less than 10 km/h, the advection is calculated using 100 % of the surface current-induced drift and 3 % of the wind-induced drift (Fingas, 2017). Note that the wind and surface currents are usually in different directions. The drag of the wind on the surface of the ocean induces the surface currents. In theory, due to the Coriolis force, surface currents are deflected by about 45° to the right of the wind direction in the Northern Hemisphere and to the left in the Southern Hemisphere (Knauss & Garfield, 2016). In practice, the spreading of oil is coupled with its advection. Typically, the physical transport of an oil spill of 1 ton (about 0.907 tonne) covers a radius of approximately 50 m within 10 min and continues to spread until it covers an area of about 12 km², reaching a thickness of less than 1 mm (Abou El-Magd et al., 2020).

The viscosity of the oil, as well as the interfacial tensions at the water–air, oil–air and oil–water interfaces, can indicate how quickly and widely oil spreads on water (Fingas, 2012). As the oil weathers, the evaporation of oil makes its viscosity and density higher. In addition, oil viscosity is related to temperature; the lower the temperature, the higher the viscosity. For most oils, this relationship is approximately exponential (Hollebone, 2017). The density of oil determines whether it sinks or floats in water; 75 % of the global seawater has a density between 1026.4 and 1028.1 kg/m³ (Knauss & Garfield, 2016), so most oil floats on seawater. However, oil undergoes a contraction process as the temperature decreases. As a consequence, “heavier” oils may sink in cold water. The description as heavy or light oil depends on the composition of different hydrocarbon components, which is influenced by the geological conditions of its origin. The American Petroleum Institute (API) defined API gravity as a measure of how heavy or light crude oil is compared to water. It is defined as follows (Hollebone, 2017):

$$\text{API} = \frac{141.5}{\text{s.g.}^{15.56}} - 131.5, \quad (1.1)$$

where $\text{s.g.}^{15.56}$ is the specific gravity of the oil or petroleum product at 15.56 °C. The

following gives an idea of the typical API value: pure water is 10° API, heavy oil is less than 25° API, medium oil is between 25 and 35° API, light oil is between 35 and 45° API (Hollebone, 2017). These oil properties, as well as environmental conditions such as sea surface temperature (SST), wind speed, and wind direction are known factors that affect the physical transport of oil (Abou Samra & Ali, 2024). It is also important to be aware of other oil properties, the flash point and the pour point, in terms of their significance for clean-up operations. The flash point is defined as the lowest temperature at which a liquid can form ignitable vapor near its surface; it should be considered to ensure the safety of clean-up operations. The pour point can limit the selection of clean-up operations. It is the lowest temperature at which an oil begins to flow. For example, if the temperature of an oil is lower than its pour point, the oil becomes semi-solid and may be lifted directly from the sea (ITOPF, 2012a).

Figure 1.3 illustrates different weathering processes of oil. Evaporation typically accounts for about 20 to 40 % of the volume loss of an oil spill within 1 to 2 days (Mackay & McAuliffe, 1989; Spaulding, 1988), and 80 % of evaporation occurs within the first two days (Fingas, 2017). For example, the volume of oil in the *Torrey Canyon* oil spill decreased by 30 to 40 % after several days (Curl & O'Donnell, 1977). Light oils generally lose a larger percentage of their volume than heavy oils do from evaporation (Mackay & McAuliffe, 1989). Several factors influence the evaporation rate, including the size of the spill area, wind speed, vapor pressure, slick thickness, and temperature (J. C. Huang, 1983). Although most oil loss is due to evaporation, the soluble components that are dissolved in water cannot be ignored because they can be particularly toxic to aquatic life (Fingas, 2017). On the other hand, since evaporation occurs faster than dissolution and some of these soluble components are also volatile, they may evaporate before dissolving (Harrison et al., 1975).

Waves or turbulence can break oil into smaller droplets, which then mix into the water column. This process, known as dispersion, is primarily driven by wind speed and direction. Other factors, such as water depth and SST, also play a role (Abou Samra & Ali, 2024). Additionally, the properties of oil also affect its dispersibility; lighter crude oils are generally more dispersible than heavier ones. At moderate wind speeds, the rate of natural dispersion is about 0.5–2 % of the oil volume per hour (Abou El-Magd et al., 2020). The process of dispersing droplets into another medium is called emulsification. Thus, dispersed oil in water is sometimes referred to as an oil-in-water emulsion (Mackay & McAuliffe, 1989). An increased surface area-to-volume ratio due to dispersion may speed up dissolution, sedimentation, and biodegradation processes (ITOPF, 2011; National Academies of Sciences, Engineering, and Medicine, 2022). The increased contact of the soluble components of oil and water allows these

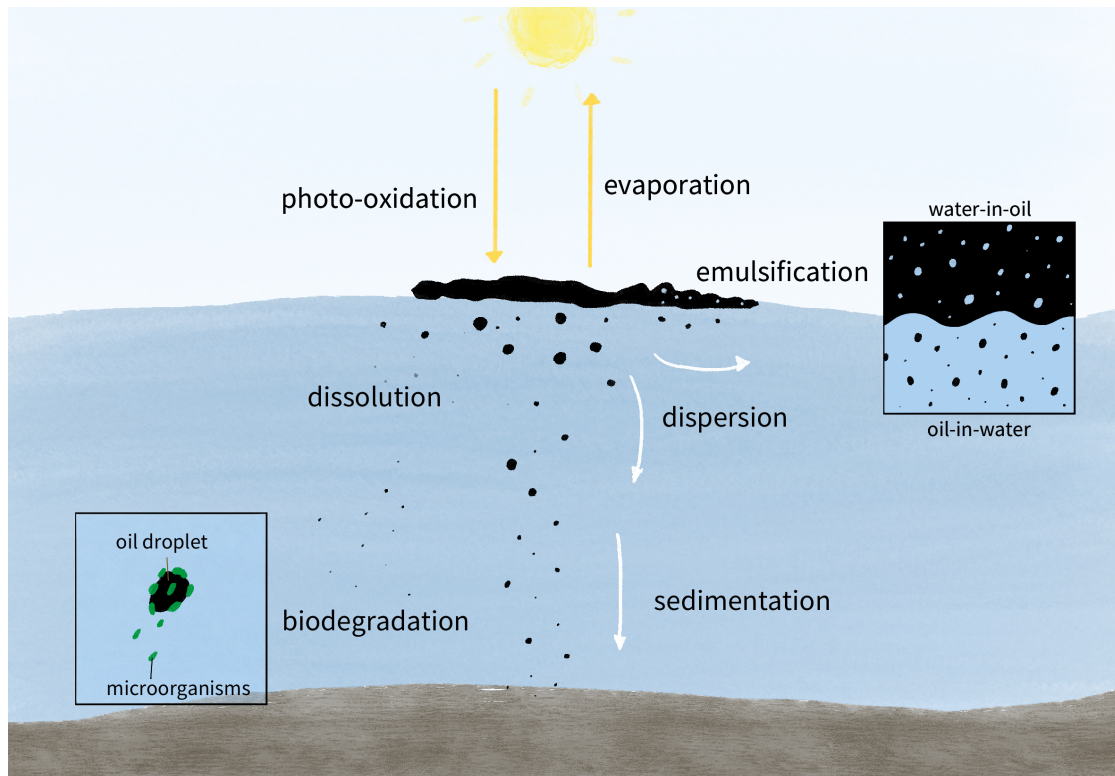


Figure 1.3: Schematic illustration of the different processes of oil weathering.

components to dissolve in water. Besides, oil droplets may collide with mineral matter in the water column; these collisions can result in the formation of heavier aggregates that sink to the bottom as sediment (Qi et al., 2021). In addition, the presence of small droplets from dispersion can increase exposure to microorganisms, which drive biodegradation, and may therefore enhance biodegradation (Loh et al., 2020). Microorganisms break down hydrocarbons, resulting in the production of oxidized compounds. Therefore, oxygen is necessary for this process, and the speed of biodegradation is affected by its availability.

On the other hand, water-in-oil emulsion, sometimes called “mousse” or “chocolate mousse” due to its appearance, has water droplets dispersed in oil. Most oil spill related studies refer to this kind of emulsion when they mention “emulsification”. The natural emulsifying agents in crude oil, mainly asphaltenes and resins, tend to attach to dispersed water droplets at the emulsion interface, preventing them from coalescence (Wong et al., 2015). Generally, water-in-oil emulsions can contain up to 80 % water (Overstreet et al., 1995). Research has shown that emulsions with higher water content remain stable for longer periods of time (Fingas & Fieldhouse, 2004). In other words, oils in this form can be really stable and difficult to degrade, so they tend to oxidize (ITOPF, 2011). Oil can be oxidized by sunlight through a process known as

photo-oxidation. During this process, hydrocarbons absorb sunlight and produce intermediate or end products; one such product is tar balls, which are semi-solid blobs of petroleum. Note that except for water-in-oil emulsions, thicker layers of very viscous oil also tend to oxidize (ITOPF, 2011).

1.1.2 Clean-up strategies

The marine environment has its own ability to recover from oil spills through various oil weathering processes explained in the previous subsection. However, different clean-up strategies can be implemented to mitigate the negative impact on the environment and marine wildlife. Figure 1.4 gives an overview of common clean-up strategies. Since most oil floats on seawater, floating booms can be used to create physical boundaries around oil slicks and constrain their movement. These oil slicks can be removed by using sorbents, skimmers, chemical dispersants, or controlled in-situ burning. Sorbents and skimmers are physical methods for removing the oil slicks. Sorbents are placed on oil slicks to absorb the oil. The absorption capacity of sorbents depends on the material they are made of. Skimmers remove oil from the water by either collecting or pumping it into storage. Oleophilic (“oil-attracting”) skimmers use materials to which oil adheres to collect oil from the sea surface and release it into a sump. Weir skimmers, on the other hand, are placed at or slightly below the interface of oil and water. This allows the oil to flow into the center hopper, where it is then pumped into storage (ITOPF, 2012b). In addition, hydraulic treatment methods are sometimes used for cleaning up stranded oil at rocky beaches. After the *Exxon Valdez* oil spill (see Figure 1.1 for its location), the oil was washed off the beach with high-pressure hot water. However, it is believed that such clean-up treatment has brought negative biological consequences to the intertidal zone (C. H. Peterson, 2001).

As mentioned in Subsection 1.1.1, dispersed oil may speed up dissolution, sedimentation, and biodegradation processes. Therefore, chemical dispersants are commonly applied to facilitate the dispersion of oil. The dispersed oil droplets are stabilized by surfactants in dispersants, which are mixtures of surfactants and solvents (Kleindienst et al., 2015). However, the use of dispersants can increase the exposure of some organisms to oil, resulting in a greater toxic effect (Boyd et al., 2001). Therefore, previous studies have examined how dispersants facilitate weathering processes, such as dissolution (Sørensen et al., 2014), sedimentation (Qi et al., 2021), and biodegradation (Brakstad et al., 2018; Prince et al., 2013), as well as their effectiveness (Loh et al., 2020) and their impact on composition and activity of microbial communities (Kleindienst et al., 2015).

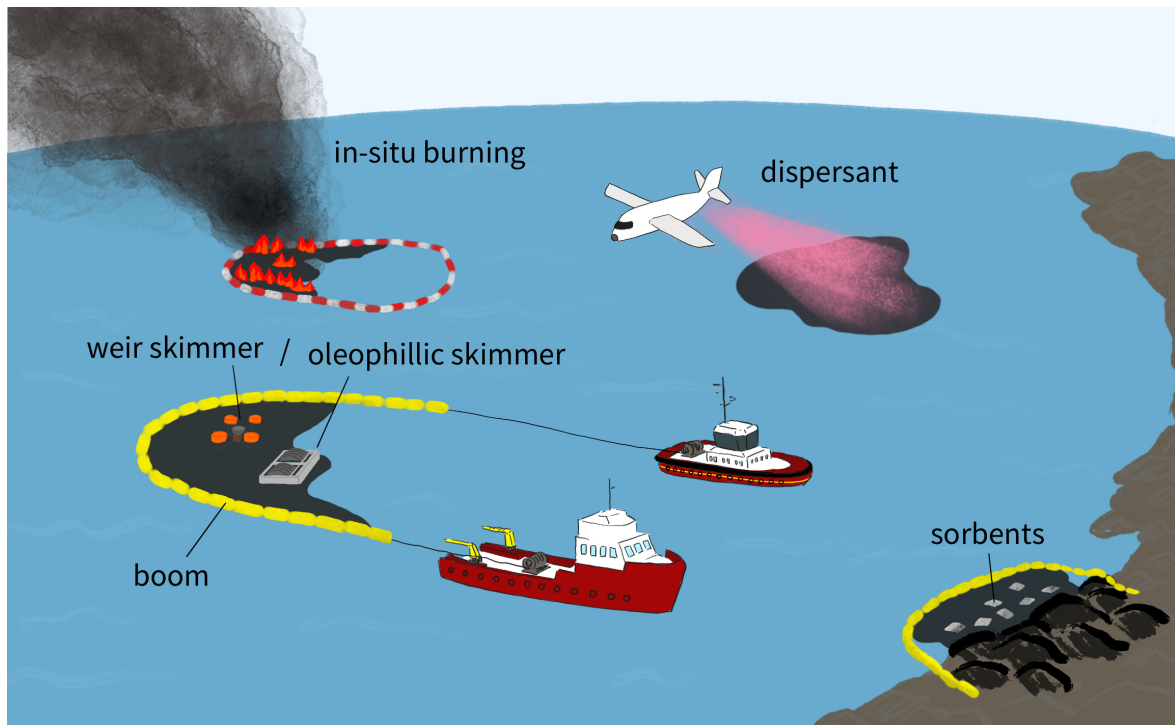


Figure 1.4: Schematic illustration of the different cleaning strategies.

In-situ burning is another method that provides an efficient response to a large area (Fingas, 2012). Ideally, it requires less equipment and labor than other clean-up methods. For example, after oil is collected with skimmers, it has to be transported and disposed of. However, in-situ burning is a final solution that can prevent the oil from spreading to other areas. It can also be used in remote areas, and is sometimes the only option, such as when oil is mixed with or on ice. On the other hand, there is the obvious disadvantage of toxic emissions in the form of large plumes of black smoke produced by burning. In addition to these clean-up strategies, bioremediation technologies have been studied to mitigate the negative impact of clean-up operations (Mapelli et al., 2017), such as the increasing toxic effect from chemical dispersants. The general idea is to enhance the metabolism of microorganisms in order to break down oil. There are two approaches: biostimulation, which supplies nutrients to indigenous microorganisms to enhance their degradation activities, and bioaugmentation, which introduces beneficial microorganisms for oil degradation.

Generally, the selection of clean-up strategies depends on the type of oil, available response resources, local regulatory framework, ambient and seasonal spill conditions, and the physical and ecological characteristics of the incident area (Walker, 2017). In practice, the environmental sensitivity index (ESI) maps indicating areas vulnerable to oil pollution due to their physical and biological resources are especially helpful for

contingency planning. These ESI maps can be created by considering different factors, such as the concentration of wildlife, human facilities, natural features, types of shoreline, and containment strategies within a given area (B. Chen et al., 2019; Fingas, 2012). Guidelines for defining sensitivity indices and creating maps have been established by several organizations, including the Association of Oil, Gas and Renewable Energy Companies of Latin America and the Caribbean (ARPEL) (Wotherspoon et al., 1997), NOAA (J. Peterson, 2002), and the International Petroleum Industry Environmental Conservation Association (IPIECA) (IPIECA et al., 2012). A more recent paper provides a thorough review of the development of the ESI, supported by various sources of literature (D’Affonseca et al., 2023).

1.1.3 Environmental impact

Oil pollution can be harmful to marine organisms due to its toxic effect if the oil components are bioavailable. As the oil weathers, it is transported into the air and water column, making it more biologically available to organisms. On the other hand, bioavailability also depends on the composition of the oil. For example, some components may be considered harmful but are less soluble in water, resulting in lower bioavailability (Boyd et al., 2001). The composition of the oil, its physical and chemical properties, and the weathering conditions all affect its concentration and toxicity. Organisms can be exposed to and affected by oil directly or indirectly through various routes, including physical contact, ingestion, inhalation, and absorption (Saadoun, 2015). Fingas (2012) provided examples of the impact of oil on different animals, some of which are presented in the following paragraphs.

The most common route of exposure is physical contact, during which organisms are coated with oil on their feathers or furs (Saadoun, 2015). These organisms, typically birds and furred mammals, rely on their coats for buoyancy and warmth. Therefore, oil can cause them to drown and lose body heat. The influence of oil on seals, sea lions, and walruses varies depending on their age. Adult specimens can withstand a lot of oiling without dying, but young ones may not have a well-developed coat that provides enough insulation yet. Additionally, their mothers may refuse to feed them, causing them to starve to death. On the other hand, seabirds covered in oil might lose heat and thus stay in land areas where they would not lose as much body heat. However, this could keep them away from their food source, causing them to starve.

Physical contact with oil also increases the likelihood of exposure through ingestion, inhalation, and absorption. Oil can be directly ingested by an organism in two ways: either by eating food that has been coated with it or by ingesting the oil directly. For example, otters and polar bears tend to groom themselves after being oiled and there-

fore ingest oil. In addition, polar bears are attracted to lubricating oil and will even drink it. Similarly, birds ingest oil when they preen their oily feathers. Ingestion of oil can change their behavior, such as stopping to lay or laying fewer eggs, or can decrease hatchability of their eggs. Oil can also be ingested indirectly by eating prey or food contaminated with oil. For example, an animal could eat prey that swallowed oil a week ago. This allows toxins to pass through the food chain and become bioaccumulated. As oil weathers, volatile oil components can evaporate and be inhaled by mammals and birds. This can lead to irritation of the respiratory tract and narcosis (Saadoun, 2015). On the other hand, oil can collide with mineral matter, forming aggregates that sediment to the bottom of the water column. Benthic invertebrates, fish, and plants may therefore absorb oil and die when the concentration of hydrocarbons is high. Such biological impact has been analyzed after some large oil spill accidents, such as the *DeepWater Horizon* oil spill (see Figure 1.1 for its location). According to a report from NOAA, it is estimated that approximately 56 100–102 400 birds of at least 93 species, 4900–7600 large juvenile and adult sea turtles, and 55 000–160 000 small juvenile sea turtles were injured or died as a result of the spill (Westerholm & Rauch III, 2016). The report also included the impact on other organisms, such as benthic resources, nearshore and shoreline resources, and marine mammals.

In addition to the biological impact on individual organisms, oil spills can have serious ecological, environmental, and socio-economic consequences. In 2020, the bulk carrier *Wakashio* ran aground on a coral reef off the southeastern coast of Mauritius and began to leak its engine fuel around two weeks later (see Figure 1.1). The spill has impacted several highly ecologically sensitive areas, including Blue Bay Marine Park, a designated Wetland of International Importance under the Ramsar Convention; Île aux Aigrettes, a coral island home to many rare and endangered species of plants and animals; and a mangrove forest, protected under the Ramsar Convention (Seveso et al., 2021). It caused huge environmental damage, which, in turn, affected the economy of Mauritius, as tourism based on natural resources has played a major role in their economy. However, the long-term ecological and environmental impacts would require examination over the course of several years. A previous study examined the long-term impact of some major oil spills (Barron et al., 2020). The *Exxon Valdez* oil spill in March 1989 (see Figure 1.1) affected the intertidal zone due to the oil itself and the clean-up operations. As of October 1992, about 2 % remained on intertidal shorelines and about 13 % remained in subtidal sediments (Wolfe et al., 1994). Even 10 years after the spill, oil remained buried under the most contaminated beaches, posing a potential hazard to organisms. Conversely, the extensive and rapid removal of oil following the *Hebei Spirit* spill (see Figure 1.1) limited its long-term impact and facilitated the

recovery of the affected ecosystem. Barron et al. (2020) summarized that the long-term ecological impacts are controlled by factors including the composition, volume, and trajectory of oil, as well as response actions and environmental conditions.

1.2 Oil slick detection with remote sensing

In order to perform a proper clean-up, several measurements should first be made to obtain the properties of the oil in question. Such information can be obtained with the help of remote sensing techniques. Remote sensing sensors receive electromagnetic (e.m.) radiation from the ocean surface within their field of view (FOV). For sensors mounted on a satellite or an aircraft, as e.m. radiation passes from the sea surface through the atmosphere to the sensor, certain constituents of the atmosphere, such as water vapor (H_2O), ozone (O_3), carbon dioxide (CO_2), and aerosols, absorb the radiation (Robinson, 2004). For example, most radiation with wavelengths shorter than 300 nm is absorbed, and ozone is considered the primary absorber (Horvath, 1993); carbon dioxide and water vapor are principal absorbers for wavelengths at around 2.5–3 μm and 5–8 μm (Schowengerdt, 2007); for wavelengths between about 20 μm and 3 mm, there is almost complete absorption (Robinson, 2004). In other ranges of the spectrum, the transmittance of e.m. waves through the atmosphere is high; these regions are referred to as atmospheric windows. Therefore, most remote sensing sensors operate in the spectral regions within these windows. Figure 1.5 illustrates parts of the e.m. spectrum on which sensors operate for oil spill detection. The gray background indicates ranges with high atmospheric absorption. Note that because the atmosphere varies from place to place and day to day, the transmittance of e.m. waves through these optical windows also varies. The horizontal bars show the spectral regions used by various passive and active sensors for oil spill detection. Detailed explanations of optical and microwave sensors are provided in Subsection 1.2.1 and Subsection 1.2.2, respectively. A combination of different sensors deployed on ships, aircrafts and satellites can provide a complete and comprehensive view of the oil, as explained in Subsection 1.2.3.

1.2.1 Optical sensors for oil slick detection

The term “optical” comes from the ancient Greek word *optikós*, meaning visible or visual. However, the optical spectrum is commonly considered to include the visible, ultraviolet (UV), and infrared (IR) spectra. The majority of solar radiation reaching the Earth’s surface has wavelengths ranging between 300 nm and 2500 nm. Therefore, sensors operating in UV, visible, and near infrared (NIR) are based on the reflectivity of sunlight. In general, the visibility of an oil slick depends on the contrast between

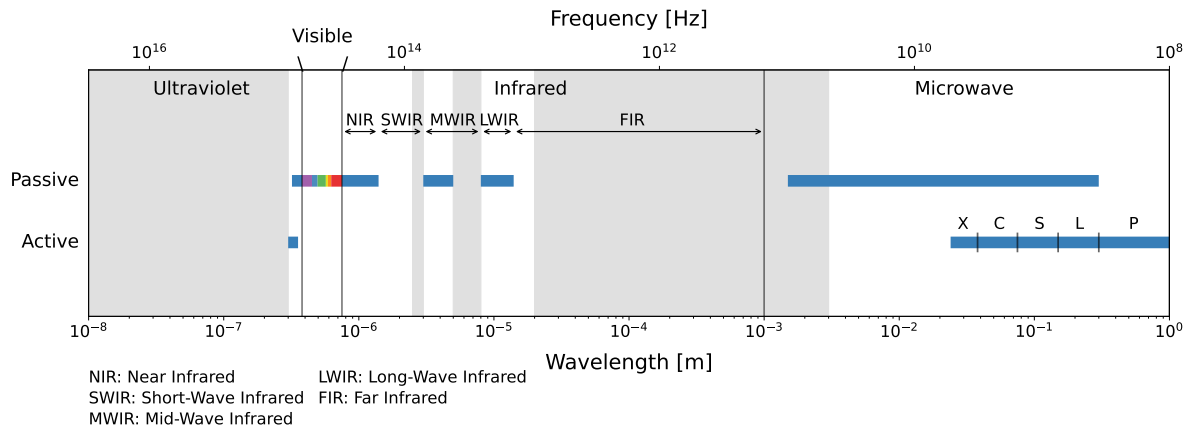


Figure 1.5: The parts of the e.m. spectrum on which the sensor operates for oil spill detection. The gray shaded areas indicate regions of high atmospheric absorption.

the slick and the surrounding water, which is affected by the position of the sun and the sensor, sea state, and the spectral characteristics and conditions of the oil (Pisano et al., 2015). Most of the thermal radiation is observed in the thermal infrared spectrum, that is, mid-wave infrared (MWIR) and long-wave infrared (LWIR). Since the far infrared (FIR) is mostly in the complete absorption range of the e.m. spectrum, sensors do not observe this range for oil slick detection purposes. The only active sensor used in the optical spectrum for oil slick detection is the laser fluorosensor, which emit illumination in the UV spectrum but receives the fluorescence emission in the visible spectrum. Table 1.1 summarizes the optical spectral regions used to observe oil slicks. The following paragraphs explain how oil slicks can be observed in different optical spectra. Most studies use short-wave infrared (SWIR) for color composite image assembly. NIR and SWIR sensors are commonly used along with visible bands observed by an imaging spectroradiometer or spectrometer (Adamo et al., 2009), or by hyperspectral and multispectral imaging (Zakzouk et al., 2024). However, studies focusing on oil signatures in the SWIR spectrum are limited. Since SWIR is dominated by both solar and thermal radiation, the concept of which will be covered in the following paragraphs about radiation in the visible and thermal spectra.

Visible & Near infrared

Photos taken in the visible spectrum can provide evidence of oil spills and are generally straightforward to interpret, since the human eye is also a passive sensor that receives radiation in the visible spectrum, ranging between 380 nm and 750 nm. According to the Bonn Agreement Handbook (Bonn Agreement, 2022), the visual shape of an

Table 1.1: Summary of optical sensors used for oil slick detection.

Spectral region		Wavelength	Passive	Active
Ultraviolet		10–380 nm	✓ (320–380 nm)	✓ (300–355 nm)
Visible		380–750 nm	✓	
Infrared	NIR	0.75–1.4 μm	✓	
	SWIR	1.4–3 μm	✓	
	MWIR	3–8 μm	✓	(3–5 μm)
	LWIR	8–14 μm	✓	
	FIR	14–1000 μm		

oil slick can suggest the probable cause of pollution. For example, long and thin oil slicks are likely the result of illegal discharges from ships; triangular slicks, with one side aligned with the wind and another aligned with the prevailing current, possibly originate from subsea releases, such as those from oil pipelines or sunken ships; a slick with some distance from a platform may result from produced water discharges; large areas covered in oil are most likely the result of an accident. In addition, the color of oil may provide hints about its volume. Table 1.2 shows the estimated oil volume based on its appearance as defined by the Bonn Agreement Oil Appearance Code (Bonn Agreement, 2022). Thinner oils tend to be silver/gray, rainbow, or metallic in color. Therefore, they are often found at the edges of thicker oils. However, visual observations may be affected by factors such as sunlight, sea state, and viewing angle. In particular, sun glint can be mistaken for oil sheens (Fingas & Brown, 2017). Depending on the conditions of the sun glint, oil can either enhance or absorb radiance, making it appear brighter or darker than its surroundings (Pisano et al., 2015). Sun glint influences images not only in the visible spectrum but also in the NIR spectrum, ranging from 0.75 μm to 1.4 μm , as the reflectivity of sunlight is a dominant factor. A previous study proposed using spectroscopic analysis of reflectance spectra to identify absorption caused by organic compounds in oil, as well as to distinguish oil from other materials in images (Clark et al., 2010). The study also found that reflectance levels and absorption due to organic compounds vary with oil thickness in the NIR spectrum. On the other hand, only minor changes were observed in the visible spectrum. This highlights the advantage of using both the visible and NIR spectra.

Thermal infrared

All objects emit thermal radiation when their temperature is above absolute zero (0 K). The radiant exitance (or radiant emittance) of a black body at certain wavelength is

Table 1.2: Estimation of oil volume based on oil appearance according to the Bonn Agreement (2022).

Appearance	Thickness [μm]	Quantity [L/km^2]
Sheen (silver/gray)	0.04–0.30	40–300
Rainbow	0.30–5.0	300–5000
Metallic	5.0–50	5000–50 000
Discontinuous True Oil Color	50–200	50 000–200 000
Continuous True Oil Color	> 200	> 200 000

proportional to the fourth power of its absolute temperature according to the Stefan–Boltzmann law. That is, higher temperature results in greater radiant exitance. The exitance is a function of wavelength and absolute temperature, and can be described by the Planck’s law. To put it another way, the exitance varies at different wavelengths for a constant temperature. According to Wien’s displacement law, the wavelength with the highest exitance is inversely proportional to the absolute temperature. The global average SST is approximately 300 K, and the exitance peak occurs at wavelengths ranging from 9 μm to 11 μm (Robinson, 2004). Therefore, LWIR, ranging between 8 μm and 14 μm , is optimal for observing SST. However, 3–5 μm in MWIR are also used, but limited by the fact that the radiation in this range is a combination of solar and thermal radiation, resulting in ambiguous results (Grierson, 1998).

Note that all of the above explanations assumed a black body as the emitter. For a gray body, a non-perfect object or surface, spectral emissivity should be considered. The spectral emissivity at a certain wavelength is defined as the ratio of its exitance to that of an ideal black body emitter at the same temperature. Combined with the information above, the exitance of a gray body (M) is proportional to its spectral emissivity (ε) and the fourth power of its absolute temperature (T). This relationship can be formulated as follows:

$$M = \varepsilon \cdot \sigma \cdot T^4, \quad (1.2)$$

where $\sigma = 5.699 \times 10^{-8} \text{ W m}^{-2} \text{ K}^{-4}$ is the Stefan–Boltzmann constant. Previous studies have shown that the IR emissivity of oil is lower than that of water and seawater (Buetner & Kern, 1965; Salisbury et al., 1993): in the 8–12 μm range, the expected emissivity is 0.993 for water, 0.986 for seawater, 0.972 for a thin film of petroleum oil, and 0.966 for a thin film of corn oil; in the 10.4–12.5 μm range, the expected emissivity is 0.989 for seawater and 0.96 for an aged crude oil slick. The difference in emissivity results in variations in the measured emitted radiance, also known as brightness temperature, which enables oil slicks to be detected with an IR radiometer. However, the emissivity also varies with the incidence angle of the sensor and surface wind speed, and these

factors should be considered (Masuda et al., 1988; Watts et al., 1996). Additionally, seaweed, sediment, organic matter, shorelines, and oceanic fronts may be mistaken for oil slicks.

Ultraviolet

Thermal IR sensors are used for oil slick detection based on the difference of brightness temperature between seawater and oil. Similarly, the difference in the reflectivity of sunlight in the UV range between oil slicks and seawater makes it possible to use UV sensors to detect oil slicks. Since most radiation with wavelengths shorter than 300 nm is absorbed by ozone, UV sensors typically observe wavelengths between 320 nm and 380 nm (Shi et al., 2015). Even thin oil with thickness of about 0.1 μm can have a high reflectivity of UV radiation (Catoe, 1973; Fingas & Brown, 2017). The reflectivity depends on oil type, water quality, and illumination conditions (Catoe, 1973). However, phenomena such as wind slicks, sun glints, and biogenic material can mistakenly be regarded as oil slicks. Therefore, UV is rarely used alone, but rather, it is commonly combined with IR because the phenomena that can be mistaken for oil slicks differ between the two sensors (Fingas & Brown, 2017).

Laser fluorosensors

Laser fluorosensors are active sensors, which can be operated day and night. They enable the monitoring of oil spill and exploration of marine petroleum resources already since the 1970s (Measures & Bristow, 1971). Generally, they are operating between 300 nm and 355 nm in UV range (Brown & Fingas, 2003). Laser fluorosensors emit a signal that electronically excites certain compounds in a material to a higher energy state. Then, as these excited molecules return to their ground state, they return fluorescence with longer wavelengths. For crude oil, the fluorescence emission is within the wavelengths of 400 nm to 550 nm in the visible band (Brown & Fingas, 2003). Another study measured the peak of fluorescence emission of various oils (Yamagishi et al., 1999): light oil at around 350–400 nm, Bunker A heavy fuel oil (marine diesel oil) at around 400–450 nm, and Bunker C heavy fuel oil (bunker oil) at around 450–500 nm. At the operating wavelengths, suspended and dissolved organic matter, such as chlorophyll and colored dissolved organic matter (CDOM), can also be excited. The peak of chlorophyll fluorescence emission is at around 685 nm, which is significantly different from the fluorescence of crude oil (Brown & Fingas, 2003). CDOM, also known as gelbstoff or yellow matter, absorbs radiation ranging from the UV to blue light spectrum, giving it a yellow-brown appearance. The dominant source of CDOM

in the coastal area is river runoff (Grüner et al., 1991). The return fluorescence has a wavelength centered at approximately 420 nm, which may interfere with the detection of thin oil films or light oil; however, for thicker oils ranging from 10 μm to 20 μm , CDOM becomes less visible or disappears from the image (Brown & Fingas, 2003). Additionally, Raman scattering of water molecules is observed, which corresponds to the concentration of fluorescent substances. The ratio of the measured Raman scattering intensity above the slick to that in the surrounding oil-free water is related to the light absorption coefficient within the oil film and thickness of the oil film (Grüner et al., 1991). Therefore, this property has been used for oil thickness estimation.

1.2.2 Microwave sensors for oil slick detection

The microwave spectrum ranges from wavelengths of 1 mm to 1 m. It is usually referred to by frequency rather than by wavelength. That is, it ranges from 300 GHz down to 300 MHz. Microwave sensors are less dependent on the weather compared to the optical sensors mentioned in the previous subsection. Additionally, they are not dependent on sunlight, allowing them to operate day and night. Both passive and active microwave sensors are used in oil slick detection.

Microwave radiometer

A microwave radiometer is a passive sensor that detects naturally occurring radiation. It typically operates at a fixed frequency ranging from 1 to 200 GHz (i.e. 300 down to 1.5 mm in wavelengths) (Robinson, 2004). The emitted spectral radiance at certain frequencies can be formulated with the Planck's law and further simplified with the Rayleigh–Jeans approximation since the microwave frequency is low. It turns out that the measured emitted radiance, also referred to as brightness temperature, has a linear relationship with the absolute temperature of the emitting surface and the emissivity of the surface. Differences in emissivity between seawater and oil slicks could result in differences in brightness temperature. Previous studies have shown that the brightness temperature is higher in areas covered by oil slicks than in the clean seawater surrounding them, and it can be regarded as a function of oil thickness (Hollinger & Mennella, 1973). Another study found that the relationship between brightness temperature and oil thickness follows a periodic pattern (Skou, 1986). Therefore, using a multiple-frequency radiometer to estimate oil thickness has been suggested (Fingas, 2018; Skou, 1986). A previous study has suggested that a radiometer operating at 30–40 GHz can provide a good estimation of the thickness of thin oil films; however, accurately determining the volume of certain films would also require a lower-frequency

radiometer, such as one operating at 10–18 GHz (Skou, 1986). Another study noted that the limitation of the microwave radiometer to the estimation of oil slick thickness is for oil thicknesses greater than about 0.05 mm (Hollinger & Mennella, 1973).

Radar

Radar, short for radio detection and ranging, is an active sensor that operates in the microwave part of the e.m. spectrum to detect objects and measure their distance from the sensor. A radar can be placed directly below the platform to observe in the nadir or near-nadir direction, as with a radar altimeter. Radar altimeters are used over the ocean to determine the topography of the ocean surface and estimate local wind speeds and significant wave heights. Alternatively, it can be placed slanted, as with a scatterometer or an imaging radar, to cover a larger area. This makes them suitable for oil spill detection. The general idea is that radar sensors emit pulses toward the sea surface at a certain incidence angle and then receive the radar backscatter. The reflected signals are a combination of specular reflections and diffuse scattering, depending on sea surface roughness, which responds to wind stress. Wind stress can be explained as the horizontal flux of momentum from the atmosphere to the ocean, driving turbulent mixing at the air–sea interface (Robinson & Fangohr, 2010). Surface films, such as oil slicks, can suppress such turbulence; this dampening effect results in low radar backscatter (Robinson, 2004).

The Bragg resonance model is widely used for interpretation of radar backscatter from the sea surface for incidence angles (θ) between 20° and 70° . Figure 1.6 illustrates a periodic wave with orange circles indicating the specific phase of the wave that have radar backscatter to the sensor. These scatterers will form constructive interference if they satisfy the Bragg condition:

$$\lambda_w \sin \theta = \frac{n\lambda}{2} \quad n = 1, 2, \dots \quad (1.3)$$

where λ is the wavelength of radar. Since ocean surface waves are a combination of waves ranging from short capillary waves with wavelengths of a few millimeters to wind-generated waves with wavelengths of hundreds of meters, λ_w denotes the ocean wavelength that fulfills the Bragg resonance for a given radar wavelength, λ . For example, considering a C-band Sentinel-1 SAR scene acquired in Interferometric Wide mode with a wavelength of 5.6 cm and an incidence angle between 29.1° and 46° , the obtained λ_w/n is between 5.8 cm and 3.9 cm. It shows that the waves that induce Bragg resonance have a wavelength similar to the radar wavelength. These waves are typically classified as gravity-capillary waves with wavelengths of a few centimeters.

Such waves are driven by wind stress, but affected by surface tension and gravity. The presence of surface films can reduce surface tension and therefore dampen the waves. However, in addition to oil slicks, other oceanic and atmospheric phenomena such as wind shadows, internal waves, upwelling, biogenic surface films, and current shear zones can also result in low radar backscatter and are known as “look-alikes”. In theory, both scatterometers and imaging radars can detect oil spills. However, scatterometers measure radar backscatter over a wide FOV. On the other hand, imaging radars, such as side-looking airborne radar (SLAR) and SAR, provide finer resolution and are therefore more commonly used. Radar backscatter varies with the incidence angle. It is usually not possible to distinguish an oil slick from its surrounding clean water at incidence angles lower than 30° (Gade et al., 1998). Although radar bandwidths ranging from X-band to P-band are commonly used in SAR, oil spill detection most often uses the L-, C-, and X-bands (Jafarzadeh et al., 2021).

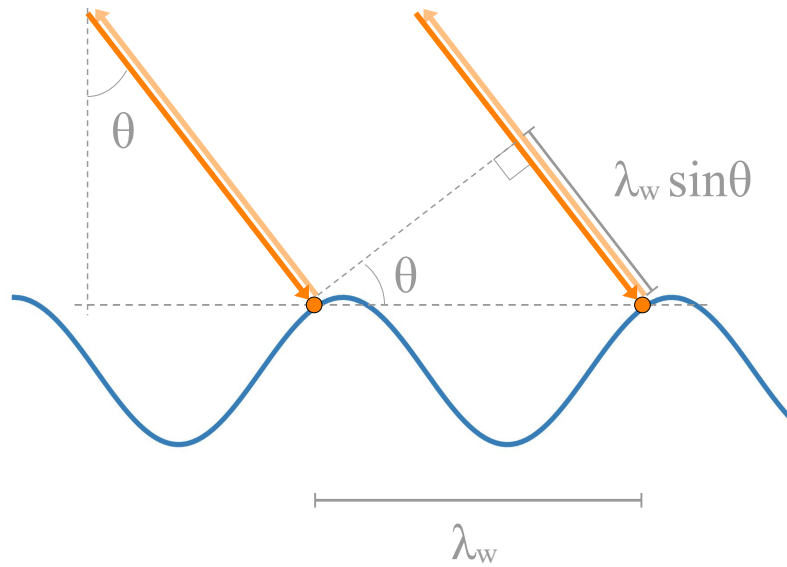


Figure 1.6: Illustration of the Bragg resonance geometry. The orange circles indicate the specific phase of the periodic waves that spectrally reflect back to the sensor. The sensor emits the signal at an incidence angle, θ . These scatterers are spaced λ_w apart and form constructive interference when they satisfy the Bragg condition in Equation 1.3.

It is usually expected that radar sensors cannot provide oil thickness estimation. However, a previous study used a series of scatterometers in an experiment to show the capability of active radar to measure oil spill thickness when the oil type is known (True et al., 1994). The study examined how various factors contribute to the radar backscatter of oil, such as oil thickness, viscosity, incidence angle, wind angle, radar frequency,

and polarization. Another study used SAR data with different bandwidths, including L-, S-, C-, and X-band, from airborne and spaceborne platforms to verify the possibility of identifying thicker oil in a slick (Jones, 2023). This could enable a more targeted clean-up response.

1.2.3 Existing oil spill monitoring systems

Oil spill monitoring systems can detect oil spills and assist the responsible authorities with decision making and emergency response, and prevent the further spreading of the oil. The sensors described in Subsections 1.2.1 and 1.2.2 can be deployed on shipborne, airborne, or spaceborne platforms to support different phases of an oil spill response.

Shipborne radar can be operated almost continuously in time and repeatedly at the oil spill sites at a low cost, providing real-time observations that are particularly useful during the clean-up period (Xu et al., 2019). A commercial shipborne oil spill detection system, the Miros OSD system, has been tested in three field trials for its ability to detect and track oil spills through continuous observation (Nost & Egset, 2006). Depending on the height of the antenna, a shipborne radar typically has a detection range of between 8 and 30 km (Fingas & Brown, 2017). With the advantages of being able to observe in fog, rain, darkness, and even in relatively high sea states (Tennyson, 1988), shipborne radars have been used in several commercial oil spill detection systems, such as Miros (Nost & Egset, 2006), SeaDarQ (Swinkels et al., 2012; van Gils, 2014) and SHIRA (Saleh, 2004). However, recent improvements and developments of these technologies have not been reported in the literature due to commercial competition and corporate confidentiality policies. Still, some studies utilized the radar data collected in oil spill accidents from shipborne radar. On 16 July 2010, two pipelines ruptured in the Xingang Port, China, causing an oil spill into the Yellow Sea. A few days after the accidents, a teaching-training ship, YUKUN, collected data from X-band radar and LWIR sensors during the clean-up operation. These data allowed researchers to develop oil spill detection methods to obtain the extent of oil slicks from shipborne radar imagery, such as thresholding (Zhu et al., 2015), adaptive thresholding (Liu et al., 2019; Xu et al., 2019), and active contour models (Xu et al., 2021), and validate their results with LWIR imagery. In addition to radar and LWIR, laser fluorosensors have also been deployed on the shipborne platforms, as presented in another study (Yamagishi et al., 2001).

Shipborne systems can be helpful for tracking the oil; however, the airborne system still plays an important role in emergency response because of its flexibility in sensor selection, allowing a combination of sensors to be used to provide essential information (e.g., oil type and oil thickness) for clean-up operations (Brown & Fingas, 2005). Ever

since the 1980s, there has been a suggested collection of sensors used for airborne oil spill monitoring, including a SLAR, IR/UV imaging devices (e.g. IR/UV line scanners), microwave radiometers, and laser fluorosensors (Robbe & Hengstermann, 2006). Some commercial software has been developed to analyze data from such multi-sensor platforms and provide an interface to support pollution management, such as the MEDUSA system (Robbe & Hengstermann, 2006) and the MSS 6000 system (Dyring & Fäst, 2004). Previous studies have also shown that unmanned aerial vehicles (UAVs) offer a more cost-effective solution than traditional aircraft and could therefore be helpful in emergency response (Brown, 2025; T. Chen & Lu, 2017; de Laurentiis et al., 2021; Jiao et al., 2019).

As for regular monitoring, the high cost and limited coverage of airborne systems typically limits their focus to areas of frequent spills, such as from ships, pipelines and oil rigs (Brown & Fingas, 2005). On the other hand, satellites have the capability for surveillance over large areas due to their wide coverage. Several early studies demonstrated the use of satellite SAR data for routine observations over certain waters (Biegert et al., 1997; Gade & Alpers, 1999; Ivanov & Ermoshkin, 2004; Ivanov et al., 2002; Lu et al., 1999; Pavlakis et al., 2001). Long-term monitoring of specific areas can provide information on the level of pollution in different zones; for example, pollution in some areas may be well aligned with major shipping routes (Gade & Alpers, 1999). It can also help to narrow down areas at risk where increased monitoring coverage is suggested, raise societal awareness, and put pressure on responsible authorities to take action (Ferraro et al., 2009; Lu et al., 1999).

These and other studies have pointed out the role of spaceborne SAR in early warning of oil spills. However, they have less flexibility in terms of observation time due to their fixed orbit; therefore, the combination of spaceborne SAR and other passive optical sensors can fill spatial and temporal gaps and enhance temporal resolution. For example, an operational system for the Southern Gulf of Mexico uses multiple spaceborne optical and radar sensors (Uribe-Martínez et al., 2024). Another study used multiple spaceborne sensors to detect and track an oil spill after a tanker accident in the Red Sea in 2019 (Vankayalapati et al., 2023). Spaceborne optical sensors use multispectral and hyperspectral imaging to acquire reflected radiation from surfaces across different spectral bands. For example, a combination of bands from Landsat-8, including green, blue, NIR, SWIR, and coastal/aerosol bands, has been used for oil slick detection (Schmidt et al., 2024). Spectral analysis can provide information about oil properties, such as thickness and type, and help distinguish actual oil spill from other features such as algal blooms (Brekke & Solberg, 2005). However, several features, including thin clouds, cloud shadows, dust, suspended sediments, and areas with shallow

water, can have reflectance like oil (Schmidt et al., 2024). Consequently, spaceborne optical data alone may not be sufficient to identify oil spills. Therefore, combining optical and SAR sensors can enhance their collective ability to detect oil spills and distinguish them from natural seepage. An example of this was presented in Bayramov et al. (2018) for long-term monitoring of the Caspian Sea.

Different platforms have different advantages and disadvantages; each plays a unique role in the overall oil spill surveillance system. In short summary, spaceborne SAR is suitable for regular surveillance over a larger area and provides early warning of an oil spill incident. Spaceborne optical images can help improve the spatial and temporal coverage and provide additional information about oil. Afterwards, a multi-sensor airborne system can collect the necessary information about the oil for clean-up operations. Combined with the local information, such as ESI maps showing vulnerable resources in the area, clean-up strategies can be implemented. During the clean-up operations, shipborne radars can help with the real-time tracking of the oil. Additionally, the automatic identification system (AIS), along with oil spill trajectory model, can be included to identify the polluters (Busler et al., 2015). The ENVISYS project was one of the early projects to connect oil spill detection using SAR with emergency management units for better decision support in the Mediterranean Sea (Theophilopoulos et al., 1996).

Since 1994, the Norwegian Kongsberg Satellite Service (KSAT) has provided a manual oil spill detection service, delivering results provided by trained operators. The operators analyze SAR images and use supporting information, such as wind speed and direction, the location of oil rigs and pipelines, national borders, and coastlines (Brekke & Solberg, 2005). Similarly, the Global Monitoring for Environment and Security (GMES) programme, a joint program of the European Commission and European Space Agency (ESA), has supported several projects such as MARCOAST (Cotton, 2007) and the CleanSeaNet service (European Maritime Safety Agency, 2017). The latter is run by the EMSA and has been operational since 2007 with a focus on European waters. Together with the African Union Commission, GMES also supported the NAFcoast project, which focused on oil spill contingency planning along the North African coast, in particular the potential threat to fishing areas (Abou El-Magd et al., 2020). This project emphasized the importance of cooperation with regional stakeholders. Although these oil spill monitoring services are either semi-automated or fully automated, alerts are only issued after confirmation by experienced operators. This helps avoid false alerts and the resulting costs of clean-up operations. However, these services can already provide information such as wind speed, sea state, and the location of offshore oil and gas infrastructure.

1.3 Oil slick detection using spaceborne SAR

Early experiments were conducted to evaluate and demonstrate the capability of spaceborne SAR for early detection of oil spills (Bern et al., 1993) and to investigate the damping effect of oil slicks observed with different bandwidths (i.e. C-band, X-band, and L-band), different polarizations, and different wind speeds (Gade et al., 1998; Masuko et al., 1995). Later, several studies focused on mapping oil spills in specific pollution hotspots such as the Gulf of Mexico (Biegert et al., 1997), European waters (Gade & Alpers, 1999), the Caspian Sea (Ivanov & Ermoshkin, 2004), the Mediterranean Sea (Pavlakakis et al., 2001), and Asian waters (Ivanov et al., 2002; Lu et al., 1999). These studies evaluated oil spill monitoring using spaceborne SAR. They also pointed to its ability to support risk management systems, as demonstrated by another study that focused on possible monitoring during an oil spill incident (Werle et al., 1997).

In order to detect spills efficiently, researchers tried to automate the oil slick detection process. As oil slicks appear as dark formations in SAR imagery, the identification of pixels containing oil can be extracted using segmentation methods, such as thresholding (Kanaa et al., 2003; Solberg et al., 1999) and edge detection based on the image histogram (Del Frate et al., 2000). However, the visibility of oil slicks decreases over time due to weathering, which affects the detectability of oil in SAR imagery (Brekke & Solberg, 2005). In addition, discriminating between oil slicks and look-alikes has been a challenging task. Previous studies used various characteristics, such as texture and geometric features of the dark formations, physical characteristics of the radar backscatter, and other contextual information (e.g., wind speed), to classify dark formations in SAR images as oil slicks or look-alikes (Brekke & Solberg, 2005; Topouzelis, 2008). In addition, the use of dual co-polarization and quad-polarization scenes has been claimed to improve classification with their additional polarimetric features (Fortuny-Guasch, 2003; Migliaccio et al., 2007); however, these polarization combinations are limited to specific missions such as SIR-C/X-SAR, RADARSAT, and TerraSAR-X. Therefore, machine learning techniques were applied for feature selection and helped to improve the accuracy of classification of oil slicks and look-alikes (Singha et al., 2013; Topouzelis et al., 2007).

Although SAR imagery has sufficient spatial resolution to detect small illegal discharges from vessels that are a few to tens of kilometers in length and less than 1 km in width (Konik & Bradtke, 2016), oil spill monitoring mostly focused on areas at high risk of oil pollution or on specific oil spills due to the high cost of commercial SAR data. In this regard, SAR data were acquired from various satellite platforms following accidents to track the spatial and temporal changes of oil slicks; examples of accidents include

the *Hebei Spirit* tanker accident in 2007 (D.-J. Kim et al., 2010; T.-S. Kim et al., 2015) and the *DeepWater Horizon* oil spill in 2010 (Garcia-Pineda et al., 2017; Marghany, 2015; Wan & Cheng, 2013) (see Figure 1.1 for their locations). These SAR data also enabled studies to compare observations from different radar bandwidths and to apply machine learning techniques for better classification of oil slicks and look-alikes. After the launch of the Sentinel-1 mission from ESA under the Copernicus Programme in 2014, the number of available and free SAR scenes has increased. From 1990 to 2020, 42 % of the research papers related to oil spill detection were published between 2016 and 2020; note that these statistics only include papers published by September 2020 (Jafarzadeh et al., 2021). The authors suggested that the launch of Sentinel-1 was the possible reason. The large amount of available Sentinel-1 data also enables the introduction of data-driven deep learning methods in remote sensing applications.

Most deep learning-based methods for SAR oil slick detection can be categorized as image classification, object detection, semantic segmentation, or instance segmentation, as shown in Figure 1.7. The general objective is to identify objects of interest in the images, such as oil spills, look-alikes, and ships. Some of the methods also define non-object classes, such as sea and land. Image classification algorithms categorize images into different classes based on the likelihood that an image belongs to each class. Object detection algorithms identify objects in images and return bounding boxes of the objects along with their corresponding classes. Semantic segmentation algorithms classify each pixel in an image as belonging to a specific class of object or non-object. Instance segmentation algorithms provide the exact boundaries of detected objects; each object has a segmentation mask showing its exact location.

Semantic segmentation methods are the most commonly used deep learning-based method for SAR oil slick detection. They directly provide the boundaries of objects of interest; however, since SAR images are large and pixel-wise classification is computationally expensive, an additional step, such as patch-based image classification, is suggested to refine the area of interest. For example, the given SAR image is divided into patches, which are then classified using a convolutional neural network (CNN) model. If the results of the patch-based classification indicate a high probability of oil presence in a given patch, a different CNN model is applied to obtain a pixel-wise classification of that patch (Shaban et al., 2021; Trujillo-Acatitla et al., 2024). On the other hand, object detection algorithms can also be used to identify regions with potential oil slicks. This would provide smaller regions of interest for the semantic segmentation method. A previous study proposed a similar idea, focusing on detecting oil slicks with SLAR and using coarse detection prior to pixel-wise classification to improve detection efficiency (Nieto-Hidalgo et al., 2018). Semantic segmentation

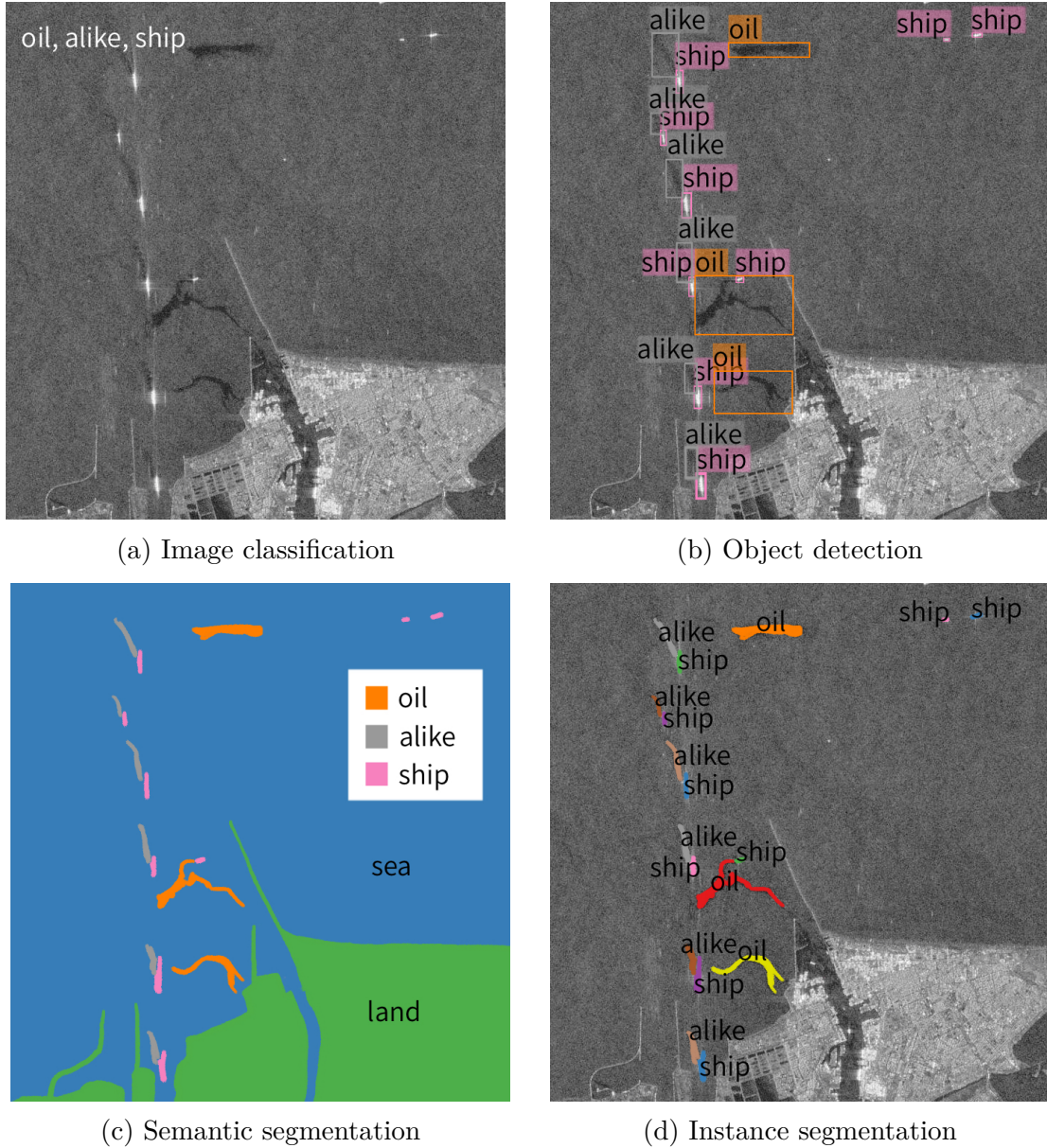


Figure 1.7: Illustration of deep learning-based methods for SAR oil slick detection.

In this example, oil spill (oil), look-alike (alike), and ship are defined as objects, while sea and land are defined as non-objects.

networks, such as U-Net, AlexNet, LinkNet, PSPNet, the DeepLab series, and SegNet, have been used in literature. Some of this literature has provided comparisons between different models (Krestenitis et al., 2019; Shanmukh & Priya, 2024). Another challenge in applying semantic segmentation methods is that oil spills typically occupy a relatively small portion of an image patch. Therefore, the imbalance of different classes should be considered during model training.

Based on the concept of object detection and semantic segmentation, instance segmentation methods offer the segmented results of objects of interest. Unlike semantic

segmentation methods, instance segmentation methods assign a mask to each individual object. This can be beneficial for oil trajectory simulation because one image may contain oil slicks from different sources. Each oil slick can have its own parameter. A commonly used instance segmentation model is Mask region-based convolutional neural network (R-CNN), which has been applied for oil slick detection but is not yet widely used (Amri et al., 2020, 2022; Yekeen & Balogun, 2020; Yekeen et al., 2020). One possible reason is that instance segmentation methods are typically more computationally complex than semantic segmentation.

These are different deep learning methods for developing an oil slick detection system. Each method has its own advantages and disadvantages depending on the purpose. For example, when it comes to an operational system, computational efficiency is one of the important factors to consider. A common challenge for all these methods is the limited availability of oil spill datasets for training models. This is due to the fact that records of spill locations and times are not always publicly accessible. Therefore, most studies have had to collect their own datasets for model training. This makes comparing results from different studies difficult. It should be noted that this thesis collected its own dataset for training and testing the system. Since it is generally not possible to obtain the type of oil, the system may consider pollution from other chemicals as oil spills, such as land-sourced wastewater.

1.4 Approach in this thesis

This thesis provides an automated oil spill detection system using spaceborne SAR data. For such a system to be useful to society, it is important and essential to cooperate with regional stakeholders. Therefore, the system is designed for the Southeastern Mediterranean Sea, in close cooperation with the Israel Oceanographic and Limnological Research (IOLR), where researchers have expertise in oil trajectory estimation.

Early studies on the automated detection of oil spills using SAR generally applied the following procedure: dark spot segmentation, feature extraction, and classification. Therefore, it may be inefficient for SAR scenes that are covered with large areas of dark formations due to look-alikes, in which case the algorithm would try to extract all the features of the dark formations for classifying them. Figure 1.8 shows an example of a SAR image covered by a large area of dark formations, which is likely due to low wind conditions. The figure illustrates the two-step approach proposed in this thesis. First, a deep learning-based object detection algorithm finds the areas of possible oil slicks, shown as bounding boxes in the figure. In this step, a sliding window is used to generate image patches for the object detection algorithm. In addition, SAR normalization

was applied by rescaling to 8-bit to optimize processing time and eliminate differences in radar backscatter between different acquisitions. The advantages of normalization have been demonstrated in previous studies (Bayramov et al., 2018; Espedal & Johannessen, 2000; Hasimoto-Beltran et al., 2023; Karathanassi et al., 2006). Second, a segmentation method is applied to obtain the final binary masks of oil slicks. Ideally, the object detection algorithm would only target oil objects. Instead of using another deep learning-based model for segmentation, this thesis uses a segmentation method based on statistical features obtained from the backscatter coefficient. Sea surface roughness is a key factor that affects radar backscatter. Therefore, radar backscatter reflects sea states and carries meaningful information (Pleskachevsky et al., 2024). For this reason, this step uses the radar backscatter coefficient instead of the normalized SAR.

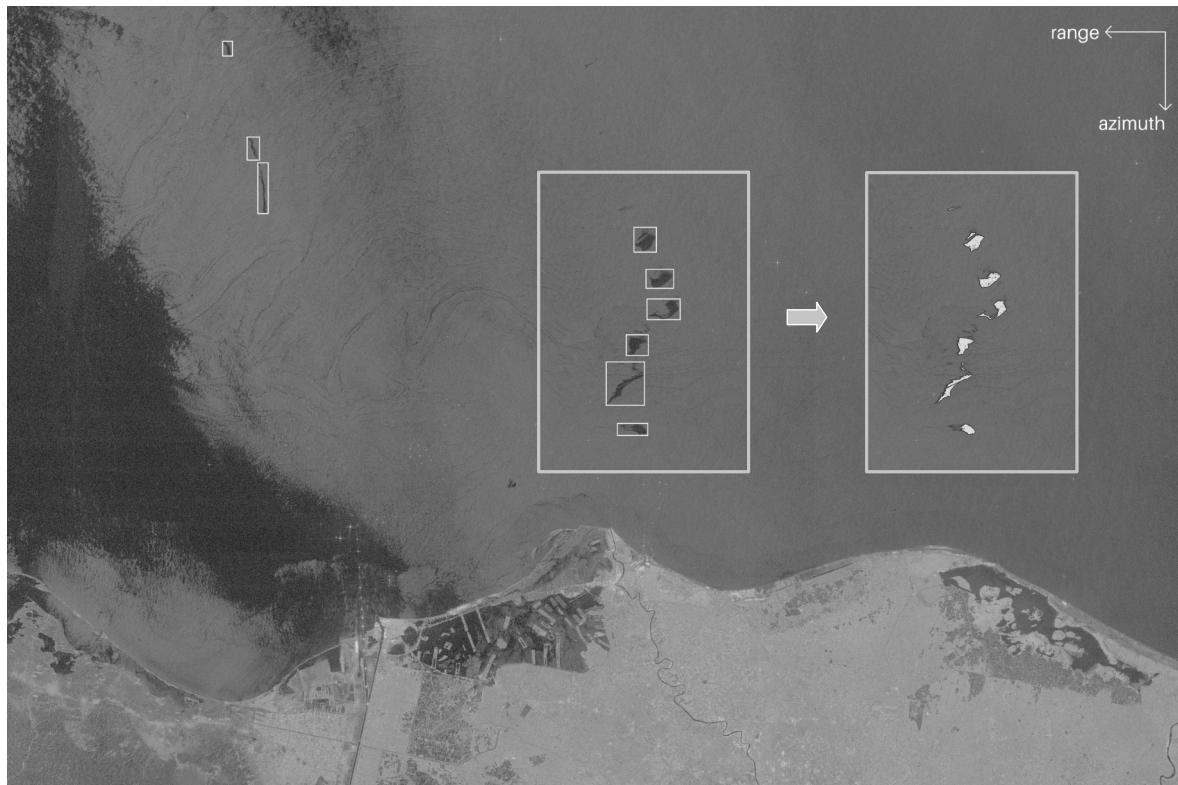


Figure 1.8: Illustration of the two-step approach proposed in this thesis. Possible oil slicks are targeted by the object detector, and the final oil binary masks are extracted by a segmentation method that focuses on these regions of interest. Sentinel-1 SAR scene taken at 03:52 UTC on 31 August 2023. The figure contains modified Copernicus Sentinel data [2023].

In theory, the proposed approach could offer a more computationally efficient detection chain than the semantic segmentation method. Additionally, different study areas have different sources and types of oil spills and look-alikes. Therefore, adapting

the developed system to a new study area may require a smaller dataset for transfer learning. Preparing a training dataset for an object-oriented method should take less time than preparing a dataset for a pixel-wise method, such as semantic segmentation. Consequently, this approach is well-suited to the objective of building an operational oil spill detection system that can easily be transferred to a different study area.

1.5 Research questions

Regular surveillance over certain areas using spaceborne SAR can contribute to providing a first warning of the occurrence of oil spills. Oil slicks dampen the gravity-capillary waves and therefore have low radar backscatter compared to the surrounding clean seawater, resulting in dark formations in SAR scenes. However, dark formations are not necessarily oil slicks; other oceanic phenomena should also be considered and understood before building an oil spill monitoring system based on SAR. The following research questions must be answered in order to develop an operational oil slick detection system using SAR:

1. **How can different oceanic phenomena manifest in SAR imagery?**
2. **How can oceanic phenomena be discriminated from oil slicks in SAR?**
3. **Can deep learning-based object detectors be used to detect oil slicks and distinguish between oil slicks and look-alikes?**
4. **What are the look-alikes that could lead to confusions for deep learning-based object detectors?**
5. **How well do deep learning-based methods perform when applied to an operational oil spill monitoring system?**

This thesis focuses on the Southeastern Mediterranean Sea as a study area, answering the research questions based on experience in this region. However, the experience from the Southeastern Mediterranean Sea can be further extended to other regions.

2 Southeastern Mediterranean Sea

The Mediterranean Sea is a semi-enclosed marginal sea. Some consider it a miniature ocean because many of the processes that occur in other oceans also occur in the Mediterranean Sea (Chiggiato et al., 2023). The Mediterranean Sea is composed of four primary basins: the Algerian, Tyrrhenian, Ionian, and Levantine basins (Elbessa et al., 2022); their locations are shown in Figure 2.1. The bounding box in Figure 2.1 shows the extent of the zoomed-in map in Figure 2.2, which indicates the focused area in this thesis. From a tectonic perspective, the zoomed-in area can be further divided into several basins, as shown in Figure 2.2 (Aksu et al., 2014; Roberts & Peace, 2007; Tassy et al., 2015). The Levantine and Herodotus basins are located in the south and are separated by the Eratosthenes Seamount. The northern basins are the Rhodes, Antalya, Cilician, and Latakia basins. Studies with a broader focus refer to the Levantine Basin as the area annotated in Figure 2.1; to avoid confusion, this area will be referred to as the Levantine Sea throughout the rest of this thesis. On the other hand, the Levantine Basin refers to the area based on regional tectonic structure, as shown in Figure 2.2.

This thesis focuses on the area outlined in red in Figure 2.2, which extends from the coastline northward to 34.7° N and westward to 30° E. The study area includes the northern entrance to the Suez Canal, which has heavy maritime traffic, resulting in a high risk of oil pollution from ships. Section 2.1 introduces the possible sources of oil pollution in the study area. The fate of oil spills and SAR signatures are both related to circulation. Therefore, Section 2.2 explains the main forcings that drive circulation and mentions factors that manifest notable SAR signatures. Section 2.3 summarizes the phenomena that may resemble oil slicks.

2.1 Oil pollution hotspot

The study area has heavy maritime traffic due to shipping through the Suez Canal and the transport of crude oil between the Mediterranean Sea and the Red Sea. This increases the possible operational oil discharges, usually associated with shipping lanes. In addition, the discovery of gas fields in the Levantine Basin since 2009 has led to increased offshore oil and gas exploration and exploitation activities, thereby raising

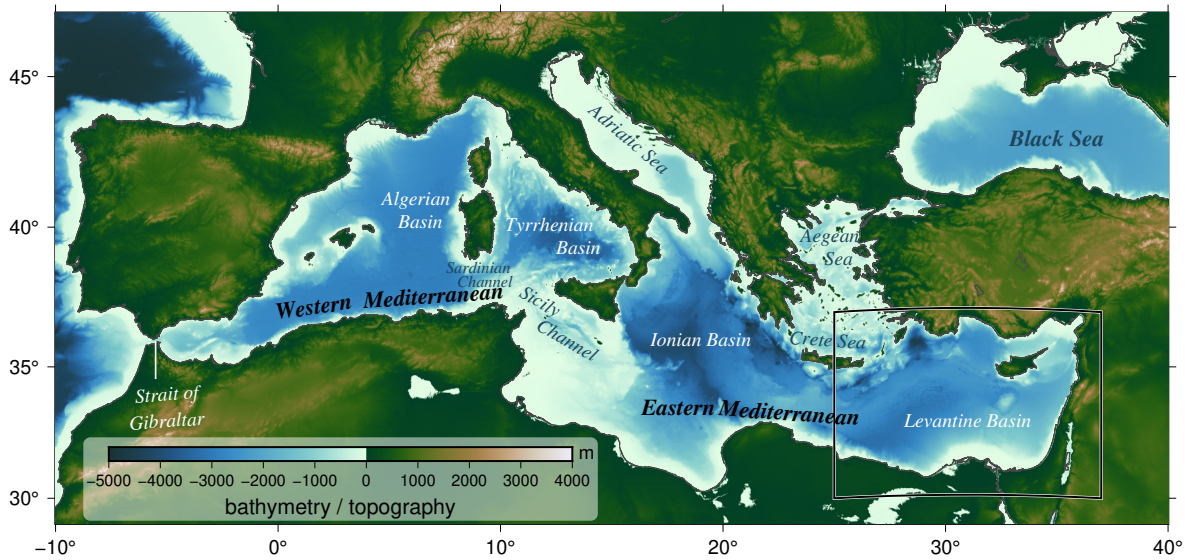


Figure 2.1: A bathymetry map of the Mediterranean Sea, which illustrates its four primary basins. The bounding box shows the extent of the zoomed-in map in Figure 2.2. The base map was plotted using the topographic and bathymetric model obtained from the General Bathymetric Chart of the Oceans (GEBCO Bathymetric Compilation Group 2023, 2023).

the risk of oil pollution. On 17 February 2021, about 550 tons (about 454 tonnes) of tar from an unknown oil spill source first beached along the central-northern shores of Israel. From 11 to 13 February, three pairs of oil slicks were observed from Sentinel-1. According to trajectory simulations, two of the slicks were likely related to the beaching on the coast, while the other pair was either unrelated or too small and had weathered by the time they reached the shoreline (Herut et al., 2024). Unfortunately, the incident occurred during the initial phase of the study, before the automated oil slick detection chain had been developed. These and other oil pollution incidents have highlighted the importance of having an oil slick detection system for early warning.

The following subsections provide an overview of shipping density (see Subsection 2.1.1) and the oil and gas exploration and exploitation activities (see Subsection 2.1.2) in the study area. On top of these factors, regional political instability, extensive coastal oil facilities, and a lack of cooperation among countries may also contribute to the Levantine Sea being an oil pollution hotspot (Polinov et al., 2021).

2.1.1 Shipping

Each year, about 600–800 million tons (about 544 to 726 million tonnes) of crude oil are transported in the Mediterranean Sea, accounting for about 30 % of the global maritime transport of crude oil (Danovaro, 2003). A later study provided a different estimate, showing that 18 % of global crude oil shipments travel through the Mediter-

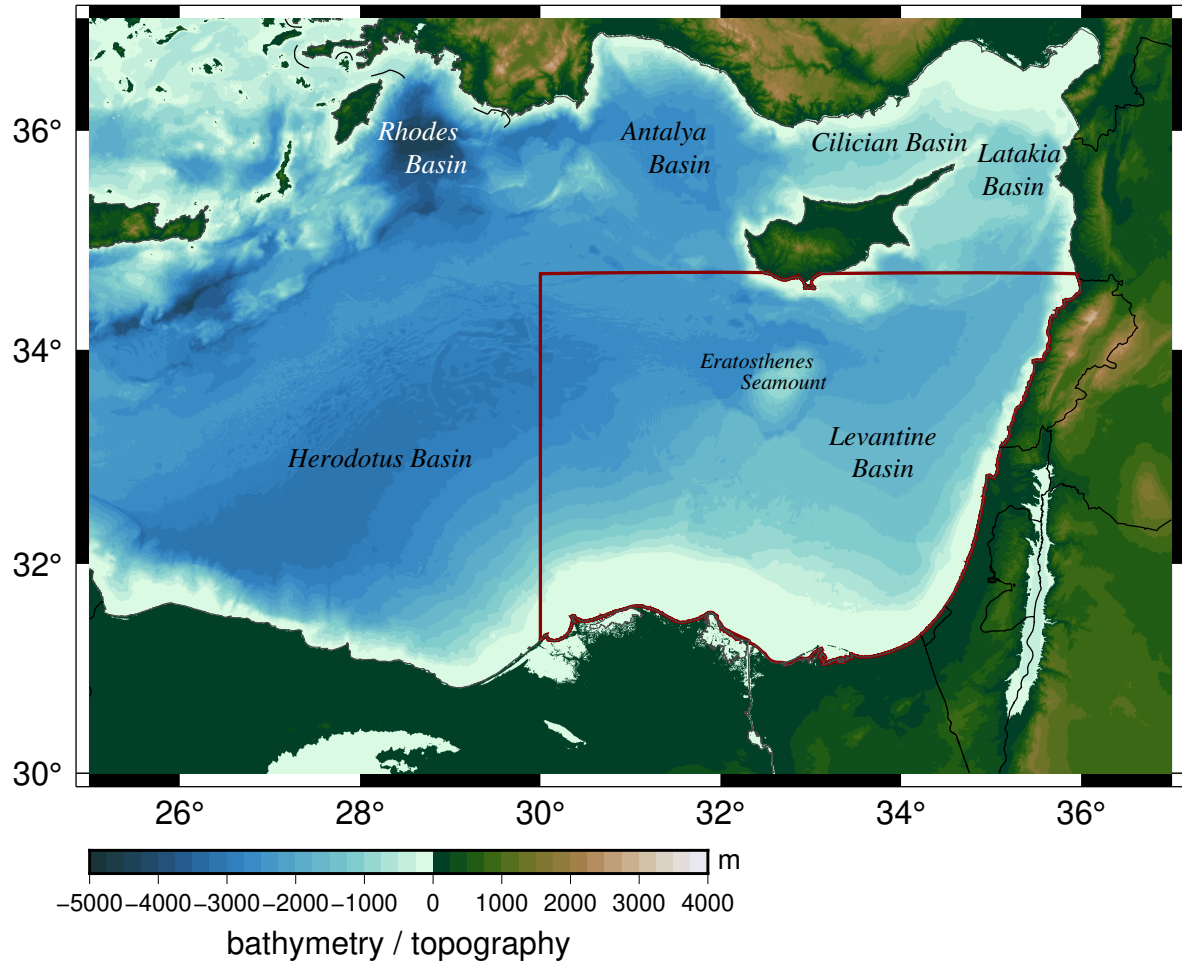


Figure 2.2: A zoomed-in map of the area within the bounding box of Figure 2.1 in the Southeastern Mediterranean Sea, which provides an overview of its different regions based on bathymetry. The enclosed areas outlined in red indicates the study area. The borders were derived from the Global Self-consistent, Hierarchical, High-resolution Geography Database (GSHHG) (Wessel & Smith, 1996).

anean Sea (Carpenter & Kostianoy, 2018). Most of the crude oil transported from the Middle East to Europe and North America goes through the Suez Canal (Abdulla & Linden, 2008). According to the Suez Canal Authority (2025), approximately 12% of global shipping trade has transited the Suez Canal for over 150 years. The high traffic in the Mediterranean Sea has led to high risks of operational oil discharges. On average, approximately 1–10 tonnes of oil are spilled from ships almost daily in the Mediterranean Sea (Carpenter & Kostianoy, 2018).

A recent study examined the geographic distribution of oil spills observed by Sentinel-1 SAR from 2014 to 2023 in the Levantine Sea, with a particular focus on the Egyptian coast (Baghdady & Abdelsalam, 2024). The study revealed that oil spills were concentrated along shipping routes and close to the Egyptian coast. Addition-

ally, oil spill incidents follow a seasonal trend. They primarily occur in the spring and summer, peaking in August, which coincides with increased maritime traffic associated with tourism and commercial shipping. However, the effectiveness of SAR observations in different seasons should also be considered. Figure 2.3 presents the number of commercial ships in each grid cell per day. These numbers were calculated from hourly AIS positions received between January 2015 and February 2021, which are provided by Cerdeiro et al. (2020). Each grid cell has a dimension of 0.005 degree by 0.005 degree, which is approximately 500 m by 500 m at the equator. The histogram shows how many pixels correspond to different numbers of commercial ships per day. Typically, regions with heavy shipping traffic can have about 330–420 ships per day. Noted that these numbers may include both moving and stationary ships.

The previous study also pointed out that many oil spill incidents occurred in the exclusive economic zone (EEZ), which extends 200 nautical miles from the coast (Baghdady & Abdelsalam, 2024). Oil spills happened frequently in the area within about 19 km (about 10.3 nautical miles) off the coast. However, oil spills within the Egyptian territorial waters (12 nautical miles off the coast) were usually smaller than those occurring further from the coast. Similar results were found in another study, which stated that most oil slicks are distributed along the coast, with 50 % of the oil slicks observed within 38 km (about 20.5 nautical miles) off the coast and 90 % within 160 km (about 86.4 nautical miles) (Dong et al., 2022). Therefore, the oil slick detection system should be tested in different zones from the coast, such as territorial waters and EEZ.

2.1.2 Discovery of oil and gas in the Levantine Basin

The discovery of several gas fields in the Levantine Basin since 2009 has driven an increase in oil and gas exploration and exploitation activities in the region. Figure 2.4 shows the approximate locations of the discovered gas fields. From 1990 to 1999, the annual release of petroleum from platforms in worldwide marine waters accounted for about 3 % of total petroleum pollution (National Research Council, 2003). However, oil pollution from offshore oil and gas platforms in the Mediterranean is likely to account for less than 1 % of the total oil pollution, and is therefore not often discussed in the literature (Carpenter & Kostianoy, 2018).

2.2 Environmental factors

The Mediterranean Sea is governed by large-scale horizontal and vertical circulation. The main forcings driving this circulation are the exchanges through the Strait of

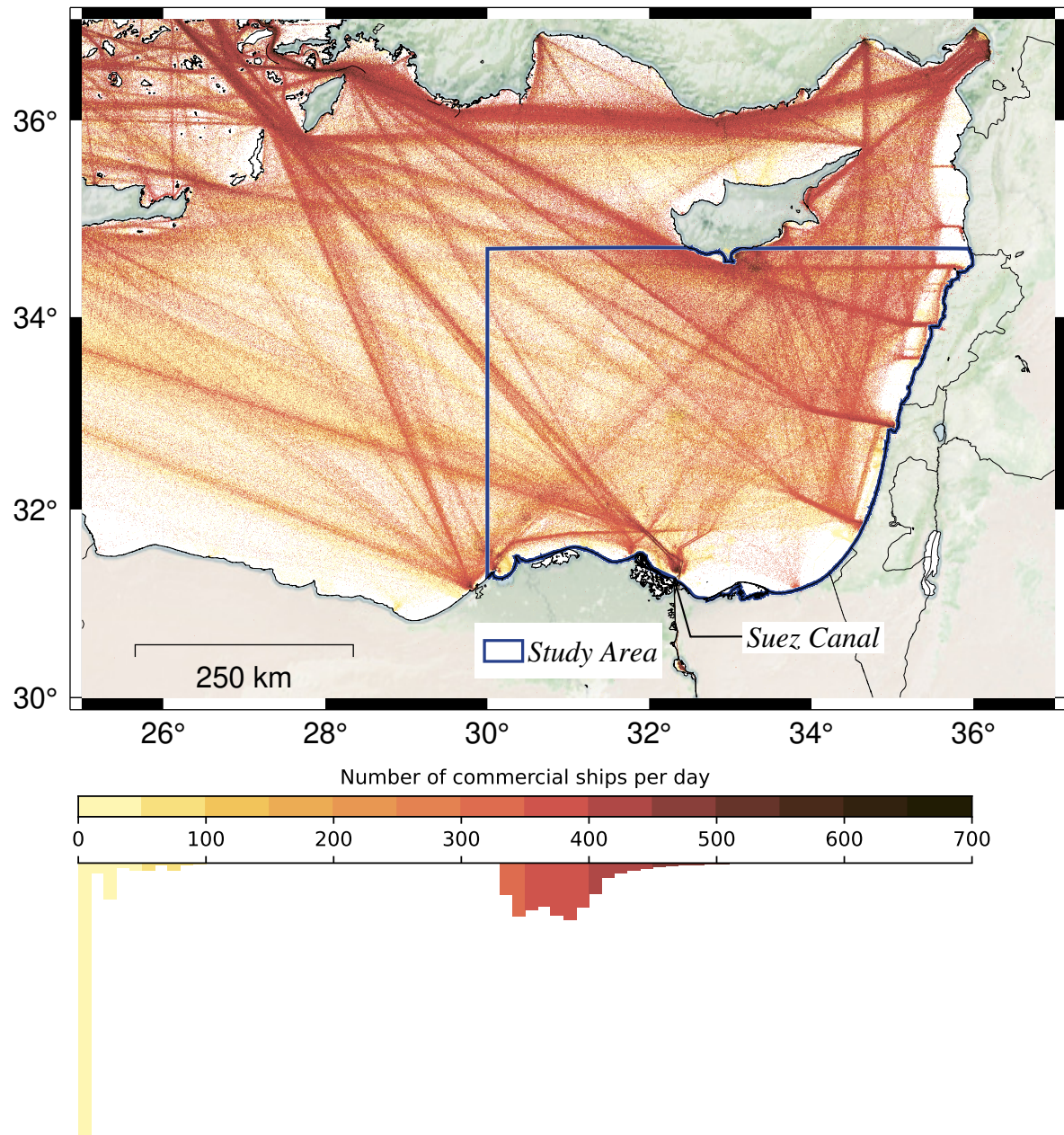


Figure 2.3: Ship density in the Levantine Sea. The map shows average numbers of commercial ships per day, calculated from the hourly AIS positions recorded from January 2015 to February 2021. The histogram shows how many pixels correspond to different numbers of commercial ships per day. Data source: IMF's World Seaborne Trade monitoring system (Cerdeiro et al., 2020); available at <https://datacatalog.worldbank.org/search/dataset/0037580/Global-Shipping-Traffic-Density> (access: 2025-05-22), licensed under CC BY 4.0 (<https://creativecommons.org/licenses/by/4.0/>). The basemap is obtained from Stevens (2020).

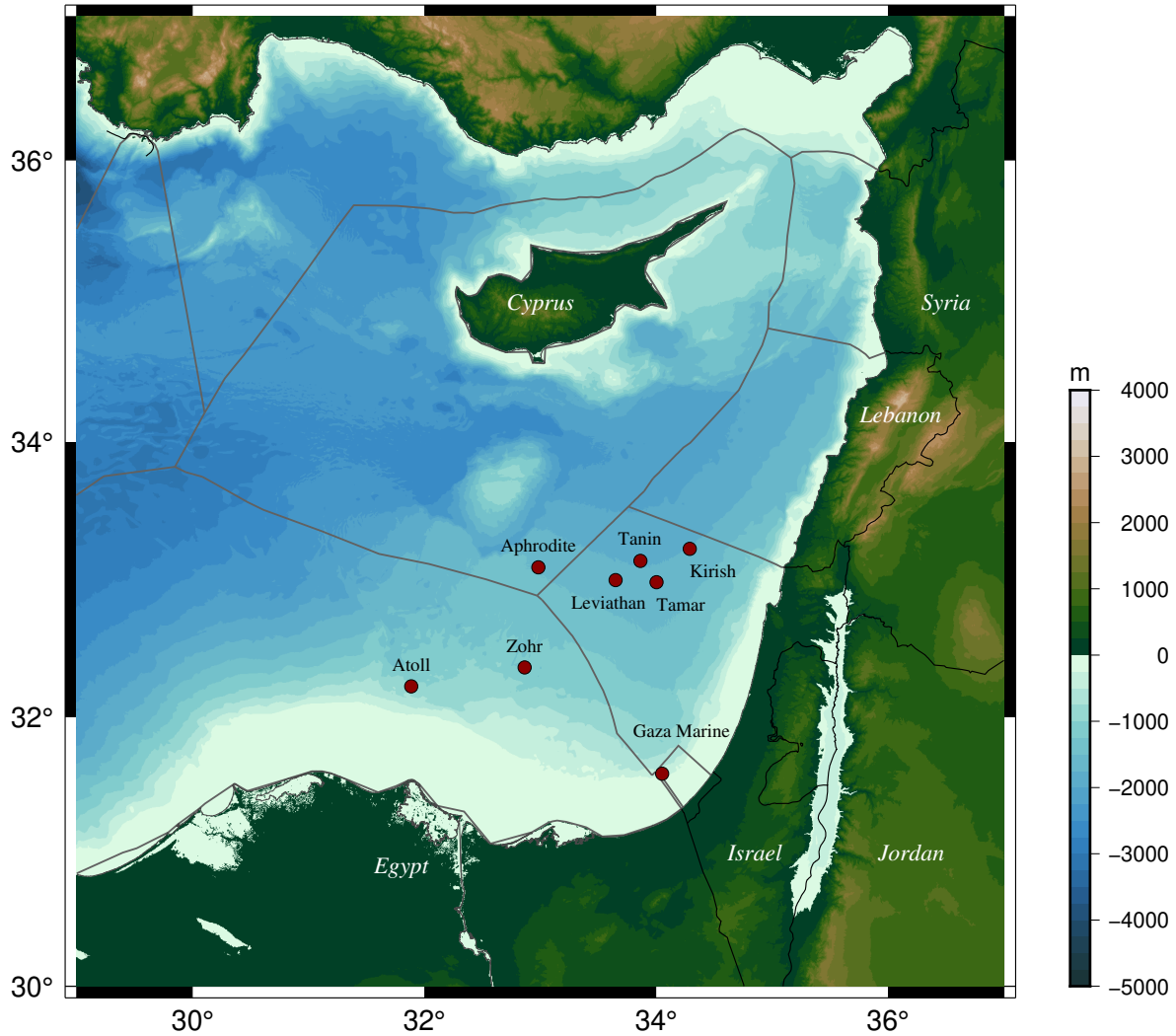


Figure 2.4: Discovery of gas fields in the Levantine Basin. The red circles indicate the approximate locations of gas fields that were discovered since 2009. The gray lines indicate the boundaries of the exclusive economic zone, which were obtained from Flanders Marine Institute (2023). These lines should not be considered the actual boundaries of any political claim. The borders in the land areas were derived from GSHHG (Wessel & Smith, 1996).

Gibraltar and the climatological mean surface flux fields (Schroeder et al., 2023).

The Atlantic Water enters the Mediterranean Sea through the Strait of Gibraltar and flows along the North African coast. After reaching the Sardinian Channel, the water typically splits into two routes. Some of the water circulates cyclonically through the Tyrrhenian Sea in the Western Mediterranean Sea as the Northern Current. Other water crosses the Sicily Channel to enter the Eastern Mediterranean Sea. It travels to the eastern part of the basin, where it is ultimately transformed into warm, saline Levantine Intermediate Water or Cretan Intermediate Water. The formation of the Intermediate Water can enhance vertical mixing in the basin and influence the phytoplankton

population. Such a journey of the Atlantic Water across the Eastern Mediterranean basin is influenced by the strong meandering currents that drive mesoscale dynamics. Another forcing that drives circulation is the climatological mean surface flux field, which include wind stress, heat (or thermal) flux, and surface freshwater flux.

These forcings can trigger certain phenomena, which manifest signatures in SAR images, making distinguishing oil slicks more difficult. Therefore, understanding these forcings can help improve the interpretation of SAR images. The following subsections provide an overview of these factors in the Levantine Sea.

2.2.1 Oceanographic forcing

Once the Atlantic Water enters the Mediterranean Sea, it undergoes continuous modification through air–sea interaction and mixing with other water masses. Strong evaporation in the Mediterranean increases the salinity and temperature of the Modified Atlantic Water, eventually leading to the formation of warm, saline Levantine Surface Water in the Levantine Sea. Depending on the location, this water then contributes to the formation of either Levantine Intermediate Water or Cretan Intermediate Water.

The cyclonic Rhodes Gyre is known to be the main source of the Levantine Intermediate Water. It covers an area ranging from 28° to 30° E and from 34.5° to 36° N (Malanotte-Rizzoli et al., 2003). However, other regions in northern Levantine Sea have also been identified as sources of the Levantine Intermediate Water, such as along the Turkish coastline (i.e. Antalya Bay) to the west of Cyprus (Lascaratos et al., 1993; Malanotte-Rizzoli et al., 2003) and the Cilician Basin (Fach et al., 2021). Some studies have suggested that the Levantine Intermediate Water only forms at the end of winter (Fach et al., 2021; Habib et al., 2023). During winter, convection events cause the Levantine Surface Water to cool down and increase in density. This dense water then sinks and forms the Levantine Intermediate Water (Hecht et al., 1988; Taillandier et al., 2022).

The surface layers of the Cretan Sea are dominated by Atlantic Water, Black Sea Water, and Levantine Surface Water. Black Sea Water with low density enters the northern Aegean Sea and follows a general cyclonic path. By the time it reaches the western Cretan Sea, it has mixed with the water masses in the Aegean Sea. This increases its salt content, giving it a salinity and temperature similar to that of Modified Atlantic Water, which enters the Cretan Sea through the eastern and western Cretan Straits and is considered to have low salinity (Velaoras et al., 2014). On the eastern side, the warm, saline Levantine Surface Water enters the Cretan Sea through the eastern Cretan Straits via the Asia Minor Current. Similar to the formation of the Levantine Intermediate Water, the Cretan Intermediate Water forms during the winter

convection as the Levantine Surface Water cools down and sinks. Inside the Cretan Sea, the Cretan Intermediate Water is generally considered to be slightly cooler, more saline, and denser than the Levantine Intermediate Water (Astraldi et al., 1999; Theocharis et al., 1999).

A part of the Intermediate Water enters the Aegean Sea and the Adriatic Sea, where it combines with the Modified Atlantic Water and forms the Eastern Mediterranean Deep Water (Schroeder et al., 2023). Other studies have presented findings on the formation of deep waters in the Cretan Sea (Gertman et al., 2006) and in the Rhodes Gyre (Malanotte-Rizzoli et al., 2003; Özsoy et al., 1993). The other part of the Intermediate Water crosses the Sicily Channel and some of it contributes to the formation of the Western Mediterranean Deep Water in the northwestern part of the basin, while some of it contributes to the Mediterranean outflow through the Strait of Gibraltar to the Atlantic Ocean (Schroeder et al., 2023). Because the Sicily Channel is shallow, the Eastern and Western Deep Waters do not mix. Figure 2.5 illustrates the vertical distribution of the water masses in the Mediterranean Sea, along with their salinity and temperature. Figure 2.6 provides a summary of the surface circulation in the Mediterranean Sea explained above.

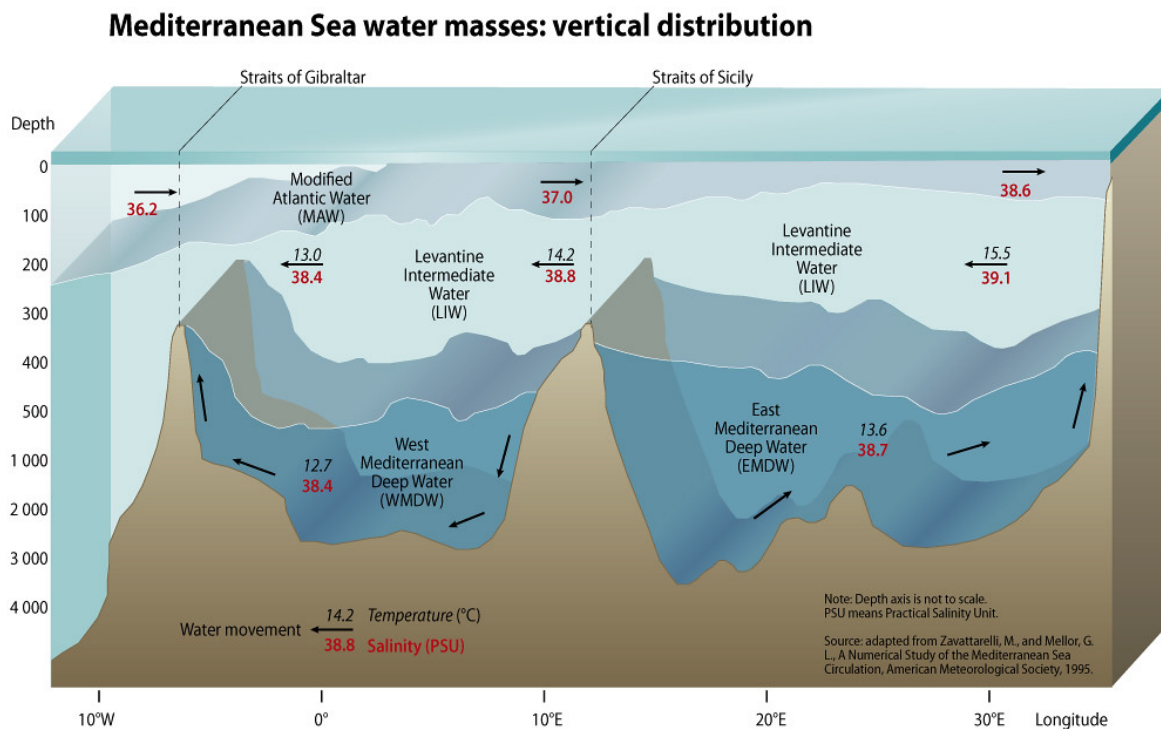


Figure 2.5: Vertical distribution of water masses in the Mediterranean Sea. Source: UNEP/MAP (2012); created by GRID-Arendal and available at: <https://www.grida.no/resources/5885>.

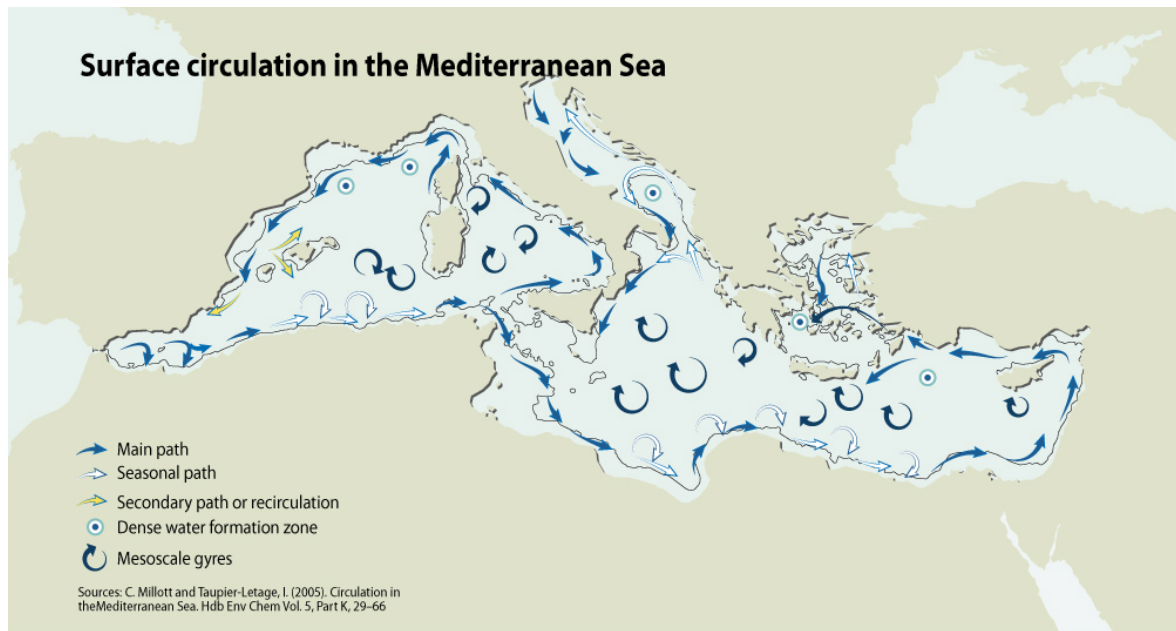


Figure 2.6: Surface circulation in the Mediterranean Sea. Source: UNEP/MAP (2012); created by GRID-Arendal and available at: <https://www.grida.no/resources/5915>.

2.2.2 Vertical mixing and biological factors

The formation of the Intermediate Water, as explained in the previous subsection, can enhance vertical mixing and convection in the formation area. Evaporation and heat loss during the winter cause a convection period in the Mediterranean Sea. This convective mixing brings nutrient-rich water from below the surface, which triggers phytoplankton blooms (Keuter et al., 2022). Phytoplankton blooms can result in the formation of biogenic surface films that appear similar to oil slicks in SAR imagery. The chlorophyll *a* (chl-*a*) concentration is frequently used as a proxy for phytoplankton biomass. Satellite measurements of chl-*a* concentration revealed that the Mediterranean Sea typically exhibits concentrations below 2 mg/m^3 , except in blooming areas during late winter and early spring. Even during the blooming seasons, the chl-*a* concentration in the oligotrophic to ultra-oligotrophic Eastern Mediterranean rarely exceeded 0.5 mg/m^3 (Siokou-Frangou et al., 2010).

The Rhodes Gyre is a well-known area of the Levantine Sea where the biomass of phytoplankton and biological production are higher than in the surrounding area (Habib et al., 2023). Specifically, the supply of nutrients in the euphotic layer of the Gyre is higher during cold winters than during mild winters (Ediger & Yilmaz, 1996). Similarly, an intense phytoplankton bloom event was observed in the southeastern Cretan Sea in early spring 2022 as a result of a cold spell, sea surface cooling, vertical mixing,

fertilization, and subsequent stratification (Teruzzi et al., 2024). In addition, nutrient-rich runoff can also cause high concentrations of nutrients in coastal waters, which may result in eutrophication and higher chl-*a* concentrations (Danovaro, 2003; Kress et al., 2019).

2.2.3 Mesoscale dynamics

The basin-scale circulation dominant in the Mediterranean Sea is cyclonic, as illustrated in Figure 2.6. Within this general circulation, there are numerous cyclonic and anticyclonic sub-basin scale eddies and gyres (Menna et al., 2012; Özsoy et al., 1989; Poulain et al., 2012), including quasi-permanent mesoscale features and strong along-shore currents (Pegliasco et al., 2021). In contrast to the open ocean, the mesoscale activity and circulation in the semi-enclosed Mediterranean are constrained by the morphology of the basin, including its coasts, islands, and shelf breaks, as well as by the meteorological forcing over the mountainous terrain (Pegliasco et al., 2021). Mesoscale activities can transport physical properties and biogeochemical tracers over long distances and across frontal boundaries, and therefore impact the large-scale water mass distribution, circulation, and ocean biology. Some areas in the Mediterranean Sea are regarded as having intense mesoscale activities, such as the Alboran Sea and the southern Algerian Basin in the Western Mediterranean Sea as well as the Levantine Sea in the Eastern Mediterranean Sea (Mason et al., 2023). The discussion here will focus on the Levantine Sea.

The Mid-Mediterranean Jet is a meandering current that flows eastward from about 24° E to the southeast of Cyprus (Menna et al., 2012). It can generate cyclonic and anticyclonic eddies and interact with other currents. There are several long-lived and recurrent eddies in the Levantine Sea, as summarized in Menna et al. (2012): the anticyclonic Ierapetra eddy, located southeast of Crete and induced by the Etesian winds; the anticyclonic Mersa-Matruh eddy, generated close to the Egyptian coast and considered a meander of the Libyo-Egyptian Current or the Mid-Mediterranean Jet; the anticyclonic Cyprus eddy, located southwest of Cyprus near the Eratosthenes Seamount and probably generated by the local bathymetry (Egorova et al., 2024); the Shikmona eddy, located off the coast of Israel and Lebanon, composed of several cyclonic and anticyclonic eddies, and regarded as a pinched-off meander from the coastal currents; the cyclonic Latakia eddy, likely generated by the interaction between the northward along-slope coastal current and the Mid-Mediterranean Jet. It should be noted that different studies may approach the formation of these eddies differently. These eddies can modulate sea surface roughness, inducing areas of surface convergence and divergence. Under moderate wind conditions, these areas appear as bright and dark lines in

SAR images (Robinson, 2010a). Additionally, surface films tend to accumulate along current shear in eddies, enhancing the SAR signature.

2.2.4 Internal waves

Internal waves occur due to the perturbations in a stratified medium. In the Mediterranean Sea, tidal forcing is the main mechanism that generates internal waves. Although tides in the Mediterranean Sea are low compared to those in most ocean basins, such as the adjacent Atlantic Ocean (Lionello, Sannino, & Vilibić, 2023), previous studies have highlighted internal waves generated by the interaction of tidal currents with bathymetric features in straits and channels, such as the Strait of Gibraltar (Morozov et al., 2002), the Sicily Channel (Cosoli et al., 2015), the Strait of Messina (Brandt et al., 1999), and the eastern Cretan Arc Straits (Velegrakis et al., 1999). The straits and channels are where water is exchanged between different seas, and such exchange of fresh water can lead to density gradients and stratified water. However, the seasonal pycnocline was also observed off the coast of Israel in the Levantine Basin above the continental shelf during the summer (Rosentraub & Brenner, 2007), where internal waves were also observed (Pelinovksy et al., 1995; Reiche et al., 2018).

Although these oceanic internal waves (OIWs) propagate within a stratified water column, they can produce surface convergence and divergence, which can either amplify or attenuate gravity-capillary waves. The alternating surface convergence and divergence result in bright and dark stripes in SAR images. Similar to the ocean, perturbations in the stratified atmosphere can generate internal waves, which are often referred to as atmospheric gravity waves (AGWs). Variations in wind stress associated with AGWs can also cause small-scale changes in sea surface roughness, resulting in similar bright and dark stripes in SAR images (Alpers & Huang, 2011). Previous studies have examined AGWs generated by orographic obstacles, such as mountains and islands (Miglietta et al., 2013; Papandrea et al., 2019). These waves are known as lee waves and have been observed in the Mediterranean Sea. Therefore, areas close to mountainous coastlines or islands are likely to experience AGWs when atmospheric conditions are favorable.

2.2.5 Atmospheric factors

This subsection introduces the climatological mean surface flux fields, one of the main forcings that drive circulation in the Mediterranean Sea, as mentioned at the beginning of this section.

Wind stress

Wind stress forces circulation at the sub-basin scale, which exhibits strong seasonal variability (Pinardi & Navarra, 1993). In addition, the interaction between wind stress and geostrophic stress can create conditions conducive to vertical convection (Robinson, 2010b). Wind stress expresses the horizontal flux of momentum from the atmosphere to the ocean and drives turbulent mixing at the air–sea interface (Robinson & Fangohr, 2010). It is defined as follows:

$$\tau = \rho \cdot C_D \cdot u^2, \quad (2.1)$$

where ρ is the air density; C_D is the dragging coefficient; u refers to the wind speed. Generally, the wind speed is normalized to 10 m above the sea surface within the lower part of a neutrally stable atmospheric boundary layer (ABL) (Robinson & Fangohr, 2010).

The movement of wind is driven by differences in air pressure, with faster winds occurring due to higher pressure gradients. According to model data from 1981 to 2010, the sea level pressure in the Mediterranean Sea tends to be lower in the summer than in the winter, and especially low pressure was observed in the Levantine Sea in July (Schroeder et al., 2023). Therefore, the dominant wind over the Levantine Sea in summer is the west-northwesterly wind (Akpınar et al., 2016). Wind speeds in the Levantine Sea are generally higher during the winter months, as evidenced by long-term wind speed estimates derived from data collected at coastal meteorological stations and numerical weather prediction models from 2009 to 2018 (Hadjipetrou & Kyriakidis, 2024). The study also found that the lowest average wind speeds typically occur in April and between October and November. The SKIRON atmospheric model, developed by the University of Athens, provides hourly wind estimates at 10 m above the sea surface in Europe (Kallos et al., 1997; Papadopoulos et al., 2001). Such a model is useful for oil trajectory simulation because winds are relevant to oil advection and weathering, such as dispersion. In addition, the optimal sea surface wind speed for SAR oil slick detection is suggested to range between 2–3 m/s and 7–12 m/s (Brekke & Solberg, 2005; Gade et al., 2000; Robinson, 2004).

Heat and freshwater fluxes

Overall, the net freshwater flux (P-E) in the Mediterranean Sea is negative throughout the year, meaning that evaporation (E) is higher than precipitation (P) (Lionello, San-nino, & Vilibić, 2023). Rain drops can dampen or roughen the sea surface, resulting in weaker or stronger radar backscattering than the surrounding area. Therefore, precipitation over the study area should also be considered to avoid misinterpreting the

SAR signatures. In general, the Mediterranean Sea follows a seasonal cycle of mean temperature and total precipitation, experiencing more precipitation and evaporation in the winter than in the summer. However, large areas near the coasts of North Africa and the Middle East remain dry throughout the year (Lionello, Giorgi, et al., 2023). The freshwater loss induces the formation of saltier and denser water masses than the Atlantic Water. For example, cool, dry winds blow from the mainland to the Rhodes area in January or February. The resulting heat loss and increased evaporation cause negative buoyancy flux. Consequently, the cool, saline surface water sinks, resulting in vertical mixing and formation of the Levantine Deep Water (Pinardi et al., 2023). Such vertical mixing can reach depths greater than 1000 m (Malanotte-Rizzoli et al., 2003). Similarly, large buoyancy losses in winter induced the deep water formation observed in the Aegean Sea and the Adriatic Sea in the Eastern Mediterranean Sea (Lascaratos et al., 1999; Ozer et al., 2020; Potiris et al., 2024).

Additionally, heat and freshwater fluxes can drive overturning circulation in vertical and zonal or meridional planes, creating clockwise circulations in the upper water column and counterclockwise circulations in deep and abyssal regions (Pinardi et al., 2019, 2023). The freshwater loss (negative P-E) in the Mediterranean basin is balanced by the inflow of Atlantic Water through the Strait of Gibraltar. This exchange drives zonal overturning circulation, in which a high-salinity tongue of the Levantine Intermediate Water flows from the eastern end of the Mediterranean Sea to the Strait of Gibraltar along a longitudinal section. Above this tongue is a low-salinity tongue of the Atlantic Water that flows through the Strait of Gibraltar into the Mediterranean Sea. In the deep to abyssal zones, the zonal overturning circulation is influenced by the transport of eddies or permanent gyres. On the other hand, the formation processes of deep and intermediate water masses induce intense vertical circulation and drive the meridional overturning circulation in these areas, including the Gulf of Lion, Adriatic Sea, Aegean Sea, and the Rhodes Gyre area.

2.3 Relevance for SAR analysis

The previous section provided an overview of circulation and its various aspects, including surface circulation, vertical distribution of water masses, vertical mixing, formation of biological surface films, mesoscale activities, internal waves, and atmospheric factors. Several of these oceanographic and atmospheric phenomena can create dark formations in SAR images that may be mistaken for oil slicks. These signatures can be caused by vertical mixing, biogenic surface films, eddies, internal waves, wind, rain cells, and other factors. Therefore, it is essential to understand the local environmental condi-

tions for accurate interpretation of the oil slicks. The following chapter explains how different phenomena manifest as signatures in SAR images will be explained and is supported by examples collected from the study area.

3 SAR Signatures

For ocean applications, sea surface roughness, which responds to wind stress, is generally regarded as a key factor. Wind stress can also induce wind-driven surface currents and drive turbulent mixing at the air–sea interface (Robinson & Fangohr, 2010). Overall, hydrodynamic modulation, surface film modulation, and ABL instability are the dominant mechanisms that modulate the surface roughness and generate SAR signatures (Robinson, 2004). Among them, hydrodynamic modulation by either surface currents or local wind stress is the most common cause. However, most SAR ocean signatures can result from one or more of these mechanisms. Therefore, understanding how different oceanic phenomena manifest signatures in SAR imagery is essential. In this chapter, a dataset with different SAR signatures is first introduced in Section 3.1. Such dataset provides a good starting point to understand the different SAR signatures and how they relate to oceanic phenomena. Explanations on the formation of different oceanic phenomena and their SAR signatures, supported by examples and supplementary materials, are provided in Section 3.2.

3.1 Dataset of oil slicks, look-alikes, and remarkable SAR signatures

At the beginning of this study, Sentinel-1 SAR products from 2015 to 2019 covering the Southeastern Mediterranean Sea were collected. Oil slicks in the SAR images were labeled as oil objects and used for training object detection algorithms. However, only image patches with oil objects are not enough for distinguishing different ocean SAR signatures. Therefore, image patches with look-alikes or other remarkable phenomena were also collected. To ensure that different sources of these SAR signatures are equally represented in the dataset, the K-Means unsupervised clustering algorithm was applied to sort them into different subgroups, and each subgroup has a similar number of image patches that contributed to the final dataset.

It takes a lot of time and effort to obtain such a dataset, which hinders many research works on applying deep learning-based methods for oil spill detection. In addition, most studies have collected their own datasets, so the results cannot be compared with other literature. Therefore, image patches from 2019 have been submitted to PANGAEA, a

data publisher for Earth and environmental science. The dataset helps researchers who are looking for an oil slick dataset to apply their object detection model by providing a common starting point. In addition, the dataset is linked to a data description paper that provides a performance evaluation of an object detector on the dataset, allowing researchers to compare their work with other studies (see Section 3.2). The dataset includes two subsets, an *oil* set of 1365 image patches with a total of 3225 oil slick objects inside and a *no-oil* set of 2290 image patches without any oil slicks inside. The citation to the dataset is given as follows:

Yang, Y.-J. & Singha, S. (2025). Oil Slicks, Look-Alikes and Other Remarkable SAR Signatures in Sentinel-1 Imagery in the Eastern Mediterranean Sea in 2019 [dataset]. *PANGAEA*. doi: 10.1594/PANGAEA.980773

The dataset is currently under review by the data publisher, PANGAEA. The following states the contributions made by the candidate to this dataset:

The candidate manually inspected the oil slicks in the dataset together with the co-author. Then, the candidate created an additional collection of image patches without oil slicks. Additionally, she used the K-means clustering method to sort the image patches into subgroups, providing a clearer picture of the types of phenomena that confuse object detection algorithms. She prepared all the necessary information for the dataset submission. The general information about the dataset is listed as follows:

Title:	Oil Slicks, Look-Alikes and Other Remarkable SAR Signatures in Sentinel-1 Imagery in the Eastern Mediterranean Sea in 2019		
Authors:	Yi-Jie Yang and Suman Singha		
Keywords:	Eastern Mediterranean Sea; look-alikes; oil slick; Sentinel-1; SAR		
Publisher:	PANGAEA		
URL:	https://doi.org/10.1594/PANGAEA.980773		
Location:	Eastern Mediterranean Sea		

Data Coverage

West-bound:	27.1212703° E	East-bound:	36.0881997° E
North-bound:	36.3715771° N	South-bound:	29.2991798° N

3.2 Explanations of ocean SAR signatures

As mentioned at the beginning of this chapter, there are several mechanisms that produce notable signatures in SAR imagery. The sources of these signatures can be grouped:

- oil slicks,
- wind,
- internal waves in the ocean and atmosphere,
- areas of mixing and vertical advection in the ocean,
- meso- and submesoscale eddies,
- biogenic surface films,
- rain cells,
- others, such as ship wakes and radio frequency interference (RFI).

Each of these mechanisms directly or indirectly modulates the surface roughness and therefore manifests SAR signatures. The previous section presented a dataset that can serve as a collection of examples of these signatures. Therefore, a data description paper uses the dataset to give an overview of different SAR signatures. It describes each phenomenon in terms of its origin, then explains how it can be seen in SAR images, and finally gives an example related to the phenomenon. The paper aims to provide a comprehensive explanation to better understand the mechanisms of these SAR signatures for readers from various backgrounds, such as remote sensing, oceanography, and machine learning. In addition, the paper provides a performance evaluation of an object detector on the dataset, allowing users of the dataset to compare their results with a previous work. The citation to the data description paper is given as follows:

Yang, Y.-J., Singha, S., Goldman, R., & Schütte, F. (2025). Dataset of Oil Slicks, Look-Alikes and Remarkable SAR Signatures Obtained from Sentinel-1 Data in the Eastern Mediterranean Sea. *Earth System Science Data*. doi: 10.5194/essd-17-6807-2025

The manuscript is published. The following states the contributions made by the candidate to this data description paper:

The candidate selected examples of different phenomena, explained the mechanisms and their SAR signatures, and drafted the entire manuscript. However, the manuscript would not have been possible without the contribution of the co-authors with their comments on the manuscript and their knowledge of SAR and oceanography.

Earth Syst. Sci. Data, 17, 6807–6837, 2025
<https://doi.org/10.5194/essd-17-6807-2025>
© Author(s) 2025. This work is distributed under
the Creative Commons Attribution 4.0 License.



Open Access
Earth System
Science
Data

Dataset of oil slicks, look-alikes and remarkable SAR signatures obtained from Sentinel-1 data in the Eastern Mediterranean Sea

Yi-Jie Yang^{1,2}, Suman Singha^{3,1}, Ron Goldman⁴, and Florian Schütte⁵

¹Team SAR Oceanography, Remote Sensing Technology Institute, German Aerospace Center (DLR), Bremen, Germany

²Faculty of Mathematics and Natural Sciences, Kiel University, Kiel, Germany

³National Centre for Climate Research, Danish Meteorological Institute (DMI), Copenhagen, Denmark

⁴Israel Marine Data Center, Israel Oceanographic and Limnological Research (IOLR), Haifa, Israel

⁵GEOMAR Helmholtz Centre for Ocean Research Kiel, Kiel, Germany

Correspondence: Yi-Jie Yang (yi-jie.yang@dlr.de, yi-jie.yang@mailbox.org)

Received: 10 April 2025 – Discussion started: 16 April 2025

Revised: 27 November 2025 – Accepted: 28 November 2025 – Published: 4 December 2025

Abstract. Publicly available datasets for oil spill detection are scarce, making it difficult to compare the performance of different detection algorithms. To address this, this paper introduces a comprehensive labeled dataset of oil slicks, look-alikes, and other remarkable oceanic phenomena, derived from Sentinel-1 Synthetic Aperture Radar (SAR) products in the Eastern Mediterranean Sea in 2019. The dataset contains 3225 oil objects across 1365 image patches, along with an additional 2290 image patches featuring look-alikes or other phenomena. Data are available at <https://doi.org/10.1594/PANGAEA.980773> (Yang and Singha, 2025).

This dataset enables researchers to evaluate their oil spill detection models and compare performance with other studies. To facilitate this, the performance of an oil spill detector from a previous study on the dataset is provided as a baseline. In addition, to help the researchers better understand what phenomena their object detector might be confusing with oil slicks, the image patches without oil objects were sorted into several subgroups. On the other hand, for researchers looking to apply object detection models to oil slick detection but lacking a starting dataset, this dataset can serve as a valuable training resource. Beyond dataset presentation, this paper also explains the formation of different oceanic phenomena and their SAR signatures, supported by examples and supplementary materials. These insights help researchers from various backgrounds, such as remote sensing, oceanography, and machine learning, better understand the sources of SAR signatures.

1 Introduction

Spaceborne Synthetic Aperture Radar (SAR) has been widely applied to marine oil pollution detection. While airborne systems play an important role in emergency response due to their flexibility in time of deployment and choice of sensors, with the advantage of wide coverage and the ability to observe at night and through clouds, spaceborne SAR can be used to monitor oil spills on a regular basis and provide early warning (Brown and Fingas, 2005; Brekke and Solberg, 2005). Oil slicks typically appear as dark formations in SAR

imagery, but other phenomena can also manifest dark formations that look similar and are difficult to distinguish. Distinguishing oil slicks from these *look-alikes* has long been a challenge.

With the increasing computational capacity and the growing number of accessible SAR scenes since the launch of Sentinel-1 in 2014, many recent studies have used deep learning-based methods to detect oil spills and distinguish them from look-alikes. However, due to the lack of publicly available oil spill datasets, most studies had to collect their own oil spill dataset for model training. Some studies col-

lected images of major accidents, such as the DeepWater Horizon incident, the Hebei Spirit oil tanker collision, and accidents reported in the local news, and cropped the acquired SAR images into multiple image patches (Chen and Wang, 2022; Hasimoto-Beltran et al., 2023; Mahmoud et al., 2023). These studies employed a limited number of SAR scenes, with less than 36 images, which means that the training dataset may not reflect the differences in radar backscatter between different acquisitions well. Other studies relied on either manual inspection by the authors (Topouzelis and Psyllos, 2012; Amri et al., 2022; Chen et al., 2023) or local collaboration with other institutions or services (Konik and Bradtke, 2016; Cantorna et al., 2019; Zeng and Wang, 2020). These studies focused on the development of new oil spill detection models, but the use of different datasets made it difficult to compare the performance of different studies.

Recognizing the challenges posed by the absence of a comprehensive dataset, Krestenitis et al. (2019) published an oil spill detection dataset. It contains approximately 1000 Sentinel-1 SAR images with their corresponding ground truth masks, indicating five classes: oil spill, look-alikes, land, ship, and sea areas. The oil spills were reported by the European Maritime Safety Agency (EMSA) through the CleanSeaNet service. However, it is not openly available, the proposal is required to obtain the dataset. On the other hand, a recent work has contributed its training dataset to Zenodo, an open repository for datasets (Trujillo-Acatitla et al., 2024). The dataset includes oil spills reported by the National Oceanic and Atmospheric Administration (NOAA) and EMSA CleanSeaNet. There are 2850 image patches, half with oil spills inside, half without oil spills but with background or look-alikes inside. These two datasets offer pixel-wise classification of the images. However, in low-wind conditions or in areas where there are frequent look-alikes, there may be large areas of dark formations. For this reason, previous studies have proposed a two-step approach with coarse detection of oil slicks over a large area and refinement of the results to a pixel-wise level (Nieto-Hidalgo et al., 2018; Yang et al., 2024). This approach can theoretically increase efficiency, as the final detection is only performed if there are detections in the first step, and may therefore be helpful for a near real-time (NRT) monitoring system. Therefore, the dataset presented in this paper provides an object-based annotation of the oil spills, which aims to support research that follows the idea of this approach.

There are many different sources of look-alikes, such as low-wind areas, internal waves, upwelling, and biogenic films, that modify the ocean surface and introduce signatures in SAR imagery. It is important to understand which types of look-alikes the model cannot distinguish well, but this information is not available in previous datasets. Therefore, the published dataset includes image patches of oil slicks and other prominent marine signatures, stored in *oil set* and *no-oil set*, respectively. For the image patches in *no-oil set*, the *K*-means unsupervised clustering algorithm was used to further

sort the patches into several subgroups to help users better understand the performance of their algorithms on different sources of look-alikes. Note that *K*-means categorizes each image as a whole under a specific cluster. In other words, unlike oil slicks in the *oil set*, which were labeled as objects, no annotation is attached to image patches in the *no-oil set*.

In addition, previous datasets used the reports from the existing service, but in many areas such services are not available. There is a lack of clear guidance on how to distinguish between different phenomena and what data can be used to support them. This paper gives examples of different phenomena and explains how SAR signatures are manifested and how they can be interpreted with the help of other supplementary materials.

This published dataset focuses on the Eastern Mediterranean Sea, which is one of the marine oil pollution hotspots due to its heavy maritime traffic (Carpenter and Kostianoy, 2016). There are 1365 image patches with 3225 oil objects in *oil set* and 2990 image patches in *no-oil set*. Section 2 provides an overview of the dataset, including the spatial distribution of the data, the preprocessing steps applied to the SAR scenes, the procedures used to collect the dataset, and the sources of supplementary material used to understand the dark formations. Section 3 describes in detail how the oil slicks were annotated and the concept of the *K*-means clustering algorithm used to classify the image patches.

The dataset and this paper can be used for different purposes. For researchers wishing to start in an area where there are no existing services for the recording of oil spills (i.e. no ground truth oil spills available), Sect. 4 can be used as a reference as it explains how oil slicks and different oceanic or atmospheric conditions contribute to SAR signatures. For studies that already have their own object detector for oil slicks, this dataset can be used as a separate dataset to test their model performance. Section 5.1 provides an evaluation of the performance of an object detector used in an NRT automated oil spill detection system developed in Yang et al. (2024). In addition, the clustered *no-oil set* can provide an indication of how to improve the model. Furthermore, the dataset can be used as a training dataset by researchers who are just starting to apply object detection algorithms to oil spill detection applications. Although the dataset only covers oil spills in the Eastern Mediterranean Sea, a previous study showed that with such a locally focused oil object detector, only a small additional dataset is needed to extend the use of the detector to another region (Yang and Schnupfhahn, 2025). Additional technical information in the Sect. 5.2 should be read before using the dataset. Section 7 summarizes how this data descriptor and dataset can be used and add value to the community.

2 Materials

This section contains information about the dataset and has the following structure: Sect. 2.1 lists general information about the SAR products and explains the corrections applied to them. Section 2.2 gives an overview of the dataset and explains the procedures for preparing this dataset. Section 2.3 shows a collection of different supplementary data that could help inspect dark formations. Note that all the time stamps shown in this paper and the dataset are in UTC. The map boundaries in figures were derived from Wessel and Smith (1996).

2.1 Sentinel-1 Data

Sentinel-1 SAR Level-1 Ground Range Detected (GRD) products were obtained from the Copernicus Open Access Hub, which provided data through the end of October 2023. The Copernicus Data Space Ecosystem operates as an improved and updated version of it and provides Earth observation data and services, including tools, graphical interfaces, and Application Programming Interfaces (APIs).

The dataset covers Sentinel-1A and Sentinel-1B products, which share the same orbit plane with a 180° orbital phasing difference; the repeat cycle was six days. Note that Sentinel-1B stopped delivering data since 23 December 2021. Sentinel-1 products from 2019 covering the Eastern Mediterranean Sea were acquired and preprocessed. The acquisitions from ascending and descending orbits in the area were taken at around 15:30–16:05 and 03:30–04:05 UTC, respectively. Those scenes are in Interferometric Wide Swath (IW) acquisition mode with a swath width of 250 km, and the incidence angle ranges between 29.1 and 46.0° . In this area, dual-polarization VV-VH products were provided. The data in cross-polarization mode (i.e., VH or HV) generally exhibit lower backscattering and, therefore, are influenced more by background and instrument noise compared to those in co-polarization mode (i.e., VV or HH) (Woodhouse, 2006). For this reason, only VV-polarized products were collected in the dataset.

A series of corrections, border noise removal, thermal noise removal, and calibration were applied to the SAR products. The continuous products were assembled and multi-looked with a factor of 2. The final backscattering coefficient, σ^0 , is given in decibels (dB). These preprocessing steps were done with the help of the Sentinel Application Platform (SNAP) Graph Processing Framework (GPF) (European Space Agency, 2020). Note that the data were preprocessed with SNAP version 8, and certain circular patterns were produced at regions with relatively low backscattering in a few images; Fig. 1 shows such an example from 27 August 2019. Therefore, some image patches collected in the dataset also contain such artifacts (see Fig. 2). As they should not be the bottleneck of the detection algorithm, these image patches are kept in the dataset.

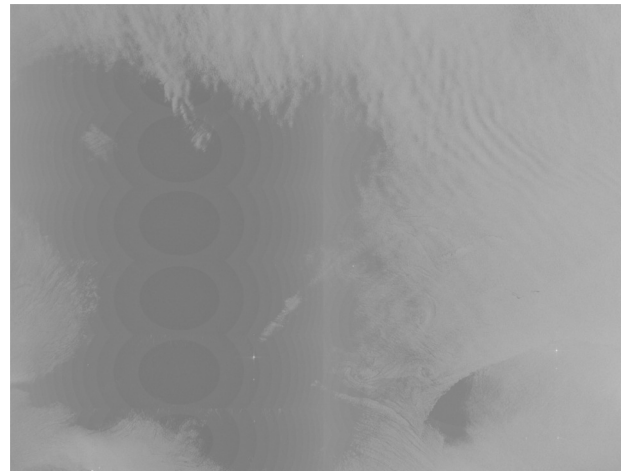


Figure 1. Preprocessed data with certain artifact produced after applying thermal noise removal in SNAP version 8. Note that the figure is a zoom-in of the entire preprocessed scene. The figure contains modified Copernicus Sentinel data (2019).

Afterwards, the preprocessed data were normalized to 0–255, for training the object detector. The normalized image, I_N , was calculated by the sigmoid function:

$$I_N = \frac{255}{1 + e^{-\frac{-(I - \beta)}{\alpha}}}, \quad (1)$$

where I is the original image value. In this study, β and α equal to the median and three times the standard deviation ($3 \cdot \sigma$), respectively, of the original image values in the corresponding preprocessed data. There is no specific function that should be applied for image normalization. The parameters used to generate the dataset were determined by the authors through trial and error, as they provide good contrast between oil slicks and their surroundings according to human eyes. The object detectors shown in Sect. 5.1 were trained using image patches for which a different image normalization method, provided by the Geospatial Data Abstraction Library (GDAL), was applied. Therefore, different image normalization methods may not be the key factor in the poor performance of the object detection algorithms. A previous study rescaled the image with maximum value equals to mean plus three times the standard deviation (Karathanassi et al., 2006).

2.2 Dataset

The published dataset utilized the annotation of oil objects in the framework of our previous study (Yang et al., 2024), where all preprocessed Sentinel-1 data covering the South-eastern Mediterranean Sea in 2019 were inspected jointly by two human interpreters. Only the dark formations agreed upon by both interpreters as oil slicks were given labels. Image patches including these labeled oil objects were gener-

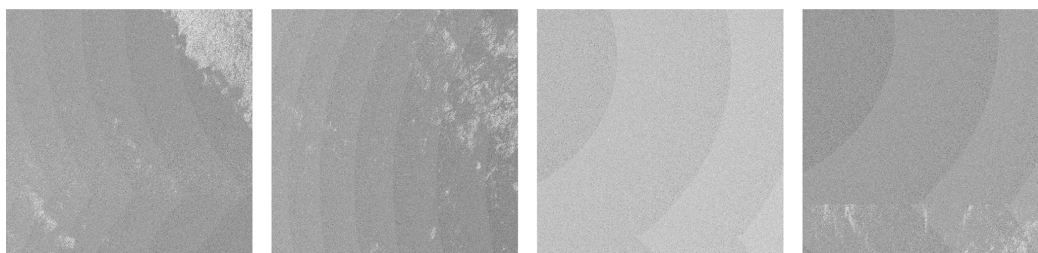


Figure 2. Image patches in the dataset with artifact as shown in Fig. 1. The tags for these image patches (from left to right) for referring to their information in the provided data table are nw-0603-03-000100, nw-0609-03-000106, nw-0547-03-000044, and nw-0553-03-000050 (see also Sect. 2.2 and Appendix A). The figure contains modified Copernicus Sentinel data (2019).

ated and stored in the *oil set*. However, without ground truth oil spills available, the labeled oil objects might not only belong to oil spills but also to other possible chemical spills. A successful oil spill detection system should be able to distinguish oil slicks from look-alikes; therefore, it is essential to take into account the image patches without oil slicks in them. In addition to the *oil set*, the published dataset also includes a *no-oil set*, which provides image patches without oil slicks but with look-alikes or other remarkable SAR signatures present.

Sources of pollution and other phenomena could differ between coastal and offshore areas. Hence, depending on whether the image patch covers land areas or not, image patches in the *oil* and *no-oil sets* are further split into *coast* and *water* subsets. The structure of the different subsets can be understood as follows:

```
oil/
  coast/
  water/
no_oil/
  coast/
  water/
```

To efficiently collect image patches for the *no-oil set*, an object detector, custom-trained with oil objects but lacking images with look-alikes, was employed to target dark formations in the collected SAR scenes. These detections were compared to the locations of the inspected oil slicks, and those that have no intersection with the oil objects were regarded as look-alikes and stored in the *no-oil set*.

To include look-alikes from different sources equally, these image patches were categorized by the *K*-means unsupervised clustering algorithm (see Sect. 3.2 for algorithm explanations). The *water* and *coast* subsets were first separated with the help of a land mask, and then they were clustered into 12 and 5 subgroups, respectively. Afterwards, 2100 and 500 image patches were randomly chosen from the two subsets, respectively. As offshore regions are of more interest, more image patches from the *water* subset were kept in the dataset. Each cluster contains a similar number of selected image patches compared to the other cluster from the

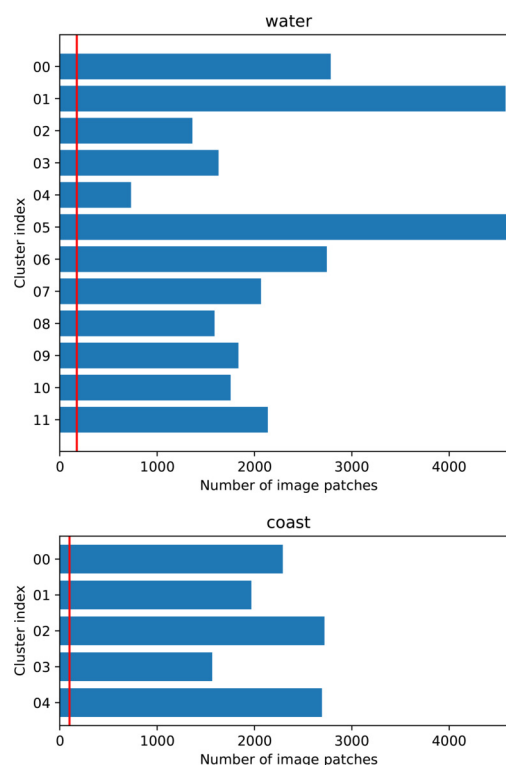


Figure 3. Numbers of image patches in different clusters by *K*-mean algorithm. The vertical red lines indicate the number of image patches randomly selected from the subsets. These image patches were then manually inspected, and the number of image patches in the final published dataset from each subgroup is presented in Table 1.

same subset. Figure 3 shows the numbers of image patches in each cluster; the red vertical lines show the number of image patches being randomly picked. It should be noted that one image patch might have dark formations from more than one source due to the complex manifestation of oceanographic phenomena on SAR imagery. Each subgroup should not be regarded as look-alikes from one specific source; the users should only consider the categories as a reference to help

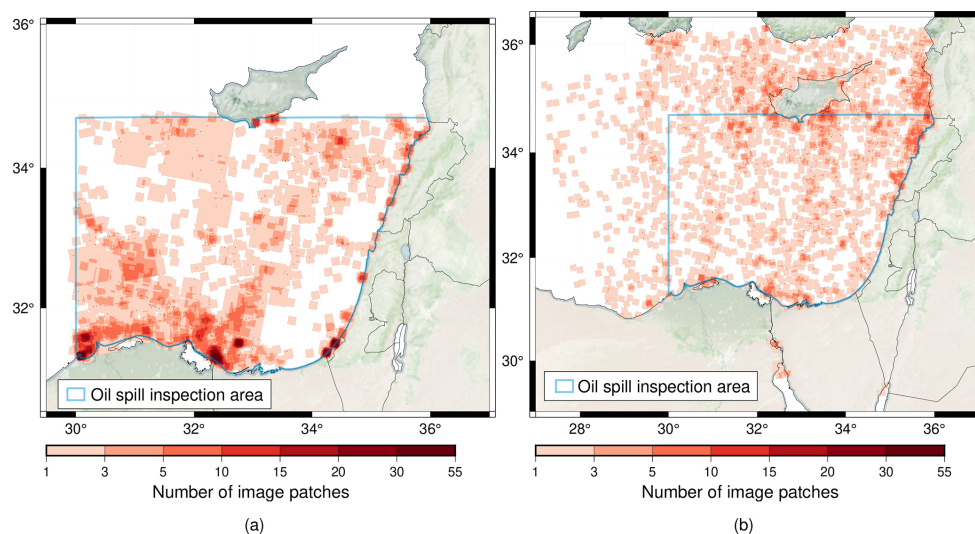


Figure 4. Heatmap of the image patches in the (a) oil and (b) no-oil sets. The base map was obtained from Stevens (2020), and the coastlines and borders were obtained from Wessel and Smith (1996).

comprehend what kinds of SAR signatures are likely to be misinterpreted by their algorithms.

Section 4 provides explanations for SAR signatures from different ocean phenomena. The dataset includes image patches in JPG format, and the corresponding annotations are in Pascal VOC XML format (Everingham et al., 2010). Figure 4 shows the heatmap of image patches in the *oil* and *no-oil* sets. The oil spill inspection area is defined from 34.7° N to the south and 36° E to the east until the coastline and marked as a blue boundary in the figure. However, all the Sentinel-1 SAR products from 2019 covering the area in longitude from 30 to 36° E and in latitude from 31 to 34.7° N were automatically examined while collecting image patches for the *no-oil* set. As the oil inspection area is smaller than the distribution extent of the image patches in the *no-oil* set, these image patches were manually inspected, and the ones with oil slicks or unknown and unsure dark formations were removed from the dataset to avoid confusion. Table 1 gives the final statistics of the published dataset. Information about image patches in the dataset is recorded in a data table in Excel format; different subsets are recorded in separate sheets. Appendix A provides an extracted data table recording the information of image patches displayed in this article. For users who would like to preprocess SAR products themselves, Sentinel-1 product IDs and the corner coordinates of the image patches are provided. The data table includes the following fields relating to image patches:

- patch name,
- Sentinel-1 product start and stop date time,
- Sentinel-1 product ID,
- dimension of the image patch in pixels,

- corner coordinates of the image patch in longitude and latitude (WGS84).

The patch name follows the naming convention:

MM_YYYYMMDD_HHMMSS_HHMMSS_PP_i

where MM refers to satellite mission, in this dataset, all the data are from Sentinel-1 mission, S1; YYYYMMDD shows the date of the product and HHMMSS shows the start and stop time of the product; PP indicates the polarization mode (e.g., VV); i is a series of numbers assigned when generated the image patches.

In the preprocessing step, continuous SAR products were assembled. Therefore, image patches might be located at the overlapping areas of the two products; in this case, both Sentinel-1 product IDs would be listed in the data table. The dimension of the image patch is default to 640 × 640 px, which is the same as the model input size for our object detector; but to keep the original shapes of some large oil slicks, there are a few image patches that have dimensions greater than the default. In this case, the object detector would rescale these image patches, but oil slicks should still be detectable.

The tie points grids in Sentinel-1 products provide the geolocation information in WGS84 geocentric coordinate system. To calculate the geolocation of the four corner points, upper left (ul), upper right (ur), bottom right (br), and bottom left (bl), of each image patch, its surrounding tie points were loaded, and the corner coordinates were estimated by the least squares fitting. The same procedure was used to obtain the object coordinates in *oil* set. For the *oil* set, additional fields for oil objects are provided:

Table 1. Statistics of the *oil set* and *no-oil set*.

Dataset	<i>oil set</i>		<i>no-oil set</i>			
Subset	<i>water</i>	<i>coast</i>	<i>water</i>	<i>coast</i>		
Number of image patches	990	375	00	172	00	76
			01	171	01	84
			02	160	02	75
			03	162	03	44
			04	81	04	72
			05	166		
			06	166		
			07	171		
			08	175		
			09	168		
			10	174		
			11	173		
			1939	351		
Number of oil objects	2284	941	n/a	n/a		

n/a – not applicable

- corner coordinates of the oil objects in longitude and latitude (WGS84),
- image coordinates of the oil objects referred to their corresponding image patch,
- the size (in pixels) of the bounding box annotating the oil object.

The data tables for *oil set* are sorted by objects; that is, if there are four oil objects in one image patch, there will be four separate rows for the four oil objects, and they should have the exactly same image patch information, such as patch name, Sentinel-1 product ID, and geolocation of the image patch. On the other hand, as there is no object in the *no-oil set*, each row refers to the information of its corresponding image patch. On top of all the fields explained earlier, each row in the table is referred to a unique tag with one image tag and an additional object tag or cluster tag.

The image tag is a two-letter subset tag followed by four-digit image serial number. The first letter of the subset tag is either o or n, referring to *oil set* and *no-oil set*, respectively; the second letter, w or c, stands for the subset *water* or *coast*. The image serial number is a sequence of numbers starting from 0001 for each subset, ordered by patch names.

In the *oil set*, each object gets an object tag with a two-digit object index and a six-digit object serial number. The object index numbers the objects in each image patch, counting from 01; the object serial number is a sequence of objects for all the objects in one subset, counting from 000001. As an example, ow-0795-01-001867 is a tag with an image tag ow-0795 and an object tag 01-001867, meaning that the ob-

ject is the first object in the 795th image patch and the 1867th object in the ow subset.

To follow the same tag format, a cluster tag with two-digit cluster index and a six-digit cluster patch serial number is assigned to each image patch in the *no-oil set*. The cluster index refers to the class assigned by *K*-means clustering methods, with 12 and 5 classes for nw and nc subsets, respectively; the index counts from 00. The cluster patch serial number is a sequence of image patches for all the image patches in one class, counting from 000001. Take nc-0308-04-000029 as an example, the image tag nc-0308 shows that this is the 308th image patch in the nc subset and the cluster tag tells that this is the 29th image patch in the 04 class.

The patch name was assigned when the image patch was generated; it contains information about the date and time of the acquisition. Since the data publisher prefers a dataset without folders, the tags are used as filenames and the folders have been removed. However, users are encouraged to rename the filenames to the patch names if they prefer. However, it should be noted that image patches from the *oil* and *no-oil* sets were generated separately, so in some rare cases the image patches may have the same names. Therefore, it is recommended to create a folder structure as explained at the beginning of this subsection.

2.3 Supplementary Data

Dark formations in SAR imagery can be caused by oil spills or look-alikes. Deliberate oil spills are mainly associated with human activities, such as offshore oil operations and oil transport. Some existing services, such as the Global Oil and Gas Extraction Tracker (GOGEC) and the European Marine Observation and Data Network (EMODnet), provide locations of oil, gas and offshore installations. These services can help to identify areas with a high potential for platform spillage. On the other hand, look-alikes can be related to a variety of oceanic, atmospheric, and geological factors that modulate the roughness of the sea surface. Supplementary materials may be used to help in cross-comparison to better comprehend the sources of dark formations. Table 2 directs the reader to various services that the authors found valuable in explaining SAR signatures or that are used in the examples shown in Sect. 2.1.

Ocean information such as wind speed, waves, sea surface temperature (SST), and chlorophyll *a* (chl *a*) concentration can be obtained from satellite, model, and in-situ data. The Ocean Virtual Laboratory (OVL) portal, funded by the European Space Agency (ESA), provides a quick and broad overview of ocean monitoring through its visualization tool. Additional information such as SAR roughness and bathymetry is also available. The other service, the Copernicus Marine Data Store (MDS) from the E.U. Copernicus Marine Service Information (CMEMS; acronym derived from its former name, Copernicus Marine Environment Monitoring Service), is an ocean data catalog with products at global

Table 2. Platforms for supplementary data.

Platform	url	Reference
Ocean Virtual Laboratory (OVL) portal	https://ovl.oceandatalab.com/ (last access: 21 June 2024)	
Copernicus Marine Data Store (MDS)	https://data.marine.copernicus.eu/ (last access: 21 June 2024)	
– Mediterranean Sea – High Resolution and Ultra High Resolution L3S Sea Surface Temperature	https://doi.org/10.48670/moi-00171	CMEMS and MDS (2024a)
– Mediterranean Sea, Bio-Geo-Chemical, L3, daily Satellite Observations (1997–ongoing)	https://doi.org/10.48670/moi-00299	CMEMS and MDS (2024b)
– Global Ocean Hourly Sea Surface Wind and Stress from Scatterometer and Model	https://doi.org/10.48670/moi-00305	CMEMS and MDS (2024c)
Copernicus Climate Data Store (CDS)	https://cds.climate.copernicus.eu/ (last access: 21 June 2024)	
Israel Meteorological Service	https://ims.gov.il/en (last access: 31 July 2024)	Ministry of Transport and Road Safety, Israel (2024)
General Bathymetric Chart of the Oceans	https://www.gebco.net/ (last access: 21 June 2024)	GEBCO Bathymetric Compilation Group (2023)

and regional scales. Similar to the OVL portal, MDS provides MyOcean Viewer, which allows users to add different products to the map viewer. Moreover, the dataset can be easily retrieved with commands using the Copernicus Marine Toolbox.

Another Copernicus service, the Climate Data Store (CDS), provides climate data such as global precipitation data; this service is implemented by the European Centre for Medium-Range Weather Forecasts (ECMWF). However, the rainfall data used in this article were obtained from the coastal weather stations obtained from the Israel Meteorological Service, provided by the Ministry of Transport and Road Safety, Israel. The service provides daily rainfall and rainfall automated recorded every 10 min. Note that these systems tend to underestimate the rainfall in major events according to the information provided by the service.

The General Bathymetric Chart of the Oceans (GEBCO) has released several global bathymetric and topography grids with a spatial resolution of 15 arcsec since 2003. This model is especially useful for providing context to SAR data in areas with varying bathymetry, which can affect the interpretation of ocean surface roughness in satellite imagery.

Section 4 explains different SAR signatures and provides examples of explanations on different dark formations with the help of the supplementary data. A summary list for those examples along with the supplementary data is provided in Sect. 4.9 (see Table 3). Note that not all the data in the dataset were confirmed with the supplementary data but with the experience of the human inspectors and their understanding of the study area.

3 Methods

3.1 Manual Inspection

As stated in Sect. 2.2, the annotations were initially done in the framework of our previous study (Yang et al., 2024) with the help of an open source image annotation tool, LabelImg (Tzutalin, 2015). Those image patches were geolocated, as in this case, referring to other supplementary materials and understanding the location of the spills is easier. However, the image patches and the oil objects in the published dataset were provided in the range and azimuth direction of the corresponding SAR products.

Continuous oil spillage from one source can be like multiple oil slicks after the physical processes. Therefore, definitions of those oil objects might be tricky; one can interpret them as one oil object or several oil objects. In addition, the extent of an oil slick might not be easy to define; for example, the evaporation of oil could make it look like it is fading away in SAR scenes. It shall be noted that different definitions of the extent of one oil object can play a vital role in model performance calculations. For example, if there is one oil object in the dataset, but the object detector considers it to be two nearby objects, they may be considered false positives if they do not pass the threshold used to define true positives (see Sect. 5.1 for performance evaluation). Figure 5 provides some image patches inside the published dataset with oil object labels to illustrate how the authors annotated the oil slicks. The tags of these image patches are provided as captions, and the explanations for tags are shown in Sect. 2.2; readers can find an extracted data table in Appendix A.

3.2 *K*-means Clustering

K-means (Lloyd, 1982; MacQueen, 1967) is an unsupervised algorithm to partition a set of observations into a specific number, k , of clusters. The concept is to obtain k clusters by satisfying that the sum of the distance between each observation and the mean vector (centroid) of its corresponding cluster is minimum; the Euclidean distance is a common way of calculating such distance. To achieve this idea, the algorithm first randomly partitions observations into k sets and calculates their centroids. Based on these centroids, each observation is assigned to its nearest cluster. Afterwards, the algorithm iteratively updates the centroid and assign observations of each cluster to a new cluster until convergence is achieved.

In image clustering, each image is represented as a feature vector in the vector space that contains the features of the image, such as texture and shape. To extract features of the image patches in the *no-oil set*, the InceptionV3 model (Szegedy et al., 2015) pre-trained with a large visual database, ImageNet (Deng et al., 2009), was used. *K*-means clustering was then applied to categorize the image patches with the help of the Scikit-learn *K*-means module. Figure 6 shows examples of image patches from each cluster (see Appendix A for the patch information).

The purpose of using the *K*-means clustering method is to provide a *no-oil set* in which the signatures of different phenomena appear more balanced. In other words, the clustering method categorized the dataset, and then the same number of image patches from each class were randomly selected. However, for better understanding the performance of the object detector on different kinds of SAR signatures, it would be ideal if all image patches within each class have similar sources of phenomena that could be explained by humans. Therefore, human interpretation was considered when selecting the number of classes, which was adjusted by reviewing image patches in different classes.

Sea states in coastal areas are often complicated by factors such as bathymetry and interaction with land. However, open water typically experiences larger-scale dynamics that can manifest a variety of different SAR signatures. Therefore, the offshore subset is expected to have a greater variety of sources of SAR signatures. Thus, the *K*-means clustering method was given 12 and 5 classes for the *nw* and *nc* subsets, respectively.

4 SAR Signatures

The radar transmits microwave pulses and some of them are reflected back to the radar, the normalized power of the received signals over the actual ground area is known as radar backscatter, σ^0 . The radar backscatter depends on radar system characteristics (e.g., polarization, wavelength, and radar geometry) and the properties of the target (e.g., shape, dielectric constant, and roughness) (Woodhouse, 2006).

For ocean applications, sea surface roughness is generally regarded as a key factor; variations in surface roughness are closely related to wind speed and direction (Robinson, 2004; Woodhouse, 2006). Winds form friction between air and water and cause small capillary waves in millimeter-to-centimeter scales. These wind-induced capillary waves are usually regular over a large area and act as resonant Bragg scatterers, which can interfere constructively if the Bragg condition is satisfied as defined:

$$2d \cdot \sin \theta = n\lambda, \quad (2)$$

where d is the spacing of the scatterers, θ is the incidence angle, λ is the radar wavelength, and n is an integer. The spacing of the scatters can be regarded as ocean wavelength. The incidence angle of Sentinel-1 IW mode ranges between 29.1 and 46.0°; therefore, according to the equation, the resonant ocean wavelength is at a similar scale as radar wavelength. In addition, the waves should travel along the range direction (either parallel or anti-parallel) to obtain the strongest resonance. This constructive interference is also known as resonant Bragg scattering or the coherence scattering mechanism. On the other hand, if the condition is not fulfilled, destructive interference occurs, and the scattered power is reduced.

The ocean surface contains small-scale capillary waves, gravity waves in meter scales, swell, and large-scale currents; therefore, the ocean surface is considered a complicated summation of a wave spectrum of different wavelengths. However, the radar returns come from these short capillary waves, which have wavelengths similar to the radar wavelengths, rather than the longer waves; hence the Bragg mechanism is often used to interpret radar backscatter at the ocean surface (Robinson, 2004).

The following subsections illustrate and explain SAR signatures due to oil slicks, different oceanic or atmospheric phenomena, or human-related activities. Some supporting materials listed in Table 2 are used to comprehend the phenomena and to better interpret the SAR signatures. If users need more detailed information about the supporting data, they should check the descriptions in Sect. 2.3 or refer to the websites in Table 2. Note that these examples are not provided in the published dataset. The published dataset only includes image patches from 2019; however, the examples are not limited to the time interval. The selections are mainly based on the accessibility of the supplementary materials and are to avoid SAR signatures due to multiple phenomena, which make it challenging to interpret. These examples are not cropped into image patches as most phenomena influence an area larger than the size of an image patch. In addition, instead of displaying them in SAR geometry in range and azimuth, they were projected to the World Geodetic System 1984 (WGS84), making it easier to compare them with different supplementary data. All the example scenes are listed at the end of this section (Sect. 4.9), so that users can download SAR scenes themselves from the Copernicus Data Space Ecosystem.

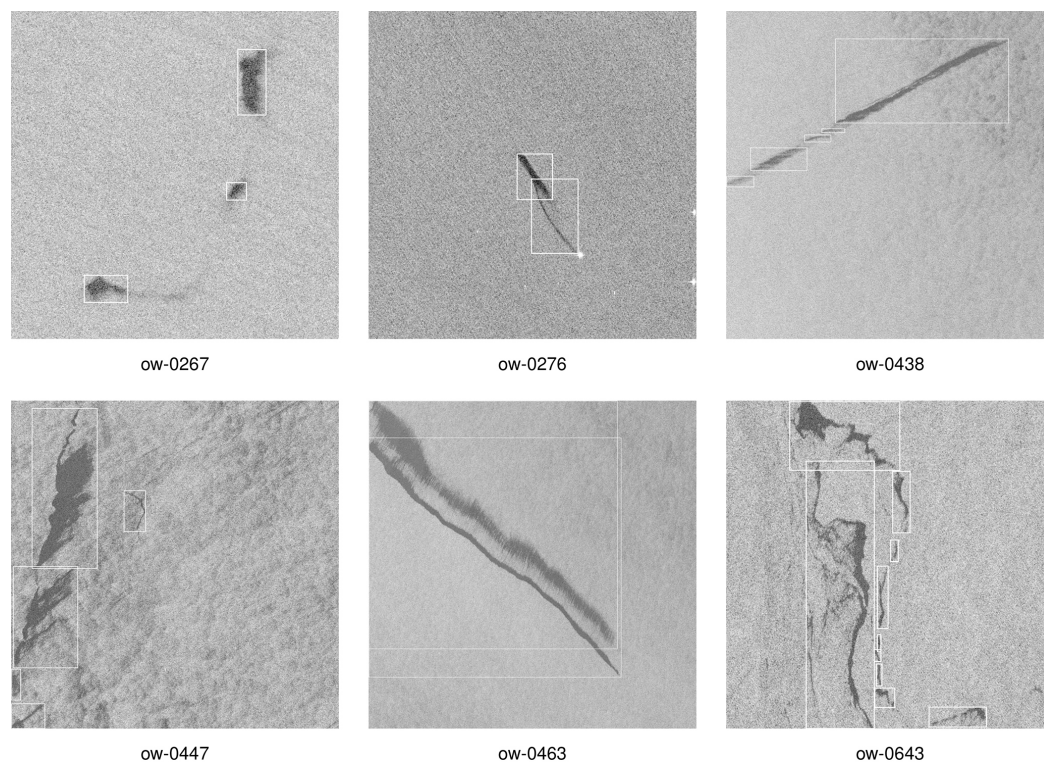


Figure 5. Image patches from the published dataset along with the labels of the oil objects marked with white bounding boxes. Their corresponding image tags (explained in Sect. 2.2) are also provided, the readers can find their further information recorded in the data table (see Appendix A). The figure contains modified Copernicus Sentinel data (2019).

4.1 Oil slicks

The presence of oil slicks decreases the surface tension of the water and lowers wind friction; therefore, short gravity and capillary waves are dampened, which reduces the radar backscatter and results in dark formation in SAR imagery. Spaceborne SAR sensors can observe a large area on a regular basis; however, to investigate the quantity, type, and thickness of the oil, it usually requires multiple sensors, such as infrared, ultraviolet, microwave radiometer, and laser fluorosensors (Ferraro et al., 2009; Fingas and Brown, 2017). This dataset was inspected without data from other sensors available; therefore, the distinction between oil spills and other possible chemical spills is not clearly defined.

Figure 7 shows SAR scenes covering an oil slick in two separate acquisitions taken at 15:49 on 3 November 2022 and at 03:52 on 4 November 2022. Separate charts show the profiles of radar backscatter sampled along the red lines, the shadowed areas mark the approximate locations of oil-induced dark formations. Wind speeds at 16:00 on 3 November 2022 and 04:00 on 4 November 2022 were acquired from CMEMS and MDS (2024c); the corresponding average wind speeds of the shown area were 3.92 and 4.09 m s^{-1} , both blowing in the southeastward direction.

The first acquisition shows an oil slick with apparent differences in backscattering compared to its surrounding areas. Though the wind conditions seemed similar, the two acquisitions had different heading and look angles; therefore, the wind-induced signatures differed and resulted in lower overall backscattering in the second acquisition. This example illustrates the dynamicity of an oil spill over time in SAR data and how oil properties, ambient wind speed and direction relative to the SAR azimuth make oil slicks appear differently in SAR data.

Reports or records are usually not provided for smaller deliberate oil discharges, meaning that there is no ground truth; thus, inspecting oil slicks should carefully consider the possibilities of dark formations from other phenomena. The following subsections introduce those *look-alikes* and provide supplementary materials to better understand the signatures.

4.2 Wind

As explained at the beginning of this section, wind is closely related to the sea surface roughness, which is a key element for SAR signatures. Under low winds, the sea surface is smooth and calm, and the backscattering will be close to the SAR noise floor; therefore, the modulation of backscat-

6816

Y.-J. Yang et al.: Dataset of oil slicks, look-alikes and remarkable SAR signatures

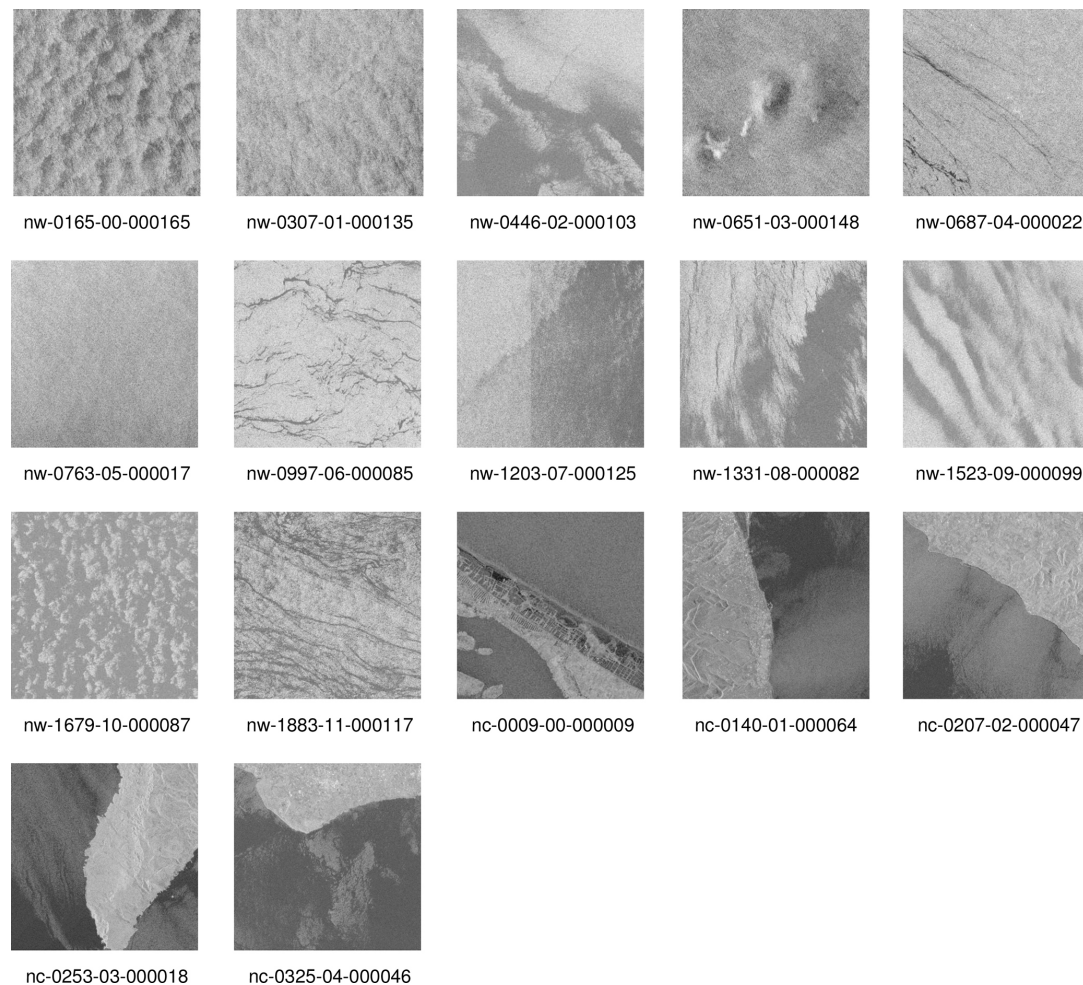


Figure 6. Image patches from different clusters in the *no-oil* set. Their corresponding tags (explained in Sect. 2.2) are also provided, the readers can find their further information recorded in the data table (see Appendix A). The figure contains modified Copernicus Sentinel data (2019).

tering from oil slicks can not be revealed. On the other hand, if the sea surface is too rough under high winds, oil slicks are also not possible to be indicated. Previous studies suggested optimal wind speed ranges between 2–3 and 7–12 m s^{−1} for oil slick detection using SAR (Gade et al., 2000; Robinson, 2004; Brekke and Solberg, 2005). As the visibility of oil slicks depends on not only SAR sensors but also the age and type of the oil, the upper and lower limits differ in different studies; this range should be considered a hint. Oil slicks can still be observed outside this range in some circumstances.

Some atmospheric phenomena can influence ocean surface roughness and result in certain SAR signatures; examples of these phenomena are the atmospheric front, phenomena related to geographic features, unstable atmospheric boundary layer (ABL), and atmospheric gravity waves (AGWs, also known as atmospheric internal waves) (Robinson, 2004).

Since AGWs form similar patterns as oceanic internal waves (OIWs), they are both explained in Sect. 4.3.

Sudden changes in wind speed and direction can create an atmospheric front that separates two air masses and is shown as a boundary between weaker and stronger radar backscatter. Similar signatures of the fronts can also be seen where winds blow from land to sea through coastal terrain. The land usually cools down during the night, but the temperature over the adjacent sea may remain, in which case the air pressure over the land would be higher than that over the sea, resulting in the wind blowing offshore. This cooler and denser air from the land rolls out to the sea and pushes the warm air over the sea upwards, creating a cold land breeze front (Robinson, 2004). Land breeze fronts usually create near-shore bands of modulated surface roughness parallel to the coast, as shown in Fig. 8. Similarly, during the night, the cool air mass from the mountains could flow down the val-

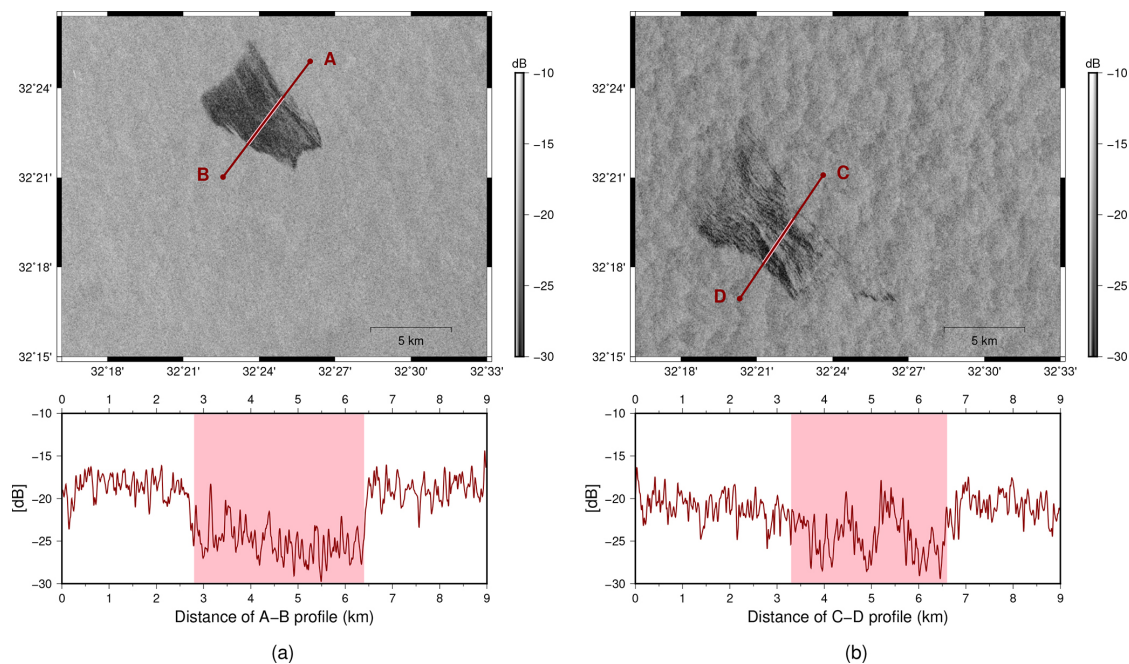


Figure 7. Examples of an oil slick appearing in SAR acquisitions at different time (a) 3 November 2022 15:49 (b) 4 November 2022 03:52, showing its changes overtime. The profiles illustrate the radar backscatter along the red line, and the shadowed area highlights approximately where the oil-induced dark formation is located. The figure contains modified Copernicus Sentinel data (2022).

ley driven by the density flow; this is known as the katabatic wind. If the mountains are located in coastal areas, the winds would blow toward the sea and spread out in a fan shape, as shown in Fig. 9a. Figure 9b indicates the topography with mountains and valleys close to the shore in Lebanon; the terrain and bathymetry model is obtained from GEBCO Bathymetric Compilation Group (2023). These katabatic wind-induced signatures tend to reoccur at roughly the same places since they are related to the topography (Robinson, 2004). Note that the bright pixels are especially distinct at the bottom part of Fig. 9a was due to radio frequency interference (RFI), which will be explained in Sect. 4.8.

Figures 8 and 9a were both taken at about 03:44 UTC, which should be 06:44 local time (UTC+3, considering daylight saving time); shortly after sunrise at about 06:03 and 06:29 local time, respectively. Land breeze and katabatic winds usually occur during the night, when the land has cooled down a lot, and before the air warms up during the day. Based on our experience inspecting SAR images in this area, the katabatic wind fronts are commonly observed in SAR images in the descending orbit (taken at around 03:45 UTC) covering the coastal areas of Lebanon and Israel. In addition, wind shelters and wind shadows can also appear as low radar backscatter along the coast or off an island.

Dynamics in the ABL driven by surface wind can increase surface roughness and lead to phenomena seen in SAR imagery. When the air is heated by a warmer sea surface, it

expands and becomes less dense than the air above it. The resulting ABL instability drives convective cells in which warm and humid air rises in updrafts and is replaced by descending cooler air. The downflow of the cold air induces a radial outflow; coupled with the wind flow, they lead to the fluctuations of surface roughness and form cellular patterns in SAR images (Robinson, 2004); such patterns can be observed in Figs. 8 and 9a.

Thermodynamic instability in ABL, mainly determined by temperature and humidity, can lead to wind streaks forming streak-like patterns in SAR (Zhou et al., 2025). These wind streaks enable the estimation of wind direction by using SAR (Lehner et al., 1998). Similar streak patterns may also result from the intersection of wind-driven surface currents and Stoke's drift of surface waves. This intersection can lead to Langmuir circulation, producing helical roll vortices that are approximately parallel to the wind direction (Langmuir, 1938; Etling and Brown, 1993). These helical rolls appear alternatively as the right and left helices, resulting in upward and downward flows between the rolls, which lead to higher and lower surface roughness and are shown as dark and bright streaks in SAR (Langmuir, 1938; Robinson, 2004). Figure 10 shows an example of such streak patterns alongside the wind speed and direction.

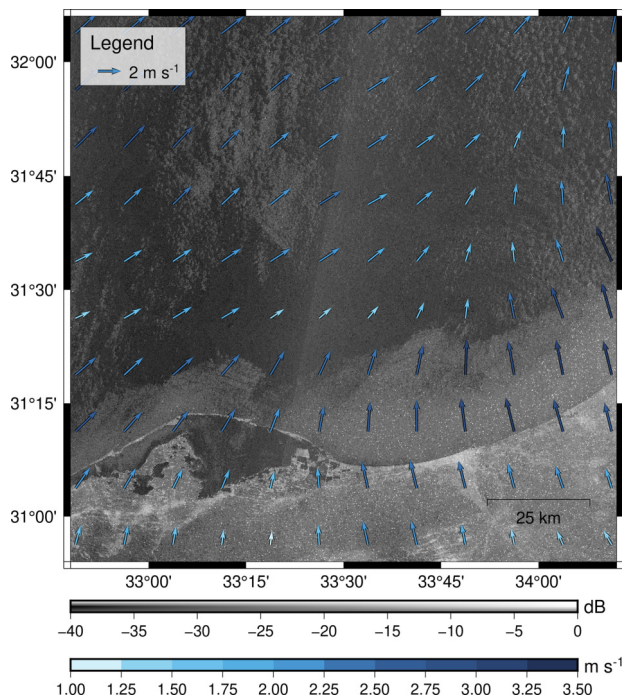


Figure 8. An example of land breeze fronts in the SAR scenes taken at 03:44 on 2 August 2023 near Egypt, plotted with the simulated wind speed at 04:00 obtain from CMEMS and MDS (2024c). The figure contains modified Copernicus Sentinel data (2023). The plotted coastline was obtained from Wessel and Smith (1996).

4.3 Internal Waves in the Ocean and Atmosphere

Internal waves can occur in any stratified medium, such as fluids with varying density. In the ocean and atmosphere, two restoring forces act on internal waves: gravity and the Coriolis force. Thus, perturbations of the vertical density gradient will generate internal waves with frequencies between the Brunt-Väisälä frequency and the Coriolis parameter.

The primary drivers of internal waves in the ocean are tides, closely followed by the wind. The particle motion of the oceanic internal waves (OIWs) produces surface convergence and divergence that modulate the short gravity and capillary waves, resulting in amplification and attenuation of these waves, respectively. As a result, the alternating convergence and divergence zones on the sea surface lead to patterns of bright and dark strips in SAR imagery (Alpers et al., 2008; Robinson, 2010; Alpers and Huang, 2011). Similar to the ocean, disturbances in atmospheric stratification also generate internal waves, often referred to as atmospheric gravity waves (AGWs).

When for example external forces push the air upward, the air gets cooler, and the water vapor saturation point is likely to be reached, which leads to the formation of clouds. On the other hand, when the air gets warmer, water evaporates, resulting in a clear sky. Therefore, when the moisture content

of the air is sufficient and the amplitude of the AGW is large enough, cloud streets and clear skies are expected to appear over the crests and troughs of the AGW, respectively. The variations of wind stress at the sea surface disturb the small surface roughness and result in dark and bright strips in SAR scenes, similar to OIW (Alpers and Huang, 2011).

Internal waves play a crucial role in energy transport within the ocean and atmosphere. The interactions of internal waves with itself, topography and other ocean or atmosphere dynamics are highly complex and not yet fully understood. Through the SAR images and the identification and clustering of possible OIW and AGW signatures by the algorithm, there is now a high number of images available, providing a better spatial and temporal resolution of the internal wave field and allowing for a deeper understanding of these processes. However, it can be challenging to distinguish between OIWs and AGWs in general and within the presented dataset. Nevertheless, the shape and structure of the wave patterns provide hints for their differentiation (Alpers and Huang, 2011), as summarized in the following. In general, OIWs are observed in low-wind areas since otherwise their SAR signatures are too weak to be detected, especially in conditions with wind speeds greater than 10 m s^{-1} ; contrastingly, AGWs can be observed at all wind speeds. In addition, OIWs mostly appear near an upwelling area or at locations where rough topography, shallow underwater ridges, sea mounts, or steep shelves are present. On the other hand, AGWs usually appear in areas where wind interacts with mountain ranges, different air masses collide, strong wind shear occurs, or convective activities are associated with cold fronts (e.g., thunderstorms).

A previous study presented OIWs propagating from the edge of the continental shelf and supported their explanation with temperature, salinity, and density profiles from a CTD probe (Liu et al., 1998). Figure 11 shows the SAR scenes taken at 15:41 on 28 March 2024 at the coast of Lebanon, plotted with the contour of bathymetry and terrain model obtained from GEBCO Bathymetric Compilation Group (2023). The bathymetry profile along the red line is shown in a separate chart. Dark and bright strips can be seen east of the continental slope (between points B and A). The strips appear to be parallel to the both the coastline and the continental slope. Therefore, the stripes may be due to oceanic internal waves generated in the interaction between currents and the slope, or due to atmospheric internal waves generated as lee waves from the mountain topography. Without additional data, such as vertical profiles of ocean and atmosphere, it is difficult to determine the sources of internal waves in this example.

Figure 12 shows the SAR scenes taken at 03:52 on 27 May 2023 and a separate profile of radar backscattering along the red line. On top of the SAR scene, the hourly sea surface wind at 04:00 on 24 May 2023 obtained from the scatterometer and model (CMEMS and MDS, 2024c) is plotted; the wind speed in this area was around 2.87 to 10.18 m s^{-1} , and

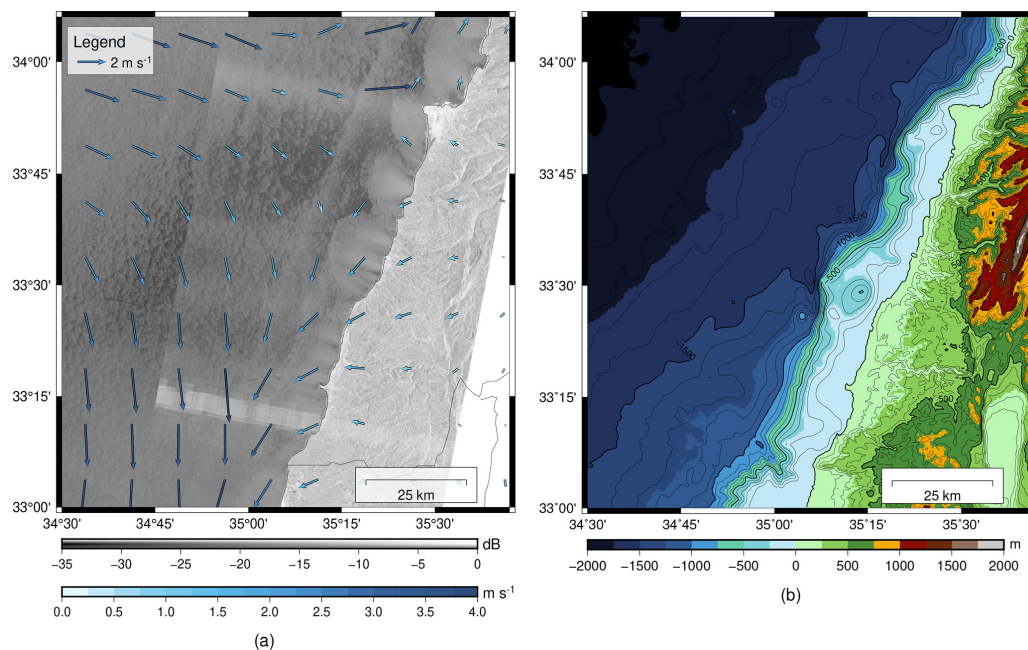


Figure 9. (a) An example of katabatic wind-induced signatures in the SAR scenes taken at 03:43 on 24 September 2022 near Lebanon, plotted with the simulated wind speed at 04:00 obtain from CMEMS and MDS (2024c). The figure contains modified Copernicus Sentinel data (2022); the coastline and borders were obtained from Wessel and Smith (1996). (b) Bathymetry and terrain models obtained from GEBCO Bathymetric Compilation Group (2023).

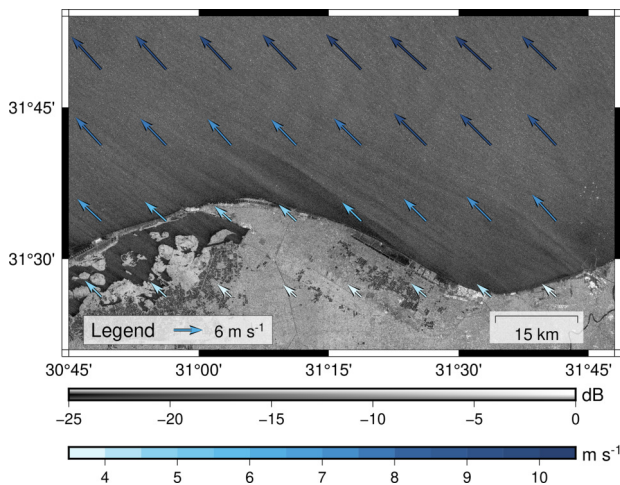


Figure 10. An example of streak patterns in the SAR scene taken at 03:52 on 27 January 2023 near Egypt, plotted with the simulated wind speed at 04:00 obtain from CMEMS and MDS (2024c). The figure contains modified Copernicus Sentinel data (2023).

the average wind speed was 7.97 m s^{-1} . The higher the wind speed, the less likely it is to be OIWs; therefore, the strip patterns are more likely to come from AGWs. Based on the consecutive scenes taken before (i.e., northern to) the shown scene, the wave patterns cover large ocean areas, which are

commonly observed in SAR scenes with AGWs (Li, 2004). In addition, streaks from AGWs are usually approximately perpendicular to the direction of the wind (Robinson, 2004; Li, 2004) and are expected to show up as narrow dark bands followed by broad bright bands alternatively (Alpers and Huang, 2011).

4.4 Areas of mixing and vertical advection in the ocean

In the ocean, there are a variety of processes that can lead to mixing or vertical advection, especially near shallow topography or the coast. In the deeper layers of the ocean, more nutrients and colder water can be found compared to the upper layers. This means that mixing or vertical advection typically results in a colder sea surface and a vertical nutrient flux, which in turn promotes chlorophyll growth. Mixing can be caused, for example, by the mentioned OIWs, which, like surface waves, can break, leading to mixing. Vertical advection typically occurs due to strong, steady winds, which create a force on the surface layer of the sea, causing it to move in the wind direction. The Coriolis force then deflects this motion to the right in the northern hemisphere (left in the southern hemisphere), a process called Ekman transport. This results in a 90° shift in the surface layer's movement. This divergence of Ekman transport brings cooler, nutrient-rich water from deeper layers to the surface, known as up-

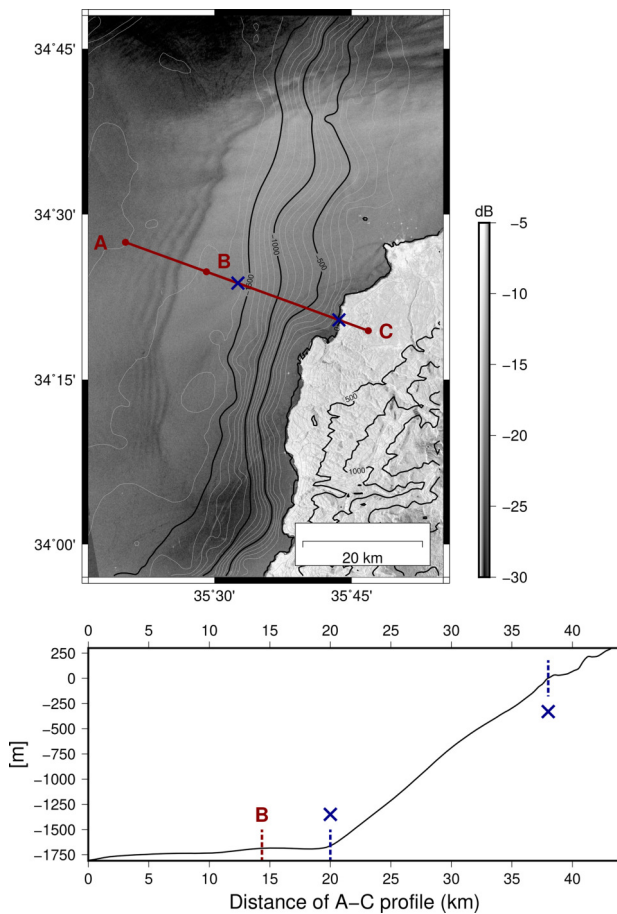


Figure 11. An example of internal waves in the SAR scene taken at 15:40 on 28 March 2024 near Lebanon, plotted with the contour of bathymetry obtain from GEBCO Bathymetric Compilation Group (2023). A separate chart illustrates the bathymetry profile along points A and C, sampled every 50 m. The figure contains modified Copernicus Sentinel data (2024).

welling, often seen along coastlines where winds blow parallel to the shore (Robinson, 2010; Knauss and Garfield, 2016).

Previous studies have shown areas of enhanced mixing and/or vertical advection in SAR imagery with various causes, such as coastal parallel winds or mixing within cyclonic eddies (Clemente-Colon and Yan, 1999; Alpers and Zeng, 2021). In upwelling regions, low backscatter in SAR imagery can be observed due to increased stability of the ABL (due to reduced wind stress from the lower SST), increased surface water viscosity (which enhances the dampening effect), and the presence of biogenic surface films (see Sect. 4.6) (Clemente-Colon and Yan, 1999). In addition to these mechanisms, the surface divergence and convergence may also play a role (Liu et al., 2016). Previous studies provided a comprehensive explanation of the areas of enhanced mixing or vertical advection in the Mediterranean Sea, for

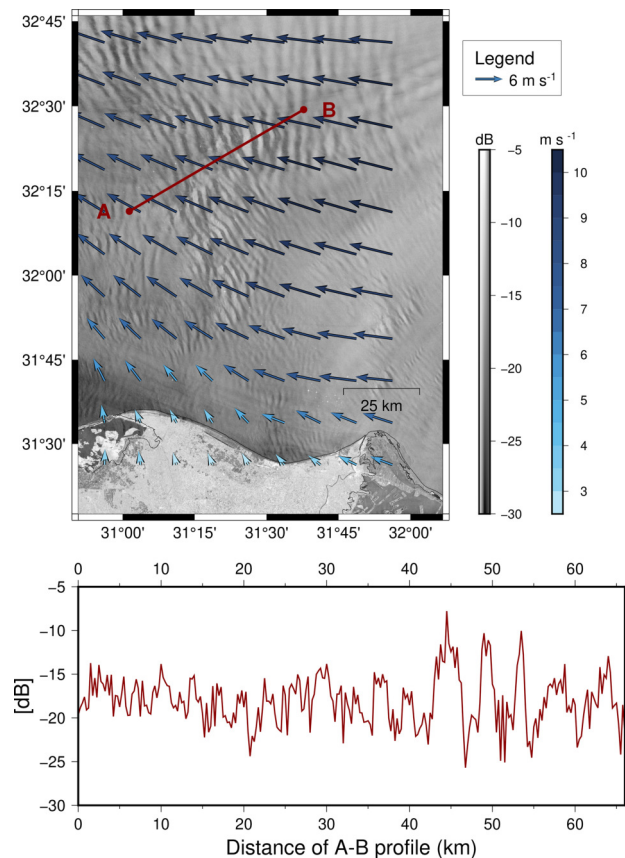


Figure 12. An example of AGWs in the SAR scene taken at 03:51 on 27 May 2023 near Egypt, plotted with the sea surface wind velocity obtain from MDS (CMEMS and MDS, 2024c). A separate chart shows the profile of radar backscatter along the red line, sampled every 250 m. The figure contains modified Copernicus Sentinel data (2023). The coastline was obtained from Wessel and Smith (1996).

example Bakun and Agostini (2001). In the region of our dataset, the following areas (mostly wind-induced upwelling zones), can be found near the coast: The coastal divergent zone on the south side of Cyprus tends to induce upwelling, especially in summer. On the other hand, the north side of Egypt is dominated by coastal convergence with downwelling, where surface water is brought downward with the flow throughout the year but is most intense in winter. Along the eastern boundary of the Mediterranean Sea, the coasts of Syria, Lebanon, and Israel, the wind generally blows eastward toward the coast. However, the slight right turnings of the wind induce some areas of upwelling.

Figure 13a shows SAR scenes covering Cyprus at 03:51 on 12 May 2019 and illustrates a possible coastal upwelling area at the southern coast of Cyprus. As suggested in Alpers and Zeng (2021), SST and chl *a* data can be used to help indicate upwelling areas; Fig. 13b and c present the corre-

sponding data at 00:00 on 12 May 2019 obtained from the SST MDS (CMEMS and MDS, 2024a; Buongiorno Nardelli et al., 2013) and chl *a* MDS (CMEMS and MDS, 2024b; Berthon and Zibordi, 2004; Volpe et al., 2019). In most areas, the patterns of both data were similar to each other. However, the southwestern coast of Cyprus had a lower chl *a* concentration than the southeastern coast, though the southwestern and southeastern coasts had similar SST. On the other hand, SAR scenes showed low radar backscatter at both the southwestern and southeastern coasts. Wind speeds were about $2\text{--}3\text{ m s}^{-3}$ in the coastal areas according to the hourly sea surface wind velocity from scatterometer and model at 04:00 on 12 May 2019 obtained from MDS (CMEMS and MDS, 2024c). Therefore, the low radar backscatter could result from low wind speeds coupled with surface divergence due to upwelling. Additionally, SAR scenes indicate possible surface films that have accumulated as linear features to the west of the dashed red line in the figure. This aligns well with the patterns of SST and chl *a* concentration.

4.5 Meso- and Submesoscale Eddies

Mesoscale eddies (the prefix “meso” means “intermediate”) describe features with radii of about 10 to 200 km and a lifetime of a few days to one year or even longer (Chelton et al., 2007). Submesoscale is defined as slightly smaller than the mesoscale, with horizontal scales of 100 m to 10 km (or less than the first baroclinic mode Rossby radius of deformation (R_d)), vertical scales smaller than the depth of the main pycnocline and a life-time of one day (McWilliams and Molemaker, 2011; Lévy et al., 2012).

Despite a long history in studies of eddy activity, various aspects regarding processes and impacts of meso- and submesoscale eddies still remain unclear. One difficulty in the past and still today is the acquisition of a sufficient database to study these short-lived and small-scale phenomena, especially in the submesoscale regime. Satellite radar altimeter observes sea surface height (SSH); the difference between SSH and mean sea surface is known as sea surface height anomaly (SSHA), indicating the small displacement of sea surface elevation due to mesoscale eddies. For example, in anticyclonic eddies, the core is less dense (warm core) and has a high SSHA. On the contrary, in cyclonic eddies, the SSHA is lower and the density in the core is higher than in the surrounding area. Chlorophyll, suspended particulates, or other optically reflective materials in the water can reveal the motion in the visible channels (Robinson, 2010). In practice, an altimeter is commonly used for monitoring mesoscale eddies (Alpers et al., 2013), whereas submesoscale eddies are observed with infrared and optical sensors or SAR (Alpers et al., 2014). As the sea surface roughness could be modulated by eddies, SAR can also manifest signatures of eddies on an even smaller scale. Eddies can result in areas of surface convergence and divergence, which under moderate wind conditions appear as bright and dark lines in SAR im-

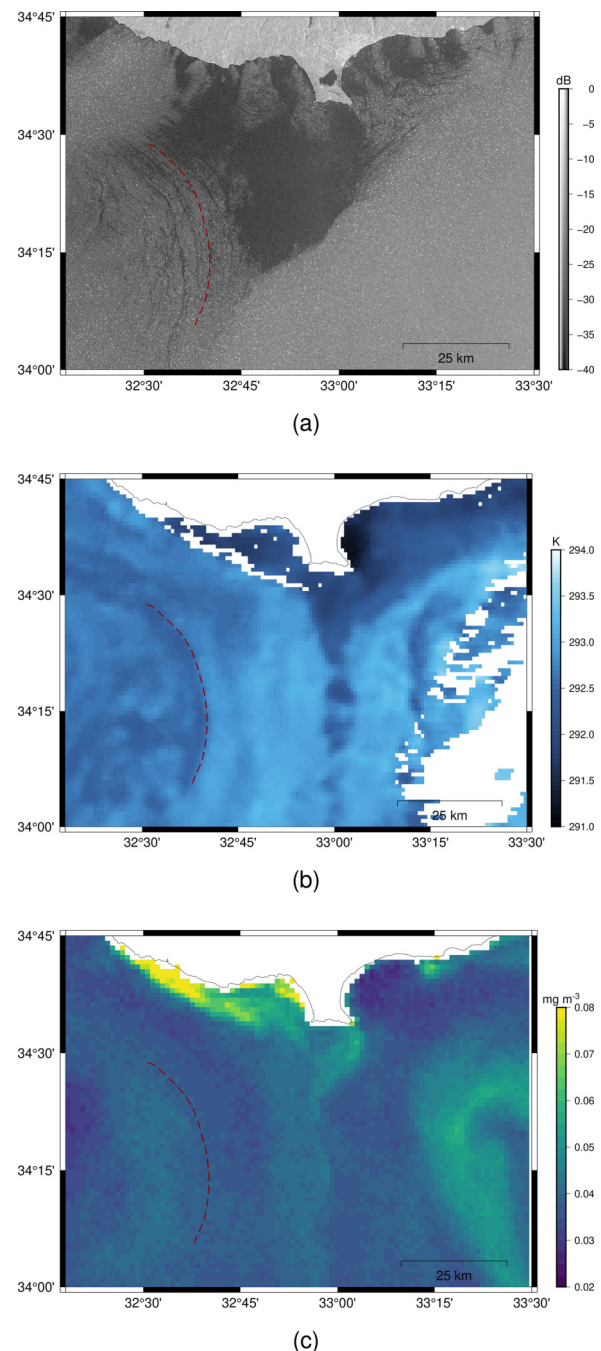


Figure 13. An example of possible coastal upwelling in southern coast of Cyprus observed by (a) SAR at 03:51 on 12 May 2019 and the supporting materials, (b) SST and (c) chl *a*, simulated at 00:00 on 12 May 2019 (CMEMS and MDS, 2024a, b). The linear features to the left of the red dashed line in SAR indicates the possible surface films accumulations, which aligns well with the patterns of SST and chl *a*. The figure contains modified Copernicus Sentinel data (2019). The plotted coastline and borders were obtained from Wessel and Smith (1996).

ages (Robinson, 2010). In addition, surface films tend to accumulate along the current shear in eddies. These films can dampen capillary waves and, in this way, enhance SAR signatures of the spiraling shear lines. They are sometimes regarded as “black” eddies in literature; on the other hand, “white” eddies refer to bright curved lines from eddies interacting with waves and current along the shear line at high wind speeds ranged between 7 and 12 m s⁻¹ (Karimova and Gade, 2013).

Pegliasco et al. (2021) provided mesoscale eddy detection and tracking methods in the Mediterranean Sea based on products from radar altimeter data from 2000 to 2015 and gave an overview of eddy occurrence in the Mediterranean Sea; the Levantine basin is dominated by anticyclone eddies (warm core rings), which last longer than six months. In the southeastern Levantine basin, SAR observations indicated that the recurrent Cyprus and Shikmona eddies, located south of Cyprus at around 34°N and west and east of 33.5°E, respectively, are dominant (Zodiatis et al., 2005; Gertman et al., 2007; Menna et al., 2012). However, the area is quite complex with cyclonic and anticyclonic eddies interacting with the alongshore cyclonic current and with each other (Gertman et al., 2007; Menna et al., 2012). Figure 14 illustrates such an example of mesoscale eddies forming spiral lines; the SAR scene was taken at 03:52 on 29 September 2022.

4.6 Biogenic Surface Film

There are two types of biogenic surface films that can reduce radar backscatter. Surface active organic molecules with hydrophobic and hydrophilic parts can form a molecular monolayer at the sea surface. The surface waves compress and dilate the molecular monolayer, leading to surface tension and surface potential gradients and thus generating the longitudinal Marangoni waves. The interaction of these waves and the transverse gravity capillary waves can result in Marangoni damping and reduce the radar backscattering (Hühnerfuss, 2006; Alpers et al., 2017). These surfactants usually originate from the wastewater or remnants of organisms in the water. Another type of biofilm consists of a much thicker layer with a high concentration of viscous floating materials such as phytoplankton, e.g., *Sargassum* and cyanobacteria (Qi et al., 2022). The accumulation of these floating materials decreases the surface tension of the water and dampens the gravity and capillary waves; this effect is similar to the effect of oil discussed in Sect. 4.1.

Marine phytoplankton are ubiquitous in the sunlit layer of the oceans as they obtain energy through photosynthesis. Satellite-based studies have shown that the Mediterranean Sea generally has low chl *a* concentration (a useful proxy for phytoplankton biomass), with concentrations often less than 0.2 mg m⁻³ with the exception of some blooming areas in the late winter and early spring (Siokou-Frangou et al., 2010). The overall chl *a* concentration from satellite and in

situ data shows a decline in the trends of west-to-east and north-to-south over the Mediterranean Sea (Siokou-Frangou et al., 2010). Even in blooming seasons, the chl *a* concentration was rarely greater than 0.5 mg m⁻³ in the Eastern Mediterranean Sea (Siokou-Frangou et al., 2010), and similar concentrations have been reported from time-series in the Northwestern Mediterranean sea (von Jackowski et al., 2024).

Under a light wind condition, the convergent surface currents accumulate surface films (e.g. algae) along the current shear in fronts and eddies (Gade et al., 2013); these films can dampen the short gravity capillary waves and reduce SAR backscatter. On the other hand, the divergent surface currents make the films less concentrated and the dampening effect is less pronounced (Robinson, 2004). The chl *a* concentration at the corresponding time and location of Fig. 14 had a maximum of 0.059 mg m⁻³ and an average of 0.010 mg m⁻³ (CMEMS and MDS, 2024b), which suggests that the spiral patterns of eddies in Fig. 14 were not due to accumulations of surface films. It is possible that the patterns were enhanced by a molecular monolayer, but this can not be confirmed without in situ water samples.

4.7 Rain cell

The rain-induced SAR signatures are contributed by a combination of surface scattering, volume scattering and attenuation of radar pulse. Modulations of the sea surface roughness can come from several causes related to the rainfall. The impinging rain drops can either dampen or roughen the sea surface, leading to strong or weak backscattering. In addition, splash products from rain drops can cause scattering. Rain cells usually produce downward airflows (i.e., downdraft), which roughen the sea surface (Alpers et al., 2016). However, splash products from rain drops cause scattering and behind where the rain cell dropped on the sea surface in the direction of wind, the wave is damped (Atlas, 1994). Figure 15 shows such an example of rain cell associated with downdraft, which roughened the sea surface and was shown as bright elliptical area. On top of that, hydrometeors also play important roles in the SAR signatures as they can cause volume scattering and attenuation of the radar pulse, which strengthen and weaken the radar backscattering, respectively (Danklmayer et al., 2009; Alpers et al., 2016). At C-band, radar signatures for rain are complicated as the decrease or increase of the radar backscatter relative to the background is related to rain rate, wind speed, incidence angle, and time evolution of the rain event (Alpers et al., 2016). For low to moderate high rain rate (smaller than 50 mm h⁻¹), the attenuation is negligible; for heavier rain, the attenuation can be greater than 1 dB (Lin et al., 2001).

Figure 16a shows a SAR scene covering the Israeli coast taken at 03:42 on 24 January 2018. The bright patches, located 5.5 to 15 km away from the coast and quasi-parallel to it, indicate possible rain-induced signatures. To get an idea

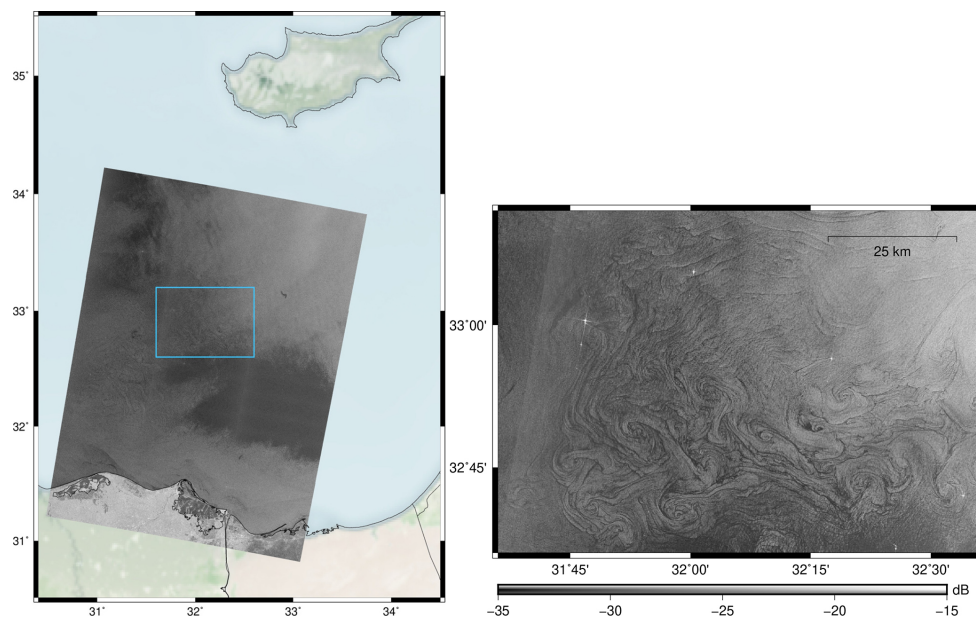


Figure 14. An example of mesoscale eddies observed by SAR at 03:52 on 29 September 2022. The right figure shows the zoomed-in area marked in blue in the left figure. The figure contains modified Copernicus Sentinel data (2022). The base map of the left figure was obtained from Stevens (2020), and the coastline and borders were obtained from Wessel and Smith (1996).

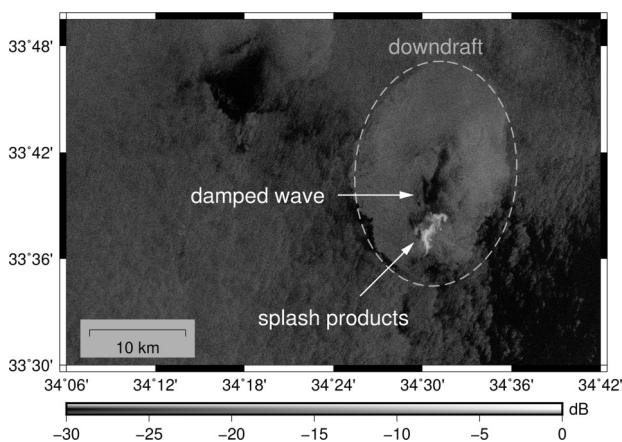


Figure 15. An example of a rain cell with downdraft patterns observed by SAR at 03:43 on 18 October 2022. The figure contains modified Copernicus Sentinel data (2022).

of the weather conditions in this region, daily and 10 min rainfall measurements from the four coastal rain stations were obtained from the Israel Meteorological Service (Ministry of Transport and Road Safety, Israel, 2024). The locations of these stations are plotted in Fig. 16a, and their daily rainfall measurements on 24 January (one day in Israel time, UTC+2) are written in brackets. Though the automated 10 min rainfall data tend to underestimate the rainfall in major events, they provide an overview of rainfall distribution for the day; Fig. 16a illustrates the 10 min rainfall data from 00:00 to 07:00 on 24 January (UTC). The Hadera Port, Tel Aviv coast, and Ashdod Port stations all reported some rainfall between 02:30 and 05:30. As the rain stations are not directly at the location of rain cells observed from SAR, rainfall at the coasts could be delayed or earlier than rainfall at the water.

for the day; Fig. 16a illustrates the 10 min rainfall data from 00:00 to 07:00 on 24 January (UTC). The Hadera Port, Tel Aviv coast, and Ashdod Port stations all reported some rainfall between 02:30 and 05:30. As the rain stations are not directly at the location of rain cells observed from SAR, rainfall at the coasts could be delayed or earlier than rainfall at the water.

4.8 Others

This section has explained oil slick and a variety of ocean and atmospheric phenomena as origins of SAR signatures. However, wakes and radio frequency interference (RFI), which are related to human activities, also cause remarkable SAR signatures. The following illustrates examples of those signatures, and related literature is provided to help users better understand them.

Moving vessels left tracks in the water as wakes; their structures can be categorized as surface waves (narrow-V wakes and Kelvin wake), turbulent wakes or vortices, and internal waves (Lyden et al., 1988). Although ships can be observed as bright patches in SAR image, ship wake patterns can provide further information such as size, direction, and speed (Rey et al., 1990); therefore, several previous studies focused on detection of ship wakes in SAR images (Lyden et al., 1988; Rey et al., 1990; Shemdin, 1990; Copeland et al., 1995; Graziano et al., 2017; Tings et al., 2023). Figure 17 shows a SAR scene taken at 03:52 on 18 October 2023 near the Port Said off the Egyptian coast. The bright pixels aligned

6824

Y.-J. Yang et al.: Dataset of oil slicks, look-alikes and remarkable SAR signatures

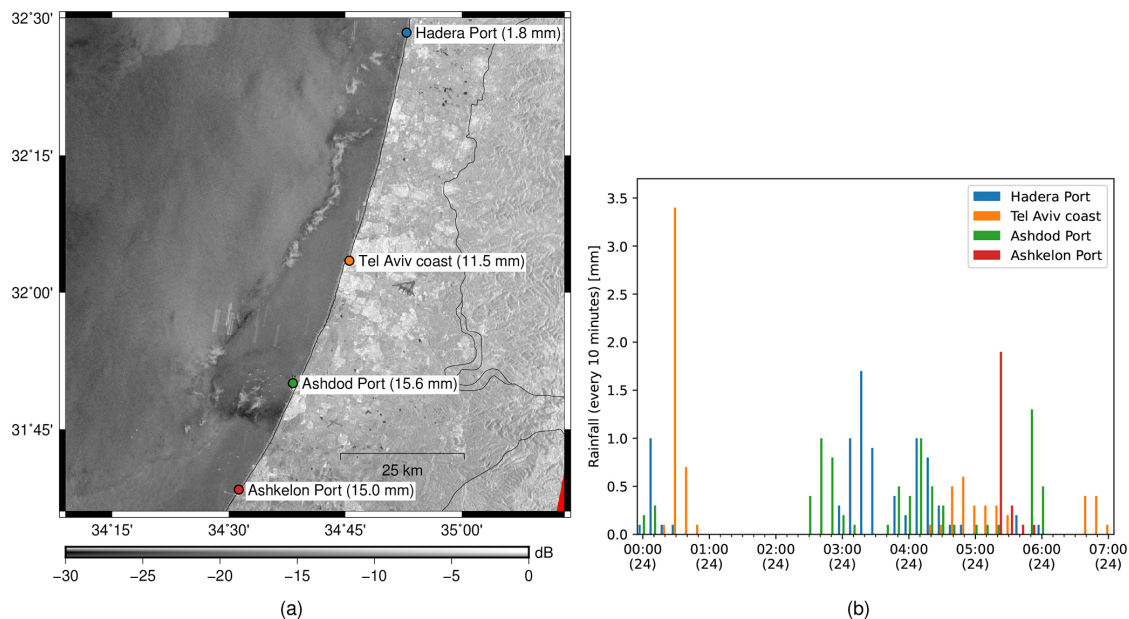


Figure 16. An example of rain cells observed by SAR at 03:42 on 24 January 2018, along with (a) daily and (b) 10 min rainfall data obtained from the Israel Meteorological Service (Ministry of Transport and Road Safety, Israel, 2024). Panel (a) contains modified Copernicus Sentinel data (2018). The coastline and borders were obtained from Wessel and Smith (1996).

in the south and north directions in the middle of the figure show vessels, along with dark linear features attached to them, which were likely due to wakes. Previous studies also pointed out that wakes from offshore wind turbines could form similar dark formations in SAR images (Christiansen and Hasager, 2005; Li and Lehner, 2013; Ahsbahs et al., 2020); however, they were not commonly seen in this study area.

As SAR is active radar, other radio services (such as communication systems, television networks, surveillance radars for air traffic control, military facilities, meteorological radars, and other spaceborne SAR sensors) with their transmitters on the same or adjacent frequency band to SAR could result in RFI, which usually appear as bright linear signatures in SAR (see Fig. 18). Several previous studies discussed the influence of those RFI on different frequency bands and proposed removal methods (Miller et al., 1997; Rosen et al., 2008; Meyer et al., 2013; Natsuaki et al., 2017; Monti-Guarnieri et al., 2017; Franceschi et al., 2021). Thanks to researchers working on the detecting and identifying RFI in Sentinel-1 data, the operational RFI detection and mitigation was activated in the SAR processor on 23 March 2022 (Franceschi et al., 2022; Hajduch et al., 2022). In other words, since then, Sentinel-1 Level-1 data has been produced under consideration of RFI mitigation. However, readers should keep the effect of RFI in mind as they might still find some data with certain RFI not being mitigated; such examples are shown in Fig. 19.

4.9 Example List

This subsection lists all Sentinel-1 SAR scenes used in the examples provided in this section. Some of the signatures covered a larger area than how they are shown in the paper; however, if readers wish to see the original SAR scenes, the information provided in Table 3 should be enough for obtaining them from the Copernicus Data Space Ecosystem. In addition, the corresponding supplementary materials used in the explanations are also listed; however, users should not limit themselves to the selection of supplementary data.

5 Usage Notes

5.1 Performance Evaluation

To make it possible for users who wish to compare their model performance with other studies, the performance of a custom-trained object detector from a previous study (Yang et al., 2024) was evaluated and is shown in this subsection. The performance on image patches with and without oil objects (i.e. *oil set* and *no-oil set*) are evaluated separately. In the following, the annotations from this published dataset are regarded as ground truth and abbreviated to *gt*. However, it shall be noted that even though the authors who prepared the dataset tried to avoid human errors, these annotations might still include false annotations. Note that this data descriptor is not intended to have a comprehensive discussion on the performance; therefore, this subsection only shows the mea-

Table 3. List of Copernicus Sentinel-1 scenes used as examples provided in Sect. 4, along with their corresponding supplementary data.

Fig.	Signature	Start Date & Time (YYYY-MM-DD hh:mm:ss)		Abs. orbit	Mission ID	Product ID	Supplementary Data
7a	Oil slick	2022-11-03	15:49:28	045732	057835	D069	
7b	Oil slick	2022-11-04	03:52:42	045739	057870	6C96	
8	Wind	2023-08-02	03:44:34 03:44:59	049691	05F9AE	7321 D5EB	– Sea surface wind velocity (CMEMS and MDS, 2024c)
9a	Wind	2022-09-24	03:43:41 03:44:06	045141	056512	74D8 F1AB	– Sea surface wind velocity (CMEMS and MDS, 2024c) – Bathymetry and terrain chart (GEBCO Bathymetric Compilation Group, 2023)
10	Wind	2023-01-27	03:52:39	046964	05A1FB	3A5D	– Sea surface wind velocity (CMEMS and MDS, 2024c)
11	Internal waves	2024-03-28	15:41:26 15:41:51	053184	0671A3	05B8 B6E5	– Bathymetry and terrain chart (GEBCO Bathymetric Compilation Group, 2023)
12	AGWs	2023-05-27	03:52:16 03:52:41	048714	05D8D7	EF08 2FEB	– Sea surface wind velocity (CMEMS and MDS, 2024c)
13	Upwelling	2019-05-12	03:51:18 03:51:43	027189	0310AB	EEF7 00AD	– SST (CMEMS and MDS, 2024a) – chl <i>a</i> concentration (CMEMS and MDS, 2024b) – Sea surface wind velocity (CMEMS and MDS, 2024c)
14	Eddies	2022-09-29	03:52:17 03:52:42	045214	056776	5889 04BC	
15	Rain cell	2022-10-18	03:43:42 03:44:07	045491	057070	3FB9 DC74	
16	Rain cell	2018-01-24	03:43:41 03:44:06	020291	022A5B	C066 A779	– Rainfall observation from Ministry of Transport and Road Safety, Israel (2024)
17	Wakes	2023-10-18	03:52:47	050814	061FD2	6D11	
18	RFI	2018-10-21	03:43:02	013245	0187C4	ABBF	
19	RFI	2023-09-24	03:52:47	050464	0613CC	CF0D	

tures, but readers can refer to Yang et al. (2024) for interpretation of the results.

For performance evaluation of object detection algorithms, intersection over union (IoU) is commonly used to indicate how accurate the detection (or known as prediction, which is a common term used in the object detection field) is compared to the ground truth and is defined as (Everingham et al., 2010):

$$\text{IoU} = \frac{\text{area}(B_{\text{detn}} \cap B_{\text{gt}})}{\text{area}(B_{\text{detn}} \cup B_{\text{gt}})}, \quad (3)$$

where $B_{\text{detn}} \cap B_{\text{gt}}$ and $B_{\text{detn}} \cup B_{\text{gt}}$ refer to the intersection and union of the bounding boxes of the detection (B_{detn}) and the ground truth (B_{gt}), respectively.

Based on IoU, the detections can be categorized as true positives (TP) or false positives (FP). TP shows the detections intersecting with the ground truth and with their IoU greater than a given threshold. On the other hand, FP shows the detections with no intersection with the ground truth, or their IoU values are smaller than the threshold. If we change the perspective and focus on ground truths, TP and false negatives (FN) are used, showing the ground truths with and without corresponding detections, respectively. The definition of one oil object might differ between ground truths and

6826

Y.-J. Yang et al.: Dataset of oil slicks, look-alikes and remarkable SAR signatures

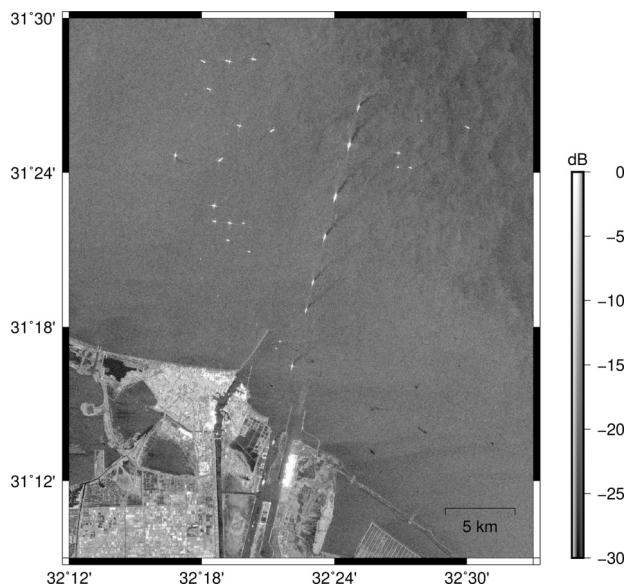


Figure 17. An example of ship wakes observed in a SAR scene taken at 03:52 on 18 October 2023 near the Port Said. The figure contains modified Copernicus Sentinel data (2023).

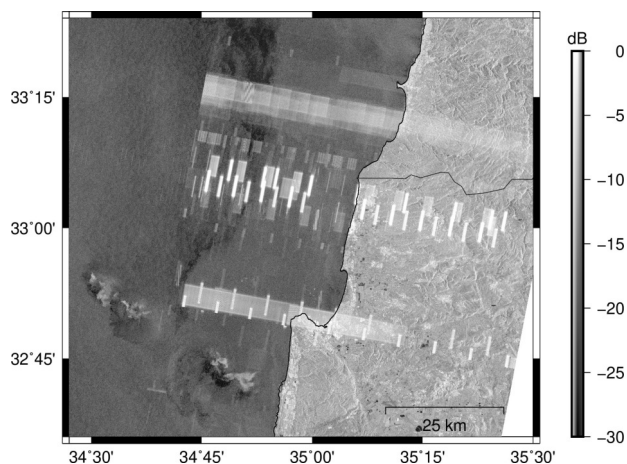


Figure 18. An example of RFI observed in a SAR scene taken at 03:43 on 21 October 2018, along with some rain cell signatures. The figure contains modified Copernicus Sentinel data (2018). The plotted coastline and borders were obtained from Wessel and Smith (1996).

detections for some complicated cases, resulting in more than one detection referring to one ground truth. Therefore, the numbers of TP for detections and ground truths might differ; in the following, they are referred to as TP_{detn} and TP_{gt} , respectively. To easily focus on the negative results of the models, the false discovery rate (FDR) and false negative rate

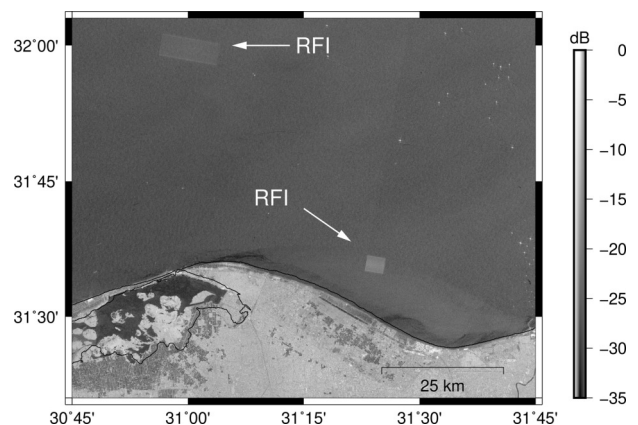


Figure 19. An example of RFI observed in a SAR scene taken at 03:52 on 24 September 2023; the RFI was not detected and mitigated by the SAR processor. The figure contains modified Copernicus Sentinel data (2023). The plotted coastline were obtained from Wessel and Smith (1996).

(FNR) are provided, they are defined as follows:

$$\begin{aligned} \text{FDR} &= \frac{\text{FP}}{\text{TP}_{\text{detn}} + \text{FP}}, \\ \text{FNR} &= \frac{\text{FN}}{\text{TP}_{\text{gt}} + \text{FN}}. \end{aligned} \quad (4)$$

Table 4 shows the performance of the two object detectors applied to a near real-time automated oil spill detection and early warning system as *YODA-enh* and *YODA-enh-aug1*, which were claimed to perform well in a previous study (Yang et al., 2024). Thresholds for filtering out the objects which have low confidence scores and IoU were applied. Note that due to different image patches used in the performance evaluation and a slightly different way of calculation, these numbers differ from those shown in the paper.

Regarding the performance on the *no-oil set*, as there are no objects inside, the measures for object detection algorithms are not appropriate. Here, image patches are simply marked as two categories, one with no detections inside and another with one or more detections inside. The former shows that the detector performs well and is not confused by the look-alikes. The latter indicates that the detector can be confused with specific signatures inside the image patches. Figure 20 shows the results of the two models on the *no-oil set* with different confidence score thresholds.

5.2 Technical Notes

There are some additional technical notes for the users:

- The annotation of the objects follows the Pascal VOC XML format; users who have their labels in different annotation format, should carefully convert the labels into the format they used.

Table 4. Performance evaluation of the models from a previous study (Yang et al., 2024) on the *oil set*.

Model		Subset	# img	# gt	# detn	# TP		# FP	# FN	FDR [%]	FNR [%]
						(gt)	(detn)				
YODA-enh	(a)	ow	990	2284	1029	1154	1023	6	1249	0.58	51.98
		oc	392	941	344	353	296	48	623	13.95	63.83
	(b)	ow	990	2284	468	515	468	0	1782	0.00	77.58
		oc	392	941	137	148	130	7	798	5.11	84.36
	(c)	ow	990	2284	468	426	425	43	1858	9.19	81.35
		oc	392	941	137	125	125	12	816	8.76	86.72
YODA-enh-aug1	(a)	ow	990	2284	787	1487	787	0	877	0.00	37.10
		oc	392	941	147	296	146	1	655	0.68	68.87
	(b)	ow	990	2284	318	520	318	0	1765	0.00	77.24
		oc	392	941	55	101	55	0	842	0.00	89.29
	(c)	ow	990	2284	318	42	42	276	2242	86.79	98.16
		oc	392	941	55	18	18	37	923	67.27	98.09

(a) $\text{thres}_{\text{score}} = 0.0$, $\text{thres}_{\text{IoU}} = 0.0$; (b) $\text{thres}_{\text{score}} = 0.5$, $\text{thres}_{\text{IoU}} = 0.0$; (c) $\text{thres}_{\text{score}} = 0.5$, $\text{thres}_{\text{IoU}} = 0.5$

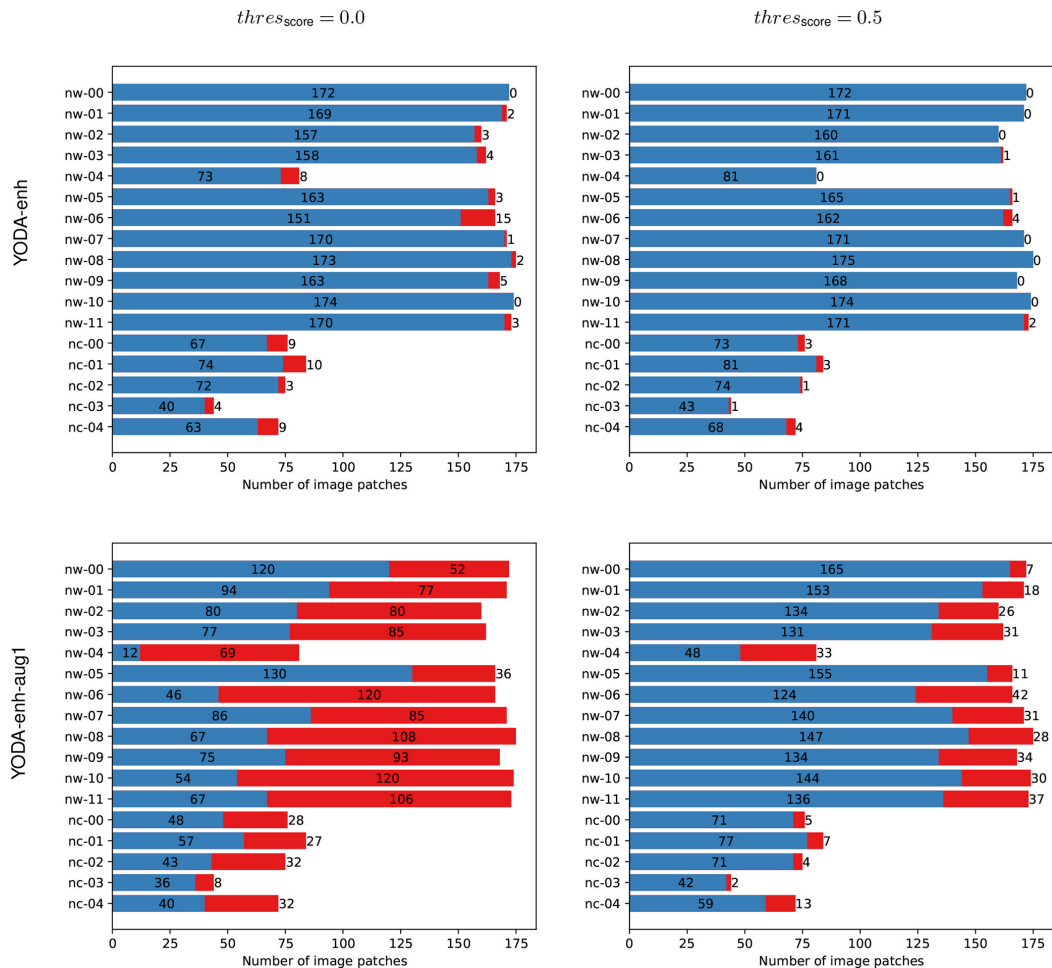


Figure 20. Numbers of image patches in the *no-oil set* that the models return detections (in red) and without any detection (in blue).

- The published dataset has only one class (i.e. oil) objects; if users have different definitions of classes in their work, they would have to make sure the performance evaluation is still valid.
- For training an object detector, the authors would suggest using a dataset without masking out the land area as some coastal information might be helpful for the detectors to learn as background information. If users wish to apply land masks to the published dataset, they can generate the corresponding mask out scenes by loading the geoinformation provided along with the dataset. A program for land masking is also provided in the GitHub repository associated with this paper.
- For an operational oil slick detection system, land masks should be considered as they can help improve the efficiency of the system and avoid false positives in the land areas. Global land masks can be obtained from sources such as Wessel and Smith (1996) and Karin (2020).
- For studies focusing on different study areas, the sources of oil slicks and geographic settings might be different from the dataset and, therefore, result in poor performance. However, it could help understand how one local model performs in a different area and lead to further discussion.
- Even though the authors aim to provide a published dataset as a test set for comparing models with different studies, users can also use the dataset to (further) train their algorithms.
- Users are encouraged to check the dataset themselves and adjust the labels when they do not fit the “style” of annotations from the users.

6 Code and data availability

The dataset with oil slicks, look-alikes, and other remarkable phenomena covering the Eastern Mediterranean Sea in 2019 can be accessed through PANGAEA via <https://doi.org/10.1594/PANGAEA.980773> (Yang and Singha, 2025). The image patches are normalized to 0–255 and saved in an 8-bit JPG format. The oil annotations are in Pascal VOC XML format. A data table recording the Sentinel-1 ID of all the image patches inside the dataset is also provided; therefore, the original Sentinel-1 products can be downloaded via the Copernicus Data Space Ecosystem. The code related to working with the dataset, including the evaluation of performance, is available on a public github repository published with Zenodo under <https://doi.org/10.5281/zenodo.17789853> (Yang, 2025).

7 Summary

This data descriptor presents a dataset containing oil slicks, look-alikes, and other notable ocean phenomena, collected for the purpose of SAR image analysis. It provides explanations and examples of various ocean SAR signatures, supported by supplementary materials, to help users better understand the sources of these signatures.

The descriptor also includes a performance evaluation of a model from a previous study (Yang et al., 2024), which was tested on this dataset. This allows users who have trained their own oil spill detectors to compare their model performance with other studies. Additionally, the dataset is a valuable resource for newcomers to the oil slick detection community, providing a ready-made dataset for starting their work.

Recent research in SAR oil spill detection has increasingly focused on machine learning techniques. Given the diverse backgrounds of researchers in this field – ranging from remote sensing and machine learning to oceanography – this data descriptor aims to bridge the knowledge gap for those less familiar with oceanographic concepts. Readers are encouraged to consult specialized textbooks on SAR signal processing (Woodhouse, 2006), physical oceanography (Knauss and Garfield, 2016), and SAR oceanography (Robinson, 1983, 2004, 2010) for more comprehensive explanations.

Appendix A: Data Table

Section 2.2 provides explanations on how the dataset is organized and how their information is stored in the data table. To explain better and provide information about the image patches shown in this article, the data information of those image patches is extracted and displayed in the following tables; the original data table can be found in the published dataset. Tables A1 and A3 show the patch names, patch dimensions, and corner coordinates of the patches in the WGS84 geocentric coordinate system. Tables A2 and A4 are continuous from Tables A1 and A3, respectively, showing the product start and stop date time and the product ID. Table A5 contains the object information, including corner coordinates of the objects in the WGS84 geocentric coordinate system, object positions referring to the corresponding image patches along the range and azimuth direction, and the bounding box size in pixels. Tables A1 and A3 record the information of image patches from *no-oil set*, which are mentioned in Figs. 2 and 6. On the other hand, Tables A3, A4, and A5 indicate the information of image patches from *oil set*, which are mentioned in Fig. 5.

Table A1. Data table showing the patch information for examples used in Figs. 2 and 6.

tag	patch_name	patch_width	height	ul_lon	ul_lat	ur_lon	ur_lat	br_lon	br_lat	bl_lon	bl_lat
nw-0547-03-000044	SI_20190319_035039_035218_VV_95	640	640	31.1062	33.3788	30.9706	33.3977	30.9475	33.2826	31.0829	33.2636
nw-0553-03-000050	SI_20190412_035040_035219_VV_12	640	640	32.3278	35.3925	32.1889	35.4121	32.1639	35.2971	32.3025	35.2774
nw-0603-03-000100	SI_20190803_035856_040035_VV_14	640	640	30.0576	35.9321	29.9176	35.9513	29.8933	35.8362	30.0331	35.8169
nw-0609-03-000106	SI_20190827_035858_040037_VV_21	640	640	29.9765	35.5871	29.8371	35.6063	29.8131	35.4911	29.9522	35.4719
nw-0165-00-000165	SI_20191220_035048_035227_VV_101	640	640	31.8779	34.4780	31.7405	34.4975	31.7165	34.3823	31.8537	34.3628
nw-0307-01-000135	SI_20191102_154017_154157_VV_101	640	640	33.9115	33.7039	34.0472	33.7251	34.0212	33.8404	33.8853	33.8192
nw-0446-02-000103	SI_20190711_035121_035303_VV_33	640	640	32.7978	35.3136	32.6592	35.3338	32.6336	35.2186	32.7720	35.1984
nw-0651-03-000148	SI_20191214_035125_035306_VV_294	640	640	31.8042	35.2799	31.6654	35.2990	31.6412	35.1839	31.7798	35.1648
nw-0687-04-000022	SI_20190406_035117_035258_VV_81	640	640	31.6319	34.9168	31.4937	34.9359	31.4704	34.8207	31.6084	34.8017
nw-0763-05-000017	SI_20190207_033454_033634_VV_22	640	640	35.6396	34.5452	35.5020	34.5642	35.4777	34.4492	35.6150	34.4302
nw-0997-06-000085	SI_20190522_155643_155737_VV_5	640	640	31.7808	32.6882	31.9154	32.7076	31.8919	32.8231	31.7572	32.8037
nw-1203-07-000125	SI_20190927_154017_154157_VV_86	640	640	34.0069	35.1136	34.1451	35.1343	34.1199	35.2495	33.9815	35.2289
nw-1331-08-000082	SI_20190531_034300_034440_VV_41	640	640	35.0884	35.5409	34.9495	35.5613	34.9242	35.4460	35.0630	35.4256
nw-1523-09-000099	SI_20190604_154838_155018_VV_33	640	640	32.7407	34.1620	32.8774	34.1821	32.8526	34.2972	32.7157	34.2772
nw-1679-10-000087	SI_20190821_035934_040114_VV_69	640	640	30.5790	31.6785	30.4463	31.6996	30.4210	31.5842	30.5535	31.5631
nw-1883-11-000117	SI_20190612_034300_034440_VV_90	640	640	35.2993	34.5986	35.1620	34.6195	35.1359	34.5043	35.2729	34.4834
nc-0009-00-000009	SI_20190216_035850_040029_VV_87	640	640	30.8020	31.5517	30.6695	31.5730	30.6439	31.4577	30.7763	31.4364
nc-0140-01-000064	SI_20191028_034227_034407_VV_119	640	640	35.5257	33.8044	35.3898	33.8258	35.3633	33.7105	35.4990	33.6891
nc-0207-02-000047	SI_20190927_035049_035228_VV_9	640	640	33.5185	34.7990	33.3810	34.8201	33.3556	34.7048	33.4929	34.6836
nc-0253-03-000018	SI_20190529_154748_154928_VV_50	640	640	32.2326	34.9748	32.3706	34.9952	32.3451	35.1106	32.2069	35.0903
nc-0325-04-000046	SI_20190909_035125_035306_VV_38	640	640	33.9199	34.9777	33.7821	34.9992	33.7550	34.8839	33.8925	34.8624

Table A2. Continuous data table from Table A1, recording the product information.

tag	start_time	end_time	Sentinel_ID
nw-0547-03-000044	2019-03-19T03:50:39	2019-03-19T03:52:18	S1B_IW_GRDH_1SDV_20190319T035104_20190319T035129_015418_01CDFB_86C8.SAFE
nw-0553-03-000050	2019-04-12T03:50:40	2019-04-12T03:52:19	S1B_IW_GRDH_1SDV_20190412T035040_20190412T035105_015768_01D985_9F88.SAFE
nw-0603-03-000100	2019-08-03T03:58:56	2019-08-03T04:00:35	S1B_IW_GRDH_1SDV_20190803T035856_20190803T035921_017416_020C16_EF88.SAFE
nw-0609-03-000106	2019-08-27T03:58:58	2019-08-27T04:00:37	S1B_IW_GRDH_1SDV_20190827T035858_20190827T035923_017766_0216ED_C8C4.SAFE
nw-0165-00-000165	2019-12-20T03:50:48	2019-12-20T03:52:27	S1B_IW_GRDH_1SDV_20191220T035048_20191220T035113_019443_024BA5_28B4.SAFE
nw-0307-01-000135	2019-11-02T15:40:17	2019-11-02T15:41:57	S1A_IW_GRDH_1SDV_20191102T154107_20191102T154132_029734_036369_FEF5.SAFE
nw-0446-02-000103	2019-07-11T03:51:21	2019-07-11T03:53:03	S1A_IW_GRDH_1SDV_20190711T035121_20190711T035146_028064_032B5E_8132.SAFE
nw-0651-03-000148	2019-12-14T03:51:25	2019-12-14T03:53:06	S1A_IW_GRDH_1SDV_20191214T035125_20191214T035150_030339_037875_3C8E.SAFE
nw-0687-04-000022	2019-04-06T03:51:17	2019-04-06T03:52:58	S1A_IW_GRDH_1SDV_20190406T035117_20190406T035142_026664_02FE02_C5A5.SAFE
nw-0763-05-000017	2019-02-07T03:34:54	2019-02-07T03:36:34	S1A_IW_GRDH_1SDV_20190207T033454_20190207T033519_025818_02DF3B_8839.SAFE
nw-0997-06-000085	2019-05-22T15:56:43	2019-05-22T15:57:37	S1B_IW_GRDH_1SDV_20190522T155643_20190522T155712_016359_01ECA7_4C33.SAFE
nw-1203-07-000125	2019-09-27T15:40:17	2019-09-27T15:41:57	S1A_IW_GRDH_1SDV_20190927T154132_20190927T154157_029209_035141_93D0.SAFE
nw-1331-08-000082	2019-05-31T03:43:00	2019-05-31T03:44:40	S1A_IW_GRDH_1SDV_20190531T034300_20190531T034325_027466_031954_5014.SAFE
nw-1523-09-000099	2019-06-04T15:48:38	2019-06-04T15:50:18	S1A_IW_GRDH_1SDV_20190604T154928_20190604T154953_027532_031B5A_1FA3.SAFE
nw-1679-10-000087	2019-08-21T03:59:34	2019-08-21T04:01:14	S1A_IW_GRDH_1SDV_20190821T040049_20190821T040114_028662_033E63_B88E.SAFE
nw-1883-11-000117	2019-06-12T03:43:00	2019-06-12T03:44:40	S1A_IW_GRDH_1SDV_20190612T034325_20190612T034350_027641_031EA9_55D4.SAFE
nc-0009-00-000009	2019-02-16T03:58:50	2019-02-16T04:00:29	S1B_IW_GRDH_1SDV_20190216T035940_20190216T040005_014966_01BF36_8C52.SAFE
nc-0140-01-000064	2019-10-28T03:42:27	2019-10-28T03:44:07	S1B_IW_GRDH_1SDV_20191028T034252_20191028T034317_018670_0232F7_237B.SAFE
nc-0207-02-000047	2019-09-27T03:50:49	2019-09-27T03:52:28	S1B_IW_GRDH_1SDV_20190927T035049_20190927T035114_018218_0224DC_62D9.SAFE
nc-0253-03-000018	2019-05-29T15:47:48	2019-05-29T15:49:28	S1B_IW_GRDH_1SDV_20190529T154903_20190529T154928_016461_01EFC4_CD23.SAFE
nc-0325-04-000046	2019-09-09T03:51:25	2019-09-09T03:53:06	S1A_IW_GRDH_1SDV_20190909T035125_20190909T035150_028939_034806_F874.SAFE

Table A3. Data table showing the patch information for examples used in Fig. 5.

tag	patch_name	patch_width	height	ul_lon	ul_lat	ur_lon	ur_lat	br_lon	br_lat	bl_lon	bl_lat
ow-0267-01-000666	SI_20190512_035118_035259_VV_1	640	640	31.4543	32.2251	31.3205	32.2448	31.2968	32.1295	31.4305	32.1099
ow-0267-02-000667											
ow-0267-03-000668											
ow-0276-01-000680	SI_20190515_160406_160546_VV_0	640	640	30.0586	31.4844	30.1915	31.5039	30.1681	31.6190	30.0351	31.5996
ow-0276-02-000681											
ow-0438-01-001124	SI_20190622_035930_040110_VV_0	1294	1294	31.5372	33.7382	31.2640	33.7815	31.2107	33.5484	31.4840	33.5051
ow-0438-02-001125											
ow-0438-03-001126											
ow-0438-04-001127											
ow-0438-05-001128											
ow-0447-01-001152	SI_20190623_035044_035223_VV_0	977	977	32.8049	31.9612	32.6023	31.9935	32.5633	31.8176	32.7660	31.7852
ow-0447-02-001153											
ow-0447-03-001154											
ow-0447-04-001155											
ow-0447-05-001156											
ow-0463-01-001189	SI_20190624_034301_034441_VV_0	1748	1748	33.5068	32.5655	33.1398	32.6186	33.0742	32.3041	33.4412	32.2509
ow-0463-02-001190											
ow-0643-01-001540	SI_20190821_154753_154933_VV_12	640	640	32.8779	31.8404	33.0111	31.8609	32.9864	31.9765	32.8532	31.9560
ow-0643-02-001541											
ow-0643-03-001542											
ow-0643-04-001543											
ow-0643-05-001544											
ow-0643-06-001545											
ow-0643-07-001546											
ow-0643-08-001547											
ow-0643-09-001548											
ow-0643-10-001549											

Table A4. Continuous data table from Table A3, recording the product information.

tag	start_time	end_time	Sentinel_ID
ow-0267-01-000666	2019-05-12T03:51:18	2019-05-12T03:52:59	S1A_IW_GRDH_1SDV_20190512T035208_20190512T035233_027189_0310AB_E893.SAFE
ow-0267-02-000667			
ow-0267-03-000668			
ow-0276-01-000680	2019-05-15T16:04:06	2019-05-15T16:05:46	S1B_IW_GRDH_1SDV_20190515T160431_20190515T160456_016257_01E988_22CD.SAFE
ow-0276-02-000681			
ow-0438-01-001124	2019-06-22T03:59:30	2019-06-22T04:01:10	S1A_IW_GRDH_1SDV_20190622T035955_20190622T040020_027787_0322FB_5391.SAFE
ow-0438-02-001125			
ow-0438-03-001126			
ow-0438-04-001127			
ow-0438-05-001128			
ow-0447-01-001152	2019-06-23T03:50:44	2019-06-23T03:52:23	S1B_IW_GRDH_1SDV_20190623T035134_20190623T035159_016818_01FA62_D8E1.SAFE
ow-0447-02-001153			
ow-0447-03-001154			
ow-0447-04-001155			
ow-0447-05-001156			
ow-0463-01-001189	2019-06-24T03:43:01	2019-06-24T03:44:41	S1A_IW_GRDH_1SDV_20190624T034351_20190624T034416_027816_0323DB_253E.SAFE
ow-0463-02-001190			
ow-0643-01-001540	2019-08-21T15:47:53	2019-08-21T15:49:33	S1B_IW_GRDH_1SDV_20190821T154818_20190821T154843_017686_021461_4D57.SAFE
ow-0643-02-001541			
ow-0643-03-001542			
ow-0643-04-001543			
ow-0643-05-001544			
ow-0643-06-001545			
ow-0643-07-001546			
ow-0643-08-001547			
ow-0643-09-001548			
ow-0643-10-001549			

Table A5. Continuous data table from Table A4, recording the object information.

tag	obj_ ul_lon	ul_lat	ur_lon	ur_lat	br_lon	br_lat	bl_lon	bl_lat	obj_patchloc_ xmin	ymin	xmax	ymax	label_size
ow-0267-01-000666	31.3541	32.1779	31.3458	32.1791	31.3445	32.1728	31.3528	32.1716	420	334	460	369	1400
ow-0267-02-000667	31.3592	32.2254	31.3475	32.2271	31.3427	32.2038	31.3544	32.2021	442	74	498	203	7224
ow-0267-03-000668	31.4055	32.1367	31.3875	32.1394	31.3855	32.1297	31.4035	32.1270	142	515	228	569	4644
ow-0276-01-000680	30.1084	31.5432	30.1230	31.5454	30.1197	31.5616	30.1051	31.5594	289	278	359	368	6300
ow-0276-02-000681	30.1124	31.5529	30.1315	31.5557	30.1262	31.5820	30.1071	31.5792	317	327	409	473	13432
ow-0438-01-001124	31.4387	33.6672	31.4193	33.6703	31.4186	33.6674	31.4381	33.6643	376	464	468	480	1472
ow-0438-02-001125	31.4521	33.6606	31.4299	33.6641	31.4287	33.6589	31.4509	33.6554	308	488	413	517	3045
ow-0438-03-001126	31.5102	33.6209	31.4874	33.6246	31.4856	33.6168	31.5085	33.6132	1	651	109	694	4644
ow-0438-04-001127	31.4950	33.6443	31.4477	33.6518	31.4439	33.6354	31.4912	33.6279	095	539	319	630	20384
ow-0438-05-001128	31.4419	33.7329	31.2973	33.7559	31.2836	33.6959	31.4282	33.6730	430	109	1115	442	228105
ow-0447-01-001152	32.7687	31.7987	32.7480	31.8020	32.7450	31.7885	32.7657	31.7852	1	902	101	977	7500
ow-0447-02-001153	32.7912	31.9593	32.7507	31.9657	32.7317	31.8796	32.7721	31.8732	062	22	257	500	93210
ow-0447-03-001154	32.7728	31.8173	32.7670	31.8182	32.7633	31.8015	32.7691	31.8005	1	799	29	892	2604
ow-0447-04-001155	32.7840	31.8726	32.7440	31.8790	32.7319	31.8244	32.7719	31.8180	6	493	199	796	58479
ow-0447-05-001156	32.7246	31.9242	32.7111	31.9264	32.7062	31.9042	32.7197	31.9020	336	267	401	390	7995
ow-0463-01-001189	33.4992	32.5301	33.2166	32.5710	33.1687	32.3412	33.4513	32.3003	1	197	1347	1474	1718842
ow-0463-02-001190	33.5066	32.5654	33.2281	32.6057	33.1786	32.3678	33.4570	32.3275	1	1	1327	1323	1752972
ow-0643-01-001540	32.9035	31.8446	32.9484	31.8515	32.9432	31.8758	32.8983	31.8689	123	1	339	136	29160
ow-0643-02-001541	32.9057	31.8665	32.9335	31.8708	32.9133	31.9652	32.8854	31.9610	155	117	289	640	70082
ow-0643-03-001542	32.9400	31.8755	32.9473	31.8767	32.9427	31.8985	32.9354	31.8974	324	137	359	258	4235
ow-0643-04-001543	32.9266	31.9080	32.9312	31.9087	32.9265	31.9309	32.9219	31.9302	294	322	316	445	2706
ow-0643-05-001544	32.9370	31.9609	32.9605	31.9645	32.9590	31.9717	32.9355	31.9681	395	597	508	637	4520
ow-0643-06-001545	32.9340	31.8996	32.9374	31.9001	32.9357	31.9079	32.9324	31.9074	320	271	336	314	688
ow-0643-07-001546	32.9215	31.9322	32.9231	31.9324	32.9218	31.9386	32.9202	31.9383	294	456	302	490	272
ow-0643-08-001547	32.9191	31.9372	32.9220	31.9377	32.9211	31.9420	32.9182	31.9416	288	485	302	509	336
ow-0643-09-001548	32.9164	31.9508	32.9247	31.9521	32.9232	31.9591	32.9149	31.9578	289	560	329	599	1560
ow-0643-10-001549	32.9188	31.9424	32.9213	31.9428	32.9196	31.9507	32.9171	31.9504	292	513	304	557	528

Author contributions. YJY and SS jointly inspected the oil slicks in SAR scenes. YJY prepared the dataset and wrote the manuscripts. SS supported with his knowledge of SAR techniques. RG and FS contributed with valuable feedback on the explanations of oceanographic and atmospheric phenomena. All authors reviewed the manuscript.

Competing interests. The contact author has declared that none of the authors has any competing interests.

Disclaimer. Publisher's note: Copernicus Publications remains neutral with regard to jurisdictional claims made in the text, published maps, institutional affiliations, or any other geographical representation in this paper. While Copernicus Publications makes every effort to include appropriate place names, the final responsibility lies with the authors. Views expressed in the text are those of the authors and do not necessarily reflect the views of the publisher.

Acknowledgements. The dataset generation was partly funded by the DARTIS project, supported by the German Federal Ministry of Education and Research under grant number 03F0823B. The authors wish to thank Copernicus Programme for providing Sentinel-1 data, Copernicus Marine Service, and the other Earth observation data. The authors would also like to thank C. Pegel, C. Schnupfhahn, and D. Günzel from the German Aerospace Center and P. Brandt from GEOMAR for their valuable feedback on the manuscripts. Additionally, the authors would like to thank the reviewers for their helpful comments.

Financial support. This research has been supported by the Bundesministerium für Bildung und Forschung (grant no. 03F0823B).

The article processing charges for this open-access publication were covered by the German Aerospace Center (DLR).

Review statement. This paper was edited by François G. Schmitt and reviewed by Merv Fingas and one anonymous referee.

References

- Ahsbahs, T., Nygaard, N. G., Newcombe, A., and Badger, M.: Wind Farm Wakes from SAR and Doppler Radar, *Remote Sensing*, 12, <https://doi.org/10.3390/rs12030462>, 2020.
- Alpers, W. and Huang, W.: On the Discrimination of Radar Signatures of Atmospheric Gravity Waves and Oceanic Internal Waves on Synthetic Aperture Radar Images of the Sea Surface, *IEEE Transactions on Geoscience and Remote Sensing*, 49, 1114–1126, <https://doi.org/10.1109/TGRS.2010.2072930>, 2011.
- Alpers, W. and Zeng, K.: On Radar Signatures of Upwelling, *Journal of Geodesy and Geoinformation Science*, 4, 17, <https://doi.org/10.11947/j.JGGS.2021.0102>, 2021.
- Alpers, W., Huang, W., and Xilin, G.: Observations of atmospheric gravity waves over the Chinese seas by spaceborne synthetic aperture radar, *Proc. Dragon (ESA SP-655)*, 2008.
- Alpers, W., Brandt, P., Lazar, A., Dagorne, D., Sow, B., Faye, S., Hansen, M. W., Rubino, A., Poulain, P.-M., and Brehmer, P.: A small-scale oceanic eddy off the coast of West Africa studied by multi-sensor satellite and surface drifter data, *Remote Sensing of Environment*, 129, 132–143, <https://doi.org/10.1016/j.rse.2012.10.032>, 2013.
- Alpers, W., Dagorne, D., and Brandt, P.: Satellite Observations of Oceanic Eddies Around Africa, Springer Netherlands, Dordrecht, 205–229, ISBN 978-94-017-8008-7, https://doi.org/10.1007/978-94-017-8008-7_11, 2014.
- Alpers, W., Zhang, B., Mouche, A., Zeng, K., and Chan, P. W.: Rain footprints on C-band synthetic aperture radar images of the ocean – Revisited, *Remote Sensing of Environment*, 187, 169–185, <https://doi.org/10.1016/j.rse.2016.10.015>, 2016.
- Alpers, W., Holt, B., and Zeng, K.: Oil spill detection by imaging radars: Challenges and pitfalls, *Remote Sensing of Environment*, 201, 133–147, <https://doi.org/10.1016/j.rse.2017.09.002>, 2017.
- Amri, E., Dardouillet, P., Benoit, A., Courteille, H., Bolon, P., Dubucq, D., and Credo, A.: Offshore Oil Slick Detection: From Photo-Interpreter to Explainable Multi-Modal Deep Learning Models Using SAR Images and Contextual Data, *Remote Sensing*, 14, <https://doi.org/10.3390/rs14153565>, 2022.
- Atlas, D.: Origin of Storm Footprints on the Sea Seen by Synthetic Aperture Radar, *Science*, 266, 1364–1366, <https://doi.org/10.1126/science.266.5189.1364>, 1994.
- Bakun, A. and Agostini, V. N.: Seasonal Patterns of Wind-Induced Upwelling/Downwelling in the Mediterranean Sea, *Scientia Marina*, 65, 243–257, <https://doi.org/10.3989/scimar.2001.65n3243>, 2001.
- Berthon, J.-F. and Zibordi, G.: Bio-optical relationships for the northern Adriatic Sea, *International Journal of Remote Sensing*, 25, 1527–1532, <https://doi.org/10.1080/01431160310001592544>, 2004.
- Brekke, C. and Solberg, A. H.: Oil spill detection by satellite remote sensing, *Remote Sensing of Environment*, 95, 1–13, <https://doi.org/10.1016/j.rse.2004.11.015>, 2005.
- Brown, C. and Fingas, M.: A review of current global oil spill surveillance, monitoring and remote sensing capabilities, in: Proceedings of the Twenty-Eighth Arctic and Marine Oil Spill Program Technical Seminar, Environment Canada, Ottawa, Ontario, OSTI ID 20638888, 789–798, <https://www.osti.gov/etdweb/biblio/20638888> (last access: 4 December 2025), 2005.
- Buonigiorno Nardelli, B., Tronconi, C., Pisano, A., and Santoleri, R.: High and Ultra-High resolution processing of satellite Sea Surface Temperature data over Southern European Seas in the framework of MyOcean project, *Remote Sensing of Environment*, 129, 1–16, <https://doi.org/10.1016/j.rse.2012.10.012>, 2013.
- Cantorna, D., Dafonte, C., Iglesias, A., and Arcay, B.: Oil spill segmentation in SAR images using convolutional neural networks. A comparative analysis with clustering and logistic regression algorithms, *Applied Soft Computing*, 84, 105716, <https://doi.org/10.1016/j.asoc.2019.105716>, 2019.
- Carpenter, A. and Kostianoy, A. G. (Eds.): Oil Pollution in the Mediterranean Sea: Part I: The International Context, The Handbook of Environmental Chemistry, Springer Cham, ISBN 978-3-030-12236-2, <https://doi.org/10.1007/978-3-030-12236-2>, 2016.

- Chelton, D. B., Schlax, M. G., Samelson, R. M., and de Szoeke, R. A.: Global observations of large oceanic eddies, *Geophysical Research Letters*, 34, <https://doi.org/10.1029/2007GL030812>, 2007.
- Chen, S., Wei, X., and Zheng, W.: ASA-DRNet: An Improved Deeplabv3+ Framework for SAR Image Segmentation, *Electronics*, 12, <https://doi.org/10.3390/electronics12061300>, 2023.
- Chen, Y. and Wang, Z.: Marine Oil Spill Detection from SAR Images Based on Attention U-Net Model Using Polarimetric and Wind Speed Information, *International Journal of Environmental Research and Public Health*, 19, <https://doi.org/10.3390/ijerph191912315>, 2022.
- Christiansen, M. B. and Hasager, C. B.: Wake effects of large offshore wind farms identified from satellite SAR, *Remote Sensing of Environment*, 98, 251–268, <https://doi.org/10.1016/j.rse.2005.07.009>, 2005.
- Clemente-Colon, P. and Yan, X.-H.: Observations of East Coast upwelling conditions in synthetic aperture radar imagery, *IEEE Transactions on Geoscience and Remote Sensing*, 37, 2239–2248, <https://doi.org/10.1109/36.789620>, 1999.
- Copeland, A., Ravichandran, G., and Trivedi, M.: Localized Radon transform-based detection of ship wakes in SAR images, *IEEE Transactions on Geoscience and Remote Sensing*, 33, 35–45, <https://doi.org/10.1109/36.368224>, 1995.
- Copernicus Sentinel data: Legal notice on the use of Copernicus Sentinel Data and Service Information, https://sentinels.copernicus.eu/documents/247904/690755/Sentinel_Data_Legal_Notice (last access: 4 December 2025), 2019–2024.
- Danklmayer, A., Doring, B. J., Schwerdt, M., and Chandra, M.: Assessment of Atmospheric Propagation Effects in SAR Images, *IEEE Transactions on Geoscience and Remote Sensing*, 47, 3507–3518, <https://doi.org/10.1109/TGRS.2009.2022271>, 2009.
- Deng, J., Dong, W., Socher, R., Li, L.-J., Li, K., and Fei-Fei, L.: ImageNet: A large-scale hierarchical image database, in: 2009 IEEE Conference on Computer Vision and Pattern Recognition, 248–255, <https://doi.org/10.1109/CVPR.2009.5206848>, 2009.
- Etling, D. and Brown, R. A.: Roll vortices in the planetary boundary layer: A review, *Boundary-Layer Meteorology*, 65, 215–248, <https://doi.org/10.1007/BF00705527>, 1993.
- E.U. Copernicus Marine Service Information (CMEMS) and Marine Data Store (MDS): Mediterranean Sea – High Resolution and Ultra High Resolution L3S Sea Surface Temperature, E.U. Copernicus Marine Service Information (CMEMS) and Marine Data Store (MDS) [data set], <https://doi.org/10.48670/moi-00171>, 2024a.
- E.U. Copernicus Marine Service Information (CMEMS) and Marine Data Store (MDS): Mediterranean Sea, Bio-Geo-Chemical, L3, daily Satellite Observations (1997–ongoing), E.U. Copernicus Marine Service Information (CMEMS) and Marine Data Store (MDS) [data set], <https://doi.org/10.48670/moi-00299>, 2024b.
- E.U. Copernicus Marine Service Information (CMEMS) and Marine Data Store (MDS): Global Ocean Hourly Sea Surface Wind and Stress from Scatterometer and Model, E.U. Copernicus Marine Service Information (CMEMS) and Marine Data Store (MDS) [data set], <https://doi.org/10.48670/moi-00305>, 2024c.
- European Space Agency: SNAP – ESA Sentinel Application Platform v8.0, <http://step.esa.int> (last access: 15 January 2021), 2020.
- Everingham, M., Van Gool, L., Williams, C. K., Winn, J., and Zisserman, A.: The PASCAL visual object classes (VOC) challenge, *International journal of computer vision*, 88, 303–338, <https://doi.org/10.1007/s11263-009-0275-4>, 2010.
- Ferraro, G., Meyer-Roux, S., Muellenhoff, O., Pavliha, M., Svetak, J., Tarchi, D., and Topouzelis, K.: Long term monitoring of oil spills in European seas, *International Journal of Remote Sensing*, 30, 627–645, <https://doi.org/10.1080/01431160802339464>, 2009.
- Fingas, M. and Brown, C.: Chapter 5 – Oil Spill Remote Sensing, in: *Oil Spill Science and Technology* (Second Edition), edited by: Fingas, M., Gulf Professional Publishing, Boston, 2nd Edn., 305–385, ISBN 978-0-12-809413-6, <https://doi.org/10.1016/B978-0-12-809413-6.00005-9>, 2017.
- Franceschi, N., Recchia, A., Piantanida, R., Giudici, D., Albinet, C., and Miranda, N.: A Global C-Band RFI Monitoring System Based on Sentinel-1 Data, in: 2021 IEEE International Geoscience and Remote Sensing Symposium IGARSS, 1658–1661, <https://doi.org/10.1109/IGARSS47720.2021.9554119>, 2021.
- Franceschi, N., Recchia, A., Piantanida, R., Hajdich, G., Vincent, P., Pinheiro, M., Miranda, N., and Albinet, C.: Operational RFI Mitigation Approach in Sentinel-1 IPF, in: *EUSAR 2022; 14th European Conference on Synthetic Aperture Radar*, 1–5, ISBN 978-3-8007-5823-4, 2022.
- Gade, M., Scholz, J., and von Viebahn, C.: On the detectability of marine oil pollution in European marginal waters by means of ERS SAR imagery, in: *IGARSS 2000, IEEE 2000 International Geoscience and Remote Sensing Symposium. Taking the Pulse of the Planet: The Role of Remote Sensing in Managing the Environment. Proceedings* (Cat. No.00CH37120), 6, 2510–2512, <https://doi.org/10.1109/IGARSS.2000.859623>, 2000.
- Gade, M., Byfield, V., Ermakov, S., Lavrova, O., and Mitnik, L.: Slicks as Indicators for Marine Processes, *Oceanography* (Washington D.C.), 26, 138–149, 2013.
- GEBCO Bathymetric Compilation Group 2023: The GEBCO_2023 Grid – a continuous terrain model of the global oceans and land, <https://doi.org/10.5285/f98b053b-0cbc-6c23-e053-6c86abc0af7b>, 2023.
- Gertman, I., Zodiatis, G., Murashkovsky, A., Hayes, D., and Brenner, S.: Determination of the locations of southeastern Levantine anticyclonic eddies from CTD data, *Rapp. Commun. Int. Mer. Mediterr.*, 38, 151, 2007.
- Graziano, M. D., Grasso, M., and D’Errico, M.: Performance Analysis of Ship Wake Detection on Sentinel-1 SAR Images, *Remote Sensing*, 9, <https://doi.org/10.3390/rs9111107>, 2017.
- Hajdich, G., Franceschi, N., Pinheiro, M., and Valentino, A.: SAR-MPC Sentinel-1: Using the RFI annotations, Report number: SAR-MPC-OTH-0540-1-0, <https://doi.org/10.13140/RG.2.2.13758.56641>, 2022.
- Hasimoto-Beltran, R., Canul-Ku, M., Díaz Méndez, G. M., Ocampo-Torres, F. J., and Esquivel-Trava, B.: Ocean oil spill detection from SAR images based on multi-channel deep learning semantic segmentation, *Marine Pollution Bulletin*, 188, 114651, <https://doi.org/10.1016/j.marpolbul.2023.114651>, 2023.
- Hühnerfuss, H.: Basic physicochemical principles of monomolecular sea slicks and crude oil spills, Springer Berlin Heidelberg.

- berg, Berlin, Heidelberg, 21–35, ISBN 978-3-540-33271-8, https://doi.org/10.1007/3-540-33271-5_4, 2006.
- Karathanassi, V., Topouzelis, K., Pavlakis, P., and Rokos, D.: An object-oriented methodology to detect oil spills, *International Journal of Remote Sensing*, 27, 5235–5251, <https://doi.org/10.1080/01431160600693575>, 2006.
- Karimova, S. and Gade, M.: Submesoscale eddies seen by spaceborne radar, *Proc. EMEC*, 665–676, 2013.
- Karin, T.: toddkarin/global-land-mask: Release of version 1.0.0, Zenodo [code], <https://doi.org/10.5281/zenodo.4066722>, 2020.
- Knauss, J. A. and Garfield, N.: Introduction to physical oceanography, Waveland Press, ISBN 978-1-4786-3250-4, 2016.
- Konik, M. and Bradtke, K.: Object-oriented approach to oil spill detection using ENVISAT ASAR images, *ISPRS Journal of Photogrammetry and Remote Sensing*, 118, 37–52, <https://doi.org/10.1016/j.isprsjprs.2016.04.006>, 2016.
- Krestenitis, M., Orfanidis, G., Ioannidis, K., Avgerinakis, K., Vrochidis, S., and Kompatsiaris, I.: Oil Spill Identification from Satellite Images Using Deep Neural Networks, *Remote Sensing*, 11, <https://doi.org/10.3390/rs11151762>, 2019.
- Langmuir, I.: Surface Motion of Water Induced by Wind, *Science*, 87, 119–123, <https://doi.org/10.1126/science.87.2250.119>, 1938.
- Lehner, S., Horstmann, J., Koch, W., and Rosenthal, W.: Mesoscale wind measurements using recalibrated ERS SAR images, *Journal of Geophysical Research: Oceans*, 103, 7847–7856, <https://doi.org/10.1029/97JC02726>, 1998.
- Li, X.: Atmospheric vortex streets and gravity waves, National Oceanic and Atmospheric Administration, Washington, DC, USA, 341–354, ISBN 0-16-073214-X, 2004.
- Li, X. and Lehner, S.: Observation of TerraSAR-X for Studies on Offshore Wind Turbine Wake in Near and Far Fields, *IEEE Journal of Selected Topics in Applied Earth Observations and Remote Sensing*, 6, 1757–1768, <https://doi.org/10.1109/JSTARS.2013.2263577>, 2013.
- Lin, I.-I., Alpers, W., Khoo, V., Lim, H., Lim, T., and Kasilingam, D.: An ERS-1 synthetic aperture radar image of a tropical squall line compared with weather radar data, *IEEE Transactions on Geoscience and Remote Sensing*, 39, 937–945, <https://doi.org/10.1109/36.921411>, 2001.
- Liu, A. K., Chang, Y. S., Hsu, M.-K., and Liang, N. K.: Evolution of nonlinear internal waves in the East and South China Seas, *Journal of Geophysical Research: Oceans*, 103, 7995–8008, <https://doi.org/10.1029/97JC01918>, 1998.
- Liu, G., Perrie, W., Kudryavtsev, V., He, Y., Shen, H., Zhang, B., and Hu, H.: Radar imaging of intense nonlinear Ekman divergence, *Geophysical Research Letters*, 43, 9810–9818, <https://doi.org/10.1002/2016GL070799>, 2016.
- Lloyd, S.: Least squares quantization in PCM, *IEEE Transactions on Information Theory*, 28, 129–137, <https://doi.org/10.1109/TIT.1982.1056489>, 1982.
- Lyden, J. D., Hammond, R. R., Lyzenga, D. R., and Shuchman, R. A.: Synthetic aperture radar imaging of surface ship wakes, *Journal of Geophysical Research: Oceans*, 93, 12293–12303, <https://doi.org/10.1029/JC093iC10p12293>, 1988.
- Lévy, M., Ferrari, R., Franks, P. J. S., Martin, A. P., and Rivière, P.: Bringing physics to life at the submesoscale, *Geophysical Research Letters*, 39, <https://doi.org/10.1029/2012GL052756>, 2012.
- MacQueen, J.: Some methods for classification and analysis of multivariate observations, in: *Proceedings of the fifth Berkeley symposium on mathematical statistics and probability*, Oakland, CA, USA, vol. 1, 281–297, 1967.
- Mahmoud, A. S., Mohamed, S. A., El-Khoriby, R. A., AbdelSalam, H. M., and El-Khodary, I. A.: Oil spill identification based on dual attention UNet model using Synthetic Aperture Radar images, *Journal of the Indian Society of Remote Sensing*, 51, 121–133, 2023.
- McWilliams, J. C. and Molemaker, M. J.: Baroclinic Frontal Arrest: A Sequel to Unstable Frontogenesis, *Journal of Physical Oceanography*, 41, 601–619, <https://doi.org/10.1175/2010JPO4493.1>, 2011.
- Menna, M., Poulain, P.-M., Zodiatis, G., and Gertman, I.: On the surface circulation of the Levantine sub-basin derived from Lagrangian drifters and satellite altimetry data, *Deep Sea Research Part I: Oceanographic Research Papers*, 65, 46–58, <https://doi.org/10.1016/j.dsr.2012.02.008>, 2012.
- Meyer, F. J., Nicoll, J. B., and Doulgeris, A. P.: Correction and Characterization of Radio Frequency Interference Signatures in L-Band Synthetic Aperture Radar Data, *IEEE Transactions on Geoscience and Remote Sensing*, 51, 4961–4972, <https://doi.org/10.1109/TGRS.2013.2252469>, 2013.
- Miller, T., Potter, L., and McCorkle, J.: RFI suppression for ultra wideband radar, *IEEE Transactions on Aerospace and Electronic Systems*, 33, 1142–1156, <https://doi.org/10.1109/7.625096>, 1997.
- Ministry of Transport and Road Safety, Israel: Israel Meteorological Service, https://ims.gov.il/en/data_gov, last access: 31 July 2024.
- Monti-Guarnieri, A., Giudici, D., and Recchia, A.: Identification of C-Band Radio Frequency Interferences from Sentinel-1 Data, *Remote Sensing*, 9, <https://doi.org/10.3390/rs9111183>, 2017.
- Natsuaki, R., Motohka, T., Watanabe, M., Shimada, M., and Suzuki, S.: An Autocorrelation-Based Radio Frequency Interference Detection and Removal Method in Azimuth-Frequency Domain for SAR Image, *IEEE Journal of Selected Topics in Applied Earth Observations and Remote Sensing*, 10, 5736–5751, <https://doi.org/10.1109/JSTARS.2017.2775205>, 2017.
- Nieto-Hidalgo, M., Gallego, A.-J., Gil, P., and Pertusa, A.: Two-Stage Convolutional Neural Network for Ship and Spill Detection Using SLAR Images, *IEEE Transactions on Geoscience and Remote Sensing*, 56, 5217–5230, <https://doi.org/10.1109/TGRS.2018.2812619>, 2018.
- Pegliasco, C., Chaigneau, A., Morrow, R., and Dumas, F.: Detection and tracking of mesoscale eddies in the Mediterranean Sea: A comparison between the Sea Level Anomaly and the Absolute Dynamic Topography fields, *Advances in Space Research*, 68, 401–419, <https://doi.org/10.1016/j.asr.2020.03.039>, 2021.
- Qi, L., Wang, M., Hu, C., and Holt, B.: On the capacity of Sentinel-1 synthetic aperture radar in detecting floating macroalgae and other floating matters, *Remote Sensing of Environment*, 280, 113188, <https://doi.org/10.1016/j.rse.2022.113188>, 2022.
- Rey, M., Tunaley, J., Folinsbee, J., Jahans, P., Dixon, J., and Vant, M.: Application Of Radon Transform Techniques to Wake Detection in Seasat-A SAR Images, *IEEE Transactions on Geoscience and Remote Sensing*, 28, 553–560, <https://doi.org/10.1109/TGRS.1990.572948>, 1990.
- Robinson, A. R.: Overview and Summary of Eddy Science, in: *Ed-dies in Marine Science*, edited by: Robinson, A. R., Springer

- Berlin Heidelberg, Berlin, Heidelberg, 3–15, ISBN 978-3-642-69003-7, https://doi.org/10.1007/978-3-642-69003-7_1, 1983.
- Robinson, I. S.: Measuring the Oceans from Space: the Principles and Methods of Satellite Oceanography, Springer Science & Business Media, ISBN 978-3-540-42647-9, 2004.
- Robinson, I. S.: Discovering the ocean from space: the unique applications of satellite oceanography, Springer Science & Business Media, ISBN 978-3-540-24430-1, <https://doi.org/10.1007/978-3-540-68322-3>, 2010.
- Rosen, P. A., Hensley, S., and Le, C.: Observations and mitigation of RFI in ALOS PALSAR SAR data: Implications for the DESDynI mission, in: 2008 IEEE Radar Conference, 1–6, <https://doi.org/10.1109/RADAR.2008.4720738>, 2008.
- Shemdin, O. H.: Synthetic aperture radar imaging of ship wakes in the Gulf of Alaska, *Journal of Geophysical Research: Oceans*, 95, 16319–16338, <https://doi.org/10.1029/JC095iC09p16319>, 1990.
- Siokou-Frangou, I., Christaki, U., Mazzocchi, M. G., Montresor, M., Ribera d'Alcalá, M., Vaqué, D., and Zingone, A.: Plankton in the open Mediterranean Sea: a review, *Biogeosciences*, 7, 1543–1586, <https://doi.org/10.5194/bg-7-1543-2010>, 2010.
- Stevens, J.: NASA Earth Observatory Map, <https://visibleearth.nasa.gov/images/147190/explorer-base-map> (last access: 8 September 2020), 2020.
- Szegedy, C., Vanhoucke, V., Ioffe, S., Shlens, J., and Wojna, Z.: Rethinking the Inception Architecture for Computer Vision, *arXiv [preprint]*, <https://doi.org/10.48550/arXiv.1512.00567>, 2015.
- Tings, B., Pleskachevsky, A., and Wiehle, S.: Comparison of detectability of ship wake components between C-Band and X-Band synthetic aperture radar sensors operating under different slant ranges, *ISPRS Journal of Photogrammetry and Remote Sensing*, 196, 306–324, <https://doi.org/10.1016/j.isprsjprs.2022.12.008>, 2023.
- Topouzelis, K. and Psyllos, A.: Oil spill feature selection and classification using decision tree forest on SAR image data, *ISPRS Journal of Photogrammetry and Remote Sensing*, 68, 135–143, <https://doi.org/10.1016/j.isprsjprs.2012.01.005>, 2012.
- Trujillo-Acatitla, R., Tuxpan-Vargas, J., Ovando-Vázquez, C., and Monterrubio-Martínez, E.: Marine oil spill detection and segmentation in SAR data with two steps Deep Learning framework, *Marine Pollution Bulletin*, 204, 116549, <https://doi.org/10.1016/j.marpolbul.2024.116549>, 2024.
- Tzutalin: LabelImg, Github [code], <https://github.com/tzutalin/labelImg> (last access: 1 July 2020), 2015.
- Volpe, G., Colella, S., Brando, V. E., Forneris, V., La Padula, F., Di Cicco, A., Sammartino, M., Bracaglia, M., Artuso, F., and Santoleri, R.: Mediterranean ocean colour Level 3 operational multi-sensor processing, *Ocean Sci.*, 15, 127–146, <https://doi.org/10.5194/os-15-127-2019>, 2019.
- von Jackowski, A., Bouchachi, N., Barral, Q.-B., Labatut, P., Marie, B., Crispi, O., Escoubeyrou, K., Paulin, C.-H., Dimier, C., Ras, J., et al.: Seasonality of amino acid enantiomers and microbial communities at MOLA time series in the NW Mediterranean Sea, *Organic Geochemistry*, 196, 104839, <https://doi.org/10.1016/j.orggeochem.2024.104839>, 2024.
- Wessel, P. and Smith, W. H. F.: A global, self-consistent, hierarchical, high-resolution shoreline database, *Journal of Geophysical Research: Solid Earth*, 101, 8741–8743, <https://doi.org/10.1029/96JB00104>, 1996.
- Woodhouse, I. H.: Introduction to Microwave Remote Sensing, CRC press, <https://doi.org/10.1201/9781315272573>, 2006.
- Yang, Y.-J.: yi-jie-yang/dataset_DARTIS_2019: Dataset code v1 (Version v1), Zenodo [code], <https://doi.org/10.5281/zenodo.17789853>, 2025.
- Yang, Y.-J. and Schnupfhaug, C.: A near real-time automated oil spill monitoring system using SAR imagery from the European Copernicus mission, in: Active and Passive Remote Sensing of Oceans, Seas, and Lakes, edited by: Frouin, R. J., Murakami, H., Choi, J.-K., and Tseng, K.-H., International Society for Optics and Photonics, SPIE, . 13264, 132640G, <https://doi.org/10.1117/12.3040472>, 2025.
- Yang, Y.-J. and Singha, S.: Oil Slicks, Look-Alikes and Other Remarkable SAR Signatures in Sentinel-1 Imagery in the Eastern Mediterranean Sea in 2019, PANGAEA [data set], <https://doi.org/10.1594/PANGAEA.980773>, 2025.
- Yang, Y.-J., Singha, S., and Goldman, R.: A Near Real-Time Automated Oil Spill Detection and Early Warning System Using Sentinel-1 SAR Imagery for the Southeastern Mediterranean Sea, *International Journal of Remote Sensing*, 45, 1997–2027, <https://doi.org/10.1080/01431161.2024.2321468>, 2024.
- Zeng, K. and Wang, Y.: A Deep Convolutional Neural Network for Oil Spill Detection from Spaceborne SAR Images, *Remote Sensing*, 12, <https://doi.org/10.3390/rs12061015>, 2020.
- Zhou, L., Zheng, G., Wang, C., Shao, J., Chen, P., Ren, L., Wan, X., Zhu, Y., and Wang, H.: Wavelength Extraction and Analysis of Wind Streaks in SAR Imagery, *IEEE Journal of Selected Topics in Applied Earth Observations and Remote Sensing*, 18, 16769–16779, <https://doi.org/10.1109/JSTARS.2025.3584105>, 2025.
- Zodiatis, G., Drakopoulos, P., Brenner, S., and Groom, S.: Variability of the Cyprus warm core Eddy during the CYCLOPS project, *Deep Sea Research Part II: Topical Studies in Oceanography*, 52, 2897–2910, <https://doi.org/10.1016/j.dsr2.2005.08.020>, 2005.

4 Development of an Automated Oil Slick Detection System

The automated oil spill detection system proposed in this thesis first targets the oil slicks with an object detection algorithm and then applies a segmentation method to obtain the exact locations covered by oil. To verify whether this procedure is feasible, the annotated oil slicks from 2015 to 2018 were used to custom train an object detector, and the corresponding result is shown in Section 4.1. Then, the custom-trained object detector was used to build the automated oil spill detection system. The system was tested on all SAR scenes covering the study area in 2019, as shown in Section 4.2.

4.1 Custom-trained oil object detector

Sentinel-1 SAR scenes covering the study area were pre-processed and manually inspected. Oil slicks in the images were manually inspected and annotated as oil objects, and a dataset of cropped images matching the input size of the object detector containing oil objects was generated. A total of 9768 oil slicks were collected from 5930 Sentinel-1 images taken between 2015 and 2018. The study used the You Only Look Once (YOLO) object detection algorithm, and also compared its performance with another well-known object detection algorithm, the Faster R-CNN. The detailed information on object detector training, object detector performance evaluation, and oil detection examples are described in the paper presented in this section. The citation to the paper is given as follows:

Yang, Y.-J., Singha, S., & Mayerle, R. (2022). A deep learning based oil spill detector using Sentinel-1 SAR imagery. *International Journal of Remote Sensing*, 43(11), 4287–4314. doi: 10.1080/01431161.2022.2109445

The manuscript is published. The following states the contributions made by the candidate to this paper:

The candidate pre-processed all Sentinel-1 SAR scenes. The manual inspection and annotation of the oil slicks was done together with a co-author. The training and performance evaluation of the object detection algorithms were performed by the candidate. The entire manuscript was written by the candidate and further improved based on the comments and suggestions of the co-authors.

A deep learning based oil spill detector using Sentinel-1 SAR imagery

Yi-Jie Yang ^{a,b}, Suman Singha^b and Roberto Mayerle^a

^aResearch and Technology Centre Westcoast, Kiel University, Büsum, Germany; ^bMaritime Safety and Security Lab, Remote Sensing Technology Institute, German Aerospace Center (DLR), Bremen, Germany

ABSTRACT

The Eastern Mediterranean Sea has been known as an oil pollution hotspot due to its heavy marine traffic and an increasing number of oil and gas exploration activities. To provide automatic detection of oil pollution from not only maritime accidents but also deliberate discharges in this region, a deep learning-based object detector was developed utilizing freely available Sentinel-1 Synthetic Aperture Radar (SAR) imagery. A total of 9768 oil objects were collected from 5930 Sentinel-1 scenes from 2015 to 2018 and used for training and validating the object detector and evaluating its performance. The trained object detector has an average precision (AP) of 69.10% and 68.69% on the validation and test sets, respectively, and it could be applied for building an early-stage oil contamination surveillance system.

ARTICLE HISTORY

Received 27 April 2022

Accepted 27 July 2022

KEYWORDS

SAR; oil pollution; object detection; deep learning

1. Introduction

Marine oil pollution has long been a serious problem for the maritime environment. Sources of oil pollution can be categorized into several groups: natural seepage, consumption of petroleum, transportation of petroleum and extraction of petroleum. Figure 1 shows the global average contributions of sources in marine waters for the years of 1975–1985 and 1990–1999 (Polinov, Bookman and Levin 2021). Most of the large oil spills come from tanker accidents, however they cover only around 8% of the total oil pollution. Illegal discharges, such as the release of oily ballast water, tanker washing residue, fuel oil sludge, engine waste and foul bilge water, account for the majority of human-caused oil pollution. Large oil spills in particular pose a great risk of environmental damage, but deliberate illegal discharges pose a constant threat to marine wildlife with potentially severe long-term consequences. The inhalation of volatile petroleum by mammals and birds at sea can cause irritation to their respiratory tract and narcosis (Saadoun 2015). Oil spill detection is therefore important not only for those maritime accidents, but also for tracking deliberate oil pollution.

Marine oil pollution ‘hotspots’ usually coincide with areas of high maritime traffic (Polinov, Bookman and Levin 2021). Offering the shortest shipping route from Asia to Europe, approximately 30% of all international merchant vessels pass through the

CONTACT Yi-Jie Yang  yi-jie.yang@mailbox.org  Research and Technology Centre Westcoast, Kiel University, Hafentörn 1, Büsum 25761, Germany

© 2022 The Author(s). Published by Informa UK Limited, trading as Taylor & Francis Group.

This is an Open Access article distributed under the terms of the Creative Commons Attribution-NonCommercial-NoDerivatives License (<http://creativecommons.org/licenses/by-nc-nd/4.0/>), which permits non-commercial re-use, distribution, and reproduction in any medium, provided the original work is properly cited, and is not altered, transformed, or built upon in any way.

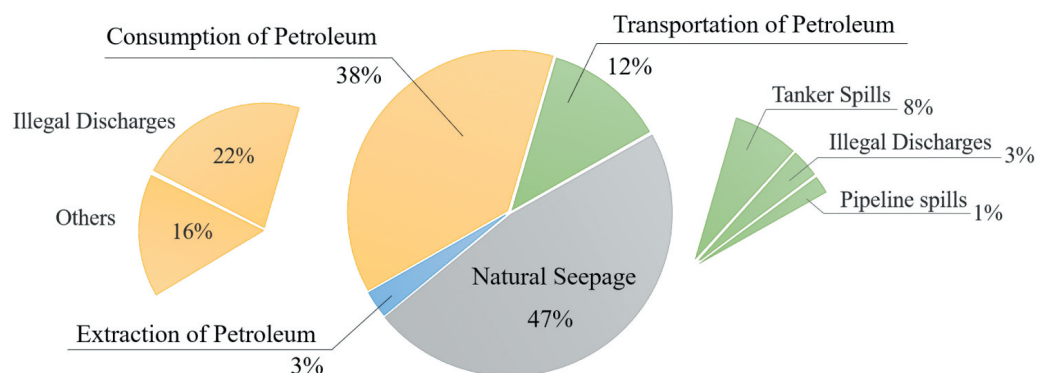


Figure 1. Main sources of petroleum entering worldwide marine waters with their average contributions for the years of 1975–1985 and 1990–1999 (Polinov, Bookman and Levin 2021).

Mediterranean Sea (REMPEC 2002). The Mediterranean Sea is also an important oil transit centre for transporting crude oil from the Middle East, North Africa and the Black Sea to Europe and North America. Around 20% to 25% of the world's oil tankers transit the Mediterranean Sea (REMPEC 2002). A previous study showed that the frequent oil spills in this area are usually related to shipping routes, oil terminals and transboundary shipping ports (Abdulla and Linden 2008). After the discovery of natural gas and oil in the Levantine basin in late 2010, there has been an increase in offshore oil and gas exploration and exploitation activities in the Eastern Mediterranean Sea. The Levantine region has thus become known as an oil spill hotspot. The situation is exacerbated by a lack of oversight due to the regional political instability (Polinov, Bookman and Levin 2021). One such oil spill event, which seriously influenced the coastline of Israel, was reported on 17 February 2021, but it could actually have already been found on satellite images on 11 February (Surkes, 28 February 2021). This and other events highlight the importance of having a reliable surveillance system for locating oil spills in the early stages in order to support the clean-up operations.

With the advantage of wide coverage and the capability of monitoring at night and during cloudy weather, spaceborne Synthetic Aperture Radar (SAR) is suitable for setting up such an early warning system. Water surface roughness is a key factor for the radar sensor to receive enough backscattered microwave energy. Small wind-induced friction between the air and the water surface causes gravity-capillary waves in the range of millimetres to centimetres (Woodhouse 2006). Oil spills dampen these waves and thus reduce radar backscatter, resulting in dark formations in contrast to the surrounding spill-free sea surface (Pavlakakis, Tarchi and Sieber 2001). However, there are many other phenomena, which can also manifest as dark regions in the radar image, such as low wind areas, natural films, wave fronts, wind sheltering by land, rain cells, wave current interaction along shears, internal waves, upwelling and eddies (Hovland, Johannessen and Digranes 1994; Topouzelis 2008). Distinguishing oil spills from these 'look-alikes' has long been a challenging task for oil spill detection with SAR.

The general procedure of detecting oil spills includes dark spot segmentation, feature extraction and classification (Solberg and Solberg 1996). Dark formations on SAR imagery are first separated from their surroundings. The features of each dark spot are then extracted and used to identify the differences between oil spills and look-alikes.

Commonly used features are statistical, geometric, textural, contextual and SAR polarimetric characteristics (Al-Ruzouq et al. 2020). The exploitation of polarimetric features, such as standard deviation of co-polarization phase difference, entropy, geometric intensity, co-polarization power ratio and polarization span, seem to be beneficial (Solberg 2012; Singha et al. 2016); however, the unavailability of quad-pol or dual-pol acquisitions on a regular basis and the limited swath of those images make it hard to be applied in an operational system. With all the extracted features, the dark spots are finally classified using a probabilistic approach as possible oil spills or look-alikes (Solberg et al. 1999; Fiscella et al. 2000). Depending on the present local sea state, oil spill composition, age of oil spill, image resolution and incidence angle of the acquisition, the backscatter properties of oil spills vary (Topouzelis 2008). Thus, machine learning algorithms are introduced to solve this challenging classification problem. Machine learning algorithms learn the relationships between the features given by previous experiences and the class (i.e. oil spill or look-alike) of each dark spot. The most commonly applied machine learning algorithms for oil spill detection are decision tree (Topouzelis and Psyllos 2012), support vector machine (SVM) (Brekke and Solberg 2008) and artificial neural network (ANN) (Singha, Bellerby and Trieschmann 2013). Deep learning is also considered as a subset of machine learning techniques. Unlike traditional machine learning algorithms, which rely on predefined features, deep learning algorithms learn directly from the data. Deep learning networks contain many layers, which are capable of constructing a hierarchy of features to increase the complexity. As deep learning is completely data driven, it requires large amounts of data for training. In the past, most of the spaceborne SAR data was acquired for oil spill detection when there were known marine accidents. However, with the advent of the Sentinel-1 mission by the European Space Agency (ESA) launched in 2014, it is now possible to detect oil spills from different sources on a regular basis with its frequent acquisitions. With the increasing volume of accessible SAR data and improvements in computational power, deep learning algorithms have been applied in oil spill detection as well.

Some studies applied U-Net to classify each pixel into a different class, such as oil spill, look-alike, ship, land and sea (Shaban et al. 2021) or simply oil spill and sea (Ronci et al. 2020). U-Net follows an encoder-decoder architecture, where the encoder gradually extracts features from low-level details to high-level information as it becomes deeper, and the decoder propagates information back to the original image dimension. As the encoder-decoder structure helps capture features at different scales, several architectures have been applied on image segmentation. DeepLabv3+ outperformed the other deep convolutional neural network (DCNN) models, U-Net, LinkNet, PSPNet and DeepLabv2, with its improvements in producing distinctive object boundaries (Krestenitis et al. 2019). Adapting the network from DeepLabv3+, an improved version was carried out and achieved better capability for multi-scale targets (Ma et al. 2022). Another study presented CBD-Net; it includes spatial and channel squeeze excitation, which collects contextual information and enhances the network's ability to distinguish boundary details. With this optimization, CBD-Net showed better completeness and correctness than U-Net, D-LinkNet and DeepLabv3 (Zhu et al. 2022). For applying deep learning-based methods, the preparation of a labelled dataset is usually the most time-consuming work, especially

for training pixel-based classifiers, which require a pixel-based mask of different classes. Therefore, there were only 35 and 21 SAR scenes used in Ma et al. (2022) and Zhu et al. (2022), respectively.

Object detectors on the other hand can only provide a detection of oil spills at a target level, but the dataset labelling work is less complex for each image, which means a larger dataset can be compiled in the same amount of time. Thus, more oil spills from different sources and of different types and sizes could be included, which might result in a higher ability to detect not only maritime accidents but also regular deliberate oil pollution. A previous study investigated a two-stage CNN to perform an initial coarse detection of objects, and based on that applied a precise pixel-wise detection on side-looking airborne radar (SLAR) imagery (Nieto-Hidalgo et al. 2018). The study pointed out the feasibility of detecting oil spills with object detection algorithms. Two other studies applied Mask-region-based convolutional neural network (Mask-RCNN) and used a total of around 2000–3000 images (Emna et al. 2020; Yekeen and Balogun 2020). Mask-RCNN can be regarded as a combination of object detection and semantic segmentation, as it first detects objects along with their classes and further segments objects into masks. However, to build a near real-time (NRT) oil spill detection system, highly efficient one-stage object detection algorithms such as You Only Look Once (YOLO) may be considered to keep the processing latency at a minimum. Following the idea that humans can easily recognize objects in an image at a glance, the YOLO object detection algorithm only looks at an entire image once to detect all objects inside along with their class probabilities (Redmon et al. 2016). It has been used in ship detection with SAR images in previous studies (Chang et al. 2019; Devadharshini et al. 2020), and one other study applied it on oil spill detection with optical imagery (Ghorbani and Behzadan 2021). However, applying YOLO on oil spill detection with SAR imagery is presented for the first time in this study.

This study developed a deep learning-based oil spill detector for the Eastern Mediterranean Sea using the YOLOv4 object detection algorithm. The object detector was trained with a total of 5930 Sentinel-1 images from 2015 to 2018, including 9768 oil spills from different sources and with different sizes collected and labelled as oil objects. With the use of such a large dataset, the capability of detecting deliberate oil spills is highlighted. CleanSeaNet is an existing service provided by the European Maritime Safety Agency (EMSA) using spaceborne SAR data to detect possible oil spills on the sea surface in European waters and sending oil spill alerts to national authorities (European Maritime Safety Agency 2017), but it is highly reliant on manual inspection, which is costly and time consuming. Therefore, this study aims to develop a deep learning-based oil spill detector for setting up an early-stage surveillance system. Different scenarios are carried out for training the object detector, and the detection results are discussed in the following sections.

The paper first introduces the used data and methods in section 2. Detailed information about the acquired SAR images is shown in subsection 2.1. Collecting oil spills and procedures of building the dataset are explained in subsections 2.2 and 2.3, respectively. The deep learning-based object detection algorithm YOLOv4 is introduced in subsection 2.4. Subsections 3.1 and 3.2 describe different scenarios for training the object detector. A further improved trained model and examples of detections are provided in subsection

3.3; the subsection also includes a comparison between the YOLOv4 custom trained model with one trained with another object detection algorithm, Faster RCNN. Section 4 summarizes the findings in this study.

2. Methodology

Oil spills in different areas might have varying patterns due to different origins, meteorological conditions, currents and circulation systems. This study focused on oil spills in the Eastern Mediterranean Sea, between longitudes 30–36°E and latitudes 31–34.7°N. The enclosed area with blue outline in Figure 2 shows the location of the study area, together with the number of collected oil spills between 2015 and 2018.

Figure 3 gives an overview of the workflow. Sentinel-1 SAR data was first pre-processed with a series of corrections, and oil spills in the images were labelled as oil objects. Then the pre-processed results were cropped into smaller images to fit the image input size of the object detector. The cropped images were categorized into different size groups (i.e. small, medium and large) to enable performing extra data augmentation on specific groups in order to increase the complexity of oil objects in the dataset. The labelled

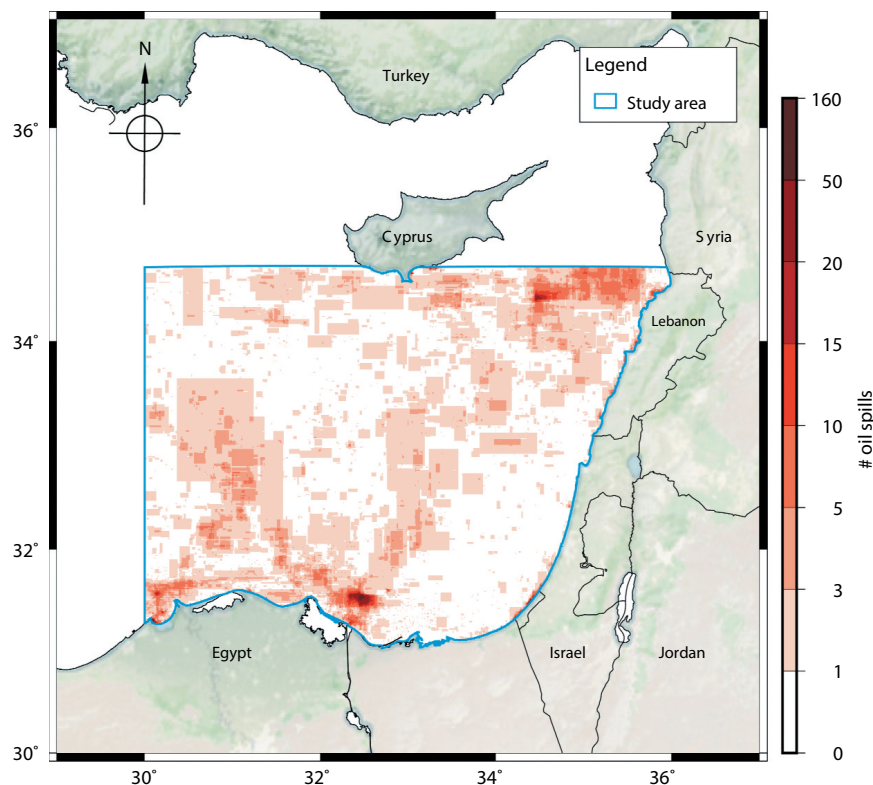


Figure 2. Visualization of study area with heat map of the amount of oil spills collected inside. The blue outline marks the study area. The red color map shows numbers of oil spills collected and manually annotated in this study from 2015 to 2018; see subsection 2.2 for detailed descriptions of manual inspection. Note that the oil spills were annotated with rectangular bounding boxes showing their extent, which are not exact polygons showing the oil spill positions. The basemap was obtained from Stevens (2020).

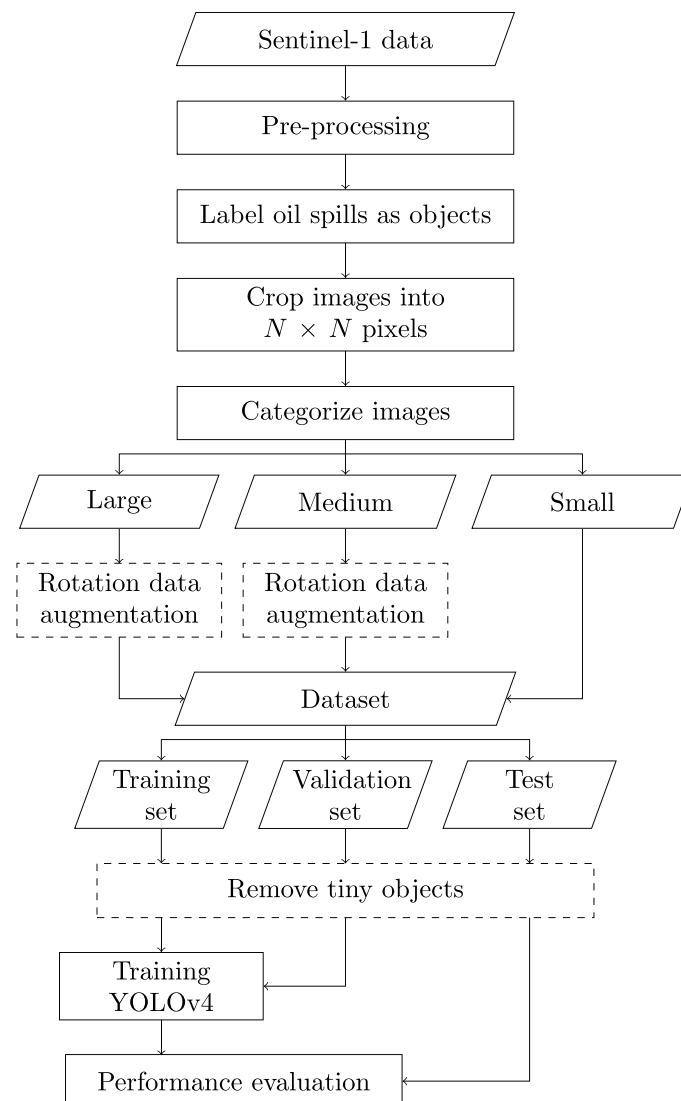


Figure 3. Workflow of this study. Oil spills inside Sentinel-1 SAR data were manually inspected and labelled as oil objects after a series of corrections in the pre-processing step. In order to fit the defined model input size for training the YOLOv4 object detector, the images were cropped into $N \times N$ px according to the object sizes and model input size. Then, images containing larger oil objects were augmented with rotation in order to increase the complexity of oil spills in the dataset; the corresponding scenario is shown in [subsection 3.2](#). Afterwards, the dataset was split into training, validation and test sets for training, fine tuning and evaluating the model. To avoid that some labelled oil objects are too small to be detected by the object detector, the annotations of oil objects below certain threshold were removed; the corresponding scenario is shown in [subsection 3.1](#).

data was then split into training, validation and test sets with proportion of 7 : 2 : 1. There is no common definition on the proportion of different sets, but all training, validation and test sets need to be representative for the task (i.e. covering different types of oil spills in different sets). Afterwards, the annotations of oil objects smaller than certain sizes were regarded as tiny objects and were removed to avoid confusing the model with

undetectable oil objects. During the training stage, the training set was used to train the object detector, and the validation set was used to find the optimal values for the hyper-parameters of the model and avoid model over-fitting on the training set. Finally, the model performance was evaluated with the test set.

Detailed information on the Sentinel-1 data used in this study can be found in [subsection 2.1](#). The labelling work is explained in [subsection 2.2](#). [Subsection 2.3](#) gives the details of building up the dataset, and the object detection algorithm is introduced in [subsection 2.4](#).

2.1. Sentinel-1 data

Sentinel-1 SAR Level-1 Ground Range Detected (GRD) Interferometric Wide mode products covering the study area were obtained from Copernicus Open Access Hub, which provides data within 24 h after observation without special subscription. For establishing an NRT warning system, the DLR collaborative ground segment will also be considered in the operational stage of the study as data inside its reception cone could be acquired within an hour. There were in total 5930 scenes from January 2015 to December 2018 used. Sentinel-1 GRD data provides dual polarization VV-VH products in the study area. In practice, cross-polarization (i.e. VH and HV) has much lower intensity and is influenced more by background and instrument noise than the co-polarization (i.e. VV and HH) (Woodhouse 2006). For this reason, SAR data from VV channel was used. The data was pre-processed with a series of corrections, including border noise removal, thermal noise removal, calibration, ellipsoid correction and conversion to decibels (dB). Note that continuous scenes in the same track were merged during the pre-processing. The pre-processing step was done automatically in a series of Python programs with the use of the Sentinel Application Platform (SNAP) Python API provided by ESA (European Space Agency 2020). The resolution of the pre-processed SAR results is 20 m × 20 m, which is similar to the original products.

2.2. Manual labelling work

To prepare the oil spill dataset for the training procedures, all the oil spills inside the pre-processed images were labelled as oil objects jointly by two authors who are experienced human interpreters. The oil objects were defined by bounding boxes, which show the extent of oil spills, with the open-source image annotation tool Labellmg (Tzutalin 2015). Note that look-alikes were not labelled but regarded as background information. Manual inspection of oil spills is based on experience and prior information including location, wind and weather condition, the period of the year and differences in their shapes compared to surroundings (Solberg et al. 1999; Topouzelis 2008). In the Eastern Mediterranean Sea, algal bloom is a common reason for look-alikes due to nutrient sources of coastal origins (e.g. increasing use of fertilizers) and strong current systems (Barale, Michel Jaquet and Ndiaye 2008). [Figure 4](#) shows an example of preprocessed data including look-alikes due to different reasons along with some visible land sourced oil spills. Algae blooms appear as dark formations with spiral patterns, which are driven by surface currents (e.g. north of the image). Dark formations surrounded by algal blooms might be low wind areas. The blue rectangle marks a region with regular oil spills from land sources. Red bounding boxes show locations of oil spills, and dark formations near

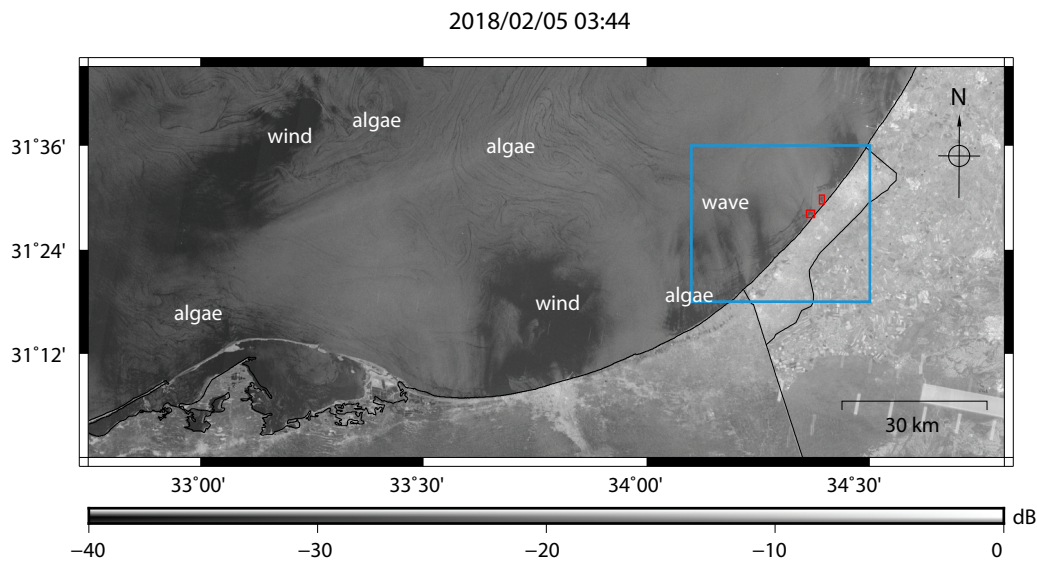


Figure 4. An example of look-alikes shown in Sentinel-1 SAR data along with some visible land sourced oil spills. The blue rectangular area has regular land sourced oil spills, which are annotated with red bounding boxes. Apart from oil spills, there are dark formations due to algae blooms (spiral patterns), low wind areas (near algae blooms) and possible wind and wave effects (in coastal area near oil spills).

coastal areas are possibly induced by wind and waves. Look-alikes make it more difficult to tell if there are oil spills in the scene and to annotate them correctly. Oil spills can be distinguished from look-alikes due to their different patterns, and also from experience of collecting regular oil spills from the area (see Figure 5 for examples).

Figure 2 shows a heat map based on the amount of oil spills collected and annotated in this study; there are in total 9768 labelled oil objects from 2015 to 2018. Regions with frequent oil spills might be related to shipping routes, locations of oil fields and oil terminals, and some regular pollution from land sources. The figure shows relatively frequent oil spills at the northern access of the Suez Canal, which has high density of ship traffic especially due to tankers transiting between Suez Canal and ports in the Eastern Mediterranean or Western Europe (O'Hagan 2007). It shall be noted that the amount of oil spills was calculated from the labelled oil objects, which are not exact polygons showing the oil spill location but the extent of the spill defined by its bounding box.

2.3. Dataset

The pre-processed images cover areas with dimensions of around 18796×24521 px and 18455×24521 px for the ascending and descending tracks, respectively. However, most of the labelled oil objects only occupy areas of less than 128×128 px, which makes it difficult for the object detector to target objects. In addition, the object detector requires a certain model input size, which might change the aspect ratios of images. To avoid training the object detector on distorted images, the pre-processed images were cropped into smaller sizes to fit the model input size. The images were cropped based on the

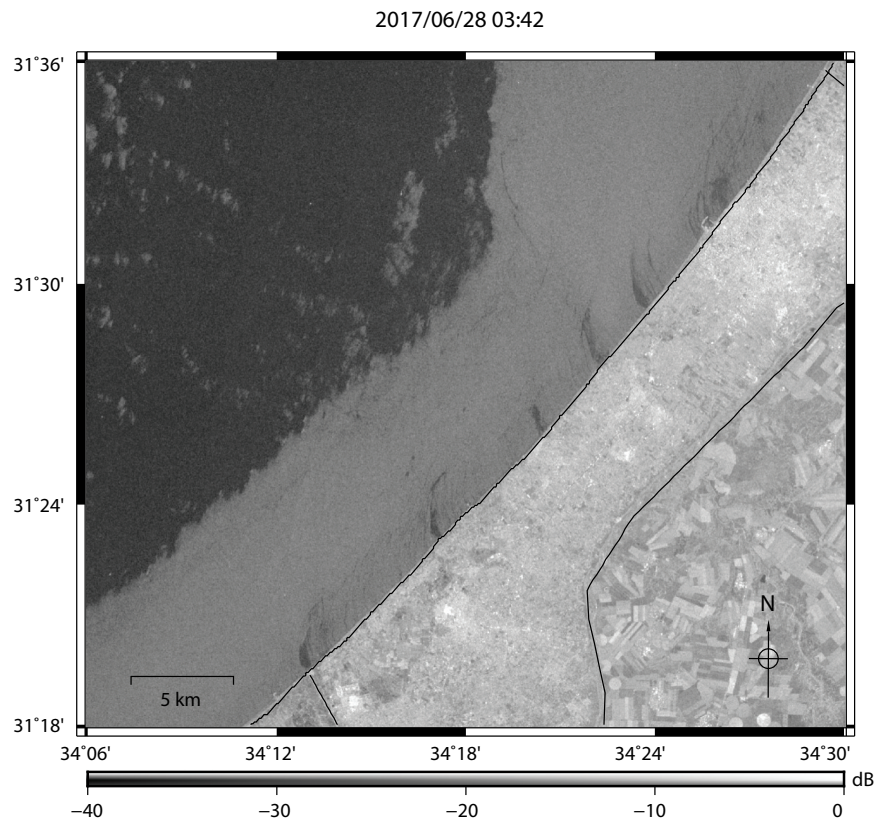


Figure 5. An example showing clear oil spills coming from land sources. This figure has the same extent as the blue outlined area shown in [Figure 4](#).

positions of the labelled oil objects. Each oil object has one corresponding cropped image; however, it might happen that there are several oil objects in one cropped image generating several cropped images with similar coverage. To avoid the same oil objects appearing in multiple images, this study filtered out most of the duplicated ones manually. Checking the labels in the dataset and filtering out the duplicated oil objects required around 40 h of work for each year (e.g. from 1 January 2017 to 31 December 2017). As the cropped images were designed based on labelled oil objects, each cropped image includes at least one oil object. Note that this does not mean that every image must contain an object during the detection process. The object detector learns not only the given objects but also the regions without annotations as background during training. Therefore, it is expected to return no object if there is none to detect. The cropped images have dimensions of $N \times N$ px, where N is equal to the maximum of the model input size and the edge lengths of the object bounding box. The model input size in this study is 640×640 px. Large oil objects could therefore result in images with sizes greater than the model input size, so they will be resampled when put into the model. With this approach, however, long and slim oil objects in such images might become undetectable when they are resampled. [Figure 6](#) shows examples of long and slim oil spills, which possibly resulted from ships. The images cover areas of around 1220 km^2 and 770 km^2 , respectively. These kinds of oil spills are usually discharged from moving ships. In the beginning, there is a larger amount of oil released, and as the ship keeps moving the

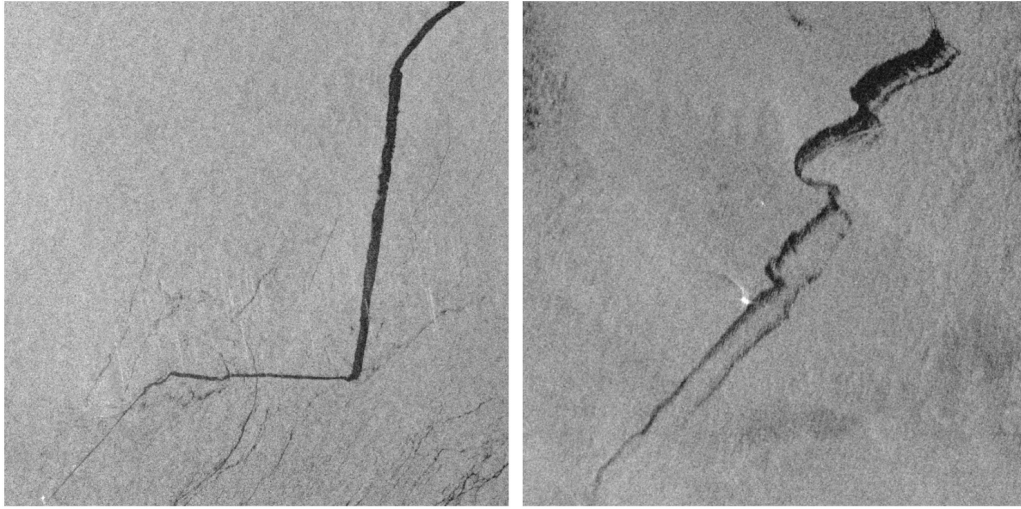


Figure 6. Examples of long and slim oil spills. The areas of the images are around 1220 km² and 770 km², respectively.

amount decreases resulting in the oil trace becoming gradually slimmer. The slimmer part of oil spills might be barely visible to the object detector. Hence, these kinds of images were manually examined again, and images with long and slim oil objects were tiled into several sub-images in order to avoid the oil spills becoming undetectable. On the contrary, if the oil objects inside the image were long and wide, they were not altered to let the model learn the entire shape of the oil spill.

The cropped images (including the tiled images after examination) were then put into different size groups based on the sizes of the largest oil objects inside. Oil spills in bounding boxes with an area smaller than 12,500 px (i.e. 5 km²) were categorized as small oil objects, and those with bounding boxes greater than or equal to 100,000 px (i.e. 40 km²) were categorized as large oil objects. The rest of the oil spills with areas in-between were regarded as medium objects. However, certain small objects were regarded as undetectable tiny objects and had their annotations removed. In this study, tiny objects were defined as follows:

$$\begin{aligned} & \text{if } h_{\text{obj}} < h_{\text{img}} \cdot T_{\text{tiny}}/h_{\text{model}} [\text{px}] \cup \\ & w_{\text{obj}} < w_{\text{img}} \cdot T_{\text{tiny}}/w_{\text{model}} [\text{px}] \Rightarrow \text{Obj} \in \text{Obj}_{\text{tiny}} \end{aligned} \quad (1)$$

where h_{obj} , h_{img} and h_{model} respectively refer to the heights of the object, image and model input; w refers to the corresponding width. T_{tiny} is the pixel threshold for defining tiny objects. The first scenario in [subsection 3.1](#) aims to find a suitable value for T_{tiny} .

[Table 1](#) shows the amount of oil objects per size category in the dataset after removing the tiny objects with $T_{\text{tiny}} = 20$ px. An imbalance with regard to the amount of objects per category can be observed because there are comparatively fewer larger oil spills than smaller ones. In addition, the larger oil spills seems to have higher shape complexity, which might be more difficult to detect. To alleviate the imbalance of oil spills in different sizes and enhance the ability of detecting larger oil spills, data augmentation was applied, focusing on images with larger oil objects. The idea of data augmentation is to increase

Table 1. Amount and percentage of oil objects with different sizes in the dataset from 2015 to 2018 after removing tiny objects.

Category	Size (px)	# Objects	%
Small	< 12500	7885	72.3
Medium	12,500–100,000	2420	22.2
Large	≥ 100000	595	5.5

the amount of data by applying slight modifications to the original dataset. The second scenario in [subsection 3.1](#) provides a comparison of model performance when applying rotation data augmentation on specific groups before model training.

After data augmentation, the whole dataset was split into training, validation and test sets. Different-sized oil objects were balanced between the sets and the objects were put into the different sets with a relative proportion of 7 : 2 : 1. Considering that there are seasonal algae in the study area, it was ensured that training, validation and test sets all contained images from different seasons and images in different sets should not originate from the same SAR acquisitions.

2.4. YOLOv4 object detection algorithm

Deep learning-based object detection algorithms work in three essential stages: feature extraction, object localization and classification. Feature extraction, the so-called backbone of an object detector, finds the representation of the input images as feature maps by using a backbone network. The network has different layers to learn multiple levels of features, and is usually trained on a large labelled dataset (e.g. ImageNet (Deng et al. 2009)). The object localization stage finds the area of the image that potentially contains an object, which is also known as the region of interest (ROI). Then, the classification stage fine tunes the proposed region and outputs the final prediction with the class of the objects. The object localization stage and the classification stage are usually called the head. An additional stage for collecting feature maps might also be included between the backbone and the head, which is regarded as the neck.

Two-stage object detection algorithms refer to those using two different networks to achieve object localization and classification in two different steps, which means that the classifier needs to detect the object class in each ROI. This step makes the object detection comparatively slow and uses a high amount of computational resources. However, one-stage object detection algorithms combine object localization and classification into one step with only a single deep neural network. YOLO is an example of a one-stage object detection algorithm (Redmon et al. 2016). One-stage object detectors are usually regarded as more efficient but less accurate. However, the accuracy and speed of the recent one-stage object detector YOLOv4 has been improved by implementing a new architecture, introducing Bag-of-Freebies (BoF) and Bag-of-Specials (BoS), and including mosaic, a new data augmentation method (Bochkovskiy, Wang and Mark Liao 2020; Wang, Bochkovskiy and Mark Liao 2021). In the preliminary stage, this study compared

the model performance of the trained objectors with and without applying mosaic data augmentation; the AP of the trained detectors on test set is 55.54% and 30.34%, respectively. The results highlight the improvement of the model from applying mosaic.

Figure 7 shows the overall structure of YOLOv4. YOLOv4 uses CSPDarknet53 as its backbone, which applies Cross Stage Partial Network (CSPNet) (Wang et al. 2020) to update the previous YOLOv3 backbone Darknet53. It further reduced the need of computational resources as CSPNet proposes a richer gradient combination while reducing the requirement of computational resources to solve the vanishing gradient problem during the training stage (Wang et al. 2020). CSPDarknet53 extracts feature maps through five residual blocks (Bochkovskiy, Wang and Mark Liao 2020), followed by Spatial Pyramid Pooling (SPP) and a modified Path Aggregation Network (PANet) as the neck. SPP enhances the receptive field, which represents all the pixels from feature maps with an impact on results. PANet has the ability to keep spatial information in order to improve the object localization. In the last stage, three *yolo* layers are applied as the head. Feature maps of different scales are collected in order to find objects with different sizes. The model input size in this study is 640×640 px, and detection feature maps down-sampled by factors of 8, 16 and 32 are generated. Therefore, the detection feature maps have dimensions of 80×80 , 40×40 and 20×20 px. In order to picture how much information can be obtained in different scales, Figure 8 shows the down-sampled images. The idea is that large objects can be detected with smaller scale (e.g. 20×20 px) and small objects need larger scale (e.g. 80×80 px) to include the necessary details.

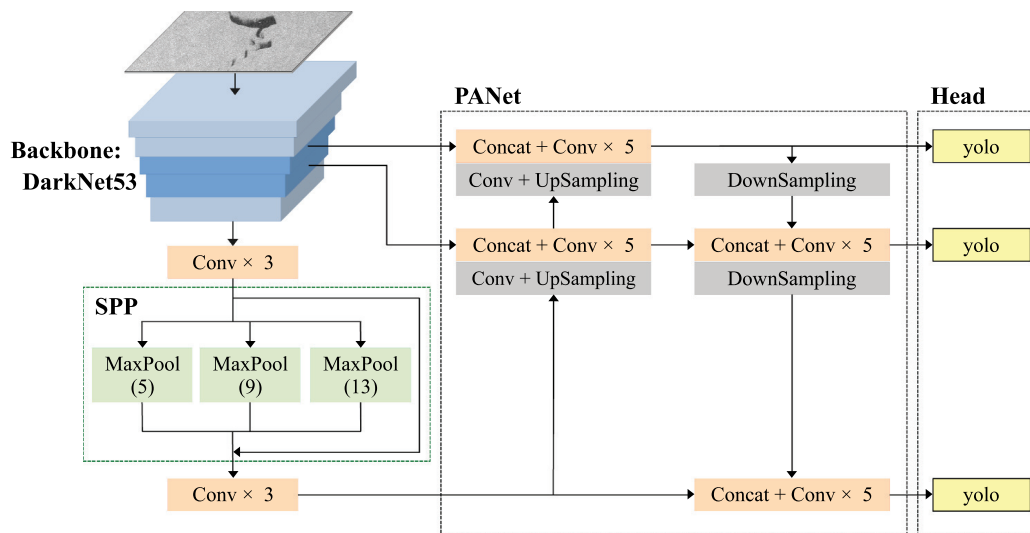


Figure 7. Overall structure of YOLOv4. The backbone CSPDarknet53 extracts feature maps through 5 residual blocks. SPP and PANet are applied to enhance the receptive field and improve the object localization, respectively. Feature maps of different scales are extracted by three *yolo* layers in the last stage in order to detect objects with different sizes. The figure incorporates elements modified from (Li et al. 2020; Hu and Wen 2021).

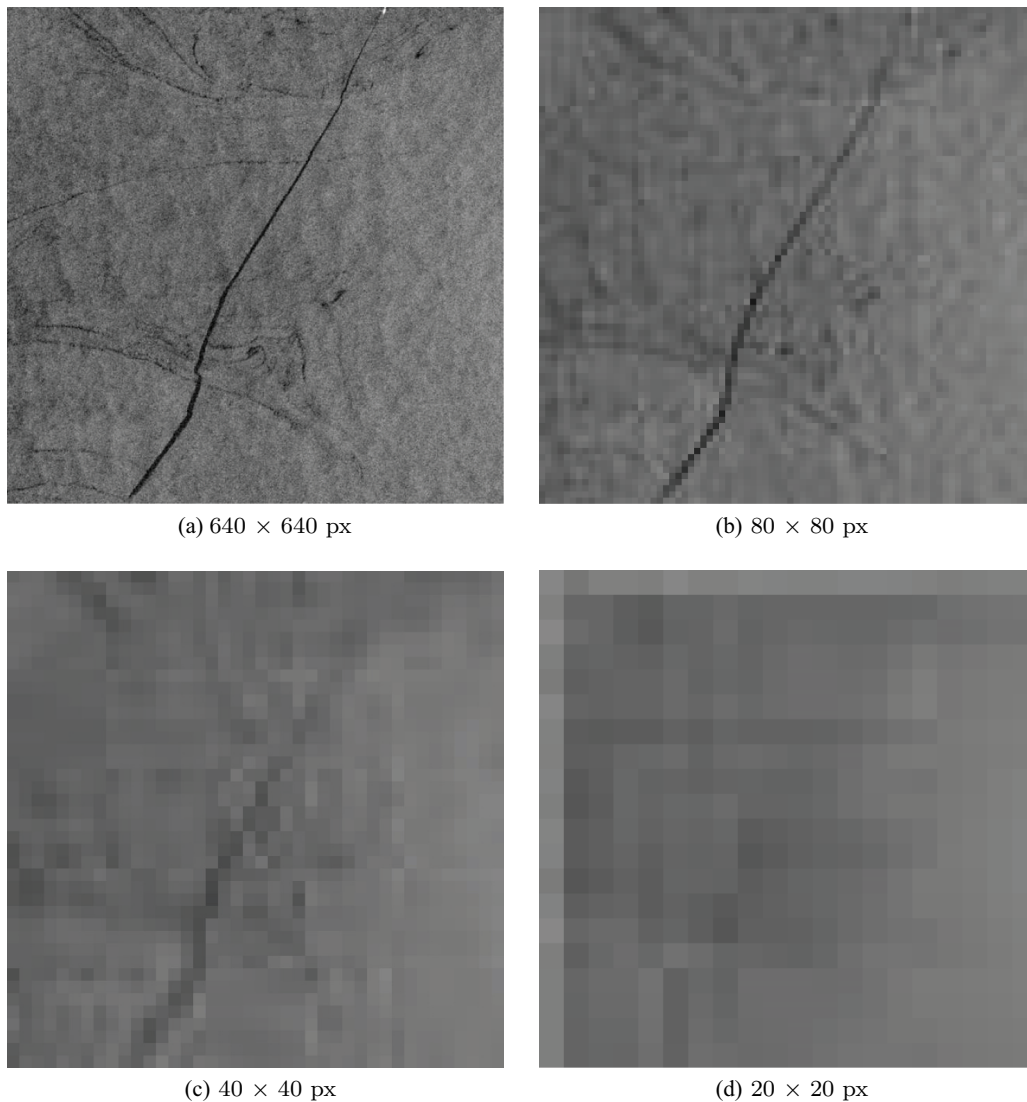


Figure 8. Images with oil spills in different scales. The images were downsampled to different dimensions. Note that the original image has a size of 1145×1145 px, which is greater than the model input size; thus, the image was downsampled to 640×640 px as shown in (a) (see [Subsection 2.3](#) for detailed explanation).

3. Results

This section presents the results obtained from training the deep learning model for oil spill detection. Different scenarios are considered and shown in the following subsections. [Subsection 3.1](#) determines the parameter T_{tiny} in Equation (1) to find a suitable measure to remove tiny oil objects. [Subsection 3.2](#) then investigates if adding additional rotation data augmentation can help improve the model performance. For training the model an Nvidia GeForce RTX 3080 GPU with 10 GB VRAM was used, which took around 7.5 h for each training run with 6000 iterations. As an initial estimation, it would require at least around

1838 image patches with a size of 640×640 px and overlap of 40 px to cover the whole study area. Detecting oil spills in these images by the trained model would take around 1 min.

To evaluate the performance of an object detector, its predictions are compared to ground truth data. As there is no real-world ground truth oil spill data available, ground truth data refers to the manually inspected objects described in [subsection 2.2](#) in this study. The comparison between predictions and ground truth can be summarized by a confusion matrix with four components: True Positive (TP), False Positive (FP), False Negative (FN) and True Negative (TN). TP shows oil objects that are correctly detected by the object detector. FP refers to cases where oil objects are detected but they do not match the ground truth. On the contrary, undetected oil objects are regarded as FN. TN is generally not applied in object detection as background is not defined in ground truth and also not present in detections.

[Figure 9](#) shows different detections of the same oil spill. The red bounding box denotes the manually inspected oil object and the yellow bounding boxes mark the detections. [Figure 9\(c\)](#) is the best match because it shows the largest overlap with the ground truth data. However, a concrete definition of correct detection should be defined. Intersect over union (IoU) is therefore used as it indicates how close the predicted area of an object is to the ground truth bounding box. It is defined as follows (Everingham et al. 2010):

$$IoU = \frac{\text{area}(B_p \cap B_g)}{\text{area}(B_p \cup B_g)} \quad (2)$$

where $B_p \cap B_g$ and $B_p \cup B_g$ respectively refer to the intersection and union of the bounding boxes of the prediction (B_p) and the ground truth (B_g). The IoU threshold is usually applied to define whether a detection is TP or FP. In this study, the IoU threshold is defined as 50%, which means that only detections with $IoU \geq 50\%$ and have the same class prediction (i.e. oil) are TP.

Based on TP, FP and FN, the recall and precision measures are used and given as follows (Goutte and Gaussier 2005):

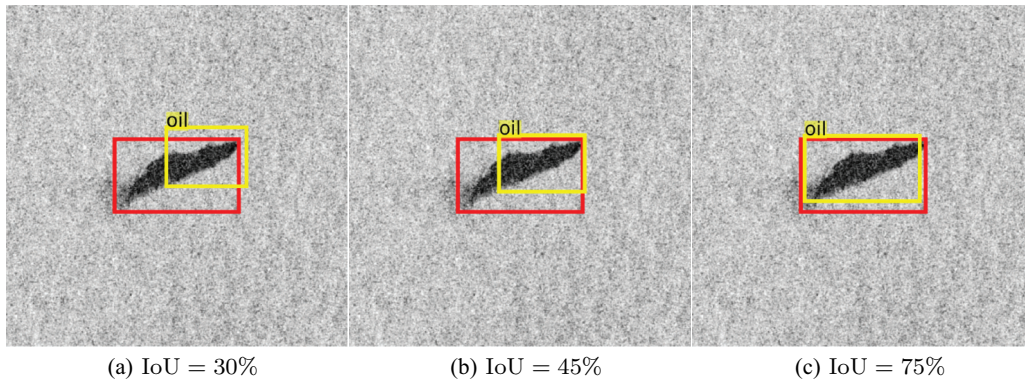


Figure 9. Examples showing detections with different IoU.

$$\begin{aligned} \text{Recall} &= \frac{TP}{(TP + FN)} \\ \text{Precision} &= \frac{TP}{(TP + FP)} \end{aligned} \quad (3)$$

Recall represents the sensitivity to detect objects, that is, among all the ground truth data, the amount of objects that are correctly detected. Precision describes the number of correctly detected objects in comparison to the ground truth data. It is desirable that the object detector has both high precision and recall. Based on these two measures, AP is defined as an average of precision values from a set of recall for a single class as follows:

$$AP = \int_0^1 P(R) dR \quad (4)$$

where R is recall, $P(R)$ is the precision at discrete recall values R . In this study, AP is calculated as an average of precision values from 11 equally spaced recall values as discrete approximation of Equation (4) analogous to the VOC2007 challenge (Everingham et al. 2010).

The trained models are evaluated by a comparison of their AP on the test sets with an IoU threshold of 50%, which was calculated with the help of a tool developed in Cartucho, Ventura and Veloso (2018) and modified by the authors. Based on results emerging from different scenarios, an improved trained model along with a selection of detection results on different types of oil spills are described in subsection 3.3. This study also compares the performance of the models trained by YOLOv4 and the well-known two-stage object detection algorithm Faster RCNN.

3.1. Remove annotations of tiny objects

In the preliminary stage of the study, the trained model generated spurious detections where no oil spill was visible. One possible explanation is that during the training procedure of the object detector, the input image is down-sampled by factors of 8, 16 and 32 in the object detection stage. Small objects need a larger scale (i.e. smaller downsampling factor) to capture their features, and objects below a certain size might be undetectable. There are tiny oil spills regularly released in the Eastern Mediterranean Sea, and hence it is possible that some of the labelled objects are invisible for the model but their annotations are in the training dataset. As a result, the trained model lacks the capability of detecting the extents of objects correctly and generates some random detections with oil spills improperly framed or even exceeding the image boundary (see Figure 10(a)).

As an initial test for removing the annotations of objects satisfying Equation (1) with T_{tiny} equal to 0, 28 and 48 px, Figure 10 shows examples of detections from different trained models (Yang, Singha and Mayerle 2021). In Figure 10(a) the model regards the oil object to cover an area larger than the oil spill of interest. It seems that the model was 'guessing' the extent of the oil object as it could not find the margin of the object well. Generally, applying a pixel threshold seems to help prevent excess detections when comparing Figure 10(a) with Figure 10(b) and Figure 10(c). Comparing T_{tiny} equal to 28 and 48 px, the trained object detector in Figure 10(b) more clearly defines the extents of

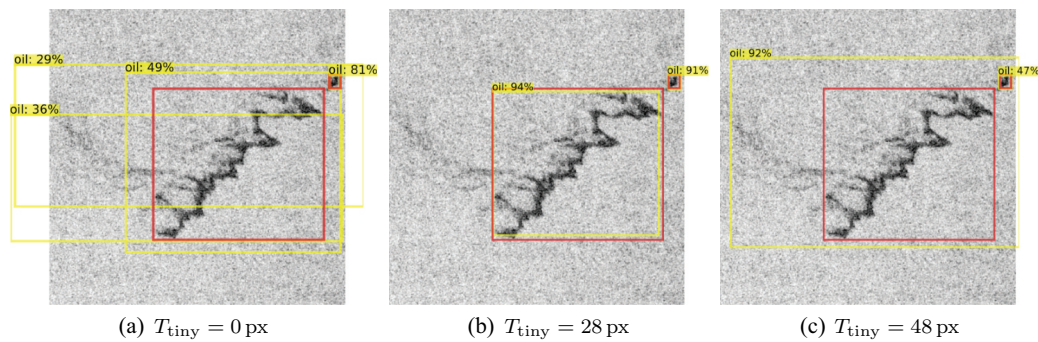


Figure 10. Examples for removal of tiny objects with varying T_{tiny} from a previous study. The yellow bounding boxes denote the detections with the confidence scores, and the red bounding boxes mark the ground truth oil spills (Yang, Singha and Mayerle 2021).

Table 2. Amount of objects in the training, validation and test sets for different cases that were used in scenario 1 (subsection 3.1), along with the AP of the trained models on the respective validation and test sets.

Case	# Objects (train/val/test sets)	AP@IoU=0.5%)	
		(val set)	(test set)
all	9947/2863/1443	64.85	61.64
rm_tiny_14	9026/2597/1308	69.12	64.08
rm_tiny_20	7616/2185/1099	64.60	65.69
rm_tiny_28	6063/1741/870	71.99	55.54

oil spills than the one in Figure 10(c). Based on this result, the removal of the annotation for tiny objects with smaller thresholds was examined further. Table 2 shows the amount of objects used in different cases and the model performance achieved. The four test cases are *all*, *rm_tiny_14*, *rm_tiny_20* and *rm_tiny_28* where T_{tiny} equals 0, 14, 20 and 28 px, respectively. When no object annotation is removed (*all*), the AP on the test set was 61.64%. After removing tiny objects, the AP was slightly improved. However, with $T_{\text{tiny}} = 28$ px the model performance actually decreased to 55.54% AP on the test set. A possible reason is that there were some removed objects observable in the image but without any annotation, so the model was misled. Overall, the test case *rm_tiny_20* with $T_{\text{tiny}} = 20$ px showed the best performance.

This scenario outlines the limitation of the object detector when targeting tiny objects. Small oil spills are not always clearly distinguishable from their surroundings due to the resolution of satellite imagery, making it difficult to properly define their extents. However, this limitation is in line with the capability of human observers who may disregard the detected tiny oil spills because of the described uncertainty. Nevertheless, the imbalance among oil spills of different sizes (see Table 1) might lead to a lower capability of detecting larger oil spills although they lead to more serious environmental damage. Therefore, decreasing the false-negative rate on detecting larger oil spills seems to be more important than increasing the ability of tiny object detection. The following subsection compares the model performance on oil spills of different sizes and provides scenarios to improve the oil spill detector.

3.2. Additional data augmentation

Table 1 shows the absolute and relative amount of oil objects used after the annotations of the tiny objects have been removed with $T_{\text{tiny}} = 20$ px. As there are small oil spills regularly appearing in the study area, 72.3% of all oil objects in the dataset have a bounding box area smaller than 12,500 px (i.e. 5 km²). In order to let the model detect oil spills of different sizes, additional rotation data augmentation was applied to images with larger oil objects in this scenario. All images were first categorized into *large*, *medium* and *small* image groups in relation to the size of the largest oil object inside. Images in the groups *large* and *medium* were rotated by 90° along with their annotations; the augmented image sets are noted as *L90_aug* and *M90_aug*, respectively. Table 3 shows the model performance for three different cases and the amount of oil objects per size group. The case *orig* is the same as case *rm_tiny_20* in subsection 3.1. The cases *L90* and *L90_M90* include the images from the case *orig* along with the additional augmented images from *L90_aug* and both *L90_aug* and *M90_aug*, respectively. Note that these different cases were tested on the same test set for model performance assessment. In these cases, there were in total 576 images in the test set.

Among the three cases, the case *L90* shows the best model performance with an AP of 69.53% and 70.55% on the validation and test sets, respectively. On the other hand, the AP of the trained object detector in the case *L90_M90* on the validation and test sets is 69.99% and 65.05%, respectively, which shows that the model is not well generalized and indicates possible model over-fitting to random patterns in the validation set. To further examine the models for their behaviours when detecting oil spills of different sizes, the test set was then split into three different subsets according to oil spill sizes (following the definition in Table 1). There were 387, 141 and 48 images in small, medium and large test subsets, respectively. Table 4 shows AP in the different cases and on the three subsets. The

Table 3. Amount of objects in the small, medium and large size groups for different cases that were used in scenario 2 (subsection 3.1), along with the AP of the trained models on the respective validation and test sets.

Case	# Objects (small/medium/large)	AP@IoU=0.5%)	
		(val set)	(test set)
orig	7785/2500/615	64.60	65.69
L90	9076/2718/1255	69.53	70.55
L90_M90	11,162/5188/1272	69.99	65.05

Table 4. The AP of the trained models on the test sets with oil spills of different sizes in scenario 2 (subsection 3.1).

Case	AP@IoU=0.5 [%] (test set)			
	all	small	medium	large
orig	65.69	74.16	56.49	38.85
L90	70.55	80.65	60.00	36.99
L90_M90	65.05	71.66	57.81	43.09

results in *L90* are better on small and medium oil spills but worse on large oil spills in comparison to the case *orig*, which does not fulfil the aim of improving the model performance on larger oil spills. In the case *L90_M90*, which not only considered the *large* subset but also included the *medium* subset for data augmentation, the model was trained on a higher complexity of oil spills. The model performance has improved for detecting large oil spills; however, it appears to be worse on *small* and *medium* subsets. Supporting this observation, Figure 11 shows different sizes of oil spills detected in the three different cases with the confidence scores as well as the manual inspections outlined in red.

Figure 11(a) shows a large oil spill, which is manually labelled as three oil objects as they were not connected with each other. The oil spill was detected by the models from the cases *orig* and *L90* as one object; however, the extents were not well predicted. One possible reason could be that images covering large areas with slim and long oil spills

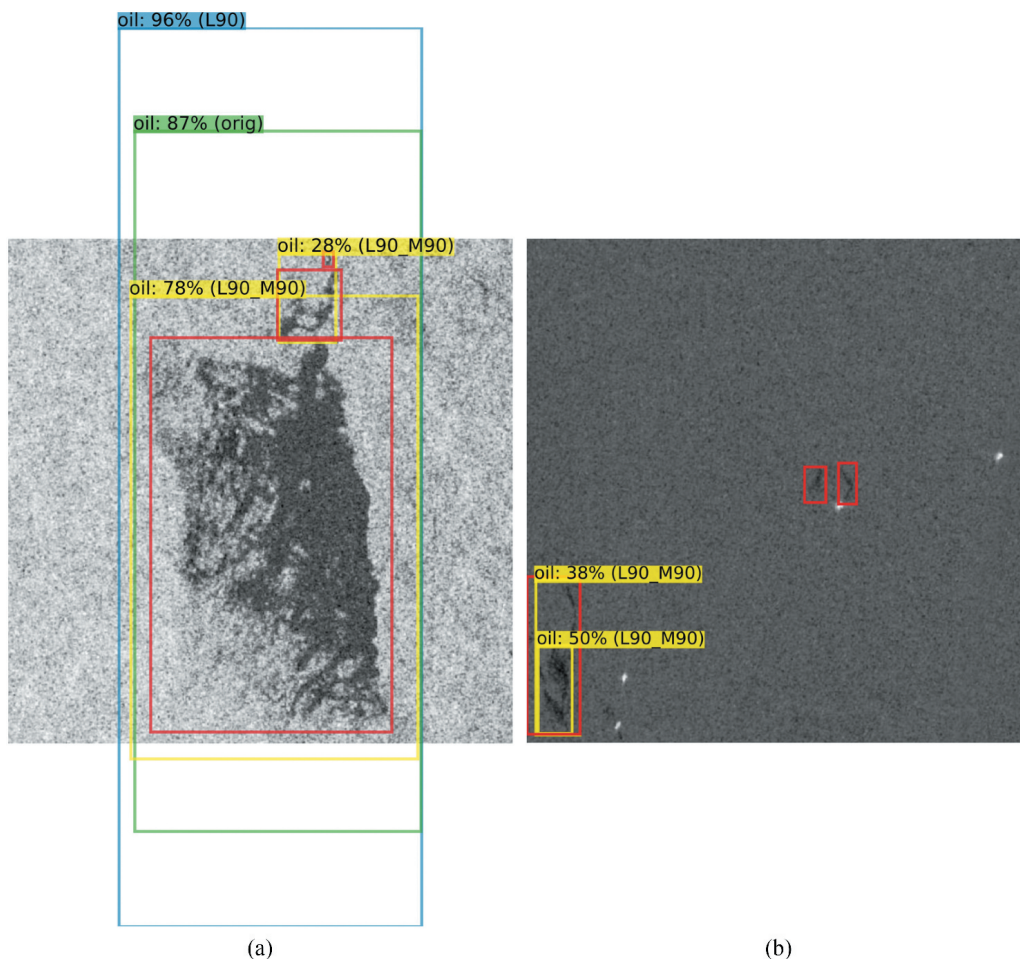


Figure 11. Examples of oil spills in (a) large and (b) medium subsets detected in different cases described in subsection 3.1. The red bounding boxes denote the manually inspected oil spills; the detection results are shown with different colors along with confidence scores. As detection results from the cases *orig* and *L90* show high consistency with the manual inspection in (b), the detections are not shown in the image to avoid confusion.

were tiled into several sub-images for training (see [Subsection 2.3](#)). With this approach, the model did not properly learn the entire shape of these oil spills and how they were separated from their surroundings. The IoU of the largest labelled oil object and detections from these two cases is 47.46% and 34.95%, respectively. On the other hand, the case *L90_M90* has IoU of 71.70% and 71.61% for the upper and bottom detections, respectively. As the case *L90_M90* included more medium oil spills, the ability of detecting margins seems to be improved. [Figure 11\(b\)](#) shows examples of small and medium oil spills. As predictions in cases *orig* and *L90* are similar to the manually labelled oil objects, only the case *L90_M90* is shown. Regarding the oil spill on the left-hand side, all the models detect it as two oil spills; one small bounding box covers the bottom part of oil spill and the other large one covers the whole oil spill. The IoU of the three detections covering the whole oil spill from cases *orig*, *L90* and *L90_M90* is 64.67%, 76.67% and 81.57%, respectively. Regarding the two oil spills in the middle, the model from case *orig* has respective IoU of 75.06% and 81.03% for the two oil spills (from left to right); the model from case *L90* has IoU of 74.60% and 79.77%, respectively. However, in the case *L90_M90* they were not detected.

In summary, by applying additional rotation augmentation on images with large and medium oil objects (i.e. case *L90_M90*), the detection of large oil spills has improved. It is likely that including data augmentation on differently shaped oil spills could help the performance of the object detector. However, in the dataset most of the large oil spills appear along with small oil spills, which means that the rotation data augmentation was also applied on some small oil objects. It is possible that the model was over-fitting on oil objects with similar shapes, especially for small oil spills, which usually appear as round shapes as shown in [Figure 12](#). As there are drawbacks for either the case *L90* or the case *L90_M90*, it was decided to not apply the additional data augmentation before further examination. A possible approach would be to apply additional data augmentation on oil

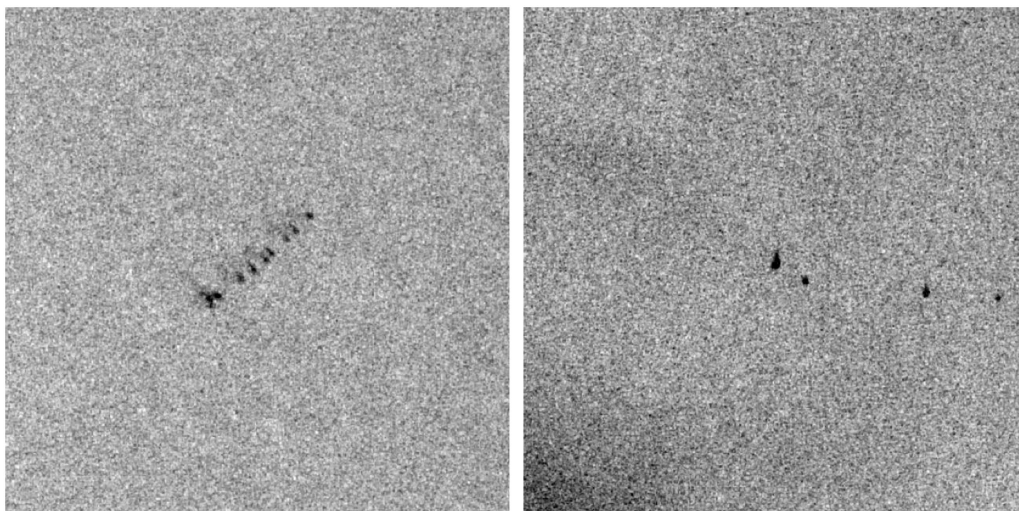


Figure 12. Examples of small round oil spills in the study area. The shown images cover areas of around 164 km² each.

spills with high complexity and to use fewer small round objects from the dataset and balancing different-sized oil objects, but the total amount of objects used for training should also be considered.

3.3. Oil spill detection with YOLOv4

According to subsection 3.1, objects regarded as tiny objects following Equation (1) with $T_{\text{tiny}} = 20$ px were removed. Though additional rotation augmentation was proven to be beneficial for large oil spill detection, it might cause over-fitting on small and medium oil spills based on the results in subsection 3.2; as a result, this technique was not applied in the following. YOLOv4 offers several built-in data augmentation techniques, which, unlike the rotation data augmentation discussed in the previous subsection, are applied to all input images. Overall, colour space data augmentation (e.g. saturation, exposure and hue values) seems to be beneficial in this study. Figure 13 shows the average loss calculated during the training in blue and the mean average precision (mAP) on the validation set in red after 1000 iterations. The average loss indicates the differences between the ground truth values and predicted values from the model. In general, the training stops after the average loss no longer decreases. Note that mAP is the mean of the AP on different classes. As only one class was in use, mAP is equal to AP in this study. The AP on the validation and test sets is 69.10% and 68.69%, respectively. The model performance is similar on the validation and test sets, which indicates that the object detector is not dependent on the given training or validation datasets.

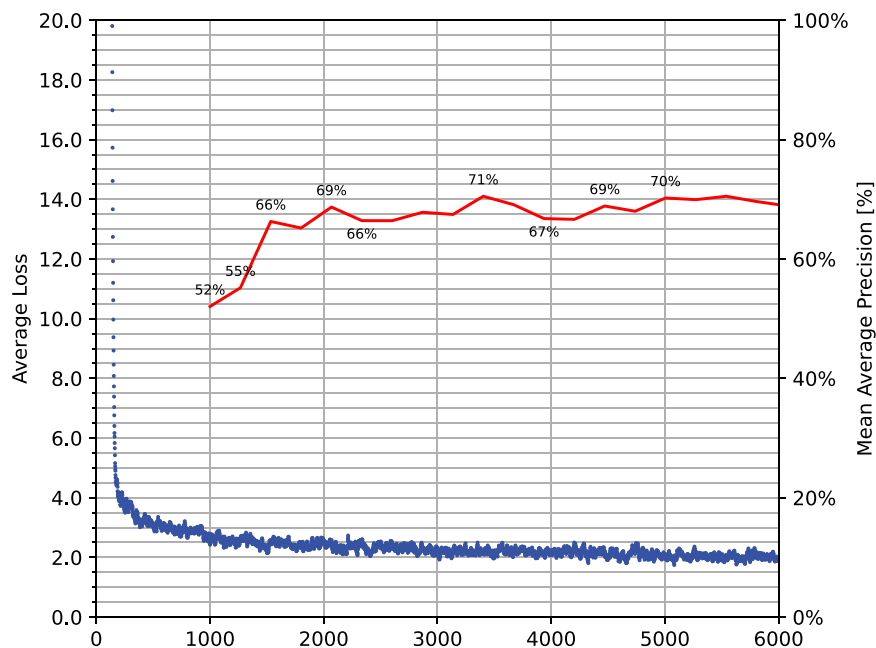


Figure 13. Average loss calculated during the training (blue), and AP on validation set (red) after 1000 iterations.

As mentioned in [subsection 2.4](#), one-stage object detection algorithms are usually considered to have high efficiency but low accuracy compared to two-stage methods. To evaluate the performance of the YOLOv4-based model, this study uses a two-stage object detection algorithm, Faster RCNN, as a baseline assessment. Faster RCNN with feature pyramid networks (FPN) as backbone was trained with the help of the Detectron2 framework, which is implemented in PyTorch (Wu et al. 2019). [Table 5](#) shows training information along with the AP on the validation and test sets of the two object detection algorithms. The iterative training was stopped when the average loss converged. As Faster RCNN requires more training iterations, it took almost double the time of YOLOv4. The Faster RCNN-based model has its AP on the training and validation sets of 70.33% and 70.26%, respectively. Comparing the two trained models, the performance seems to be similar; however, the faster training time of YOLOv4 is advantageous for development stage where training has to be performed several times.

In the following, various examples of oil spills detected by the YOLOv4-based model will be shown in [Figures 14–17](#). Manually inspected oil spills are denoted as red bounding boxes and the detection results are outlined in yellow along with confidence scores. Note that some oil spills are separately annotated as they are not actually connected, but may appear like a continuous oil spill in the figures due to scaling.

[Figure 14](#) shows examples of relatively long oil spills, which are generally detected. [Figure 14\(a,b\)](#) are examples of wide and long oil spills, which were detected similarly to the given annotations. Considering slim and long oil spills, [Figure 14\(c,d\)](#) show that they were not as confidently detected as the wider ones and their margins were not well detected. These kinds of oil spills usually cover a large area and form complicated shapes due to ocean currents (see also [Figure 6](#)). As previously explained (see [subsection 2.3](#)), slim and long oil spills were tiled into several sub-images in case the oil spills might otherwise be too thin for the model to learn and to detect. Therefore, the full shape of these kinds of oil spills was not well learned, especially as large oil spills only occupied 5.5% of the collected oil objects (see [Table 1](#)), so there were even less long and slim oil spills. As a result, especially long and slim oil spills were not as well detected as wider ones.

As mentioned in [section 1](#), small oil spills regularly occurred in the study area, so detecting oil spills of this kind is also an aim of this study. [Figure 15](#) shows examples of those oil spills, which were small but numerous. Note that there were some oil spills detected by the object detector but not annotated as they were regarded as tiny objects defined by Equation (1) with $T_{\text{tiny}} = 20$ px and removed from the annotations. It seems that the object detector possesses a good capability of detecting these small oil spills and it could actually detect tiny objects below the given T_{tiny} . Based on the comparisons

Table 5. Training information along with the AP of the trained models on the validation and test sets from YOLOv4 and Faster RCNN, the two well-known object detection algorithms.

Method	# Iteration	Training Time	AP@IoU=0.5%)	
			(val set)	(test set)
YOLOv4	6000	7.5 h	69.10	68.69
Faster RCNN	160,000	14 h	70.33	70.26

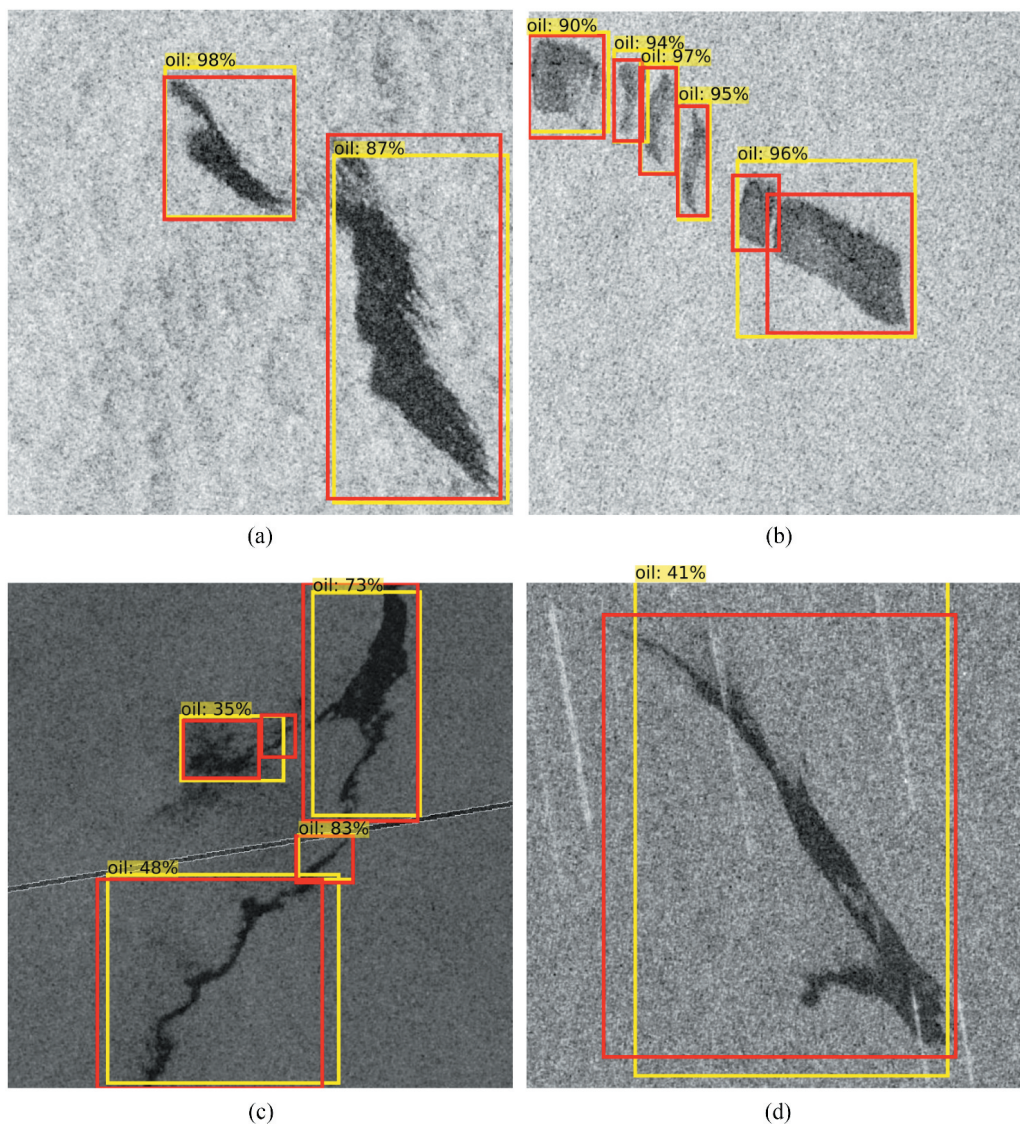


Figure 14. Examples of long oil spills detected by the trained object detector described in subsection 3.3. Some long and wide oil spills were well detected in (a) and (b); however, some slim oil spills were not confidently detected in (c) and (d).

between different T_{tiny} shown in subsection 3.1, applying $T_{\text{tiny}} = 20$ px resulted in the best AP. Objects are defined as tiny when either dimension is smaller than the given T_{tiny} in Equation (1). However, the aspect ratio of the object was not considered so that the model might be able to detect objects even if one dimension is smaller than T_{tiny} . Examining the behaviour of the model for detecting small oil objects more closely might help, such as providing some man-made oil objects with different sizes and aspect ratios and designing a more rigorous rule for tiny object definition.

Figure 16 shows examples of oil spills near look-alikes. In Figure 16(a), oil spills were detected well even with look-alikes nearby. However, it is not clear in Figure 16(b) if the object detector detected the oil spill correctly as it was covered by look-alikes. Note that in

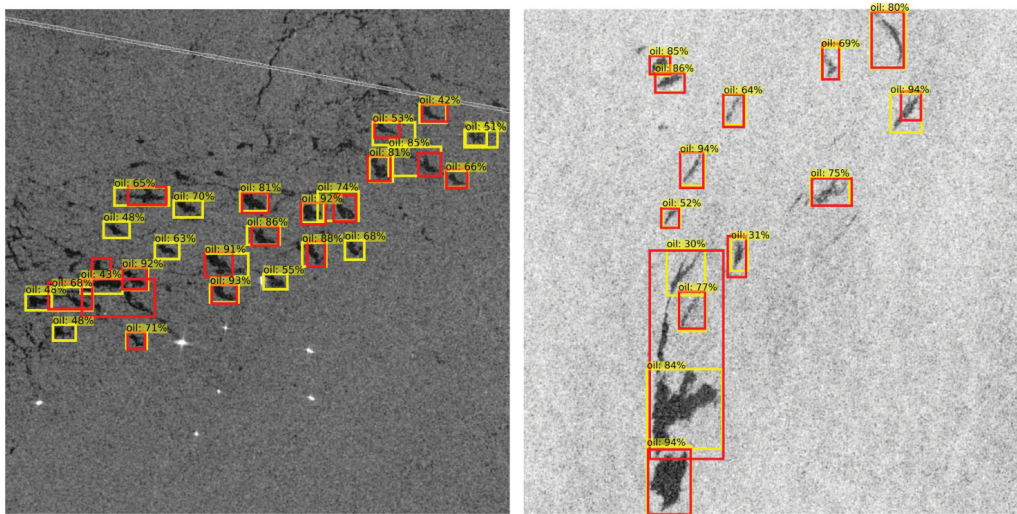


Figure 15. Examples of areas covering numerous small oil spills, which were mostly well detected. Note that some oil spills were detected by the trained object detector (in yellow) but not marked as manually inspected oil spills (in red). These oil spills satisfy the definition of tiny object in Equation (1) with $T_{\text{tiny}} = 20$ px and their annotations were removed.

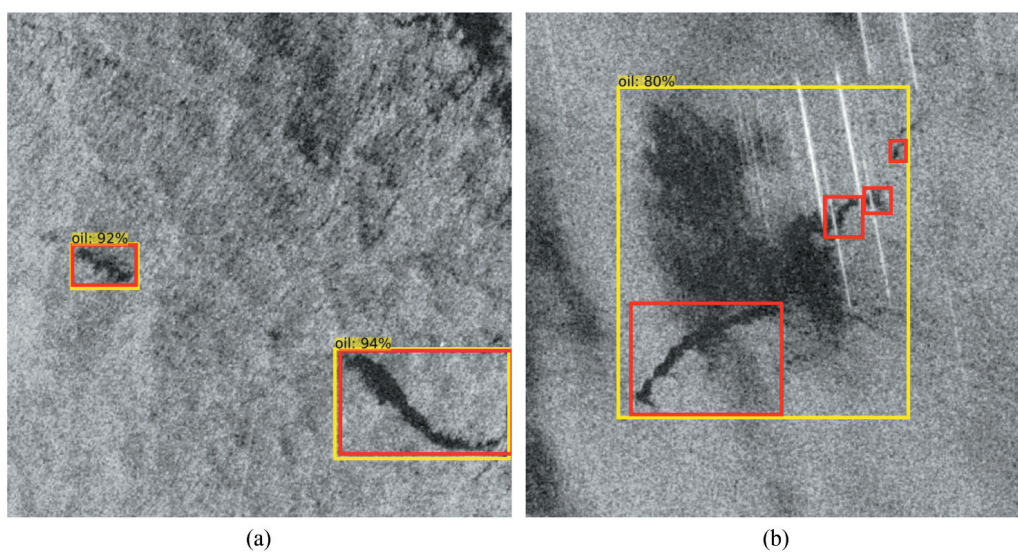


Figure 16. Examples of oil spills which appeared near look-alikes. Oil spills were well detected in (a), but it was not clearly if it detected oil spills or look-alikes in (b).

order to not mislead the model, oil spills covered by look-alikes were not annotated (as shown in the figure). As look-alikes were included in the dataset only when they appeared near oil spills, the trained detector might recognize only limited types of look-alikes. Increasing the amount of look-alikes used as background information during training might help improve the ability of distinguishing oil spills and look-alikes.

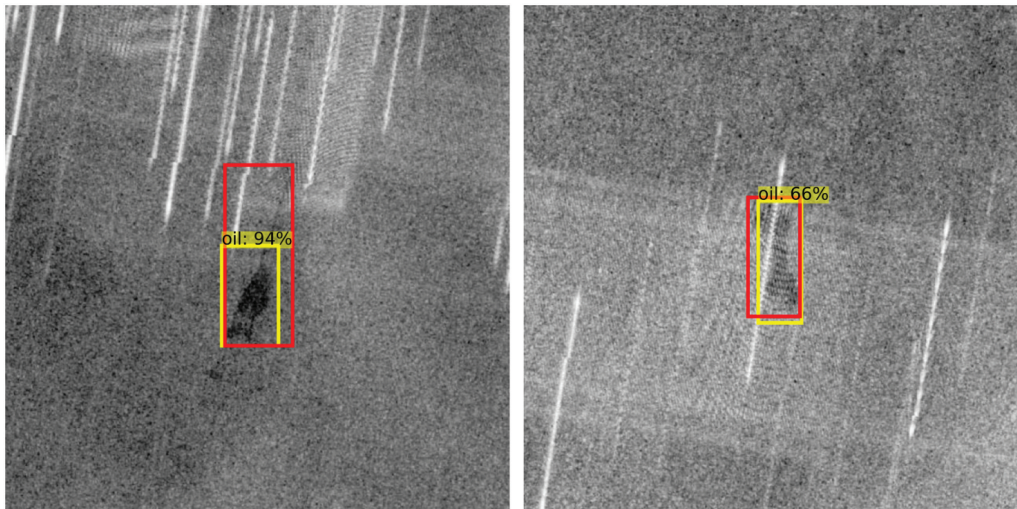


Figure 17. Examples of oil spills with interference caused by active transponders, which influence certain regions constantly. However, the object detector was still able to detect these oil spills well.

In the Eastern Mediterranean Sea, active transponders are commonly used for security reasons and interfere with the SAR signal, in some regions constantly. When the active transponders happen to be operating in similar frequency domain as SAR signal, it might lead to constructive or destructive interference. Figure 17 shows oil spills covered by these interfering signals. However, the object detector could still detect the main parts of the oil spills. Regular oil spills in certain areas are likely caused by the same or similar sources, which result in less complexity in types and shapes of oil spills. Hence, the object detector was able to learn and detect them well.

4. Discussion and conclusion


To tackle the need of an early warning system for detecting oil spills on a regular basis in the Eastern Mediterranean Sea, this study evaluated the possibility of using a YOLOv4-based object detection algorithm for automatic detection of oil spills. In this study, a total of 5930 Sentinel-1 scenes from 2015 to 2018 were used, which contain 9768 oil spills. After carrying out a variety of scenarios to find suitable parameters and data augmentation methods in subsections 3.1 and 3.2, the trained object detector was presented in subsection 3.3. The AP of the object detector, with IoU threshold equal to 50%, on the validation and test sets is 69.10% and 68.69%, respectively. Comparing it to the Faster RCNN-based model, which has AP of 70.33% and 70.26% on the validation and test sets, respectively, the two models have similar performance. However, training the Faster RCNN model took almost twice as long. In recent years, more studies have focused on machine learning and deep learning techniques using large amounts of SAR data. Some well-performing deep learning-based oil spill detection methods are discussed in the following. Note that different studies used different measures to evaluate the model performance, and the definitions of these measures may even be slightly different.

One previous study used a total of 1112 SAR images and trained with different semantic segmentation methods. IoU for different classes is used as performance metric in the study, and U-Net and DeepLabv3+ achieve IoU of 53.79% and 53.38% on the class oil spill, respectively (Krestenitis et al. 2019). Another study presented an improved DeepLabv3+ and used a total of 35 Sentinel-1 scenes; it obtains IoU of 91.58% for the class oil spill (Ma et al. 2022). One other study used 14 ALOS PALSAR and 7 Sentinel-1 scenes and trained the CBD-Net, where it reached 84.20% and 91.20% precision on datasets from the two different satellite missions, respectively (Zhu et al. 2022). As a small amount of images leads to a lack of complexity in types, shapes and backscatter values of oil spills in SAR images, the models trained with fewer images performed better than the ones with larger datasets. However, two previous studies applied Mask-RCNN on similar amounts of data (i.e. 2000–3000 images) and achieved 98.7% precision on oil spill detection and 65% mean IoU for different classes in (Yekeen and Balogun 2020) and (Emna et al. 2020), respectively. The various sources of oil spills, purposes of those studies and even the difficulties of obtaining ground truth oil spills make it difficult to compare the results from these different studies.

With reference to the previously mentioned studies, the trained oil spill detector has reasonably good performance, especially for detecting oil spills with different sizes and even when oil spills were covered by the interference of active transponders. However, long and slim oil spills as well as their extent were not confidently detected. As shown in subsection 3.2, it is hard to train a model which performs well with a wide variety of object sizes. Increasing the amount of long and slim oil spills and balancing different size oil spills used for training might help improve the model performance in future.

Oil spills near look-alikes were also distinguished well, but oil spills covered by look-alikes were not always clearly detected. It appeared that the model was misled as in these cases, it detected the whole look-alike and the oil spill covered by it as one big oil spill. In this study, all images used for training contained at least one oil object. This means the patterns of look-alikes were only learned when there were oil spills nearby, so that adding images with only look-alikes (i.e. without any annotation) into training as background information might help the object detector to differentiate better between oil spills and look-alikes caused by various sources.

The collected oil spills were mostly related to shipping routes, oil terminals and transboundary shipping ports, and depending on the circulation systems in different regions oil spills may drift differently. It is possible that the detector may have inferior performance in other areas, where the majority of oil spills originate from different sources (e.g. oil platforms and natural seepage). To detect oil spills in other regions, it is possible to apply transfer learning, which uses the knowledge of the existing model in new tasks. Instead of learning from scratch, the existing model will be regarded as a pre-trained model and further trained on additional datasets with oil spills of different origins. Likewise, the capability of the current detector on different SAR sensors cannot be guaranteed, but applying transfer learning for different SAR sensors is feasible and should be straightforward for C-band sensors (e.g. RADARSAT Constellation Mission). Nevertheless, the provided trained object detector is a suitable module to set up an oil spill surveillance system in the Eastern Mediterranean Sea. The results of this study are

4312  Y. -J. YANG ET AL.

the basis of an improved oil spill detector, which lays the ground for building an efficient early warning system in the near future.

Acknowledgements

This study is part of the DARTIS project, which was supported by the German Federal Ministry of Education and Research under Grant number 03F0823B. The authors wish to thank Copernicus for providing Sentinel-1 data on Open Access Hub. We would also like to thank ESA for developing SNAP and the user support provided on the Scientific Toolbox Exploitation Platform (STEP) forum. We are grateful to the developers and all the contributors of YOLOv4 for their wonderful work at <https://github.com/AlexeyAB/darknet>.

Disclosure statement

No potential conflict of interest was reported by the author(s).

Funding

The work was supported by the Bundesministerium für Bildung und Forschung [03F0823B].

ORCID

Yi-Jie Yang  <http://orcid.org/0000-0002-4098-8119>

References

- Abdulla, A. and O. Linden. 2008. *Maritime Traffic Effects on Biodiversity in the Mediterranean Sea: Review of Impacts, Priority Areas and Mitigation Measures*. Malaga, Spain: IUCN Centre for Mediterranean Cooperation .
- Al-Ruzouq, R., M. Barakat a Gibril, A. Shanableh, A. Kais, O. Hamed, S. Al-Mansoori, and M. Ali Khalil. 2020. "Sensors, Features, and Machine Learning for Oil Spill Detection and Monitoring: A Review." *Remote Sensing* 12 (20): 3338. doi:10.3390/rs12203338.
- Barale, V., J. Michel Jaquet, and M. Ndiaye. 2008. "Algal Blooming Patterns and Anomalies in the Mediterranean Sea as Derived from the SeaWiFS Data Set (1998-2003)." *Remote Sensing of Environment* 112 (8): 3300–3313. doi:10.1016/j.rse.2007.10.014.
- Bochkovskiy, A., C.-Y. Wang, and H.-Y. Mark Liao. 2020. "YOLOv4: Optimal Speed and Accuracy of Object Detection." *arXiv preprint arXiv:2004.10934*.
- Brekke, C. and A. H. Solberg. 2008. "Classifiers and Confidence Estimation for Oil Spill Detection in ENVISAT ASAR Images." *IEEE Geoscience and Remote Sensing Letters* 5 (1): 65–69. doi:10.1109/LGRS.2007.907174.
- Cartucho, J., R. Ventura, and M. Veloso. 2018. "Robust Object Recognition Through Symbiotic Deep Learning in Mobile Robots." In *2018 IEEE/RSJ International Conference on Intelligent Robots and Systems (IROS)*, Madrid, Spain, 2336–2341.
- Chang, Y.-L., A. Anagaw, L. Chang, Y. Chun Wang, C.-Y. Hsiao, and W.-H. Lee. 2019. "Ship Detection Based on YOLOv2 for SAR Imagery." *Remote Sensing* 11 (7): 786. doi:10.3390/rs11070786.
- Deng, J., W. Dong, R. Socher, L. Li-Jia, K. Li, and L. Fei-Fei. 2009. "ImageNet: A Large-Scale Hierarchical Image Database." In *2009 IEEE Conference on Computer Vision and Pattern Recognition*, Miami, FL, USA, 248–255. IEEE.

- Devadharshini, S., R. Kalaipriya, R. Rajmohan, M. Pavithra, and T. Ananthkumar. 2020. "Performance Investigation of Hybrid YOLO-VGG16 Based Ship Detection Framework Using SAR Images." In *2020 International Conference on System, Computation, Automation and Networking (ICSCAN)*, Pondicherry, India, 1–6.
- Emna, A., B. Alexandre, P. Bolon, M. Véronique, C. Bruno, and O. Georges. 2020. "Offshore Oil Slicks Detection from SAR Images Through the Mask-RCNN Deep Learning Model." In *2020 International Joint Conference on Neural Networks (IJCNN)*, Glasgow, UK, 1–8. IEEE.
- European Maritime Safety Agency. 2017. "The CleanSeaNet Service: Taking Measurements to Detect and Deter Marine Pollution." *Brochure*. <http://www.emsa.europa.eu/csn-menu/download/2913/2123/23.html>
- European Space Agency. 2020. "SNAP - ESA Sentinel Application Platform V8.0." <http://step.esa.int>
- Everingham, M., L. Van Gool, C. K. Williams, J. Winn, and A. Zisserman. 2010. "The PASCAL Visual Object Classes (VOC) Challenge." *International Journal of Computer Vision* 88 (2): 303–338. doi:10.1007/s11263-009-0275-4.
- Fiscella, B., A. Giancaspro, F. Nirchio, P. Pavese, and P. Trivero. 2000. "Oil Spill Detection Using Marine SAR Images." *International Journal of Remote Sensing* 21 (18): 3561–3566. doi:10.1080/014311600750037589.
- Ghorbani, Z. and A. H. Behzadan. 2021. "Monitoring Offshore Oil Pollution Using Multi-Class Convolutional Neural Networks." *Environmental Pollution* 289: 117884. doi:10.1016/j.envpol.2021.117884.
- Goutte, C. and E. Gaussier. 2005. "A Probabilistic Interpretation of Precision, Recall and F-Score, with Implication for Evaluation." In *Advances in Information Retrieval*, edited by D. E. Losada and J. M. Fernández-Luna, Vol. 3408, 345–359. 04. Berlin Heidelberg: Springer.
- Hovland, H. A., J. A. Johannessen, and G. Digranes. 1994. "Slick Detection in SAR Images." In *1994 IEEE International Geoscience and Remote Sensing Symposium (IGARSS)*, Pasadena, CA, USA, Vol. 4, 2038–2040.
- Hu, G. and C. Wen. 2021. "Traffic Sign Detection and Recognition Based on Improved YOLOv4 Algorithm." *International Journal of Computer Applications Technology and Research* 10 (6): 161–165. doi:10.7753/IJCATR1006.1006.
- Krestenitis, M., G. Orfanidis, K. Ioannidis, K. Avgerinakis, S. Vrochidis, and I. Kompatsiaris. 2019. "Oil Spill Identification from Satellite Images Using Deep Neural Networks." *Remote Sensing* 11 (15): 1762. doi:10.3390/rs11151762.
- Li, Y., H. Wang, L. M. Dang, T. N. Nguyen, D. Han, A. Lee, I. Jang, and H. Moon. 2020. "A Deep Learning-Based Hybrid Framework for Object Detection and Recognition in Autonomous Driving." *IEEE Access* 8: 194228–194239. doi:10.1109/ACCESS.2020.3033289.
- Ma, X., J. Xu, P. Wu, and P. Kong. 2022. "Oil Spill Detection Based on Deep Convolutional Neural Networks Using Polarimetric Scattering Information from Sentinel-1 SAR Images." *IEEE Transactions on Geoscience and Remote Sensing* 60: 1–13.
- Nieto-Hidalgo, M., A. Javier Gallego, P. Gil, and A. Pertusa. 2018. "Two-Stage Convolutional Neural Network for Ship and Spill Detection Using SLAR Images." *IEEE Transactions on Geoscience and Remote Sensing* 56 (9): 5217–5230. doi:10.1109/TGRS.2018.2812619.
- O'Hagan, C. 2007. "Use of GIS for Assessing the Changing Risk of Oil Spills from Tankers." In *Conference paper presented at 3rd Annual Arctic Shipping Conference, St Petersburg, Russia*, 17–20.
- Pavakis, P., D. Tarchi, and A. J. Sieber. 2001. On the monitoring of illicit vessel discharges using spaceborne SAR remote sensing - a reconnaissance study in the Mediterranean sea. In *Annales des Télécommunications*, Vol. 56 (11), 700–718. doi:10.1007/bf02995563.
- Polinov, S., R. Bookman, and N. Levin. 2021. "Spatial and Temporal Assessment of Oil Spills in the Mediterranean Sea." *Marine Pollution Bulletin* 167: 112338. doi:10.1016/j.marpolbul.2021.112338.
- Redmon, J., S. Divvala, R. Girshick, and A. Farhadi. 2016. "You Only Look Once: Unified, Real-Time Object Detection." In *2016 IEEE Conference on Computer Vision and Pattern Recognition (CVPR)*, Las Vegas, NV, USA, 779–788.
- REMPEC. 2002. *Towards Sustainable Development of the Mediterranean Region: Protecting the Mediterranean Against Maritime Accidents and Illegal Discharges from Ships*. Malta. <http://hdl.handle.net/20.500.11822/11254>.

- Ronci, F., C. Avolio, M. Di Donna, M. Zavagli, V. Piccialli, and M. Costantini. 2020. "Oil Spill Detection from SAR Images by Deep Learning." In *2020 IEEE International Geoscience and Remote Sensing Symposium (IGARSS)*, Waikoloa, HI, USA, 2225–2228. IEEE.
- Saadoun, I. M. 2015. Impact of Oil Spills on Marine Life Larramendy, Marcelo L., Soloneski, Sonia. *Emerging Pollutants in the Environment-Current and Further Implications*. Rijeka, Croatia: IntechOpen. p. 75–105. doi:10.5772/60455.
- Shaban, M., R. Salim, H. Abu Khalifeh, A. Khelifi, A. Shalaby, S. El-Mashad, A. Mahmoud, M. Ghazal, and A. El-Baz. 2021. "A Deep-Learning Framework for the Detection of Oil Spills from SAR Data." *Sensors* 21 (7): 7 doi:10.3390/s21072351.
- Singha, S., T. J. Bellerby, and O. Trieschmann. 2013. "Satellite Oil Spill Detection Using Artificial Neural Networks." *IEEE Journal of Selected Topics in Applied Earth Observations and Remote Sensing* 6 (6): 2355–2363. doi:10.1109/JSTARS.2013.2251864.
- Singha, S., R. Ressel, D. Velotto, and S. Lehner. 2016. "A Combination of Traditional and Polarimetric Features for Oil Spill Detection Using TerraSAR-X." *IEEE Journal of Selected Topics in Applied Earth Observations and Remote Sensing* 9 (11): 4979–4990. doi:10.1109/JSTARS.2016.2559946.
- Solberg, A. H. S. 2012. "Remote Sensing of Ocean Oil-Spill Pollution." *Proceedings of the IEEE* 100 (10): 2931–2945. doi:10.1109/JPROC.2012.2196250.
- Solberg, A. H. S. and R. Solberg. 1996. "A Large-Scale Evaluation of Features for Automatic Detection of Oil Spills in ERS SAR Images." In *1996 IEEE International Geoscience and Remote Sensing Symposium (IGARSS)* Lincoln, NE, USA, Vol. 3, 1484–1486.
- Solberg, A. H. S., G. Stovrik, R. Solberg, and E. Volden. 1999. "Automatic Detection of Oil Spills in ERS SAR Images." *IEEE Transactions on Geoscience and Remote Sensing* 37 (4): 1916–1924. doi:10.1109/36.774704.
- Stevens, J. 2020. "NASA Earth Observatory Map." Accessed 8 September 2020. <https://visibleearth.nasa.gov/images/147190/explorer-base-map>
- Surkes, S. 2021. "Satellite Images of Oil Slicks off Coast Show Recent Spill Far from a One-Off." *The Times of Israel*, February 28 <https://www.timesofisrael.com/satellite-images-of-oil-slicks-off-coast-show-recent-spill-far-from-a-one-off/>
- Topouzelis, K. N. 2008. "Oil Spill Detection by SAR Images: Dark Formation Detection, Feature Extraction and Classification Algorithms." *Sensors* 8 (10): 6642–6659. doi:10.3390/s8106642.
- Topouzelis, K. and A. Psyllos. 2012. "Oil Spill Feature Selection and Classification Using Decision Tree Forest on SAR Image Data." *ISPRS Journal of Photogrammetry and Remote Sensing* 68: 135–143. doi:10.1016/j.isprsjprs.2012.01.005.
- Tzutalin. 2015. "Labellimg." <https://github.com/tzutalin/labellimg>
- Wang, C.-Y., A. Bochkovskiy, and H.-Y. Mark Liao. 2021. "Scaled-YOLOv4: Scaling Cross Stage Partial Network." In *Proceedings of the IEEE/CVF Conference on Computer Vision and Pattern Recognition (CVPR)* Nashville, TN, USA, June, 13029–13038.
- Wang, C.-Y., H.-Y. Mark Liao, W. Yueh-Hua, P.-Y. Chen, J.-W. Hsieh, and I.-H. Yeh. 2020. "CSPnet: A New Backbone That Can Enhance Learning Capability of CNN." In *Proceedings of the IEEE/CVF Conference on Computer Vision and Pattern Recognition Workshops* Seattle, WA, USA, 390–391.
- Woodhouse, I. H. 2006. *Introduction to Microwave Remote Sensing*. Boca Raton, FL, USA: CRC press.
- Wu, Y., A. Kirillov, F. Massa, L. Wan-Yen, and R. Girshick. 2019. "Detectron2." <https://github.com/facebookresearch/detectron2>
- Yang, Y.-J., S. Singha, and R. Mayerle. 2021. "Fully Automated SAR Based Oil Spill Detection Using YOLOv4." In *2021 IEEE International Geoscience and Remote Sensing Symposium (IGARSS)* Brussels, Belgium, 5303–5306.
- Yekeen, S.T. and A.L. Balogun. 2020. "Automated Marine Oil Spill Detection Using Deep Learning Instance Segmentation Model." *The International Archives of Photogrammetry, Remote Sensing and Spatial Information Sciences* 43: 1271–1276. doi:10.5194/isprs-archives-XLIII-B3-2020-1271-2020.
- Zhu, Q., Y. Zhang, Z. Li, X. Yan, Q. Guan, Y. Zhong, L. Zhang, and D. Li. 2022. "Oil Spill Contextual and Boundary-Supervised Detection Network Based on Marine SAR Images." *IEEE Transactions on Geoscience and Remote Sensing* 60: 1–10.

4.2 Automated oil spill detection and early warning system

After verifying the applicability of the object detection algorithm to oil spill detection, an automated oil spill detection and early warning system was developed following the approach proposed in Section 1.4 (see Figure 1.8). Based on the trained oil object detector, a YOLO-based Oil Detection Algorithm (YODA) was developed to use different strategies to search the entire SAR scene(s) for oil slicks. The detected oil slicks are then sent to a segmentation method that generates binary masks showing their exact locations. Finally, the trajectory of the oil slicks is simulated to provide decision makers to plan the oil spill response. A detailed description of the entire system and its performance on one year data in 2019 is included in the paper presented in this section. The citation to the paper is given as follows:

Yang, Y.-J., Singha, S., & Goldman, R. (2024). A Near Real-Time Automated Oil Spill Detection and Early Warning System Using Sentinel-1 SAR Imagery for the Southeastern Mediterranean Sea. *International Journal of Remote Sensing*, 45(6), 1997–2027. doi: 10.1080/01431161.2024.2321468

The manuscript is published. The following states the contributions made by the candidate to this paper:

The candidate developed several parts of the system, from the automated download of Sentinel-1 scenes to the delivery of oil binary masks. She also further improved the custom-trained object detector from the paper shown in Section 4.1 and evaluated the performance of YODA with different detectors and in different regions. The performance evaluation used oil slicks in 2019. The manual inspection and annotation of them were done together with a co-author. In addition, she collected continuous SAR observations over the same oil slicks, and compared them with the estimated oil trajectory provided by a co-author.



A near real-time automated oil spill detection and early warning system using Sentinel-1 SAR imagery for the Southeastern Mediterranean Sea

Yi-Jie Yang^{ib a,b}, Suman Singha^{ib a,c} and Ron Goldman^d

^aMaritime Safety and Security Lab, Remote Sensing Technology Institute, German Aerospace Center (DLR), Bremen, Germany; ^bResearch and Technology Centre Westcoast, Kiel University, Büsum, Germany; ^cNational Centre for Climate Research (NCKF), Danish Meteorological Institute (DMI), Copenhagen, Denmark; ^dIsrael Marine Data Center (ISRAMAR), Israel Oceanographic and Limnological Research (IOLR), Haifa, Israel

ABSTRACT

The ecological and environmental impact of marine oil pollution underlines the importance and necessity of an oil spill surveillance system. This study proposes an operational automated oil spill detection and early warning system to help take quick action for oil combating operations. Oil slicks in the spaceborne Sentinel-1 synthetic aperture radar (SAR) data are detected by a trained deep learning-based oil object detector. These detected oil objects are segmented into binary masks based on the similarity and discontinuity of the backscattering coefficients, and their trajectory is simulated. The detection process was tested on one-year SAR acquisitions in 2019, covering the Southeastern Mediterranean Sea; the false discovery rate (FDR) and false negative rate (FNR) are 23.3% and 24.0%, respectively. The system takes around 1.5 h from downloading SAR images to providing slick trajectory simulation. This study highlights the capabilities of using deep learning-based techniques in an operational oil spill surveillance service.

ARTICLE HISTORY

Received 30 October 2023
Accepted 11 February 2024

KEYWORDS

SAR; oil pollution; near real-time oil spill detection; deep learning; oil slick trajectory simulation

1. Introduction

The spreading and drifting of marine oil slicks can impact aquatic wildlife in large areas and have long-term biological and ecological consequences. A spill of 1 ton of oil can cover a radius of 50 m with a thickness of 10 mm within 10 min; as it continues spreading, even such a small spill could influence an area of around 12 km² before it disintegrates into smaller fragments (El-Magd et al. 2020). To reduce the negative impact of a spill, counter-measures should be applied as soon as possible. A near real-time (NRT) detection system is necessary to enable such a rapid response. Due to its high maritime traffic, the Eastern Mediterranean Sea is known as an oil pollution 'hotspot' and a vital oil transit centre (Kostianoy, Kostianaia, and Soloviev 2020; Polinov, Bookman, and Levin 2021; Zodiatis, Coppini, et al. 2017). This makes an oil spill surveillance system increasingly necessary.

CONTACT Yi-Jie Yang ✉ yi-jie.yang@dlr.de; yi-jie.yang@mailbox.org 📧 Maritime Safety and Security Lab, Remote Sensing Technology Institute, German Aerospace Center (DLR), Am Fallturm 9, Bremen 28359, Germany

© 2024 The Author(s). Published by Informa UK Limited, trading as Taylor & Francis Group.

This is an Open Access article distributed under the terms of the Creative Commons Attribution License (<http://creativecommons.org/licenses/by/4.0/>), which permits unrestricted use, distribution, and reproduction in any medium, provided the original work is properly cited. The terms on which this article has been published allow the posting of the Accepted Manuscript in a repository by the author(s) or with their consent.

Remote sensing is widely used for oil spill detection since it acquires information without physical contact. These sensors can be categorized into optical and microwave sensors, and they are usually equipped on shipborne, airborne or spaceborne platforms. Optical images are likely to be influenced by weather conditions and daylight; thus, microwave sensors, such as spaceborne synthetic aperture radar (SAR) and side-looking airborne radar (SLAR), are preferable for a regular surveillance system. With a lower cost for observing a larger area, spaceborne SAR is commonly used in the field. Oil dampens gravity-capillary waves and reduces radar backscatter, resulting in dark formations in SAR scenes. However, other phenomena, such as algae, low wind areas, wind sheltering, and eddies, also manifest as dark regions and are regarded as 'look-alikes' (Hovland, Johannessen, and Digranes 1994; Topouzelis 2008). A previous study showed the possible short- and long-term contribution of oil spills on phytoplankton blooms (Tang et al. 2019), highlighting the importance of distinguishing algae and oil spills in polluted hotspots.

Conventional oil slick detection in SAR images includes dark formation segmentation, feature extraction and classification of oil slicks and look-alikes (Solberg and Solberg 1996). Dark formations are first separated from their surroundings, and their features are then extracted to identify the difference between oil slicks and look-alikes. Previous studies applied artificial neural networks (ANN) to learn features and search for the best feature combinations to classify oil slicks and look-alikes (Mera, Veronica Bolon-Canedo, and Alonso-Betanzos 2017; Stathakis, Topouzelis, and Karathanassi 2006). However, the radar complexity, source and age of oil spills, and weather conditions make it difficult to segment dark formations correctly (Mera, Veronica Bolon-Canedo, and Alonso-Betanzos 2017; Topouzelis et al. 2007). Therefore, some studies segmented dark formations with one ANN and extracted features for classification with another ANN (Singha, Bellerby, and Trieschmann 2013; Topouzelis et al. 2007). Previous studies highlighted the advantages of quad-polarimetric and dual-polarimetric HH-VV SAR observations on discriminating oil slicks from look-alikes (Migliaccio, Nunziata, and Buono 2015; Singha et al. 2016); however, the limited acquisitions of these polarimetric data make it hard to apply in an operational system.

With a large amount of accessible SAR data after the advent of the Sentinel-1 mission by the European Space Agency (ESA) in 2014 and the increasing computational capability, deep learning algorithms have been increasingly applied in oil slick detection. Instead of classifying certain dark formations as oil spills or look-alikes, a previous study applied semantic segmentation methods to categorize each pixel into one of the following classes: sea surface, oil spill, look-alike, ship or land (Krestenitis et al. 2019). There were 1112 Sentinel-1 SAR images with 1250×650 px used, and different models, such as UNet, LinkNet, PSPNet, DeepLabv2 and DeepLabv3+, were compared. However, another study pointed out that oil spills only represented around 1.2% of the total pixels, which might lead to hindrances in directly applying the semantic segmentation method to entire SAR scenes (Shaban et al. 2021). Therefore, the authors proposed a two-step approach; each image patch was classified by Convolutional Neural Networks (CNN), and patches with more than 1 pixel containing oil spills were fed to UNet for segmentation. Another study followed similar procedures but integrated oil spill classification and segmentation into a single framework by applying multi-task Generative Adversarial Networks (GANs) (Fan and Liu 2023).

Applying machine learning techniques can help reduce the work of human interpretation. However, extending the techniques from a limited dataset to an operational service is challenging. For studies using pixel-wise classification or semantic segmentation, one advantage is that the exact locations covered with oil are predicted; however, applying them to an operational service might be computationally intensive as they classify each pixel of the given images, which are the entire SAR scenes. Therefore, previous studies have utilized the oil spill detection tool provided in the Sentinel Application Platform (SNAP) toolbox, which identifies suspicious dark formations with thresholding and generates image patches containing areas of interest (Dhavalikar and Choudhari 2022; El-Magd et al. 2021). After obtaining the image patches, the authors applied dark spot detection, feature extraction and classification methods to acquire the final detections of oil slicks (Dhavalikar and Choudhari 2022).

This study proposes a different approach: The entire SAR scenes are cropped into image patches with preferable dimensions by using sliding windows, and a trained deep learning-based oil object detector examines these patches to retrieve oil slicks. Afterwards, a segmentation method separates the slicks and their surroundings to obtain the exact areas covered with oil. Previous studies have proven the capabilities of applying object detection algorithms, such as faster region-based CNN (Faster RCNN) and You Only Look Once version 4 (YOLOv4), for oil slick detection (Huang et al. 2022; Yang, Singha, and Mayerle 2022). The proposed oil slick detection system integrates into an early warning system, which helps estimate oil-contamination regions and aids in planning an oil combatting response. The European Maritime Safety Agency (EMSA) has provided an NRT 'CleanSeaNet' service since 2007; the operators assess images, identify the possible pollution and send alerts to national authorities (Carpenter 2016; European Maritime Safety Agency 2017; Singha, Vespe, and Trieschmann 2013). Such a service also contributed to a decision support system, which provides oil slick prediction models to assist the response agencies (Zodiatis et al. 2016). This study aims to provide a fully automated system which only requires the operators to confirm the results before sending alerts to its users.

The paper first introduces the structure of the surveillance system in [Section 2](#). Detailed information about the satellite data is shown in [Subsection 2.1](#). [Subsection 2.2](#) introduces a custom-trained object detector from a previous study and explains the improvements done in this study. The utilization of the trained object detector and the segmentation method for oil binary mask generation are described in [Subsection 2.3](#). The explanation of oil trajectory simulation is given in [Subsection 2.4](#). [Subsection 3.1](#) then evaluates the performance of the system and discusses its advantages and disadvantages in different circumstances. The model simulations for oil trajectory are compared to SAR observations as a validation study in [Subsection 3.2](#). Afterwards, [Subsection 3.3](#) demonstrates the operational system and provides a latency test. Finally, [Section 4](#) summarizes the outlook and limitations of the system and outlines possible future implementations.

2. Methodology

[Figure 1](#) shows the structure of the oil spill detection and early warning system, which contains five subsystems: satellite data processing, oil spill detection, forecasts of synoptic conditions, oil slick trajectory simulation and web interface. In the satellite data

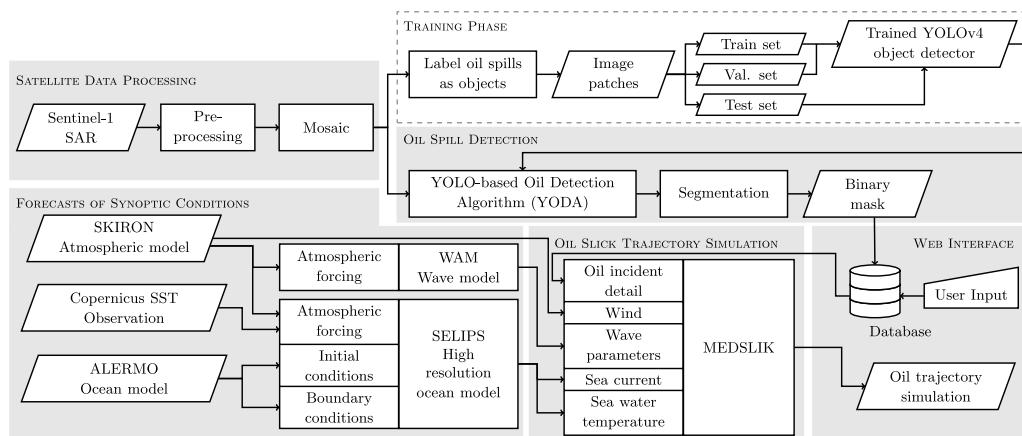


Figure 1. Structure of the oil spill detection and early warning system using the object detector from the training phase and comprising five subsystems: satellite data processing, oil spill detection, forecasts of synoptic conditions, oil slick trajectory simulation and web interface (see [Subsection 2](#) for detailed explanation).

processing subsystem, Sentinel-1 SAR data is acquired and preprocessed with a series of corrections, and the latest coverage of preprocessed SAR over the study area is generated as a mosaic to make it easier to help visualize the whole area and understand the relationship between acquisitions better. [Subsection 2.1](#) covers the information on Sentinel-1 data and the processing details.

Afterwards, the mosaic is delivered to the oil spill detection subsystem, including a YOLO-based oil detection algorithm (YODA) and a segmentation method. YODA automatically generates image patches, examines these image patches with an object detector from the training phase, and returns detections. The details about training the object detector are explained in [Subsection 2.2](#), and the strategy of detecting oil spills over the whole study area is described in [Subsection 2.3.1](#). However, as the detections are defined by bounding boxes, not the exact region covered by oil slicks, the bounding boxes of detections are turned into binary masks by the segmentation method described in [Subsection 2.3.2](#). Subsequently, the simulations of the oil slick trajectory and fate are performed by the MEDSLIK model (Zodiatis et al. 2012), which uses daily forecasts of synoptic conditions and the oil slick binary masks; detailed information regarding oil trajectory simulation is explained in [Subsection 2.4](#). The oil slick trajectory simulation subsystem is connected to an online interface, which enables decision-makers to perform simulations with their annotations and information and visualize the results; examples of the web interface are shown in [Subsection 3.3](#). The results can be exported as geographic information system (GIS) compliant files, allowing users to display them with their preferred software. The system is currently running in the pre-operational phase.

The whole system focuses on the area between longitudes 31.5–36°E and latitudes 31–33.7°N in the Southeastern Mediterranean Sea defined by the dashed boundary in [Figure 2](#), where the ocean circulation model for simulating oil trajectory is applicable. However, to increase the number of oil objects for training the detector, satellite data is collected in an enlarged area with longitude and latitude extended to the west at 30°E and north at 34.7°N, respectively (i.e. the solid boundary in the figure). The heat map in

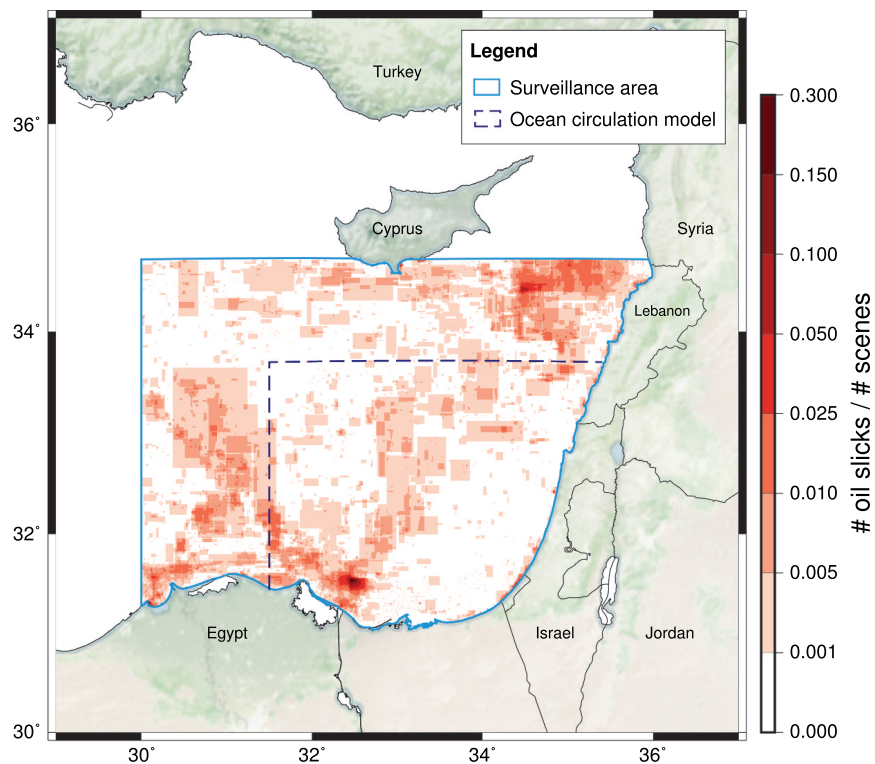


Figure 2. Study area map showing the extent of used data and model, along with a heatmap showing the chance of each pixel containing oil slicks collected from 2015 to 2018 in the previous study (Yang, Singha, and Mayerle 2022). The solid and dashed boundaries define the extent of sentinel-1 SAR acquisitions automatically downloaded by the system and the applicable area for oil trajectory simulation, respectively. Note that the oil slicks were defined by rectangular bounding boxes showing their extents but not the exact coverage. The base map and borders were obtained from Stevens (2020) and Wessel and Smith (1996), respectively.

Figure 2 illustrates the chance of oil slicks occurring in a Sentinel-1 SAR observation on each location based on a collection of manually inspected oil objects from 2015 to 2018 described in the previous study (Yang, Singha, and Mayerle 2022). As each SAR acquisition covers only part of the surveillance area, the number of scenes covering each location varies. There were at least 240, at most 755 and an average of 402 scenes covering each location from 2015 to 2018. Therefore, each pixel value on the heat map shows the ratio of the number of collected oil objects and the number of scenes covering that pixel.

2.1. Satellite data processing subsystem

Sentinel-1 SAR Level-1 Ground Range Detected (GRD) products are obtained from Copernicus Open Access Hub. Without a special subscription, the data is usually available within 24 hours after observation (European Space Agency 2013). Sentinel-1 SAR was a constellation of two satellites, Sentinel-1A and Sentinel-1B. However, after the Sentinel-1B anomaly on 23 December 2021, ESA and the European Commission (EC) announced the end of the Sentinel-1B mission on 3 August 2022 (European Space Agency 2022a). Thus, the current Sentinel-1 mission includes only Sentinel-1A data,

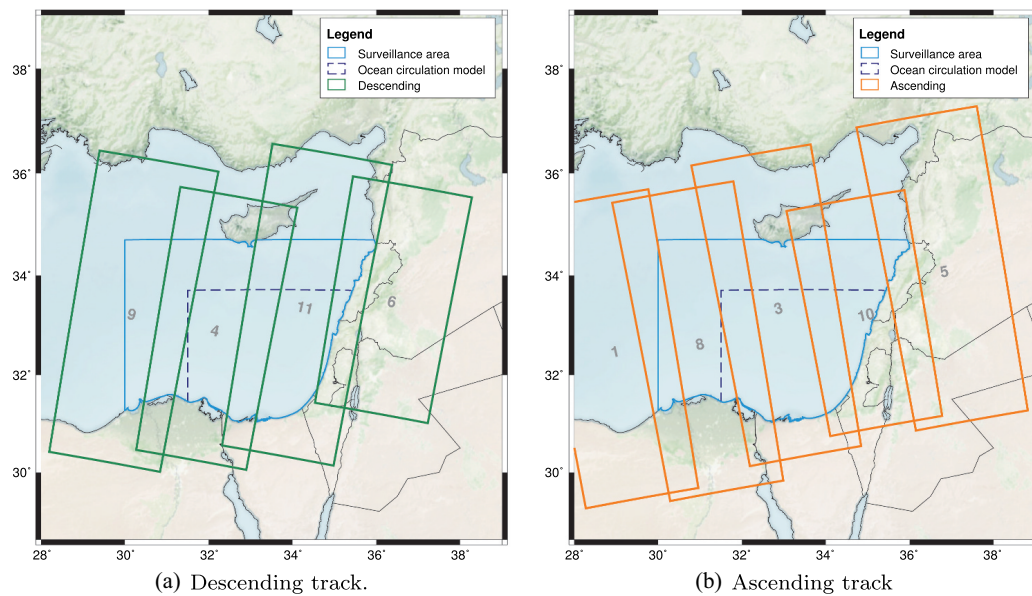


Figure 3. Coverage of sentinel-1A tracks in the study area defined in Figure 2, along with the estimated passing day index starting with 24 December 2021 in a 12-day period (i.e. 24 December 2021 has day index 1). The descending tracks pass the study area at around 03:30–04:05 UTC and the ascending ones pass at around 15:30–16:05 UTC.

and the revisiting period increased from 6 to 12 days. Figure 3 indicates the coverage of Sentinel-1A tracks over the study area along with the passing day index in a 12-day period starting with 24 December 2021 (i.e. the passing day index of 24 December 2021 is 1). The descending and ascending tracks pass the study area at around 03:30–04:05 and 15:30–16:05 UTC, respectively; they are usually available on Copernicus Data Hub at around 22:00 UTC. With the plan for the future launch of Sentinel-1C and Sentinel-1D (European Space Agency 2022b), it is worthwhile to have an operational system relying on the Sentinel-1 mission. However, adapting the system for using other SAR missions is also possible.

After download, Sentinel-1 SAR data is preprocessed with a series of corrections, including border noise removal, thermal noise removal, calibration, ellipsoid correction and conversion to decibels (dB). These are applied automatically using the SNAP Python API provided by ESA (European Space Agency 2020). Afterwards, a mosaic of different preprocessed scenes covering the study area is generated to make it easier to check the location of the new coming scenes by comparing them with the previous ones. Skipping the mosaic step and directly working on preprocessed images in SAR geometry is also possible. However, in the training stage and the pre-operational phase of the system, mosaics provide a more straightforward way for experts in different fields to compare SAR with additional information (e.g. wind speed). Therefore, the training phase and the oil spill subsystem use mosaics as input.

2.2. Training phase

In a previous study (Yang, Singha, and Mayerle 2022), oil slicks inside mosaics were examined and manually annotated as oil objects with bounding boxes with a total of 9768 oil objects

from 2015 to 2018; they were collected in *oil set*. Based on the positions of these oil objects, the original mosaics were cropped into image patches with dimensions of $N \times N$ px, where N equals the maximum of the model input size (i.e. 640×640 px) and the edge lengths of the object bounding box. Afterwards, these labelled image patches were used to custom train the deep learning-based YOLOv4 object detection algorithm (Bochkovskiy, Wang, and Liao 2020) on one-class objects (i.e. oil objects). A final detector reached an average precision (AP) on the validation and test sets of 69.10% and 68.69%, respectively.

During training, the detector learns the features of objects and negative samples where no object is located. However, each image patch contained at least one oil object; hence, the detector only learned the patterns of look-alikes and the background signatures when there were oil objects nearby. In the preliminary stage of this study, applying the object detector trained with only *oil set* to YODA returned false detections focusing on dark signatures which were not oil slicks. To further improve the detector on targeting only oil slicks but not look-alikes, besides *oil set*, image patches without oil objects but with look-alikes or other remarkable signatures (e.g. radio frequency interference) were collected as *no-oil set* and used for training. Note that image patches in *no-oil set* were not given any annotation but were regarded as negative samples for object detectors to learn. Figure 4 gives some examples of these image patches. Take the left-most image patch as an example, the darker pixels show look-alikes, and the brighter pixels show clean sea surfaces; both are learned as negative samples. Therefore, though *no-oil set* did not intentionally collect clean sea surfaces, they were considered and learned in training. Table 1 shows the numbers of image patches in *oil set* and *no-oil set*.

Data augmentation is commonly applied to increase the amount of data for training. The previous study has shown the improvement of object detectors trained with additional augmented datasets in detecting larger oil objects. However, it performed worse in targeting smaller oil objects; thus, the study suggested further examinations before applying data augmentation. In this study, the trained object detector is applied to YODA; hence how data augmentation might help is also examined by

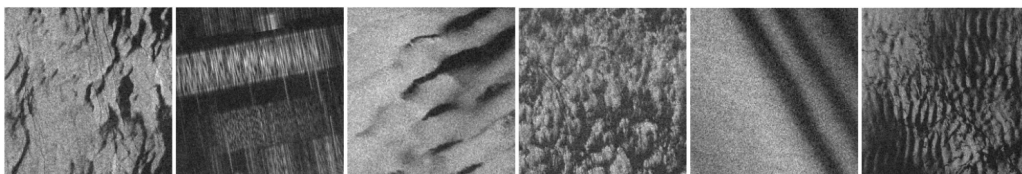


Figure 4. Examples of image patches from the *no-oil set* showing look-alikes and other remarkable features.

Table 1. Numbers of image patches collected in the *oil set* and *no-oil set*.

Dataset	# Image patches	
	<i>oil set</i>	<i>no-oil set</i>
training	4273	4369
validation	1218	1245
test	576	747

comparing the performance of YODA with using different object detectors. An additional augmented dataset was obtained from the rotation of image patches in *oil set* and *no-oil set* by 90°, 180° and 270°. To ensure the dataset for performance evaluation is not used in the training phase, mosaics in 2019 were inspected jointly by two experienced human interpreters, and the annotations are used as ground truth for comparison in [Section 3](#).

According the previous study (Yang, Singha, and Mayerle 2022), object detectors have their limitation on targeting tiny objects, which were defined as:

$$\begin{aligned} \text{if } & h_{\text{obj}} < h_{\text{img}} \cdot T_{\text{tiny}}/h_{\text{model}}[\text{px}] \cup \\ & w_{\text{obj}} < w_{\text{img}} \cdot T_{\text{tiny}}/w_{\text{model}}[\text{px}] \\ \Rightarrow & \text{Obj} \in \text{Obj}_{\text{tiny}}, \end{aligned} \quad (1)$$

where h_{obj} , h_{img} and h_{model} respectively refer to the heights of the object, image and object detector model input; w refers to the corresponding width. T_{tiny} is a threshold for defining tiny objects, it was revealed that tiny objects with $T_{\text{tiny}} = 20\text{px}$ were difficult to be detected by the object detector. Therefore, the threshold T_{tiny} is also applied in this study.

2.3. Oil spill detection subsystem

In the oil spill detection subsystem, YODA examines mosaics with an object detector from the training phase. The strategies of applying such a detector to target oil objects inside mosaics automatically and the followed-by segmentation method are explained in the following.

2.3.1. YODA

Generally, the dataset used in the training phase should be representative of the actual tasks in operation. For instance, if oil objects mostly occupy areas of around $128 \times 128\text{px}$, however, the dimensions of images used for the training and operational phases are $640 \times 640\text{px}$ and $10240 \times 10240\text{px}$, respectively, then the detector is likely to perform poorly in operation. Thus, YODA first generates image patches from mosaic results by sliding windows with default dimensions of $640 \times 640\text{px}$ and $1280 \times 1280\text{px}$ and their corresponding sliding distances of 600px and 1200px , respectively. These image patches are rescaled to 8-bit with pixel values from 0 to 255 in order to eliminate the difference among backscatter values of different acquisitions and to optimize the processing time (Bayramov, Kada, and Buchroithner 2018); note that this procedure was executed in the training phase as well.

After the initial image patches are generated, the trained object detector goes through all these patches to find oil objects inside. The detections are examined again with regard to being too close to the border of the image patches or covering an area of more than 75% of the respective image patch. In the former case, another image patch will be generated with the detected object in the centre of the image; in the latter case, an enlarged image patch will be used. Several iterations are executed automatically until all the detections fit the criteria. The performance of YODA is evaluated by comparing the final detections with the manual inspections in 2019 and shown in [Subsection 3.1](#).

2.3.2. Segmentation section

After obtaining detections from YODA, they are segmented into binary masks, defining the exact locations covered by oil. Figure 5 summarizes the procedures in YODA and illustrates the segmentation approach. As the detector defines slick boundaries inaccurately in some cases, the bounding boxes of the detections are extended in each direction by a certain ratio, and the extended areas are defined as the regions of interest (ROIs). Mosaics are rescaled to 8-bit images in YODA; however, the segmentation section utilizes the backscattering coefficient in order to segment the oil slick pixel by pixel as accurately as possible. The ROIs from the mosaics are loaded as image patches, and each pixel is substituted by the median of all the pixels in the kernel area for reducing speckle noise. This procedure is also known as median blur, the kernel areas is set to 5×5 px to 10×10 px depending on the size of ROI.

Discontinuity and similarity are the two basic properties used in segmentation algorithms (Gonzalez and Woods 2018). As oil slicks dampen the gravity-capillary waves and reduce radar backscatter, they usually appear as dark formations compared to the slick-free sea surface. To distinguish oil slicks and look-alikes, classifiers in previous studies learned different features such as statistical, geometrical, textural, contextual and SAR polarimetric characteristics (Al-Ruzouq et al. 2020). As one of the statistical features, the power-to-mean ratio is commonly applied for defining the homogeneity of either oil slicks or their surroundings (Singha, Bellerby, and Trieschmann 2013; Solberg et al. 1999). Therefore, it could also be employed for detecting the discontinuity of the oil slick and its surroundings. The power-to-mean ratio of each pixel in the ROI is calculated with its surrounding pixels and defined as σ/μ , where σ and μ refer to the standard deviation and mean of the backscatter coefficients, respectively. The edge between a slick and its surroundings is hence revealed by the discontinuity of σ/μ and extracted with a certain threshold.

However, in this study area, oil spills commonly appear near ships or at the coasts where the backscatter coefficients are higher compared to sea surface and slicks. To

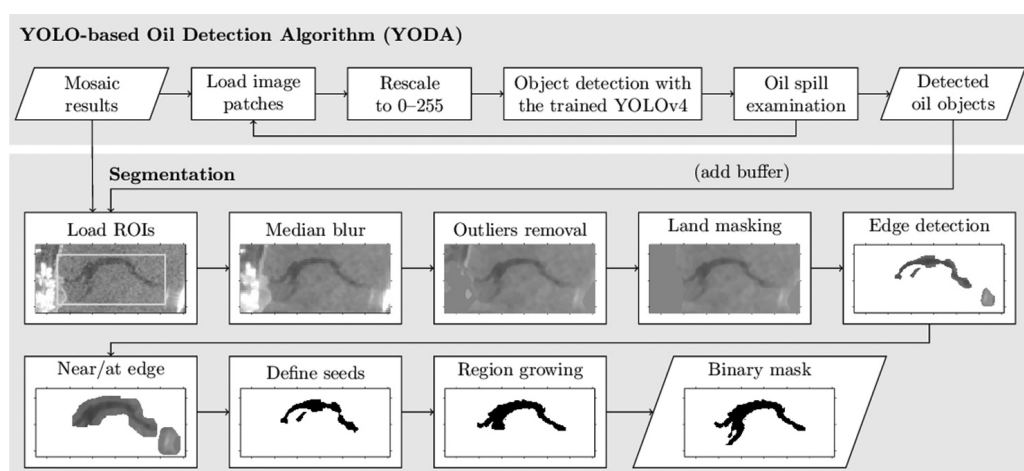


Figure 5. Detailed structure of the oil spill detection subsystem (see Figure 1 for the structure of the entire system). The explanations on YODA and the segmentation step are shown in Subsections 2.3.1 and 2.3.2, respectively.

prevent these outliers (i.e. brighter pixels) and pixels covering land areas from interfering with the edge detection, they are identified by the constant false alarm rate (CFAR) algorithm (Brusch et al. 2011) and a land mask, respectively, and replaced by the average value of the remaining pixels in the ROI prior to the edge detection. In CFAR algorithm, each pixel (target pixel) in the ROI is surrounded by a guard area and then further by a background area. The system uses 19×19 px and 39×39 px for the guard and background windows, respectively. The mean (μ_b) and standard deviation (σ_b) of the background pixels are used to calculate a threshold for finding bright pixels:

$$T = \mu_b + n \cdot \sigma_b, \quad (2)$$

where constant parameter n for scaling the threshold is set to 15.

Considering pixels lying on or near edge as a small subset, based on the distribution of their backscattering values, a threshold is defined for obtaining oil pixels inside the subset; these oil pixels are then regarded as seed points. Afterwards, a final oil slick binary mask can be generated by growing the seed points recursively based on similarity to their neighbouring pixels, which is defined by the mean and standard deviation of the backscatter coefficients among the seed points and the pixels passing the criteria in the previous iterations. Subsection 3.2 provides examples of oil binary masks generated by the proposed segmentation method.

2.4. Oil slick trajectory simulation subsystem

Oil binary masks from the segmentation section in the oil spill detection subsystem are delivered to the oil slick trajectory simulation subsystem, which uses the forecasts of synoptic conditions and applies a Lagrangian 3D oil numerical MEDSLIK model to emulate oil advection – diffusion and weathering processes (e.g. evaporation, dispersion and emulsification). The slick is divided into Lagrangian parcels as representations for the advection – diffusion processes and simulates their motion at the water surface (Zodiatis et al. 2012).

Advection of oil at the sea surface is driven by wind, sea currents, and waves. The MEDSLIK model uses the common ‘wind factor’ approach (Zodiatis et al. 2017), where the wind-induced drift is computed as a fraction of the wind speed (i.e. wind factor) and directed at a certain angle to the wind direction. In this study, the default simulations use 3.1% as the wind factor and set the wind direction as the direction of the wind-induced drift. The wind-induced drift is computed from the SKIRON atmospheric model provided by the University of Athens (Kallos et al. 1997; Papadopoulos, Katsafados, and Kallos 2001). The current-induced drift is computed from subsurface sea current velocity to avoid double counting the wind influence; the simulated modelled velocity is interpolated to 30 m depth. The forecast of subsurface ocean current, along with sea water temperature, is provided by the SELIPS high-resolution ocean model (Goldman et al. 2014, 2015), which uses the SKIRON model, the Copernicus sea surface temperature (SST) observations and the ALERMO ocean model (Korres and Lascaratos 2003). The wave-induced Stokes drift is derived from significant wave height, mean wave period and mean wave direction from the WAM wave model (Gertman et al. 2006), which uses wind forecast from SKIRON. Diffusion is emulated by a random walk model calculated with a given diffusion coefficient; the default coefficient is set to $2.0 \text{ m}^2 \cdot \text{s}^{-1}$. Figure 1 illustrates the relations between

different models to support the explanations above. It should be noted that wind velocity and sea water temperature are used to compute weathering processes in MEDSLIK (Mackay 1980; Mackay et al. 1980).

Once the oil slick is detected, the information of time, location, slick volume and oil type with default parameters is provided to the oil slick trajectory simulation subsystem for simulating the trajectory. It checks the availability of daily forecast datasets from each model (i.e. SKIRON, SELIPS and WAM) to run a simulation using the most up-to-date forecasts at any time. For past events, the synoptic forcing is created from the concatenation of the first day from each forecast dataset. The SKIRON, SELIPS and WAM models provide hourly output at a horizontal resolution of 0.05° , $0.01^\circ \times 0.00833^\circ$ and 0.125° , respectively.

The subsystem is connected to a web interface with a database and a processing backend. The web interface displays the oil spill simulation results, which can be downloaded by users. It also allows users to execute simulations with their own incident scenarios or by modifying the existing scenarios. The incident details and simulation parameters are stored in the database. The processing backend manages the simulation queue, converts the MEDSLIK output to georeferenced file formats, monitors the state of the forecast datasets and processes new SAR observations.

The uncertain oil properties, such as oil type, slick thickness and age, from SAR observations make simulating oil transport and fate challenging. The default slick parameters are thickness of $1 \mu\text{m}$ and medium crude oil type (API gravity is 33). The defaults are relevant to the automatic simulations, but users can use the web interface to prepare and execute another simulation with modified oil type and volume. Subsection 3.2 compares estimated oil trajectory with continuous SAR observations to evaluate the performance of the oil slick trajectory simulation subsystem.

3. Results and discussion

This section first explains the calculation of the performance assessment of YODA in Subsection 3.1. Subsections 3.1.1 and 3.1.2 are then compared to the performance of YODA applying object detectors trained with different datasets and data augmentation configurations, respectively. Afterwards, YODA is further tested on one-year data in Subsection 3.1.3; its advantages and disadvantages over different regions are also covered in the discussion. Subsection 3.2 compares SAR observations with oil slick trajectory simulation, supplied with several examples. In the end, Subsection 3.3 illustrates the whole oil slick detection and early warning system and provides a latency test.

3.1. Performance assessment of YODA

YODA goes through the input mosaics with sliding windows, targets oil objects inside with the custom-trained detector, and outputs the information of oil objects. Each detection is followed by a confidence score, which indicates the probability of an oil object appearing in the bounding box and how well the box fits the object (Redmon et al. 2016). The confidence score is defined as:

$$S_{\text{conf, class}_i} = P(\text{class}_i|\text{obj}) \cdot P(\text{obj}) \cdot \text{IoU}, \quad (3)$$

where $P(obj)$ refers to the probability that the bounding box contains an object, and $P(class_i|obj)$ denotes the conditional class probability showing that if an object is located at the grid cell, how likely it belongs to a specific class i . IoU represents the intersection over union, indicating how accurately the box predicts and defined as (Everingham et al. 2010):

$$IoU = \frac{\text{area}(B_p \cap B_g)}{\text{area}(B_p \cup B_g)}, \quad (4)$$

where $B_p \cap B_g$ and $B_p \cup B_g$ respectively refer to the intersection and union of the bounding boxes of the prediction (B_p) and the ground truth (B_g). In the testing, there should not be ground truth while running the object detector. Predictions from the object detector are mentioned as detections in the following paragraphs and abbreviated as *detn* in the tables. As there is no real ground truth data for oil slicks, ground truth (written as *gt* in the following tables) refers to manually inspected oil slicks described in Subsection 2.2.

Only detections with confidence scores greater than a certain threshold, $thres_{score}$, are regarded as valid detections and compared to manual inspections. Suppose a valid detection has a corresponding manual inspection such that their IoU is greater than the prescribed $thres_{IoU}$. In that case, it is considered a True Positive (TP) detection, and its corresponding manual inspection belongs to TP as well. As mentioned in Subsection 2.3, the detections are examined with several iterations in YODA, so that there might be several detections targeting the same slicks if they do not satisfy the criteria of combination. Therefore, the numbers of TP in manual inspections and detections might be different. Note that detections which have intersections with each other can be considered in one ROI in the segmentation section. False Positive (FP) refers to the detections where there is no matched manual inspection. On the other hand, the manual inspections that are not targeted by the detector belong to False Negative (FN). It is relatively important for an operational system to focus on how negative results influence the performance of the system. Thus, false discovery rate (FDR) and false negative rate (FNR) are used in the following subsections, they are defined as follows:

$$\begin{aligned} FDR &= \frac{FP}{(TP + FP)}, \\ FNR &= \frac{FN}{(TP + FN)}. \end{aligned} \quad (5)$$

Some manual inspections have intersected detections but belong to FN because their IoU do not pass $thres_{IoU}$ or the detections have confidence scores lower than $thres_{score}$. On the other hand, some detections are regarded as FP due to their poor IoU with the manual inspections. Figure 6 shows an oil slick outlined in blue and its corresponding detection in pink; the smaller slick in the figure is not annotated to avoid confusion. In this example, the extent of the slick was not defined precisely, which indicates the need for improvement in the precision of the object detector. However, this kind of FP does not target look-alikes, and the segmentation section can still define the exact coverage of the oil. On the contrary, it is especially important to reduce the number of FP originating from look-alikes, as they might lead to unnecessary cleanup operations. Therefore, the calibrated FDR and FNR are introduced and defined as:

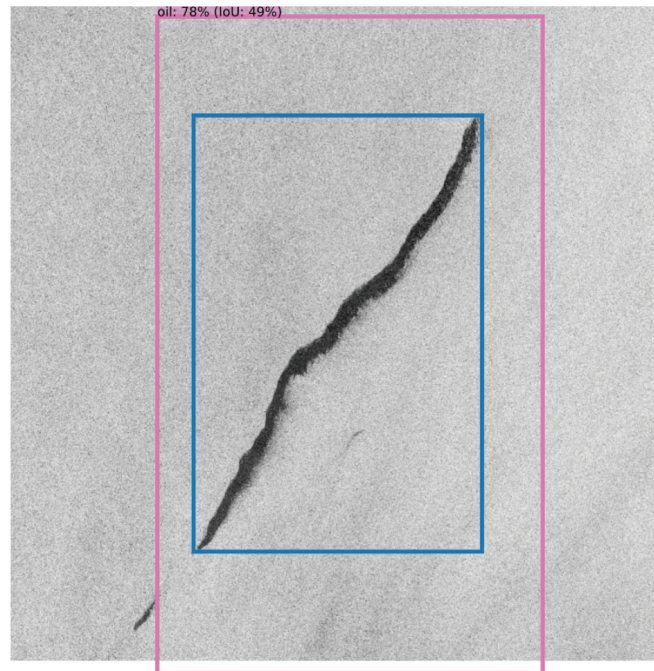


Figure 6. An example of FP, which does not lead to false alerts, is shown. The blue and pink bounding boxes mark the manual inspection and the detection, respectively. Note that this example focuses on the selected oil slick, so the smaller slick in the scene is not annotated to avoid confusion.

$$\begin{aligned} FDR_{cal} &= \frac{FP_{cal}}{(TP + FP)}, \\ FNR_{cal} &= \frac{FN_{cal}}{(TP + FN)}, \end{aligned} \quad (6)$$

where FP_{cal} shows the detections targetting at look-alikes and FN_{cal} shows the oil slicks with no detection (either valid or invalid detections) intersected. The difference between original and calibrated FDR shows the ratio of detections targetting oil slicks but are not precise enough. Similarly, the difference between original and calibrated FNR shows the ratio of manual inspections that are not detected or detected but with a lower confidence score. In the following discussion, $thres_{score} = 50\%$ and $thres_{IoU} = 50\%$ are applied.

3.1.1. Adding additional no-oil dataset

As mentioned in Subsection 2.3.1, considering *no-oil set* in training might help improve the performance of the object detector on avoiding FP. In order to verify this assumption, the performance of YODA applying detector trained with *oil set* is compared to applying an enhanced detector trained with both the *oil* and *no-oil sets*; in the following, *YODA-orig*

Table 2. Performance assessment of YODA using two custom-trained object detectors on one-month mosaics in June 2019 (see Subsection 3.1.1 for detailed comparison).

Version	# detn	# TP		# FP		# FN		FDR [%]		FNR [%]	
		gt	detn	orig	cal	orig	cal	orig	cal	orig	cal
YODA-orig	1707	191	370	1337	1182	75	9	78.3	69.2	28.2	3.4
YODA-enh	257	124	179	78	54	142	55	30.4	21.0	53.4	20.7

#gt = 266, $thres_{score} = 50\%$, $thres_{IoU} = 50\%$

and *YODA-enh* refer to YODA applying the two detectors, respectively. Table 2 shows the measures of *YODA-orig* and *YODA-enh* for testing on one-month mosaics in 2019. The calibrated FDR of *YODA-orig* was 69.2% but *YODA-enh* had its FDR decreased to 21.0%, indicating the substantial improvement of the detector on avoiding FP by applying additional *no-oil* set into training. As *YODA-orig* detected 1707 objects while there were only 266 manual inspections, the detector likely targeted most of the dark formations, which had similar patterns as oil slicks, and led to a low calibrated FNR of 3.4%. Regarding *YODA-enh*, the original and calibrated FNR were different by 32.7%, meaning that those detections were not defining the extent of the slicks well or not confident enough (i.e. confidence scores smaller than $thres_{score}$).

To further analyze if FNR associates with the sizes of oil objects, manual inspections were categorized into different size groups and shown in Table 3. Oil objects were sorted according to the area of the corresponding bounding boxes. If the area is smaller than 12500px (i.e. 5 km²), the object belongs to the *small* group; on the other hand, in the *large* group the area is greater than or equal to 100000px (i.e. 40 km²). The remaining objects belong to the *medium* group. According to the table, the detector had relatively high original FNR on *medium* and *large* groups, meaning it works worse on detecting larger oil objects. One possible reason is that *small* oil objects occupied around 72.3% of all manual inspections; thus, the detector is better at detecting smaller objects. Among all the *large* oil objects, 14.3% of them were not detected, and 64.3% of their corresponding detections should be improved to pass the thresholds. It is likely due to the lack of examples in the dataset and the complexity of the larger oil objects in shapes. Therefore, to increase the number of larger oil objects in training, data augmentation focusing on them could be beneficial.

3.1.2. Additional augmented dataset

The following compares the FDR and FNR of YODA applying detectors trained with different data augmentation configurations; the inspection time was from January to June 2019. As the previous subsection has proven that adding *no-oil* set for training is beneficial for lowering the FDR, the detectors applied to YODA in this subsection used the same dataset as detector in *YODA-enh* but included an additional augmented dataset. Image patches containing oil objects in *large* or *medium* groups were rotated by 90°, 180° and 270° and saved in the augmented dataset. Table 4 shows the numbers of image patches and data augmentation configurations of different object detectors applied to YODA. The detectors for *YODA-enh-aug1* and *YODA-enh-aug3* included the augmented dataset with the rotation of 90° and three different rotation angles, respectively. The detector for *YODA-enh-aug3b* used the same *oil* set as the one for *YODA-enh-aug3* but considered the augmentation of the *no-oil* set to balance the numbers of scenes in the *oil* and *no-oil* sets.

Table 3. Extended comparison from Table 2 focusing on the changes in FN and FNR of *YODA-enh* for different size groups.

Group	# gt	FN		FNR [%]	
		orig	cal	orig	cal
(1) Small	208	99	39	47.6	18.8
(2) Medium	44	32	14	72.7	31.8
(3) Large	14	11	2	78.6	14.3
all	266	142	55	53.4	20.7

$thres_{score} = 50\%$, $thres_{IoU} = 50\%$

Table 4. Overview of the selection of datasets and the numbers of oil objects used for different custom-trained detectors used in YODA described in Subsection 3.1.2. The application of rotation data augmentation with 90°, 180° and 270° are also noted.

Version	oil set			no-oil set		
	orig	aug (L+M)	#	orig	aug	#
YODA-enh	✓		6067	✓		6361
YODA-enh-aug1	✓	✓ (90)	8555	✓		6361
YODA-enh-aug3	✓	✓ (90, 180, 270)	13531	✓		6361
YODA-enh-aug3b	✓	✓ (90, 180, 270)	13531	✓	✓	12722

Table 5. Performance assessment of YODA using different custom-trained object detectors on six-month data from January to June 2019. Detailed comparisons are explained in Subsection 3.1.2.

Version	# detn							FDR [%]				FNR [%]			
		# TP		# FP		# FN		orig		cal		orig		cal	
		gt	detn	orig	cal	orig	cal	all	L+M	all	L+M	all	L+M	all	L+M
YODA-enh	2099	695	1400	699	453	965	431	33.3	52.6	21.6	43.2	58.1	74.3	26.0	33.9
YODA-enh-aug1	1798	638	1165	633	410	1022	538	35.2	49.3	22.8	38.6	61.6	64.4	32.4	32.9
YODA-enh-aug3	2024	586	1136	888	683	1074	422	43.9	69.3	33.7	63.8	64.7	66.6	25.4	25.5
YODA-enh-aug3b	831	339	635	196	92	1321	929	23.6	42.9	11.1	32.6	79.6	84.4	56.0	59.7

#gt = 1660, $thres_{score} = 50\%$, $thres_{iou} = 50\%$

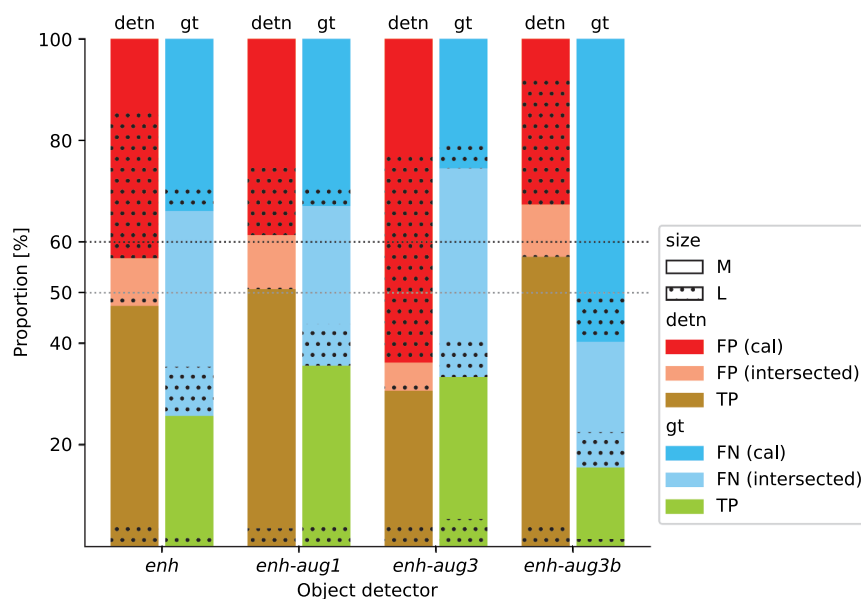


Figure 7. The proportion of positive and negative results on *large* and *medium* oil objects with different custom-trained detectors for YODA applied; this figure is used as an extended comparison from Table 5. The proportions of TP and FP among all the detections are displayed in brown and red, respectively. As for the manual inspections, TP and FN are displayed in green and blue, respectively. The lighter colours show negative results where manual inspections and detections have intersections. A detailed comparison can be found in Subsection 3.1.2.

Table 5 indicates the performance of YODA using different object detectors. Since it is better at detecting *small* oil objects according to Subsection 3.1.1, the performance on *large* and *medium* oil objects is emphasized; their FDR and FNR are listed in separate

columns, and the detection results on these objects are visualized in [Figure 7](#). There seems to be a slight improvement of *YODA-enh-aug1* on FNR in comparison to *YODA-enh*; however, the ratio of calibrated FP (i.e. the calibrated FDR) on *large* oil objects has decreased. Regarding FNR, *YODA-enh-aug1* lowered the original FNR, but the calibrated one did not differ much. It seems that different detectors have similar abilities to detect *large* and *medium* oil objects, but there were more detections from *YODA-enh-aug1* passing the thresholds than the ones from *YODA-enh*.

To further investigate how different rotation augmentations might help with the performance, *YODA-enh-aug1* and *YODA-enh-aug3* are compared. As mentioned in [Subsection 3.1.1](#), adding image patches with look-alikes or other remarkable features could help; however, with the imbalanced numbers of images in the *oil* and *no-oil* sets for training the detector for *YODA-enh-aug3*, FDR has increased. In other words, it shall be essential to have similar numbers of images with and without oil objects inside, and *YODA-enh-aug3b* supports this assumption as it had the lowest FDR among all. However, there were only 831 detections but around 1660 manual inspections; the detector seems conservative, which led to a relatively high FNR.

In summary, *YODA-enh* had the best overall performance; however, *YODA-enh-aug1* worked better on targeting larger oil objects. Considering the impact of large oil slicks on the environment, *YODA-enh-aug1* is the most suitable for the system. However, both of them have pros and cons; thus, they are compared further in the following subsection, which focuses on the performances on one-year mosaics and discusses their competence in different regions.

3.1.3. Performance of the YODA on one-year data

Since algae distribution, maritime traffic and wind condition might vary monthly or seasonally, testing YODA for an entire year is necessary. [Figure 8](#) shows the spatial distribution of the manually inspected oil slicks collected in 2019 and marks the different zones for performance assessment in the following paragraphs. Oil could cause long-term biological and ecological consequences; thus, to raise the environmental awareness of the authorities, it is vital to highlight the pollution within the territorial waters, where it might damage the vulnerable coastal and marine ecosystems of its corresponding countries. The territorial waters are defined as 12 nautical miles (around 22 km) off the coast; the green line illustrates the region by extending the coastline for 22 km. Note that it is not definitive for the actual territorial waters boundaries.

Concerning sources of look-alikes, [Figure 9](#) gives an example on 22 January 2023, illustrating possible land-sourced chemical or oil spills, ship-based discharges, wind-induced look-alikes and algae. Wind-induced look-alikes commonly appeared off the east coast and interfered with detecting oil slicks. As they were not commonly seen off the south coast, the red line in [Figure 8](#) separates the coastal region into the *Eastcoast* and *Southcoast* zones. Usually, wind-induced look-alikes covered a larger area compared to the coastal spills; thus, the orange line, extended from the coastline by 5 km, splits the *Eastcoast* zone into *Eastcoast-5* and *Eastcoast-22* zones.

This study focuses on the area where the ocean circulation model is applicable; the model area excluding the coastal zones is defined as *Sea-in* zone, 47.1% of the oil objects in 2019 located in this zone. Unlike the coastal area, which contained different sources of spills and look-alikes, oil spills away from the coast in the study area were mainly from

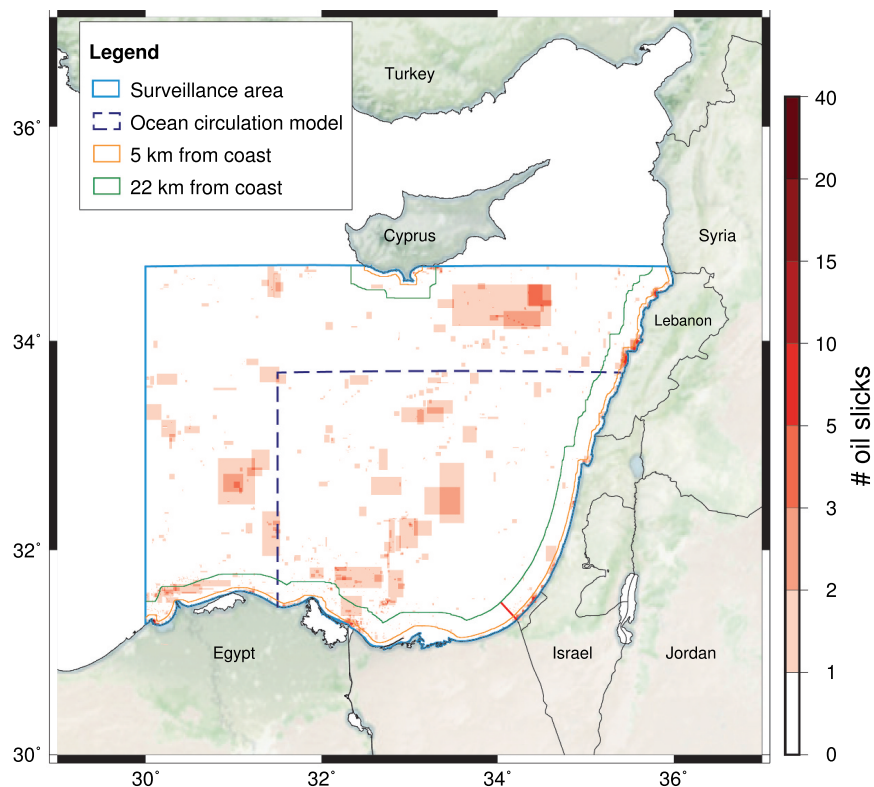


Figure 8. Based on the definition of the study area shown in Figure 2, different zones are marked for further discussion on the performance of YODA in different locations described in Subsection 3.1.3. The heatmap shows the number of oil slicks collected from 2019 for testing YODA. The red line separates the east and south coasts.

ships. For this reason, the non-coastal area outside the model area is included in the comparison and considered as *Sea-out* zone. Oil objects and detections are categorized into different zones regarding the location of their centre coordinates. Table 6 summarizes the definition of different zones and shows the number of manual inspections in each zone.

Table 7 shows the performance of *YODA-enh* and *YODA-enh-aug1* in different zones. Overall, they both had similar FDR, but *YODA-enh* had a lower FNR than *YODA-enh-aug1*, meaning that *YODA-enh* detected more oil objects; this aligns with the findings in Subsection 3.1.2. Similar results are also shown in the *Sea-in* and *Sea-out* zones but with lower calibrated FNR, possibly due to fewer wind shadows as look-alikes in these zones.

Previous studies suggested the ideal wind speed range should be between 3 and 7–10 m/s for visualizing oil slicks in SAR observations since there was a high possibility of look-alikes due to low wind and thinner slicks might be invisible with the strong wind due to a combination of oil dispersion (Brekke and Solberg 2005). To better understand how wind speed might influence performance, (Figures 10 and Figure 11) illustrate the monthly performance and the monthly mean wind speed from the SKIRON forecast, respectively, in 2019. Among all the monthly performances, both *YODA-enh* and *YODA-enh-aug1* seem to have the worst performance in December, where FDR and FNR were high. In December and

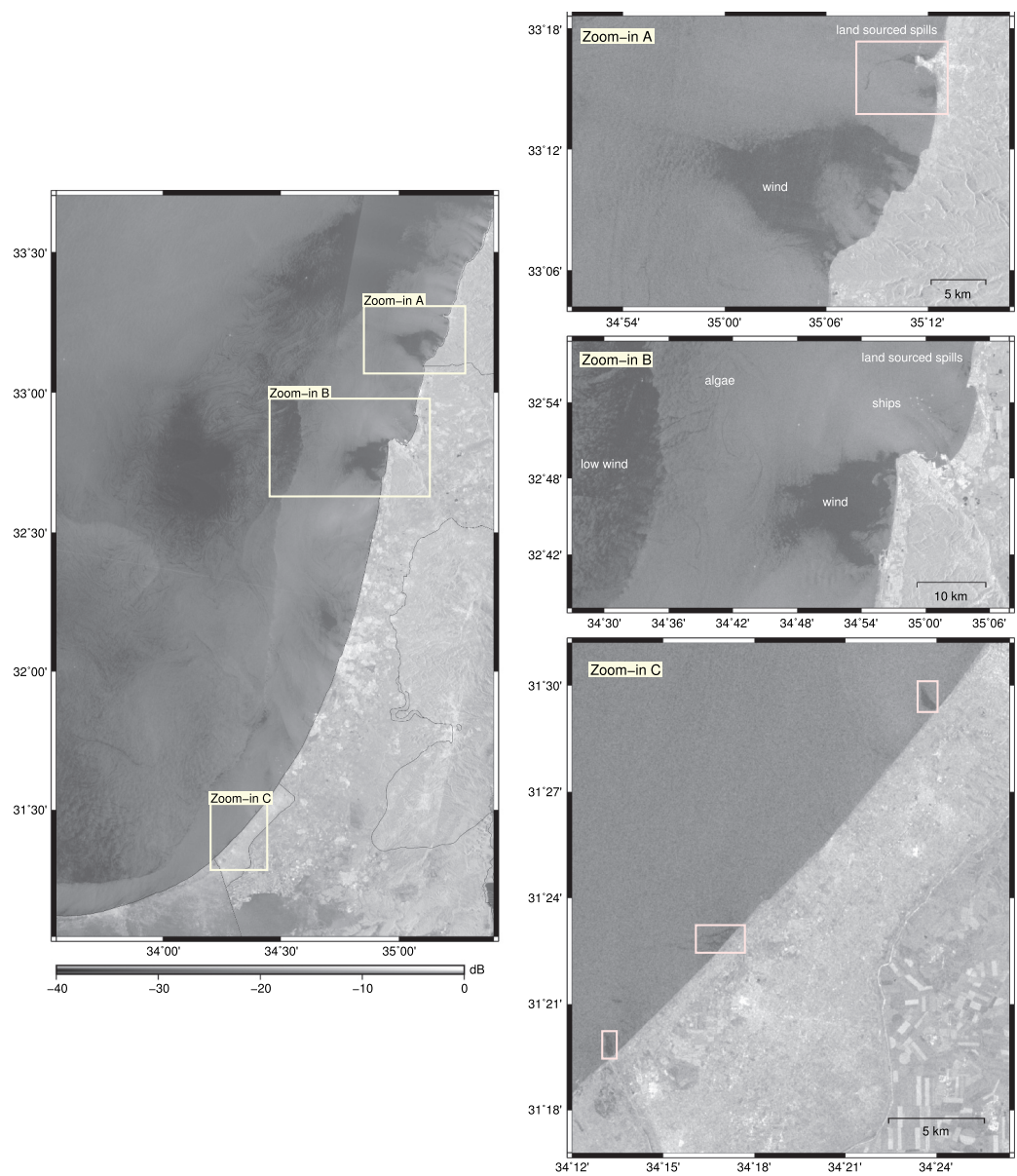


Figure 9. A mosaic on 22 January 2023 at 03:44 showing different sources of dark formations. Zoom-in areas a and B present some common wind-induced look-alikes, algae, land-sourced spills, and discharges from ships. Zoom-in area C shows a hotspot with regular land-sourced spills.

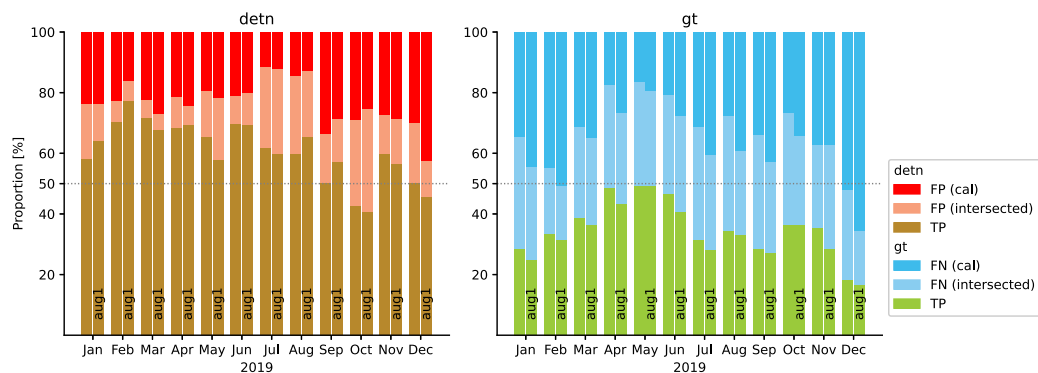
Table 6. Definition of different zones in the study area and numbers of manually inspected oil slicks are listed. The geographic locations are illustrated in [Figure 8](#).

Zone	# gt	Descriptions
Eastcoast-5	287	Within 5km off the east coast in the model area
Eastcoast-22	40	Between 5km and 22km off the east coast in the model area
Southcoast	493	Within 22km off the south coast in the model area
Sea-in	731	Model area excluding the zones described above
Sea-out	747	Surveillance area excluding the coastal areas and the zones described above

Table 7. Performance assessment of YODA-enh and YODA-enh-aug1 in different zones on one-year mosaics from January to December 2019.

Version	Zone	# detn	# TP		# FP		# FN		FDR [%]		FNR [%]	
			gt	detn	orig	cal	orig	cal	orig	cal	orig	cal
YODA-enh	Eastcoast-5	342	131	231	111	77	236	116	32.5	22.5	64.3	31.6
	Eastcoast-22	98	14	45	53	47	33	11	54.1	48.0	70.2	23.4
	Southcoast	559	224	382	177	86	324	151	31.7	15.4	59.1	27.6
	Sea-in	902	323	496	406	244	406	147	45.0	27.1	55.7	20.2
	Sea-out	1021	314	619	402	227	466	168	39.4	22.2	59.7	21.5
	overall	2922	1006	1773	1149	681	1465	593	39.3	23.3	59.3	24.0
YODA-enh-aug1	Eastcoast-5	281	127	194	87	65	240	152	31.0	23.1	65.4	41.4
	Eastcoast-22	55	15	27	28	23	32	11	50.9	41.8	68.1	23.4
	Southcoast	407	188	314	93	38	360	225	22.9	9.3	65.7	41.1
	Sea-in	849	305	455	394	225	424	188	46.4	26.5	58.2	25.8
	Sea-out	1052	303	555	497	280	477	214	47.2	26.6	61.2	27.4
	overall	2644	938	1545	1099	631	1533	790	41.6	23.9	62.0	32.0

$thres_{score} = 50\%$, $thres_{iou} = 50\%$

**Figure 10.** The monthly proportion of positive and negative results of YODA-enh and YODA-enh-aug1 illustrating the possible influence of strong wind and algae seasons explained in Subsection 3.1.3. The bars without annotation and annotated with *aug1* refer to YODA-enh and YODA-enh-aug1, respectively.

January, the strong wind might lead to poor visibility on slimmer oil slicks and result in high calibrated FNR in these months. On the contrary, October was the month with the overall lowest wind speeds ranging from 2 to 5 m/s, especially in the regions closer to the coast where the mean wind speed was lower than 3 m/s. The FDR seems to be high as there might be more SAR observations with wind speeds lower than the recommended speed. Therefore, wind speed should be considered in the system to provide more reliable results.

A previous study highlighted the operational oil spills with sizes of about 1–10 tonnes released by ships that occurred almost daily in the Mediterranean Sea (Kostianoy, Kostianaia, and Soloviev 2020). Heavy shipping activities, mainly due to the Suez Canal, have caused the *Southcoast* zone to become an oil pollution hotspot, especially near the Port Said according to Figures 2 and Figure 8. Wind-induced look-alikes were less common in this zone than the *EastCoast*; however, the intersection of ships and the water surface might cause ship wakes and result in lower radar backscatter compared to their surroundings (Tings, Pleskachevsky, and Wiehle 2023). In other words, ship wake was one possible source of look-alikes in the heavy ship traffic *SourthCoast*. Figure 12 shows an

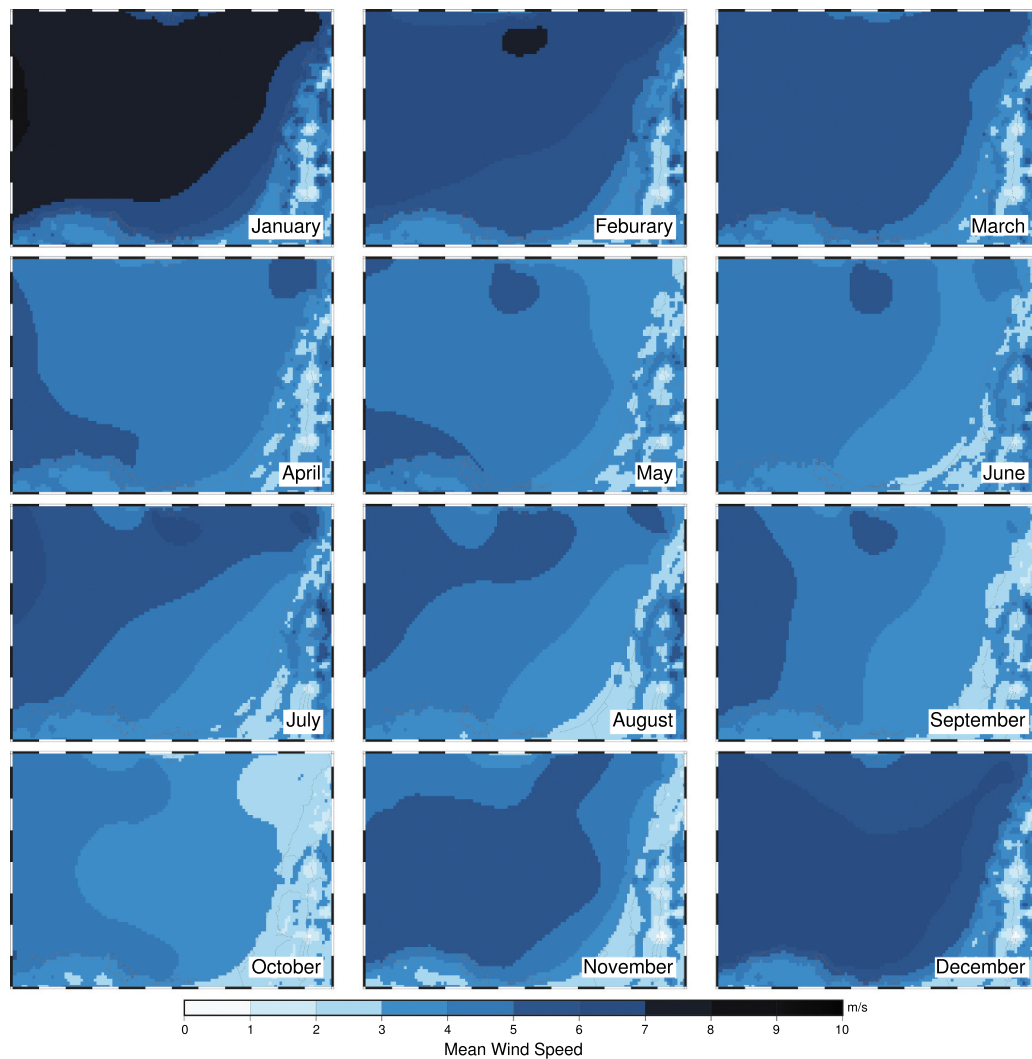


Figure 11. Monthly average of the wind speed in 2019 from SKIRON.

example of oil slicks and ship wakes in the same SAR observation where the backscatter values of slicks were lower than those of ship wakes.

The calibrated FDR of *YODA-enh* and *YODA-enh-aug1* were 15.4% and 9.3%, respectively, which were relatively low compared in other zones. It indicated that most of the detections in this zone were correct; however, the calibrated FNR of *YODA-enh* and *YODA-enh-aug1* were 27.6% and 41.1%, respectively, which were higher than overall. As thin slicks or slicks propagated and evaporated after a few days on the water might lead to similar low backscatter values as ship wakes do, the distinction between them is challenging. Therefore, the detectors were more conservative with sending the detections of oil, which led to low FNR. Considering FDR, *YODA-enh-aug1* seems suitable in this zone for reducing the possibility of sending false alarms. However, including ship and wake information might help avoid possible FP; in this case, *YODA-enh* with lower FNR could also be applied.

Similar results are also shown in the *Eastcoast-5* zone, where the calibrated FNR were relatively high compared to other zones, especially for *YODA-enh-aug1*. There were ship discharges near the ports in both zones but more land-sourced spills in this zone, according

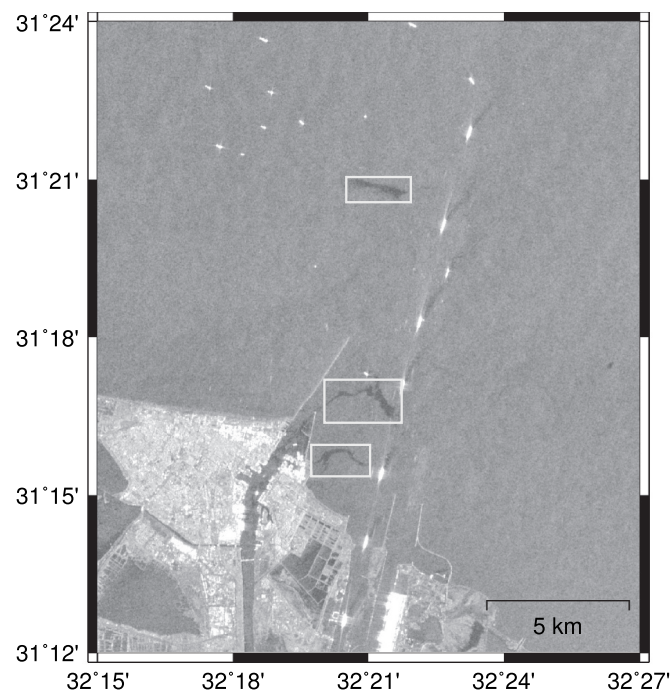


Figure 12. An example on 7 July 2022 at 03:51 showing oil slicks along with ship wakes near Port Said off the Egyptian coast. The bounding boxes define slicks, and dark formations near ships (bright pixels) are likely to be ship wakes.

to the manual inspections in this study. On top of that, these land-sourced spills were commonly interfered with by wind-induced dark formations or active transponders; the latter are commonly used for security reasons in the Eastern Mediterranean Sea. [Figure 13](#) shows an example SAR scene with radio frequency interference.

Concerning the *Eastcoast-22* zone, the FDR seems to be relatively high for both *YODA-enh* and *YODA-enh-aug1*. As the common wind-induced look-alikes in this zone might confuse the interpretation of spills, dark formations near such look-alikes were not annotated as oil objects in the training stage unless there was clear evidence. In addition, image patches with these unsure dark formations were not included in either the *oil* or the *no-oil* sets mentioned in [Table 1](#) for training the detectors. However, those unsure dark formations were not avoidable for testing the system performance on one-year data. In

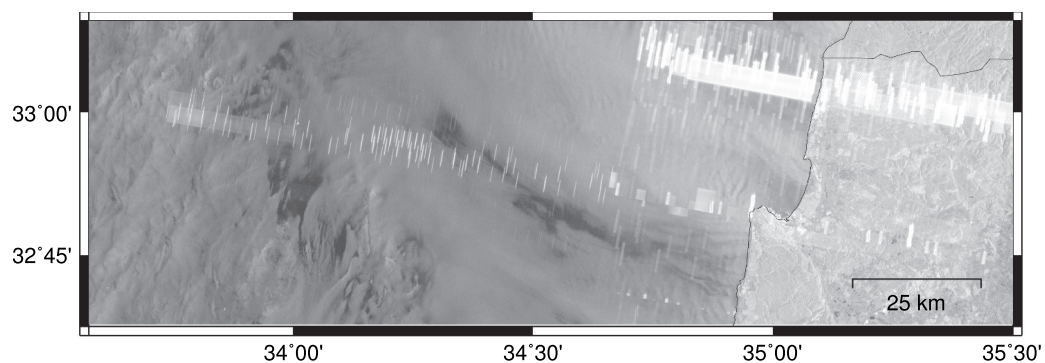


Figure 13. An example on 28 February 2017 at 03:42 shows radio frequency interference on SAR, which constantly appears in certain regions.

other words, some detections might target actual spills but be defined as FP because those spills were not annotated as oil objects. Therefore, considering synoptic conditions at the corresponding time of SAR observations might help increase the quality of manual inspections and the confidence of detections.

3.2. Comparison between SAR observations and slick trajectory simulation

In Subsection 3.1, the performance of YODA was evaluated. After detecting oil slicks, they are segmented into binary masks and delivered to the MEDSLIK model for hourly estimation of the slick trajectory. In some cases, the same oil slicks appeared in SAR observations from different Sentinel-1 orbits at different time, which could help understand how SAR observations and simulations are similar or different from each other. Several oil slicks in continuous SAR observations are presented in the following, the continuous observations are all around 12 hours apart. The distance between centroids of SAR observation and trajectory simulation are computed and used for comparison. Both *YODA-enh* and *YODA-enh-aug1* were applied to the selected cases as illustrations on how different detectors target oil slicks.

The annotations of figures in this subsection follow the same format. Detections annotated in mosaics from *YODA-enh* and *YODA-enh-aug1* are displayed as blue (light) and orange (dark) bounding boxes, respectively; their confidence scores are attached to the bounding boxes (see Equation 3 for the definition of confidence scores). In Subsection 3.1, only valid detections (i.e. detections passing the confidence score threshold, $thres_{score}$) are discussed; however, all detections in the selected cases are displayed in this subsection. As for comparing SAR observations and simulations, the black binary masks display SAR observations sent to the MEDSLIK model for trajectory simulation. The estimated positions are marked in light blue and compared to the corresponding binary masks (in grey) acquired from SAR, and the overlapped areas are shown in orange; their centroids are shown as black and blue crosses for SAR observation and simulation,

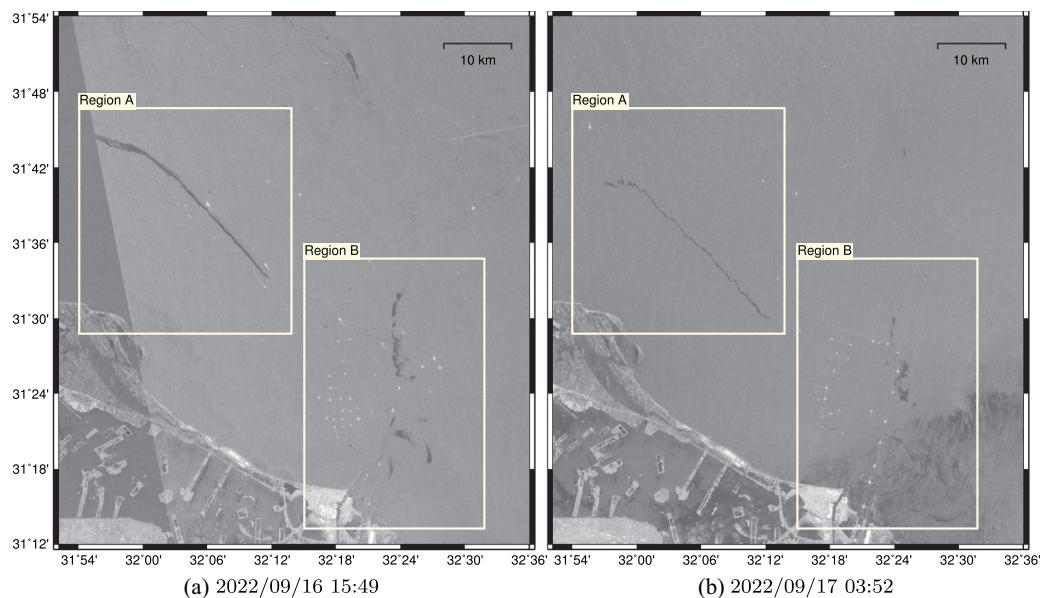


Figure 14. An example of several oil slicks near Port Said off the Egyptian coast continuously observed by SAR on 16 and 17 September 2022. The detections and simulations are compared in different zoom-in maps Figures 15 and Figure 16 for regions a and B, respectively.

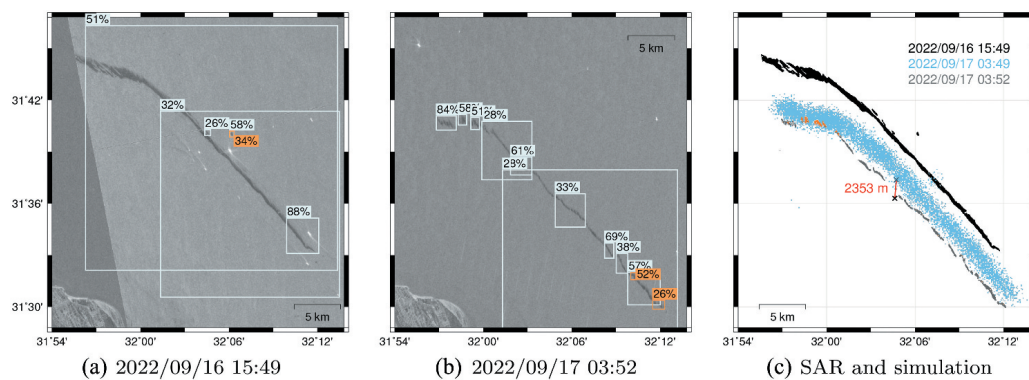


Figure 15. Zoom-in maps of region a in Figure 14 showing detections on two continuous SAR acquisitions and a comparison between SAR observations and trajectory simulation.

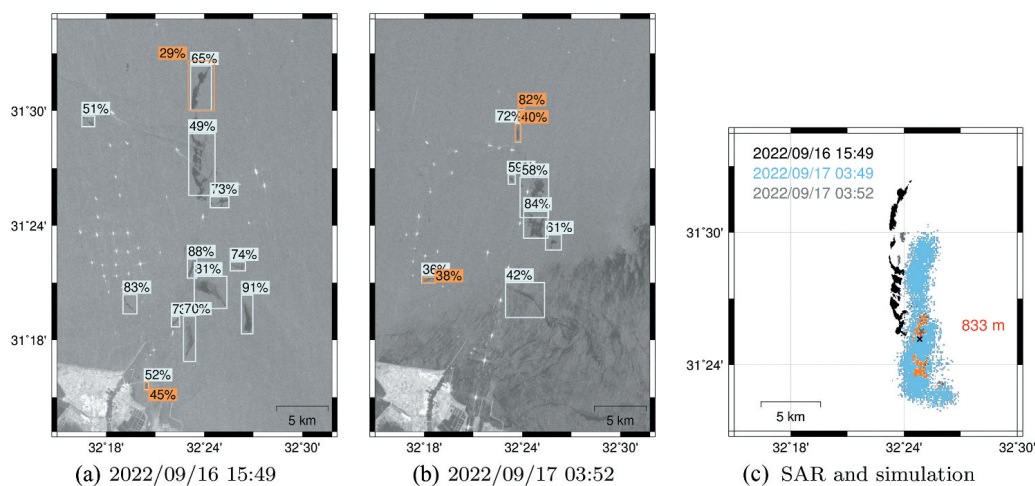


Figure 16. Zoom-in maps of region B in Figure 14 showing detections on two continuous SAR acquisitions and a comparison between SAR observations and trajectory simulation focusing on the northern slicks.

respectively. The red line marks the distance between the two centroids. Note that simulations are calculated not only for forward but also for backward estimations.

Figure 14 shows oil slicks on 16 and 17 September 2022 at an oil spill hotspot off the Egyptian coast according to the heatmap in Figure 2. Most of the slicks were located in the zoom-in regions A and B and presented in zoom-in maps in Figures 15 and Figure 16, respectively. As there were look-alikes covering areas closer to the coast on 17 September, the comparison between simulation and SAR observation only focuses on the northern slicks. Overall, most of the observed slicks covered smaller areas after 12 hours; however, the simulations show that they might influence larger regions. The oil is assumed to be composed of volatile component and non-volatile residue in the model. The evaporation of each parcel is an exponential decay process. At the same time, there is eddy diffusivity and spreading processes which redistribute the concentration of oil and of the oil parcels.


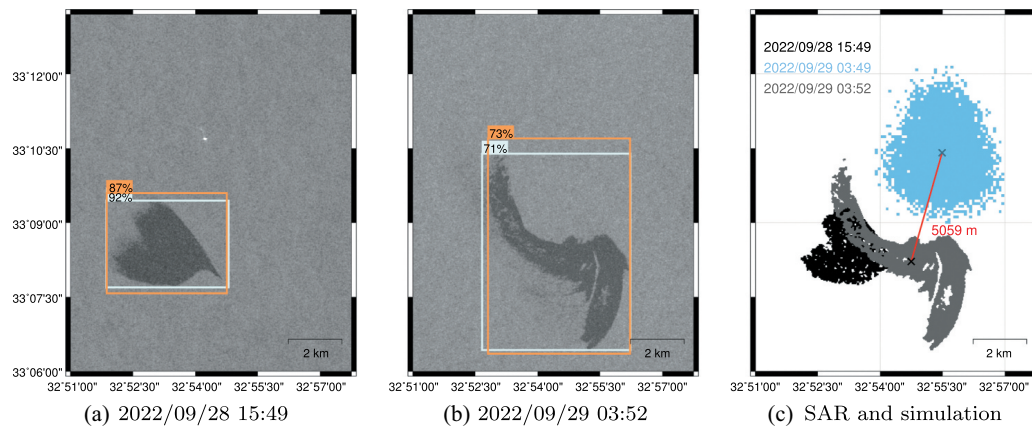
2020  Y-J. YANG ET AL.

Figure 17. An example of an oil slick with its shape changed significantly observed by SAR on 28 and 29 September 2022, showing the detections on two SAR scenes and a comparison between SAR observations and trajectory simulation.

It is possible that the diffusivity is overestimated; the actual slick evaporated, dissolved into the water, or had low concentrations so they were not able to be detected.

However, in some cases, SAR observations and trajectory simulations did not align well, Figure 17 shows such an example on 28 and 29 September 2022. The shape of the slick has changed by the wind and currents according to SAR observations. The most likely reason for the misfit between forecast and detection is the uncertainty in the numerical forecasts of current and wind. By assimilation of velocity observations, the forecast may be improved. In that respect, the misfit between observation and forecast could potentially be used to improve the forecast quality at oil spill hot spots. Moreover, Li et al. (2022) have presented a machine learning approach using reanalysis and forecast to train a system that corrects the wind field and improves the error of oil forecast. This case is notable because the slick occurred near the centre of an eddy, so changes in circulation direction and the resulting deformations of the slick are more pronounced.

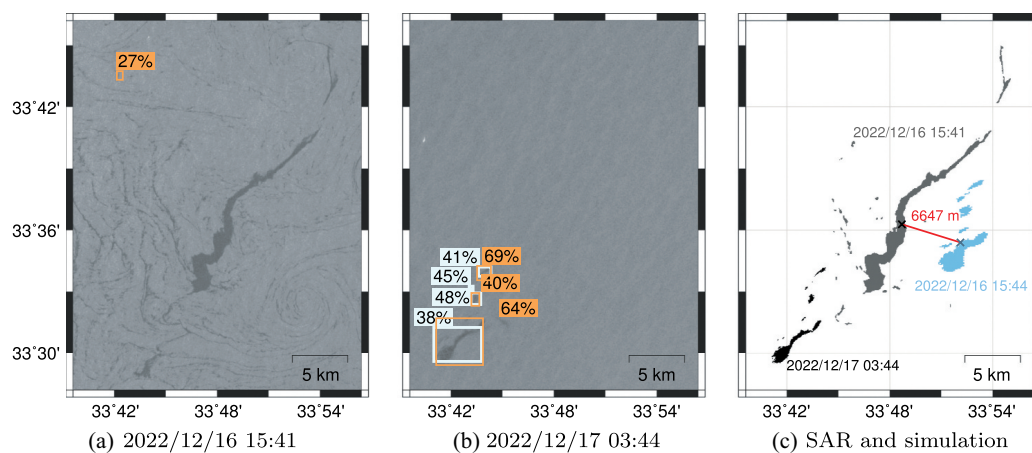


Figure 18. An example of a possible oil slick appeared near look-alikes on 16 December 2022; the observation on the next day and its backward simulation from the following day helped confirm the slick.

Another example demonstrates the advantage of oil trajectory simulation, which helps indicate oil slicks surrounded by look-alikes. Figure 18 shows oil slicks on 16–17 December 2022. There were some look-alikes on 16 December, which might be algal blooms driven by currents and made it hard to distinguish whether there was a slick. SAR observation on 17 December shows a slick having similar shape to the possible slick on 16 December and its location fits with the travelling direction from trajectory simulation. Though the size of the possible slick on 16 December covered much larger area than the one on 17 December, which is likely due to the evaporation of the oil, it is reasonable to consider those two slicks as one slick at different time. Currently, both *YODA-enh* and *YODA-enh-aug1* could not find the slick on 16 December as it was surrounded by look-alikes. However, for continuous surveillance on a specific study area, simulation of slicks is beneficial for helping the system to focus on certain regions likely to contain possible oil slicks which are derived from the trajectory estimation of oil from previous scenes.

To compare *YODA-enh* and *YODA-enh-aug1*, the following discussion focuses on their detections in the above examples. In the first example (see Figures 15 and Figure 16), *YODA-enh* performed better than *YODA-enh-aug1*. Most of the slicks were detected by *YODA-enh* though the continuous slicks were considered as many detections. As explained in Subsection 2.3, sliding windows are applied to generate image patches for feeding the detector. If the detections do not pass the defined criteria, they are examined again in the new image patches. In some situations, the size of image patches would be larger than the default sizes of the sliding windows. There should be an upper limit for the size of image patches; otherwise, the slim and long oil slicks could be invisible to the object detector. Therefore, it is reasonable to return several detections for one single long and slim slick. In addition, the segmentation method combines the overlapping detections and generates one binary mask. As one long oil slick could be regarded as several detections, it might lead to the poor system performance shown in Subsection 3.1.

Oil slicks in the second example (see Figure 17) appeared at the wind condition that was suitable for SAR observation, both oil slicks were wide and distinct from their surrounding. Thus, both detectors targeted the slicks correctly with high confidence scores. However, in the last example (see Figure 18), both detectors did not find oil slicks on 16 December; *YODA-enh-aug1* even had a false detection on look-alikes with a low confidence score of 27%. It is likely that the patterns of such look-alikes are similar to some oil slicks the detector learned during training. Such results align well with the comparison in Subsection 3.1.2 (see Table 5) that *YODA-enh-aug1* has better performance on larger oil slicks, but *YODA-enh* performs better overall. Considering 17 December (see Figure 18(b)), both detectors targeted the oil slicks, but none of the detections from *YODA-enh* passed $thres_{score}$. *YODA-enh-aug1* showed higher confidence scores on detecting those oil slicks.

3.3. Oil spill detection and early warning system

Figure 19 provides the approximate time stamps for the operational system and illustrates the system on 28 September 2022. The Sentinel-1 SAR descending and ascending tracks pass the study area at around 03:30–04:05 and 15:30–16:05 UTC, respectively. Usually, they are available on Copernicus Open Access Hub at around 22:00 UTC. Therefore, the forecasts of the


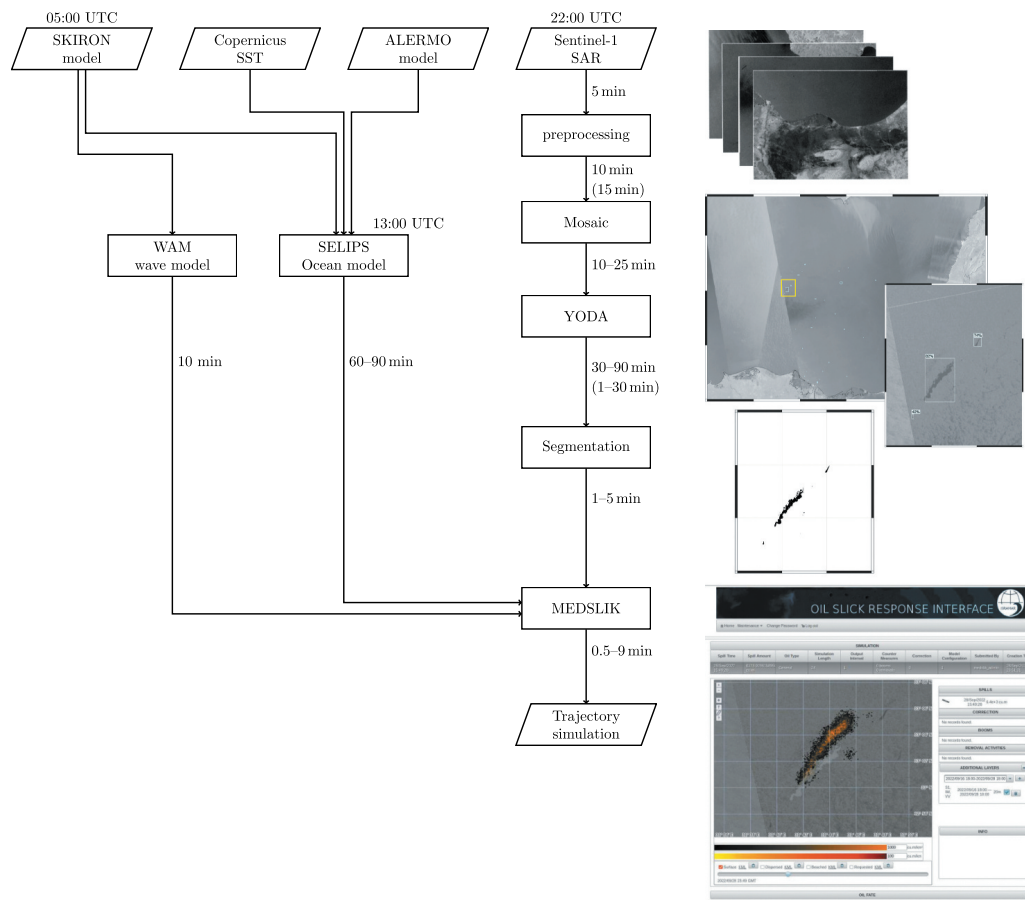
2022  Y-J. YANG ET AL.

Figure 19. The operational chain of the proposed oil spill detection and early warning system, along with the time stamps for each process. The CPU-only and GPU machines are compared from downloading sentinel-1 data to delivering oil binary masks to the MEDSLIK model. The time stamps in brackets show the different latency from the GPU machine. See [Subsection 3.3](#) for further explanation.

synoptic conditions should be ready for the trajectory simulation using the MEDSLIK model. In any case, it should be possible to obtain the forecasts from the day before. From downloading Sentinel-1 data to delivering oil binary masks to the MEDSLIK model, two different machines are compared in the latency test. One is a CPU-only machine which uses Intel Xeon E7-8857v2 CPU and 256 GB RAM; another has Nvidia GeForce RTX 3080 GPU with 10 GB VRAM, AMD Ryzen 7 3700X CPU and 32 GB RAM. The latency of YODA highly depends on the complexity of SAR scenes, as the complex scenes would increase the number of iterations. The major differences are the time intervals for the preprocessing step and YODA; time stamps for the GPU machine are noted in brackets. Because of the limited RAM, the GPU machine is slower in the preprocessing section as fewer scenes can be processed in parallel; however, using GPU increases the efficiency of detecting oil objects. Therefore, deploying on a machine with multi-core CPU, sufficient RAM and a GPU for deep learning inference can achieve optimal latency. The trajectory simulation is set to 24 durations in the automatic system; increasing the duration will result in more time costs. The system also offers tools for users to define their polygons (see [Figure 20](#)).

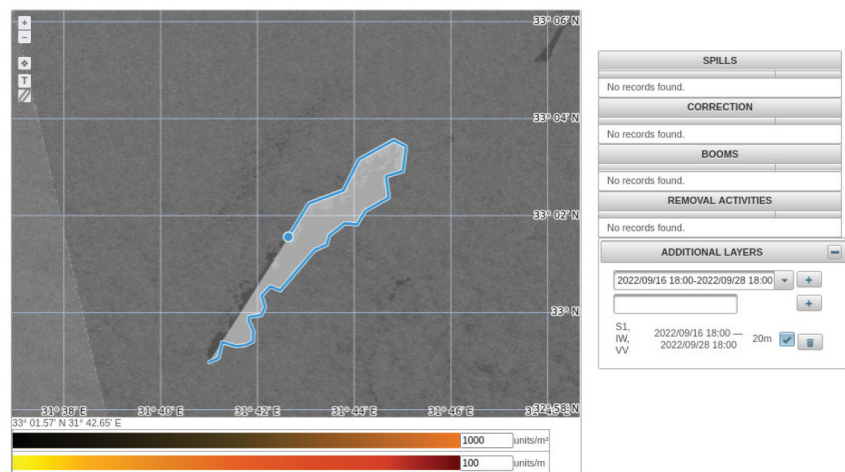



Figure 20. A screenshot of the web interface showing how users can define their own oil binary masks.

However, skipping the mosaic step and working on preprocessed scenes in SAR geometry is possible and should accelerate the system. From preprocessing SAR scenes to delivery of trajectory simulation, it takes around 1.5 h for the current system. As shown in Figure 19, it takes 10–25 min to generate a mosaic covering the study area, which could be a helpful step in the pre-operational stage, as mentioned in Subsection 2.1. However, skipping the mosaic step and working on preprocessed scenes in SAR geometry is possible and should accelerate the system.

4. Conclusion

This study developed an automated system which provides regular surveillance over the Southeastern Mediterranean Sea and sends detections to human operators for confirmation. The performance of applying different custom-trained object detectors for YODA was evaluated in Subsection 3.1; *YODA-enh* and *YODA-enh-aug1* stood out as performing better than the others and had similar overall calibrated FDR of 23.3% and 23.9%, respectively. However, *YODA-enh* had a lower calibrated FNR of 24.0% than 32.0% from *YODA-enh-aug1*, meaning that *YODA-enh-aug1* missed more slicks. To further compare them and evaluate the slick trajectory simulation from the MEDSLIK model, several oil slicks in consecutive SAR observations were carried out in Subsection 3.2. Both *YODA-enh* and *YODA-enh-aug1* worked well in some cases but did not find oil slicks in other cases; thus, it might be important to analyse their superiority over different criteria.

Various sources of look-alikes appeared regularly in the study area and influenced the performance, especially for algae, wind-induced dark formations and ship wakes. Algae occur seasonally, and their density could be provided by chlorophyll-like pigment concentration (*chl*) data, which might help with filtering out the possible FP. In the *EastCoast* zone where wind-induced look-alikes appeared regularly, both detectors had high calibrated FDR of 48% and 41.8% for *YODA-enh* and *YODA-enh-aug1*, respectively. On the other hand, ship wakes commonly appeared in the *SouthCoast* zone with heavy ship traffic also led to high calibrated FNR of 41.1% for *YODA-enh-aug1*. Therefore, including additional information, such

2024  Y.-J. YANG ET AL.

as *chl*, synoptic conditions and ship and wake information, is suggested for providing more reliable results and determination of detection confidence and alert levels.

The proposed automated early warning oil spill surveillance system provides execution results and reports within around 1.5 h after downloading SAR observations with a GPU machine. To accelerate the system, future work could include wind speed and *chl* density information in YODA to focus on subareas of the given surveillance area, which have ideal wind speed range and low *chl* density. Alternatively, changing the system structure to work on preprocessed data in SAR geometry can also speed up the system. Oil slicks appear differently under different circumstances, such as wave height, oil volume, wind speed, oil type, sea surface temperature and currents (Bayramov, Kada, and Buchroithner 2018). Therefore, the proposed system might be limited to the types and sources of oil slicks commonly occurring in the Southeastern Mediterranean Sea. However, regarding the system as a prototype combining deep learning-based object detection algorithm and segmentation method to apply in other oil pollution hotspots is feasible.

Acknowledgements

This work is part of the DARTIS project, supported by the German Federal Ministry of Education and Research under grant number 03F0823B and the Israeli Ministry of Science and Technology under grant number 03F0823A. The authors wish to thank Copernicus for providing Sentinel-1 data on Open Access Hub.

Disclosure statement

No potential conflict of interest was reported by the author(s).

Funding

The work was supported by the Bundesministerium für Bildung und Forschung [03F0823B]; Ministry of Science and Technology, Israel [03F0823A].

ORCID

Yi-Jie Yang  <http://orcid.org/0000-0002-4098-8119>

Suman Singha  <http://orcid.org/0000-0002-1880-6868>

Data Availability statement

The data that support the findings of this study are available from the corresponding author, Y.-J. Yang, upon reasonable request.

References

- Al-Ruzouq, R., M. Barakat A Gibril, A. Shanableh, A. Kais, O. Hamed, S. Al-Mansoori, and M. Ali Khalil. 2020. "Sensors, Features, and Machine Learning for Oil Spill Detection and Monitoring: A Review." *Remote Sensing* 12 (20): 3338. <https://doi.org/10.3390/rs12203338>.

- Bayramov, E., M. Kada, and M. Buchroithner. 2018. "Monitoring Oil Spill Hotspots, Contamination Probability Modelling and Assessment of Coastal Impacts in the Caspian Sea Using SENTINEL-1, LANDSAT-8, RADARSAT, ENVISAT and ERS Satellite Sensors." *Journal of Operational Oceanography* 11 (1): 27–43. <https://doi.org/10.1080/1755876X.2018.1438343>.
- Bochkovski, A., C.-Y. Wang, and H.-Y. M. Liao. 2020. "YOLOv4: Optimal Speed and Accuracy of Object Detection." *ArXiv Preprint*. <https://doi.org/10.48550/arXiv.2004.10934>.
- Brekke, C., and A. H. S. Solberg. 2005. "Oil spill detection by satellite remote sensing." *Remote Sensing of Environment* 95 (1): 1–13. <https://doi.org/10.1016/j.rse.2004.11.015>.
- Brusch, S., S. Lehner, T. Fritz, M. Soccorsi, A. Soloviev, and B. van Schie. 2011. "Ship Surveillance with TerraSAR-X." *IEEE Transactions on Geoscience and Remote Sensing* 49 (3): 1092–1103. <https://doi.org/10.1109/TGRS.2010.2071879>.
- Carpenter, A. 2016. "European Maritime Safety Agency Activities in the Mediterranean Sea." In *The Handbook of Environmental Chemistry*, edited A. Carpenter and A. G. Kostianoy, 191–213, Vol. 83. Cham: Springer. https://doi.org/10.1007/698_2016_18.
- Dhavalikar, A. S., and P. C. Choudhari. 2022. "Detection and Quantification of Daily Marine Oil Pollution Using Remote Sensing." *Water, Air, & Soil Pollution* 233 (8): 336. <https://doi.org/10.1007/s11270-022-05752-0>.
- El-Magd, I. A., M. Zakzouk, A. M. Abdulaziz, and E. M. Ali. 2020. "The Potentiality of Operational Mapping of Oil Pollution in the Mediterranean Sea Near the Entrance of the Suez Canal Using Sentinel-1 SAR Data." *Remote Sensing* 12 (8): 1352. <https://doi.org/10.3390/rs12081352>.
- El-Magd, I. A., M. Zakzouk, E. M. Ali, and A. M. Abdulaziz. 2021. "An Open Source Approach for Near-Real Time Mapping of Oil Spills Along the Mediterranean Coast of Egypt." *Remote Sensing* 13 (14): 2733. <https://doi.org/10.3390/rs13142733>.
- European Maritime Safety Agency. 2017. "The CleanSeasnet Service: Taking Measurements to Detect and Deter Marine Pollution." Brochure. Accessed May 31, 2023. <http://www.emsa.europa.eu/csn-menu/download/2913/2123/23.html>.
- European Space Agency. 2013. "Data Distribution Schedule." Accessed April 19, 2023. <https://sentinel.esa.int/web/sentinel/missions/sentinel-1/data-distribution-schedule>.
- European Space Agency. 2020. "SNAP - ESA Sentinel Application Platform V8.0." <http://step.esa.int>.
- European Space Agency. 2022a. "End of Mission of the Copernicus Sentinel-1B Satellite." Accessed August 3, 2022. <https://sentinels.copernicus.eu/web/sentinel/-/end-of-mission-of-the-copernicus-sentinel-1b-satellite/>.
- European Space Agency. 2022b. "Launches Secured for five Sentinel Satellites." Accessed December 7, 2022. https://www.esa.int/Applications/Observing_the_Earth/Copernicus/Launches_secured_for_five_Sentinel_satellites.
- Everingham, M., L. Van Gool, C. K. Williams, J. Winn, and A. Zisserman. 2010. "The PASCAL Visual Object Classes (VOC) Challenge." *International Journal of Computer Vision* 88 (2): 303–338. <https://doi.org/10.1007/s11263-009-0275-4>.
- Fan, J., and C. Liu. 2023. "Multitask GANs for Oil Spill Classification and Semantic Segmentation Based on SAR Images." *IEEE Journal of Selected Topics in Applied Earth Observations and Remote Sensing* 16:2532–2546. <https://doi.org/10.1109/JSTARS.2023.3249680>.
- Gertman, I., A. Murashkovsky, V. Levin, G. Kallos, and D. S. Rosen. 2006. "Wave Monitoring and Wind Input as Key Issues in Operational Wave Forecasting Systems." In *Proceedings of the Fourth International Conference on EuroGOOS 'European Operational Oceanography: Present and Future'*, edited by H. Dahlin, N. C. Flemming, P. Marchand, and S. E. Petersson, 743–749. Brest, France: EuroGOOS Office and European Commission.
- Goldman, R., E. Biton, E. Brokovich, S. Kark, and N. Levin. 2015. "Oil Spill Contamination Probability in the Southeastern Levantine Basin." *Marine Pollution Bulletin* 91 (1): 347–356. <https://doi.org/10.1016/j.marpolbul.2014.10.050>.
- Goldman, R., S. Efrati, Y. Lehahn, I. Gertman, and E. Heifetz. 2014. "Comparison of Remotely Sensed Chlorophyll and Lagrangian Coherent Structures for Velocity Field Validation." In *EGU General Assembly Conference Abstracts*, 10332. Vienna, Austria.
- Gonzalez, R. C., and R. E. Woods. 2018. *Digital Image Processing*. New York, USA: Pearson Education.

- Hovland, H. A., J. A. Johannessen, and G. Digranes. 1994. "Slick Detection in SAR Images." In *Proceedings of 1994 IEEE International Geoscience and Remote Sensing Symposium (IGARSS)*, Vol. 4, 2038–2040. Pasadena, CA, USA.
- Huang, X., B. Zhang, W. Perrie, L. Yingcheng, and C. Wang. 2022. "A Novel Deep Learning Method for Marine Oil Spill Detection from Satellite Synthetic Aperture Radar Imagery." *Marine Pollution Bulletin* 179:113666. <https://doi.org/10.1016/j.marpolbul.2022.113666>.
- Kallos, G., S. Nickovic, A. Papadopoulos, D. Jovic, O. Kakaliagou, N. Misirlis, L. Boukas, et al. 1997. "The Regional Weather Forecasting System SKIRON: An Overview." In *Proceedings of the Symposium on Regional Weather Prediction on Parallel Computer Environments*, Vol. 15, 17. Athens, Greece: University of Athens, Greece.
- Korres, G., and A. Lascaratos. 2003. "A One-Way Nested Eddy Resolving Model of the Aegean and Levantine Basins: Implementation and Climatological Runs." *Annales Geophysicae* 21 (1): 205–220. <https://doi.org/10.5194/angeo-21-205-2003>.
- Kostianoy, A., E. A. Kostianaia, and D. M. Soloviev. 2020. "Oil Pollution in the Mediterranean Waters of Egypt" Edited by Elbeih, S. F., Negm, A. M., Kostianoy, A. *Environmental Remote Sensing in Egypt*. Springer Geophysics. Cham: Springer. 305–328. https://doi.org/10.1007/978-3-030-39593-3_11.
- Krestenitis, M., G. Orfanidis, K. Ioannidis, K. Avgerinakis, S. Vrochidis, and I. Kompatsiaris. 2019. "Oil Spill Identification from Satellite Images using Deep Neural Networks." *Remote Sensing* 11 (15): 1762. <https://doi.org/10.3390/rs11151762>.
- Li, Y., W. Huang, X. Lyu, S. Liu, Z. Zhao, and P. Ren. 2022. "An Adversarial Learning Approach to Forecasted Wind Field Correction with an Application to Oil Spill Drift Prediction." *International Journal of Applied Earth Observation and Geoinformation* 112:102924. <https://doi.org/10.1016/j.jag.2022.102924>.
- Mackay, D. 1980. "Calculation of the Evaporation Rate of Volatile Liquids." In *Proceedings of 1980 National Conference on Control of Hazardous Material Spills*, 361–368. Louisville, KY, USA.
- Mackay, D., I. Buist, R. Mascarenhas, and S. Paterson. 1980. *Oil Spill Processes and Models*. En40-980/1980E-PDF. Ottawa, Ontario, Canada: Environmental Impact Control Directorate.
- Mera, D., J. M. Cotos Veronica Bolon-Canedo, and A. Alonso-Betanzos. 2017. "On the Use of Feature Selection to Improve the Detection of Sea Oil Spills in SAR Images." *Computers & Geosciences* 100:166–178. <https://doi.org/10.1016/j.cageo.2016.12.013>.
- Migliaccio, M., F. Nunziata, and A. Buono. 2015. "SAR polarimetry for sea oil slick observation." *International Journal of Remote Sensing* 36 (12): 3243–3273. <https://doi.org/10.1080/01431161.2015.1057301>.
- Papadopoulos, A., P. Katsafados, and G. Kallos. 2001. "Regional Weather Forecasting for Marine Application." *Global Atmosphere Ocean System* 8 (2–3): 219–237. <https://doi.org/10.1080/1023673029000003543>.
- Polinov, S., R. Bookman, and N. Levin. 2021. "Spatial and Temporal Assessment of Oil Spills in the Mediterranean Sea." *Marine Pollution Bulletin* 167:112338. <https://doi.org/10.1016/j.marpolbul.2021.112338>.
- Redmon, J., S. Divvala, R. Girshick, and A. Farhadi. 2016. "You Only Look Once: Unified, Real-Time Object Detection." In *2016 IEEE Conference on Computer Vision and Pattern Recognition (CVPR)*, 779–788. Las Vegas, NV, USA.
- Shaban, M., R. Salim, H. Abu Khalifeh, A. Khelifi, A. Shalaby, S. El-Mashad, A. Mahmoud, M. Ghazal, and A. El-Baz. 2021. "A Deep-Learning Framework for the Detection of Oil Spills from SAR Data." *Sensors* 21 (7): 7. <https://doi.org/10.3390/s21072351>.
- Singha, S., T. J. Bellerby, and O. Trieschmann. 2013. "Satellite Oil Spill Detection Using Artificial Neural Networks." *IEEE Journal of Selected Topics in Applied Earth Observations and Remote Sensing* 6 (6): 2355–2363. <https://doi.org/10.1109/JSTARS.2013.2251864>.
- Singha, S., R. Ressel, D. Velotto, and S. Lehner. 2016. "A Combination of Traditional and Polarimetric Features for Oil Spill Detection Using TerraSAR-X." *IEEE Journal of Selected Topics in Applied Earth Observations and Remote Sensing* 9 (11): 4979–4990. <https://doi.org/10.1109/JSTARS.2016.2559946>.

- Singha, S., M. Vespe, and O. Trieschmann. 2013. "Automatic Synthetic Aperture Radar Based Oil Spill Detection and Performance Estimation via a Semi-Automatic Operational Service Benchmark." *Marine Pollution Bulletin* 73 (1): 199–209. <https://doi.org/10.1016/j.marpolbul.2013.05.022>.
- Solberg, A. H. S., and R. Solberg. 1996. "A Large-Scale Evaluation of Features for Automatic Detection of Oil Spills in ERS SAR Images." In *Proceedings of 1996 IEEE International Geoscience and Remote Sensing Symposium (IGARSS)*, Vol. 3, 1484–1486. Lincoln, NE, USA.
- Solberg, A. H. S., G. Storvik, R. Solberg, and E. Volden. 1999. "Automatic Detection of Oil Spills in ERS SAR Images." *IEEE Transactions on Geoscience and Remote Sensing* 37 (4): 1916–1924. <https://doi.org/10.1109/36.774704>.
- Stathakis, D., K. Topouzelis, and V. Karathanassi. 2006. "Large-Scale Feature Selection Using Evolved Neural Networks." In *Image and Signal Processing for Remote Sensing XII*, edited by L. Bruzzone, 636513. Vol. 6365. Stockholm, Sweden: International Society for Optics and Photonics, SPIE. <https://doi.org/10.1117/12.688149>.
- Stevens, J. 2020. "NASA Earth Observatory Map." Accessed September 8, 2020. <https://visibleearth.nasa.gov/images/147190/explorer-base-map>.
- Tang, D., J. Sun, L. Zhou, S. Wang, R. P. Singh, and G. Pan. 2019. "Ecological Response of Phytoplankton to the Oil Spills in the Oceans." *Geomatics, Natural Hazards and Risk* 10 (1): 853–872. <https://doi.org/10.1080/19475705.2018.1549110>.
- Tings, B., A. Pleskachevsky, and S. Wiehle. 2023. "Comparison of Detectability of Ship Wake Components Between C-Band and X-Band Synthetic Aperture Radar Sensors Operating Under Different Slant Ranges." *ISPRS Journal of Photogrammetry and Remote Sensing* 196:306–324. <https://doi.org/10.1016/j.isprsjprs.2022.12.008>.
- Topouzelis, K. N. 2008. "Oil Spill Detection by SAR Images: Dark Formation Detection, Feature Extraction and Classification Algorithms." *Sensors* 8 (10): 6642–6659. <https://doi.org/10.3390/s8106642>.
- Topouzelis, K., V. Karathanassi, P. Pavlakis, and D. Rokos. 2007. "Detection and Discrimination Between Oil Spills and Look-Alike Phenomena Through Neural Networks." *ISPRS Journal of Photogrammetry and Remote Sensing* 62 (4): 264–270. <https://doi.org/10.1016/j.isprsjprs.2007.05.003>.
- Wessel, P., and W. H. F. Smith. 1996. "A Global, Self-Consistent, Hierarchical, High-Resolution Shoreline Database." *Journal of Geophysical Research: Solid Earth* 101 (B4): 8741–8743. <https://doi.org/10.1029/96JB00104>.
- Yang, Y.-J., S. Singha, and R. Mayerle. 2022. "A Deep Learning Based Oil Spill Detector Using Sentinel-1 SAR Imagery." *International Journal of Remote Sensing* 43 (11): 4287–4314. <https://doi.org/10.1080/01431161.2022.2109445>.
- Zodiatis, G., G. Coppini, L. Perivoliotis, R. Lardner, T. Alves, N. Pinardi, S. Liubartseva, M. De Dominicis, E. Bourma, and A. Augusto Sepp Neves. 2017. "Numerical Modeling of Oil Pollution in the Eastern Mediterranean Sea." In *The Handbook of Environmental Chemistry*, edited by A., Carpenter and A. Kostianoy, 215–254. Vol. 83. Cham: Springer. https://doi.org/10.1007/698_2017_131.
- Zodiatis, G., M. De Dominicis, L. Perivoliotis, H. Radhakrishnan, E. Georgoudis, M. Sotillo, R. W. Lardner, et al. 2016. "The Mediterranean Decision Support System for Marine Safety Dedicated to Oil Slicks Predictions." *Deep Sea Research Part II: Topical Studies in Oceanography* 133:4–20. <https://doi.org/10.1016/j.dsr2.2016.07.014>.
- Zodiatis, G., R. Lardner, T. M. Alves, Y. Krestenitis, L. Perivoliotis, S. Sofianos, and K. Spanoudaki. 2017. "Oil Spill Forecasting (Prediction)." *Journal of Marine Research* 75 (6): 923–953. <https://doi.org/10.1357/002224017823523982>.
- Zodiatis, G., R. Lardner, D. Solovyov, X. Panayidou, and M. De Dominicis. 2012. "Predictions for Oil Slicks Detected from Satellite Images Using MyOcean Forecasting Data." *Ocean Science* 8 (6): 1105–1115. <https://doi.org/10.5194/os-8-1105-2012>.

5 Summary

The aim of this thesis is to develop an oil spill detection system that can contribute to the early management of oil spill incidents. The concept of the system has been presented in Section 1.4: a deep learning-based object detector targets the oil spills and is followed by a segmentation method to obtain the final oil binary masks indicating the location of the oil. Data-driven deep learning methods generally require a large amount of data to train the model, which hinders many research works from applying their own architectures to oil spill detection tasks. Therefore, Section 3.1 has presented a part of the dataset used in this thesis, which can be further used in other studies. Before developing such an oil spill detection system, it is important to understand different ocean SAR signatures so that false alarms of oil spills can be avoided; comprehensive explanations were provided in Section 3.2. Afterwards, Section 4.1 has evaluated the capability of the object detector to target oil slicks. The implementation of the oil spill detection system was carried out in Section 4.2. Section 1.5 has addressed the research questions that should be considered in accordance with the entire system development process. These questions have already been implicitly answered in Chapters 3 and 4. A summary and concise answers to these questions are provided in Section 5.1.

From the beginning of this thesis to the present, many studies have provided valuable insights into oil slick detection. However, this thesis still makes a unique contribution to the field, as summarized in Section 5.2. The developed system has been continuously maintained and improved since the articles addressed in the thesis were published. Section 5.3 summarizes the current state of the system. As mentioned in Subsection 1.2.3, different platforms play unique roles in overall oil spill surveillance. This thesis focuses on the benefits of spaceborne SAR; however, in addition to the spaceborne SAR oil spill detection system, other information can be integrated to better support clean-up operations. Therefore, Section 5.4 offers an outlook of the study, highlighting its potential future developments that could benefit society.

5.1 Progress on research questions

A set of research questions were raised in Section 1.5, which will be answered below based on the results presented in this thesis.

1. How can different oceanic phenomena manifest in SAR imagery?

(Section 3.2)

Sea surface roughness is generally considered a key factor for ocean applications using SAR. Wind speed plays an important role in oceanography because it directly affects the surface roughness and produces certain signatures. Sudden changes in wind speed and direction can create a wind front, shown as a boundary between weaker and stronger radar backscatter; such signatures can be observed near the coast at night when the wind blows offshore, resulting in land breeze wind fronts. Similarly, the katabatic wind blows over coastal terrain toward the sea and spreads out as a fan shape. Moreover, the instability of the ABL can lead to convective cells, which cause fluctuations in surface roughness and create cellular patterns in SAR images, and can also lead to the occurrence of helical roll vortices, which are seen as dark and bright wind streaks. As for rainfall, rain-induced signatures are a combination of surface scattering, volume scattering, and attenuation of the radar pulse. Rain cells can create downward airflow (i.e. downdraft) and roughen the sea surface, which can be seen as bright elliptical areas. The rain drops can either dampen or roughen the sea surface, and the splash products from rain drops can cause strong backscatter.

In addition to atmospheric and weather conditions, various phenomena can cause convergence or divergence of the ocean surface, roughen or smooth the gravity-capillary waves, and thus induce high or low radar backscatter. Furthermore, the accumulation of surface films can contribute to the dampening of the waves and result in dark formations in SAR images. Disturbances in the stratified ocean or atmosphere can induce internal waves, also known as OIW and AGWs, respectively. The particle motion of the internal waves creates surface convergence and divergence, which appear as light and dark strips in SAR images. Regions of mixing and vertical advection are also likely to have some notable SAR signatures. For example, an upwelling region is an area that tends to exhibit increased ABL stability, increased surface water viscosity, the presence of biogenic surface films, and surface divergence. All of these contribute to low radar backscatter. Eddies can also induce areas of surface convergence and divergence, and surface films tend to accumulate along the current shear, resulting in SAR signatures of spiral shear lines.

2. How can oceanic phenomena be discriminated from oil slicks in SAR?

(Section 3.2)

Various oceanic phenomena can produce dark formations in SAR and can be difficult to distinguish from oil slicks. However, additional data, such as sea surface wind speed,

SST, chl-*a* concentration, bathymetry and topography, can be used to provide more information. First of all, the sea surface wind speed can be used to determine whether or not a SAR acquisition is within the optimal wind speed range between 2–3 m/s and 7–12 m/s for oil spill detection (Brekke & Solberg, 2005; Gade et al., 2000; Robinson, 2004). It can also indicate whether the conditions are ideal for observing OIWs, which are typically observed by SAR in low wind areas. As they tend to occur close to an upwelling area or where there is rough topography, shallow underwater ridges, sea mounts or steep shelves, a bathymetric model can be used to help interpret possible OIWs. On the other hand, similar signatures of AGWs usually occur in areas where, for example, the wind interacts with mountain ranges, different air masses collide, and strong wind shear occurs, so wind direction and terrain models can be helpful. Terrain models also provide the possible coastal areas where katabatic winds are likely to occur during the night and produce certain fan-shaped signatures off the coast.

Biogenic surface films are the most common look-alikes that are challenging for oil spill detection methods using SAR to distinguish from oil slicks; chl-*a* concentrations are used for phytoplankton biomass and can therefore be used to identify the biogenic surface films. Areas of mixing and vertical advection can lead to the growth of nutrients and hence the presence of biogenic surface films; the sea surface temperature also changes due to vertical water exchange. In addition, biogenic surface films tend to accumulate along the current shear in fronts and eddies. However, other suspended particulates can also cause the eddies to become more pronounced on SAR imagery, but they may not be reflected in the chl-*a* concentration.

Other sources of look-alikes that are important, especially in an area with high ship traffic or wind farms, are the wakes from ships or wind turbines. The wakes can be very similar to oil slicks that have remained on the ocean for a few days, whose radar backscatter may become less distinct after physical processes such as evaporation, or similar to tanker wash residues that are a mixture of oil and water. Since ship wakes are associated with the movement of the ship, they tend to have relatively linear patterns. On the other hand, the physical transport of oil is related to its properties as well as environmental conditions. As a result, they rarely follow specific linear patterns after physical transport. Depending on the spatial resolution of SAR sensors, ships and wind turbines may not always be visible; thus, AIS data and offshore infrastructure maps, such as European Marine Observation and Data Network (EMODnet), can be helpful in determining the locations of ships and wind turbines. Note that those offshore infrastructure maps also provide locations of oil and gas exploitation and exploration activities, which can be the source of oil leakage.

3. Can deep learning-based object detectors be used to detect oil slicks and distinguish between oil slicks and look-alikes? (Section 4.1 and Section 4.2)

Many deep learning-based object detection algorithms have been pre-trained on a large labeled dataset, such as ImageNet (Deng et al., 2009), Microsoft COCO (Lin et al., 2014), and PASCAL VOC (Everingham et al., 2012), and users can take a pre-trained model as a starting point to perform transfer learning on their specific tasks. However, since these detectors focus on optical images, how they perform with SAR images needed to be evaluated; therefore, a manually inspected oil slick dataset was prepared.

In the preliminary phase of this study, the pre-trained YOLO model was custom trained on the oil dataset with images in radar backscatter values in decibels and in radar backscatter values but normalized to 8-bit integer values. The model trained with normalized images performed better and faster because the normalization eliminates the difference between the backscatter values of different images and limits the numbers to integers. Such a detector can successfully identify oil slicks in SAR images with average precision (AP) of 69.10% and 68.69% on the validation and test sets, respectively, demonstrating the capability of object detectors to target oil slicks in SAR. However, with a limited number of images covering look-alikes, the detector did not perform well in distinguishing oil slicks from look-alikes. Therefore, a collection of look-alikes and other remarkable phenomena was used to further train the model, which decreased the false discovery rate (FDR) on one month of data from 69.2% to 21.0%, but the false negative rate (FNR) were increased from 3.4% to 20.7%. The performance of the model was further improved by training with different data augmentation configurations. In this thesis, the object detector learns only one class of object (i.e. oil), images with look-alikes were not given any annotation and were therefore regarded as background information for the object detectors. The variety of oil slicks and look-alikes that are provided in the training influences how well the object detector can distinguish between oil slicks and look-alikes.

4. What are the look-alikes that could lead to confusions for deep learning-based object detectors? (Section 3.2 and Section 4.2)

To evaluate the performance and limitations of the oil detection algorithm in different regions of the study area, it was tested on one year of data from 2019, and its performance was assessed by zone. More examples collected during the operational phase of the system were presented in Section 4.2 as examples for oil slick trajectory simulation. The custom trained object detectors used in YODA were also tested on a

no-oil dataset where image patches do not contain oil objects. The dataset was first separated into *coast* and *water* subsets, depending on whether the image patch covered land area or not, and then categorized into different subgroups using the unsupervised K-Means clustering method.

Overall, there were higher proportions of coastal image patches (i.e. *coast* subset) which the model returned detections. In the east coast of the Mediterranean Sea, wind-induced signatures, such as katabatic wind-induced fan-shape signatures and wind shadows, were common sources of look-alikes close to the coast. Oil slicks may not be observed with high confidence, especially in combination with low wind conditions in some months (e.g., September and October 2019). Slightly further from the coast, OIWs in certain areas can be generated due to steep shelves. In these regions, pollution likely comes from land-sourced spills or ship-based discharges. Note that the chemical spills in this thesis were broadly treated as “oil” objects. In contrast to the east coast, where wind-induced look-alikes were quite dominant, the south coast has heavy shipping traffic and ship wakes can be a common source of look-alikes.

For the non-coastal image patches (i.e. *water* subset), there seem to be more detections in the nw-04 and nw-06 subgroups. As the subgroups were categorized using the unsupervised K-Means clustering method, they were not labeled as specific sources of look-alikes. However, based on human interpretation, the image patches in these two subgroups appear to primarily consist of filamentous dark formations that could be small areas of mesoscale eddies. Since the Levantine Basin is dominated by anticyclonic eddies that last longer than six months according to the literature (Pegliasco et al., 2021), some scenes covered mesoscale eddies which showed pronounced accumulation of surface films along the current shear. Compared to the Western Mediterranean Sea, the chl-*a* concentration in the Eastern Mediterranean Sea is low, even during the blooming season in the late winter and early spring. Therefore, it is difficult to determine whether or not the spiral patterns of eddies seen by SAR are due to the accumulation of biogenic surface films. As a result, it may not be possible to use the chl-*a* concentration to filter out the areas likely to contain algae rather than oil slicks. Similarly, in the upwelling areas where chlorophyll growth is expected, the chl-*a* concentration was not high enough to create a threshold for targeting these areas. Rather, it can be used as an additional piece of information to check the detection results in the end.

5. How well do deep learning-based methods perform when applied to an operational oil spill monitoring system? (Section 4.2)

The main motivation of this thesis is to develop an automated oil spill monitoring system that can contribute to society. Although various services have been introduced

in Subsection 1.2.3, the application of deep learning-based methods as part of an operational system has not been shown much in previous studies. Section 4.2 presented the system developed in this thesis; the oil spill detection unit contains YODA and a segmentation method. Two object detectors were applied to YODA as YODA-enh and YODA-enh-aug1 and their performance in different regions was discussed. The FDR and the FNR were calculated to indicate the system performance; FDR shows the ratio of false positives among all the detections; FNR shows the ratio of false negatives among all the manual inspected oil slicks. Overall, YODA-enh had a FDR of 23.3 % and a FNR of 24.0 %; YODA-enh-aug1 had a FDR of 23.9 % and a FNR of 32.0 %. They had a similar FDR, however, YODA-enh-aug1 missed more oil slicks and had a higher FNR. Both of them had a relatively high FDR, 48.0 % and 41.8 %, in the zone between 5 km and 22 km off the Lebanese and Israeli coasts. Look-alikes in the coastal areas, especially at the east coast of the Mediterranean, seemed to be more complicated to distinguish from actual oil spills, and some of these look-alikes were also difficult to interpret manually. Therefore, the system also had some difficulties targeting oil slicks in this region. As explained in Section 3.2, supplementary data can help with the interpretation. In other words, including other data sources into the system could possibly help improve the performance of the system.

For an operational system, not only the performance is important, but also the latency. The operational system took about 1.5 h from obtaining the Sentinel-1 scenes to delivery of oil binary masks. Typically, four Sentinel-1 scenes are covered within the study area for each track. They are pre-processed together and then form a mosaic of the latest SAR coverage over the study area, which provides a more straightforward way to visualize the entire area and compare it to the previous scenes. However, this step took about 10–25 min, which could be skipped to speed up the system. This thesis proved the possibility of building such an early warning system with SAR and deep learning-based object detectors. However, further improvements on its accuracy and latency are foreseen.

In addition to operating system latency, the time from SAR observation to availability for download by users should also be considered. In the study area, SAR images are typically taken at around 03:30–04:05 for descending acquisitions and 15:30–16:05 for ascending acquisitions, with images available online at around 22:00. The ERATOS-THENES Centre of Excellence in Cyprus and the German Aerospace Center (DLR) teams in the EXCELSIOR H2020 project are collaborating to establish an Earth observation data acquisition station. This station will provide real-time satellite data for the Eastern Mediterranean, Middle East, and North Africa regions (EXCELSIOR 2020, 2025). In the near future, the delay between SAR observations and user availability

may no longer be a bottleneck in these regions.

5.2 Integration of the results into the current level of knowledge

Early studies followed a conventional workflow of dark spot segmentation, feature extraction, and classification. The focus was on obtaining as much information as possible about the features of oil. The launch of Sentinel-1 in 2014 marked a new era in the detection of oil pollution using SAR. Since then, an increasing number of research papers have been published on using deep learning methods. Many of these studies have proposed semantic segmentation models that provide reliable pixel-wise classification of oil slicks. However, most of these studies approached oil slick detection as a deep learning task, focusing primarily on developing novel model architectures. Therefore, there is a lack of emphasis on how to apply these methods to an operational system that can address oil pollution in the real world.

This thesis presents a two-step system that employs an object detector-based model, YODA, to identify oil slicks and a segmentation method to generate final binary masks of the oil. A recent study addressed a similar approach, using an object detector based on Faster R-CNN to locate oil slicks. However, instead of using a mathematically based segmentation method, the authors applied a semantic segmentation model, U-Net++, to obtain the final binary masks (X. Huang et al., 2025). Another study used YOLOv8 as an object detector, followed by an adapted Segment Anything Model to obtain the masks of categories, including oil spill, look-alike, ship, land, and sea surface. The final results were returned from an ordered mask fusion module that fuses the masks and categories (Wu et al., 2024). Deep learning methods are still evolving, and scientists and engineers continue to develop computational-efficient models. Recent models can likely provide better detection results than the one proposed in this thesis. However, this thesis provides a basic structure that can be used with any deep learning model.

5.3 Further improvement on the oil slick detection algorithm

The oil spill detection system introduced in Section 4.2 was operational from August 2022 until the end of October 2023, regularly sending results to the local partner; the system was tested for two months before being put into operation. All results were double-checked by the candidate before being sent to avoid any false alarms. It took about 1.5 h from obtaining the Sentinel-1 scenes (typically four scenes covering the study area) to delivering the binary masks. The Sentinel-1 scenes were georeferenced in the pre-processing step, and a mosaic of the most recent coverage of pre-processed SAR

in the study area was then generated. The mosaics provide an easy way to compare SAR with other information, such as wind speed and sea surface temperature, and are particularly useful in the early stages of system development.

These mosaics cover the entire study area, which is larger than the area covered by the most recent SAR acquisitions. Therefore, an additional step is applied to focus only on the latest acquisitions. Spaceborne SAR is observed with an azimuth angle, which is a non-zero angle relative to the north direction. Consequently, geolocated SAR scenes appear as parallelograms in the mosaic image. Image patches are generated in geocoordinates, so edge patches include both the latest and old acquisitions. Thus, an additional step is necessary to obtain the observed date and time of the detected objects. However, these additional steps can be eliminated if all operations are performed in SAR geometry instead.

Therefore, the system was revised so that all operations are performed in SAR geometry, but the final oil binary masks are geocoded for easy tracking of their locations. With such revisions, operating the system on the same four SAR scenes can be reduced to about 17 min. This improvement was presented and published in a conference paper (Yang & Schnupfhnag, 2024). Later, the latency of the system was further improved by revision of different parameters given to the system execution. For two Sentinel-1 scenes, it took around 6 min 8 s from obtaining the scenes to delivering the oil binary masks. A detailed explanation on the system improvements is presented in another conference paper (Yang & Schnupfhnag, 2025).

5.4 Outlook

This thesis has presented an automated oil spill detection system using SAR with the test area in the Southeastern Mediterranean Sea. The capability of using object detection algorithms to build such a system has been evaluated. Currently, the system only uses Sentinel-1 SAR data because they are free of charge and follow a fixed schedule. However, SAR data from other missions can also be included in the system either for regular surveillance or on demand when oil slicks are detected. Moreover, the automated download and processing of spaceborne optical images before and after the SAR observations with detected oil slicks can be considered. This can help to extend the temporal observation of the spill.

The current system provides detections with their locations and the confidence scores returned by the object detector. However, additional information, such as wind speed, wind direction, offshore gas and oil installations, and AIS data, can help provide a more complete understanding of the local conditions of the SAR observations. In addition,

ESI maps should be provided to the system to identify environmentally sensitive areas and address the risk level of the oil. By integrating different types of information into the system, decision support teams can get a more complete picture of the incident. Unfortunately, such information is not publicly available in some areas. In addition, in order to expand the system to other study areas, the system should first be tested for its ability to detect oil spills in those areas, as the sources and shapes of the oil pollution may be different and affect the detection ability. Therefore, local oil spill reports can help in collecting incidents for verification of the system, but such reports may not be accessible or may be limited to local languages. Moreover, clean-up operations require action by local authorities. All of these reasons underscore the necessity and importance of local cooperation in pollution monitoring and management.

The delay between SAR observation and availability for users, as mentioned in Subsection 5.1, includes the time from observation to contact with the nearest ground station for downlink and further data processing at the ground stations (e.g. the generation of Level-1 data). Oil slicks on the ocean surface change rapidly with time, currently the fate of oil relies on model simulation. Therefore, on-board processing has been considered for time-critical applications. Instead of processing data at ground stations, moving this step, and even the detection of oil, to the satellite can reduce overall latency and make emergency response more efficient. However, the computing power on-board of satellites is significantly lower compared to ground stations due to power limitations and hardening against radiation, requiring efficient software implementation optimized for the target hardware. Previous studies provided a prototype that mimicked on-board hardware resources for image formation (i.e., from raw data to Level-1 data), alert generation for ship detection and extreme weather detection (Wiehle et al., 2022), and the application of computationally complex deep learning-based methods (Günzel & Mandapati, 2025). These studies highlighted the possibility of future work on on-board processing of oil spill detection, which could be of great assistance in oil spill management.

Bibliography

- Abdulla, A., & Linden, O. (Eds.). (2008). *Maritime traffic effects on biodiversity in the Mediterranean Sea. volume 1, review of impacts, priority areas and mitigation measures*. IUCN.
- About El-Magd, I., Zakzouk, M., Abdulaziz, A. M., & Ali, E. M. (2020). The potentiality of operational mapping of oil pollution in the Mediterranean Sea near the entrance of the Suez Canal using Sentinel-1 SAR data. *Remote Sensing*, 12(8), 1352. <https://doi.org/10.3390/rs12081352>
- About Samra, R. M., & Ali, R. R. (2024). Tracking the behavior of an accidental oil spill and its impacts on the marine environment in the Eastern Mediterranean. *Marine pollution bulletin*, 198, 115887. <https://doi.org/10.1016/j.marpolbul.2023.115887>
- Adamo, M., de Carolis, G., de Pasquale, V., & Pasquariello, G. (2009). Detection and tracking of oil slicks on sun-glittered visible and near infrared satellite imagery. *International Journal of Remote Sensing*, 30(24), 6403–6427. <https://doi.org/10.1080/01431160902865772>
- Aitani, A. M. (2004). Oil refining and products. In *Encyclopedia of energy* (pp. 715–729). Elsevier. <https://doi.org/10.1016/B0-12-176480-X/00259-X>
- Akpınar, A., Yılmaz, E., Fach, B., & Salihoglu, B. (2016). Physical oceanography of the eastern mediterranean sea. *The Turkish part of the Mediterranean sea*, 43, 250.
- Aksu, A. E., Hall, J., Yaltırak, C., Çınar, E., Küçük, M., & Çifçi, G. (2014). Late Miocene–recent evolution of the Finike Basin and its linkages with the Beydağları complex and the Anaximander Mountains, Eastern Mediterranean. *Tectonophysics*, 635, 59–79. <https://doi.org/10.1016/j.tecto.2014.04.042>
- Alpers, W., & Huang, W. (2011). On the discrimination of radar signatures of atmospheric gravity waves and oceanic internal waves on synthetic aperture radar images of the sea surface. *IEEE Transactions on Geoscience and Remote Sensing*, 49(3), 1114–1126. <https://doi.org/10.1109/TGRS.2010.2072930>
- Amri, E., Benoit, A., Philippe, B., Migebielle, V., Conche, B., & Oppenheim, G. (2020). Offshore oil slicks detection from SAR images through the Mask-RCNN

- deep learning model. *2020 International Joint Conference on Neural Networks (IJCNN)*, 1–8. <https://doi.org/10.1109/IJCNN48605.2020.9206652>
- Amri, E., Dardouillet, P., Benoit, A., Courteille, H., Bolon, P., Dubucq, D., & Credo, A. (2022). Offshore oil slick detection: From photo-interpreter to explainable multi-modal deep learning models using SAR images and contextual data. *Remote Sensing*, *14*(15), 3565. <https://doi.org/10.3390/rs14153565>
- Astraldi, M., Balopoulos, S., Candela, J., Font, J., Gacic, M., Gasparini, G., Manca, B., Theocharis, A., & Tintoré, J. (1999). The role of straits and channels in understanding the characteristics of Mediterranean circulation. *Progress in Oceanography*, *44*(1-3), 65–108. [https://doi.org/10.1016/S0079-6611\(99\)00021-X](https://doi.org/10.1016/S0079-6611(99)00021-X)
- Baghdady, S. M., & Abdelsalam, A. A. (2024). Ten years of oil pollution detection in the Eastern Mediterranean shipping lanes opposite the Egyptian coast using remote sensing techniques. *Scientific reports*, *14*(1), 18057. <https://doi.org/10.1038/s41598-024-67983-x>
- Barron, M. G., Vivian, D. N., Heintz, R. A., & Yim, U. H. (2020). Long-term ecological impacts from oil spills: Comparison of Exxon Valdez, Hebei Spirit, and Deepwater Horizon. *Environmental Science & Technology*, *54*(11), 6456–6467. <https://doi.org/10.1021/acs.est.9b05020>
- Bayramov, E., Kada, M., & Buchroithner, M. (2018). Monitoring oil spill hotspots, contamination probability modelling and assessment of coastal impacts in the Caspian Sea using Sentinel-1, Landsat-8, RADARSAT, Envisat and ERS satellite sensors. *Journal of Operational Oceanography*, *11*(1), 27–43. <https://doi.org/10.1080/1755876X.2018.1438343>
- Bern, T. I., Wahl, T., Andersen, T., & Olsen, R. (1993). Oil spill detection using satellite based SAR - experience from a field experiment. *Photogrammetric Engineering and Remote Sensing; (United States)*, *59*:3. <https://www.osti.gov/biblio/6311687>
- Biegert, E. K., Berry, J. L., Baker, R. N., Dupont, D., & Scantland, S. (1997). Gulf offshore applications project detects oil slicks using RADARSAT. *International symposium on geomatics in the era of RADARSAT*.
- Bonn Agreement. (2022). Bonn agreement aerial operations handbook. Retrieved June 19, 2025, from https://www.bonnagreement.org/site/assets/files/17600/aoh_part_iii_guidelines_detection_investigation_evaluation.pdf
- Boyd, J. N., Scholz, D., & Walker, A. H. (2001). *American Petroleum Institute*. Retrieved May 28, 2025, from <https://meridian.allenpress.com/iosc/article/2001/2/1213/138698/EFFECTS-OF-OIL-AND-CHEMICALLY-DISPERSED-OIL-IN-THE>

- Brakstad, O. G., Farooq, U., Ribicic, D., & Netzer, R. (2018). Dispersibility and biotransformation of oils with different properties in seawater. *Chemosphere*, 191, 44–53. <https://doi.org/10.1016/j.chemosphere.2017.10.012>
- Brandt, P., Rubino, A., Quadfasel, D., Alpers, W., Sellschopp, J., & Fiekas, H.-V. (1999). Evidence for the influence of Atlantic–Ionian Stream fluctuations on the tidally induced internal dynamics in the Strait of Messina. *Journal of Physical Oceanography*, 29(5), 1071–1080. [https://doi.org/10.1175/1520-0485\(1999\)029<1071:EFTIOA>2.0.CO;2](https://doi.org/10.1175/1520-0485(1999)029<1071:EFTIOA>2.0.CO;2)
- Brekke, C., & Solberg, A. H. (2005). Oil spill detection by satellite remote sensing. *Remote Sensing of Environment*, 95(1), 1–13. <https://doi.org/10.1016/j.rse.2004.11.015>
- Brown, C. E. (2025). Chapter 8 - Laser fluorosensors for oil spill detection. In M. Fingas (Ed.), *Oil spill science and technology* (pp. 525–544). Elsevier. <https://doi.org/10.1016/B978-0-443-21703-6.00010-2>
- Brown, C. E., & Fingas, M. (2005). A review of current global oil spill surveillance, monitoring and remote sensing capabilities. *Proceedings of the Twenty-Eighth Arctic and Marine Oil Spill Program Technical Seminar. Environment Canada, Ottawa, Ontario*, 789–798.
- Brown, C. E., & Fingas, M. F. (2003). Review of the development of laser fluorosensors for oil spill application. *Marine pollution bulletin*, 47(9-12), 477–484. [https://doi.org/10.1016/S0025-326X\(03\)00213-3](https://doi.org/10.1016/S0025-326X(03)00213-3)
- Buettner, K. J. K., & Kern, C. D. (1965). The determination of infrared emissivities of terrestrial surfaces. *Journal of Geophysical Research*, 70(6), 1329–1337. <https://doi.org/10.1029/JZ070i006p01329>
- Busler, J., Wehn, H., & Woodhouse, L. (2015). Tracking vessels to illegal pollutant discharges using multisource vessel information. *The International Archives of the Photogrammetry, Remote Sensing and Spatial Information Sciences*, XL-7/W3, 927–932. <https://doi.org/10.5194/isprsarchives-XL-7-W3-927-2015>
- Carpenter, A., & Kostianoy, A. G. (Eds.). (2018). *Oil pollution in the Mediterranean Sea: Part I: The international context*. Springer International Publishing.
- Catoe, C. E. (1973). Remote sensing techniques for detecting oil slicks. *Journal of Petroleum Technology*, 25(03), 267–278. <https://doi.org/10.2118/3941-PA>
- Cerdeiro, D. A., Komaromi, A., Liu, Y., & Saeed, M. (2020). *World seaborne trade in real time: A proof of concept for building AIS-based nowcasts from scratch*. International Monetary Fund. <https://doi.org/10.5089/9781513544106.001>
- Chen, B., Ye, X., Zhang, B., Jing, L., & Lee, K. (2019). Chapter 22 - Marine oil spills—preparedness and countermeasures. In C. Sheppard (Ed.), *World seas:*

- An environmental evaluation* (pp. 407–426). Academic Press. <https://doi.org/10.1016/B978-0-12-805052-1.00025-5>
- Chen, T., & Lu, S. (2017). Subcategory-aware feature selection and SVM optimization for automatic aerial image-based oil spill inspection. *IEEE Transactions on Geoscience and Remote Sensing*, 55(9), 5264–5273. <https://doi.org/10.1109/TGRS.2017.2704107>
- Chiggiato, J., Schroeder, K., Mourre, B., Miramontes, E., Lionello, P., Marcos, M., Pinardi, N., Mason, E., Álvarez, M., & Trincardi, F. (2023). Chapter 1 - Introduction. In K. Schroeder & J. Chiggiato (Eds.), *Oceanography of the Mediterranean Sea* (pp. 1–11). Elsevier. <https://doi.org/10.1016/B978-0-12-823692-5.00002-9>
- Clark, R. N., Swayze, G. A., Leifer, I., Livo, K. E., Kokaly, R., Hoefen, T., Lundeen, S., Eastwood, M., Green, R. O., Pearson, N., et al. (2010). *A method for quantitative mapping of thick oil spills using imaging spectroscopy*. US Department of the Interior, Geological Survey.
- Cosoli, S., Drago, A., Ciralo, G., & Capodici, F. (2015). Tidal currents in the Malta–Sicily Channel from high-frequency radar observations. *Continental Shelf Research*, 109, 10–23. <https://doi.org/10.1016/j.csr.2015.08.030>
- Cotton, D. (2007). MARCOAST - operational marine oil spill and water quality monitoring services. *OCEANS 2007 - Europe*, 1–5. <https://doi.org/10.1109/OCEANSE.2007.4302252>
- Curl, H. C., & O'Donnell, K. (1977). Chemical and physical properties of refined petroleum products. *NOAA Technical Memorandum ERL MESA-17*.
- D'Affonseca, F. M., Vieira Reis, F. A. G., Corrêa, C. V. d. S., Wieczorek, A., Giordano, L. d. C., Marques, M. L., Rodrigues, F. H., Costa, D. M., Kolya, A. d. A., Veiga, V. M., Santos, S. F., Magalhães, L. M., Gatto, I. T., & Riedel, P. S. (2023). Environmental sensitivity index maps to manage oil spill risks: A review and perspectives. *Ocean & Coastal Management*, 239, 106590. <https://doi.org/10.1016/j.ocecoaman.2023.106590>
- Danovaro, R. (2003). Pollution threats in the Mediterranean Sea: An overview. *Chemistry and Ecology*, 19(1), 15–32. <https://doi.org/10.1080/0275754031000081467>
- de Laurentiis, L., Jones, C. E., Holt, B., Schiavon, G., & Del Frate, F. (2021). Deep learning for mineral and biogenic oil slick classification with airborne synthetic aperture radar data. *IEEE Transactions on Geoscience and Remote Sensing*, 59(10), 8455–8469. <https://doi.org/10.1109/TGRS.2020.3034722>

- Del Frate, F., Petrocchi, A., Lichtenegger, J., & Calabresi, G. (2000). Neural networks for oil spill detection using ERS-SAR data. *IEEE Transactions on Geoscience and Remote Sensing*, 38(5), 2282–2287. <https://doi.org/10.1109/36.868885>
- Deng, J., Dong, W., Socher, R., Li, L.-J., Kai Li, & Li Fei-Fei. (2009). ImageNet: A large-scale hierarchical image database. *2009 IEEE Conference on Computer Vision and Pattern Recognition*, 248–255. <https://doi.org/10.1109/CVPR.2009.5206848>
- Dong, Y., Liu, Y., Hu, C., MacDonald, I. R., & Lu, Y. (2022). Chronic oiling in global oceans. *Science (New York, N.Y.)*, 376(6599), 1300–1304. <https://doi.org/10.1126/science.abm5940>
- Dyring, A., & Fäst, O. (2004). MSS 6000 puts the aircraft in the oil spill tracking network. *Interspill 2004*. https://www.interspill.org/downloads/archive/420_dyringfost.pdf
- Ediger, D., & Yilmaz, A. (1996). Characteristics of deep chlorophyll maximum in the Northeastern Mediterranean with respect to environmental conditions. *Journal of Marine Systems*, 9(3), 291–303. [https://doi.org/10.1016/S0924-7963\(96\)00044-9](https://doi.org/10.1016/S0924-7963(96)00044-9)
- Egorova, V. M., Sokolovskiy, M. A., & Zodiatis, G. (2024). A three-layer model of hydrodynamic processes in the Cyprus Eddy system. *Ocean Dynamics*, 74(1), 19–36. <https://doi.org/10.1007/s10236-023-01584-6>
- Elbessa, M., Abdelrahman, S., Tonbol, K., & Shaltout, M. (2022). Modeling the future scenarios for surface temperature and wind regime over the South-Eastern Levantine Basin, Egypt. *Egyptian Journal of Aquatic Biology and Fisheries, Volume 26*, 541–564. <https://doi.org/10.21608/ejabf.2022.244114>
- Espedal, H. A., & Johannessen, O. M. (2000). Cover: Detection of oil spills near offshore installations using synthetic aperture radar (SAR). *International Journal of Remote Sensing*, 21(11), 2141–2144. <https://doi.org/10.1080/01431160050029468>
- European Maritime Safety Agency. (2017). The CleanSeaNet service: Taking measurements to detect and deter marine pollution. <http://www.emsa.europa.eu/csn-menu/download/2913/2123/23.html>
- Everingham, M., van Gool, L., Williams, C. K. I., Winn, J., & Zisserman, A. (2012). The PASCAL visual object classes challenge 2012 (VOC2012). *Results*.
- EXCELSIOR 2020. (2025). EXCELSIOR Infrastructure. Retrieved August 3, 2025, from <https://excelsior2020.eu/infrastructure/>
- ExxonMobil. (2014). Oil spill response field manual. *ExxonMobil Research and Engineering Company*. Retrieved May 26, 2025, from <https://enviro-usa.com/exxon-mobil-oil-spill-response-field-manual/>

- Fach, B. A., Orek, H., Yilmaz, E., Tezcan, D., Salihoglu, I., Salihoglu, B., & Latif, M. A. (2021). Water mass variability and Levantine Intermediate Water formation in the Eastern Mediterranean between 2015 and 2017. *Journal of Geophysical Research: Oceans*, 126(2). <https://doi.org/10.1029/2020JC016472>
- Fay, J. A. (1971). Physical processes in the spread of oil on a water surface. *International Oil Spill Conference Proceedings, 1971*(1), 463–467. <https://doi.org/10.7901/2169-3358-1971-1-463>
- Ferraro, G., Meyer-Roux, S., Muellenhoff, O., Pavliha, M., Svetak, J., Tarchi, D., & Topouzelis, K. (2009). Long term monitoring of oil spills in European seas. *International Journal of Remote Sensing*, 30(3), 627–645. <https://doi.org/10.1080/01431160802339464>
- Fingas, M. (2012). *The basics of oil spill cleanup* (Third Edition). CRC press. <https://doi.org/10.1201/b13686>
- Fingas, M. (2017). Chapter 8 - Introduction to spill modeling. In M. Fingas (Ed.), *Oil spill science and technology* (pp. 419–453). Gulf Professional Publishing. <https://doi.org/10.1016/B978-0-12-809413-6.00008-4>
- Fingas, M. (2018). The challenges of remotely measuring oil slick thickness. *Remote Sensing*, 10(2), 319. <https://doi.org/10.3390/rs10020319>
- Fingas, M., & Brown, C. E. (2017). Chapter 5 - Oil spill remote sensing. In M. Fingas (Ed.), *Oil spill science and technology* (pp. 305–385). Gulf Professional Publishing. <https://doi.org/10.1016/B978-0-12-809413-6.00005-9>
- Fingas, M., & Fieldhouse, B. (2004). Formation of water-in-oil emulsions and application to oil spill modelling. *Journal of hazardous materials*, 107(1-2), 37–50. <https://doi.org/10.1016/j.jhazmat.2003.11.008>
- Flanders Marine Institute. (2023). Maritime Boundaries Geodatabase: Maritime boundaries and Exclusive Economic Zones (200NM), version 12. Retrieved June 2, 2025, from <https://www.marineregions.org/>
- Fortuny-Guasch, J. (2003). Improved oil slick detection and classification with polarimetric SAR. *Applications of SAR Polarimetry and Polarimetric Interferometry*, 529.
- Gade, M., & Alpers, W. (1999). Using ERS-2 SAR images for routine observation of marine pollution in European coastal waters. *The Science of the total environment*, 237-238, 441–448. [https://doi.org/10.1016/S0048-9697\(99\)00156-4](https://doi.org/10.1016/S0048-9697(99)00156-4)
- Gade, M., Scholz, J., & von Viebahn, C. (2000). On the detectability of marine oil pollution in european marginal waters by means of ERS SAR imagery. *IGARSS 2000. IEEE 2000 International Geoscience and Remote Sensing Symposium. Taking the Pulse of the Planet: The Role of Remote Sensing in Managing the*

- Environment. Proceedings (Cat. No.00CH37120)*, 2510–2512. <https://doi.org/10.1109/IGARSS.2000.859623>
- Gade, M., Alpers, W., Hühnerfuss, H., Masuko, H., & Kobayashi, T. (1998). Imaging of biogenic and anthropogenic ocean surface films by the multifrequency/multi-polarization SIR-C/X-SAR. *Journal of Geophysical Research: Oceans*, 103(C9), 18851–18866. <https://doi.org/10.1029/97JC01915>
- Garcia-Pineda, O., Holmes, J., Rissing, M., Jones, R., Wobus, C., Svejksky, J., & Hess, M. (2017). Detection of oil near shorelines during the Deepwater Horizon oil spill using synthetic aperture radar (SAR). *Remote Sensing*, 9(6). <https://doi.org/10.3390/rs9060567>
- GEBCO Bathymetric Compilation Group 2023. (2023). The GEBCO_2023 grid - a continuous terrain model of the global oceans and land. <https://doi.org/10.5285/f98b053b-0cbc-6c23-e053-6c86abc0af7b>
- Gertman, I., Pinardi, N., Popov, Y., & Hecht, A. (2006). Aegean Sea water masses during the early stages of the Eastern Mediterranean Climatic Transient (1988–90). *Journal of Physical Oceanography*, 36(9), 1841–1859. <https://doi.org/10.1175/JPO2940.1>
- Grierson, I. T. (1998). Use of airborne thermal imagery to detect and monitor inshore oil spill residues during darkness hours. *Environmental management*, 22(6), 905–912. <https://doi.org/10.1007/s002679900157>
- Grüner, K., Reuter, R., & Smid, H. (1991). A new sensor system for airborne measurements of maritime pollution and of hydrographic parameters. *GeoJournal*, 24(1), 103–117. <https://doi.org/10.1007/BF00213062>
- Günzel, D., & Mandapati, S. (2025). Satellite on-board processing of synthetic aperture radar data for rapid delivery of latency sensitive maritime information products. In R. J. Frouin, H. Murakami, J.-K. Choi, & K.-H. Tseng (Eds.), *Active and passive remote sensing of oceans, seas, and lakes* (p. 5). SPIE. <https://doi.org/10.1117/12.3040646>
- Habib, J., Ulses, C., Estournel, C., Fakhri, M., Marsaleix, P., Pujo-Pay, M., Fourier, M., Coppola, L., Mignot, A., Mortier, L., & Conan, P. (2023). Seasonal and interannual variability of the pelagic ecosystem and of the organic carbon budget in the Rhodes Gyre (eastern Mediterranean): Influence of winter mixing. *Biogeosciences*, 20(15), 3203–3228. <https://doi.org/10.5194/bg-20-3203-2023>
- Hadjipetrou, S., & Kyriakidis, P. (2024). High-resolution wind speed estimates for the Eastern Mediterranean Basin: A statistical comparison against coastal meteorological observations. *Wind*, 4(4), 311–341. <https://doi.org/10.3390/wind4040016>

- Harrison, W., Winnik, M. A., Kwong, P. T. Y., & Mackay, D. (1975). Crude oil spills. Disappearance of aromatic and aliphatic components from small sea-surface slicks. *Environmental Science & Technology*, 9(3), 231–234.
- Hasimoto-Beltran, R., Canul-Ku, M., Díaz Méndez, G. M., Ocampo-Torres, F. J., & Esquivel-Trava, B. (2023). Ocean oil spill detection from SAR images based on multi-channel deep learning semantic segmentation. *Marine pollution bulletin*, 188, 114651. <https://doi.org/10.1016/j.marpolbul.2023.114651>
- Hecht, A., Pinardi, N., & Robinson, A. R. (1988). Currents, water masses, eddies and jets in the Mediterranean Levantine Basin. *Journal of Physical Oceanography*, 18(10), 1320–1353. [https://doi.org/10.1175/1520-0485\(1988\)018<1320:CWMEAJ>2.0.CO;2](https://doi.org/10.1175/1520-0485(1988)018<1320:CWMEAJ>2.0.CO;2)
- Herut, B., Goldman, R., Ozer, T., Lazar, A., Biton, E., Gertman, I., Silverman, J., Segal, Y., Sisma-Ventura, G., Gertner, Y., Rubin-Blum, M., Belkin, N., & Rahav, E. (2024). Tar pollution event (2021) at the Southeastern Levantine oligotrophic basin, short-term impacts and operational oceanography perspectives. *Marine pollution bulletin*, 198, 115892. <https://doi.org/10.1016/j.marpolbul.2023.115892>
- Hollebone, B. (2017). Chapter 3 - oil physical properties: Measurement and correlation. In M. Fingas (Ed.), *Oil spill science and technology* (pp. 185–207). Gulf Professional Publishing. <https://doi.org/10.1016/B978-0-12-809413-6.00003-5>
- Hollinger, J. P., & Mennella, R. A. (1973). Oil spills: Measurements of their distributions and volumes by multifrequency microwave radiometry. *Science (New York, N.Y.)*, 181(4094), 54–56. <https://doi.org/10.1126/science.181.4094.54>
- Horvath, H. (1993). Atmospheric light absorption—a review. *Atmospheric Environment. Part A. General Topics*, 27(3), 293–317. [https://doi.org/10.1016/0960-1686\(93\)90104-7](https://doi.org/10.1016/0960-1686(93)90104-7)
- Huang, J. C. (1983). A review of the state-of-the-art of oil spill fate/behavior models. *International Oil Spill Conference Proceedings*, 1983(1), 313–322. <https://doi.org/10.7901/2169-3358-1983-1-313>
- Huang, X., Zhang, B., & Perrie, W. (2025). A two-stage deep learning method for marine oil spill localization and segmentation from synthetic aperture radar images. *IEEE Journal of Selected Topics in Applied Earth Observations and Remote Sensing*, 18, 12315–12327. <https://doi.org/10.1109/JSTARS.2025.3567859>
- IPIECA, IMO, & OGP. (2012). Sensitivity mapping for oil spill response. Retrieved June 16, 2025, from <https://www.ipieca.org/resources/sensitivity-mapping-for-oil-spill-response>

- ITOPF. (2011). Fate of marine oil spills. Retrieved May 28, 2025, from <https://www.itopf.org/knowledge-resources/documents-guides/tip-02-fate-of-marine-oil-spills/>
- ITOPF. (2012a). Clean-up of oil from shorelines. Retrieved June 17, 2025, from <https://www.itopf.org/knowledge-resources/documents-guides/tip-07-clean-up-of-oil-from-shorelines/>
- ITOPF. (2012b). Use of skimmers in oil pollution response. Retrieved May 30, 2025, from <https://www.itopf.org/knowledge-resources/documents-guides/tip-05-use-of-skimmers-in-oil-pollution-response/>
- ITOPF. (2025). Oil tanker spill statistics 2024. Retrieved June 10, 2025, from https://www.itopf.org/fileadmin/uploads/itopf/data/Documents/Company__Lit/Oil_Spill_Stats_brochure_2024.pdf
- Ivanov, A. Y., & Ermoshkin, I. S. (2004). Mapping oil spills in the Caspian Sea using ERS-1/ERS-2 SAR image quick-looks and GIS. *Gayana (Concepción)*, 68(2). <https://doi.org/10.4067/S0717-65382004000200054>
- Ivanov, A. Y., He, M.-X., & Fang, M. (2002). Oil spill detection with the RADARSAT SAR in the waters of the Yellow and East China Sea: A case study. *23rd Asian Conference on Remote Sensing*, 25–29.
- Jafarzadeh, H., Mahdianpari, M., Homayouni, S., Mohammadimanesh, F., & Daboor, M. (2021). Oil spill detection from synthetic aperture radar earth observations: A meta-analysis and comprehensive review. *GIScience & Remote Sensing*, 58(7), 1022–1051. <https://doi.org/10.1080/15481603.2021.1952542>
- Jiao, Z., Jia, G., & Cai, Y. (2019). A new approach to oil spill detection that combines deep learning with unmanned aerial vehicles. *Computers & Industrial Engineering*, 135, 1300–1311. <https://doi.org/10.1016/j.cie.2018.11.008>
- Jones, C. E. (2023). An automated algorithm for calculating the ocean contrast in support of oil spill response. *Marine pollution bulletin*, 191, 114952. <https://doi.org/10.1016/j.marpolbul.2023.114952>
- Kallos, G., Nickovic, S., Papadopoulos, A., Jovic, D., Kakaliagou, O., Misirlis, N., Boukas, L., Mimikou, N., Sakellaris, G., Papageorgiou, J., et al. (1997). The regional weather forecasting system SKIRON: An overview. In *Proceedings of the symposium on regional weather prediction on parallel computer environments* (p. 17, Vol. 15).
- Kanaa, T., Tonye, E., Mercier, G., Onana, V. P., Ngono, J. M., Frison, P. L., Rudant, J. P., & Garelo, R. (2003). Detection of oil slick signatures in SAR images by fusion of hysteresis thresholding responses. *2003 IEEE International Geoscience and Remote Sensing Symposium (IGARSS). Proceedings (IEEE Cat.*

- No.03CH37477*), 4, 2750–2752 vol.4. <https://doi.org/10.1109/IGARSS.2003.1294573>
- Karathanassi, V., Topouzelis, K., Pavlakis, P., & and, D. R. (2006). An object-oriented methodology to detect oil spills. *International Journal of Remote Sensing*, 27(23), 5235–5251. <https://doi.org/10.1080/01431160600693575>
- Keuter, S., Silverman, J., Krom, M. D., Sisma-Ventura, G., Yu, J., Tsemel, A., Ben-Ezra, T., Sher, D., Reich, T., Koplovitz, G., & Frada, M. J. (2022). Seasonal patterns of coccolithophores in the ultra-oligotrophic South-East Levantine Basin, Eastern Mediterranean Sea. *Marine Micropaleontology*, 175, 102153. <https://doi.org/10.1016/j.marmicro.2022.102153>
- Kim, D.-J., Moon, W. M., & Kim, Y.-S. (2010). Application of TerraSAR-X data for emergent oil-spill monitoring. *IEEE Transactions on Geoscience and Remote Sensing*, 48(2), 852–863. <https://doi.org/10.1109/TGRS.2009.2036253>
- Kim, T.-S., Park, K.-A., Li, X., Lee, M., Hong, S., Lyu, S. J., & Nam, S. (2015). Detection of the Hebei Spirit oil spill on SAR imagery and its temporal evolution in a coastal region of the Yellow Sea. *Advances in Space Research*, 56(6), 1079–1093. <https://doi.org/10.1016/j.asr.2015.05.040>
- Kleindienst, S., Paul, J. H., & Joye, S. B. (2015). Using dispersants after oil spills: Impacts on the composition and activity of microbial communities. *Nature reviews. Microbiology*, 13(6), 388–396. <https://doi.org/10.1038/nrmicro3452>
- Knauss, J. A., & Garfield, N. (2016). *Introduction to physical oceanography* (Third Edition). Waveland Press.
- Konik, M., & Bradtke, K. (2016). Object-oriented approach to oil spill detection using Envisat ASAR images. *ISPRS Journal of Photogrammetry and Remote Sensing*, 118, 37–52. <https://doi.org/10.1016/j.isprsjprs.2016.04.006>
- Kress, N., Rahav, E., Silverman, J., & Herut, B. (2019). Environmental status of Israel's Mediterranean coastal waters: Setting reference conditions and thresholds for nutrients, chlorophyll-a and suspended particulate matter. *Marine pollution bulletin*, 141, 612–620. <https://doi.org/10.1016/j.marpolbul.2019.02.070>
- Krestenitis, M., Orfanidis, G., Ioannidis, K., Avgerinakis, K., Vrochidis, S., & Kompatsiaris, I. (2019). Oil spill identification from satellite images using deep neural networks. *Remote Sensing*, 11(15), 1762. <https://doi.org/10.3390/rs11151762>
- Lascaratos, A., Roether, W., Nittis, K., & Klein, B. (1999). Recent changes in deep water formation and spreading in the Eastern Mediterranean Sea: A review. *Progress in Oceanography*, 44(1-3), 5–36. [https://doi.org/10.1016/S0079-6611\(99\)00019-1](https://doi.org/10.1016/S0079-6611(99)00019-1)

- Lascaratos, A., Williams, R. G., & Tragou, E. (1993). A mixed-layer study of the formation of Levantine Intermediate Water. *Journal of Geophysical Research*, 98(C8), 14739–14749. <https://doi.org/10.1029/93JC00912>
- Lin, T.-Y., Maire, M., Belongie, S., Hays, J., Perona, P., Ramanan, D., Dollár, P., & Zitnick, C. L. (2014). Microsoft COCO: Common objects in context. In D. Fleet, T. Pajdla, B. Schiele, & T. Tuytelaars (Eds.), *Computer vision – ECCV 2014* (pp. 740–755). Springer International Publishing.
- Lionello, P., Giorgi, F., Rohling, E., & Seager, R. (2023). Chapter 3 - Mediterranean climate: Past, present and future. In K. Schroeder & J. Chiggiato (Eds.), *Oceanography of the Mediterranean Sea* (pp. 41–91). Elsevier. <https://doi.org/10.1016/B978-0-12-823692-5.00011-X>
- Lionello, P., Sannino, G., & Vilibić, I. (2023). Chapter 6 - Surface wave and sea surface dynamics in the Mediterranean. In K. Schroeder & J. Chiggiato (Eds.), *Oceanography of the Mediterranean Sea* (pp. 161–207). Elsevier. <https://doi.org/10.1016/B978-0-12-823692-5.00007-8>
- Liu, P., Li, Y., Xu, J., & Wang, T. (2019). Oil spill extraction by X-band marine radar using texture analysis and adaptive thresholding. *Remote Sensing Letters*, 10(6), 583–589. <https://doi.org/10.1080/2150704X.2019.1587197>
- Loh, A., Shankar, R., Ha, S. Y., An, J. G., & Yim, U. H. (2020). Stability of mechanically and chemically dispersed oil: Effect of particle types on oil dispersion. *The Science of the total environment*, 716, 135343. <https://doi.org/10.1016/j.scitotenv.2019.135343>
- Lu, J., Lim, H., Liew, S. C., Bao, M., & Kwok, L. K. (1999). Ocean oil pollution mapping with ERS synthetic aperture radar imagery. *IEEE 1999 International Geoscience and Remote Sensing Symposium. IGARSS'99 (Cat. No.99CH36293)*, 1, 212–214 vol.1. <https://doi.org/10.1109/IGARSS.1999.773450>
- Mackay, D., & McAuliffe, C. D. (1989). Fate of hydrocarbons discharged at sea. *Oil and Chemical Pollution*, 5(1), 1–20. [https://doi.org/10.1016/S0269-8579\(89\)80002-4](https://doi.org/10.1016/S0269-8579(89)80002-4)
- Malanotte-Rizzoli, P., Manca, B. B., Marullo, S., Ribera d'Alcalá, M., Roether, W., Theoharis, A., Bergamasco, A., Budillon, G., Sansone, E., Civitarese, G., Conversano, F., Gertman, I., Hernt, B., Kress, N., Kioroglou, S., Kontoyannis, H., Nittis, K., Klein, B., Lascaratos, A., . . . Kovacevic, V. (2003). The Levantine Intermediate Water Experiment (LIWEX) group: Levantine basin—a laboratory for multiple water mass formation processes. *Journal of Geophysical Research*, 108(C9). <https://doi.org/10.1029/2002JC001643>

- Mapelli, F., Scoma, A., Michoud, G., Aulenta, F., Boon, N., Borin, S., Kalogerakis, N., & Daffonchio, D. (2017). Biotechnologies for marine oil spill cleanup: Indissoluble ties with microorganisms. *Trends in biotechnology*, 35(9), 860–870. <https://doi.org/10.1016/j.tibtech.2017.04.003>
- Marghany, M. (2015). Automatic detection of oil spills in the Gulf of Mexico from RADARSAT-2 SAR satellite data. *Environmental Earth Sciences*, 74(7), 5935–5947. <https://doi.org/10.1007/s12665-015-4617-y>
- Mason, E., Barceló-Llull, B., Sánchez-Román, A., Rodríguez-Tarry, D., Cutolo, E., Delepoulle, A., Ruiz, S., & Pascual, A. (2023). Chapter 8 - Fronts, eddies and mesoscale circulation in the Mediterranean Sea. In K. Schroeder & J. Chiggiato (Eds.), *Oceanography of the Mediterranean Sea* (pp. 263–287). Elsevier. <https://doi.org/10.1016/B978-0-12-823692-5.00003-0>
- Masuda, K., Takashima, T., & Takayama, Y. (1988). Emissivity of pure and sea waters for the model sea surface in the infrared window regions. *Remote Sensing of Environment*, 24(2), 313–329. [https://doi.org/10.1016/0034-4257\(88\)90032-6](https://doi.org/10.1016/0034-4257(88)90032-6)
- Masuko, H., Kobayashi, T., Okamoto, K.-I., & Alpers, W. (1995). Observation of artificial slicks with SIR-C/X-SAR around Japan. *1995 International Geoscience and Remote Sensing Symposium, IGARSS '95. Quantitative Remote Sensing for Science and Applications*, 1, 227–229 vol.1. <https://doi.org/10.1109/IGARSS.1995.520244>
- Measures, R., & Bristow, M. (1971). The development of a laser fluorosensor for remote environmental probing. *Joint Conference on Sensing of Environmental Pollutants*, 1121.
- Menna, M., Poulain, P.-M., Zodiatis, G., & Gertman, I. (2012). On the surface circulation of the Levantine sub-basin derived from Lagrangian drifters and satellite altimetry data. *Deep Sea Research Part I: Oceanographic Research Papers*, 65, 46–58. <https://doi.org/10.1016/j.dsr.2012.02.008>
- Migliaccio, M., Gambardella, A., & Tranfaglia, M. (2007). SAR polarimetry to observe oil spills. *IEEE Transactions on Geoscience and Remote Sensing*, 45(2), 506–511. <https://doi.org/10.1109/TGRS.2006.888097>
- Miglietta, M. M., Zecchetto, S., & de Biasio, F. (2013). A comparison of wrf model simulations with SAR wind data in two case studies of orographic lee waves over the Eastern Mediterranean Sea. *Atmospheric Research*, 120–121, 127–146. <https://doi.org/10.1016/j.atmosres.2012.08.009>
- Morozov, E. G., Trulsen, K., Velarde, M. G., & Vlasenko, V. I. (2002). Internal tides in the Strait of Gibraltar. *Journal of Physical Oceanography*, 32(11), 3193–3206. [https://doi.org/10.1175/1520-0485\(2002\)032<3193:ITITSO>2.0.CO;2](https://doi.org/10.1175/1520-0485(2002)032<3193:ITITSO>2.0.CO;2)

- National Academies of Sciences, Engineering, and Medicine. (2022). *Oil in the sea IV: Inputs, fates, and effects*. National Academies Press. <https://doi.org/10.17226/26410>
- National Research Council. (2003). *Oil in the sea III: Inputs, fates, and effects*. National Academy Press. <https://doi.org/10.17226/10388>
- Nieto-Hidalgo, M., Gallego, A.-J., Gil, P., & Pertusa, A. (2018). Two-stage convolutional neural network for ship and spill detection using SLAR images. *IEEE Transactions on Geoscience and Remote Sensing*, 56(9), 5217–5230. <https://doi.org/10.1109/TGRS.2018.2812619>
- Nost, E., & Egset, C. N. (2006). Oil spill detection system - results from field trials. *OCEANS 2006*, 1–6. <https://doi.org/10.1109/OCEANS.2006.306905>
- Overstreet, R., Galt, J. A., United States. Environmental Protection Agency. Region V., United States. National Oceanic, Atmospheric Administration. Hazardous Materials Response, & Assessment Division. (1995). *Physical processes affecting the movement and spreading of oils in inland waters* (Vol. 95-7). U.S. Dept. of Commerce, National Oceanic and Atmospheric Administration, Hazardous materials Response and Assessment Division.
- Ozer, T., Gertman, I., Gildor, H., Goldman, R., & Herut, B. (2020). Evidence for recent thermohaline variability and processes in the deep water of the Southeastern Levantine Basin, Mediterranean Sea. *Deep Sea Research Part II: Topical Studies in Oceanography*, 171, 104651. <https://doi.org/10.1016/j.dsr2.2019.104651>
- Özsoy, E., Hecht, A., & Ünlüata, Ü. (1989). Circulation and hydrography of the Levantine Basin. results of POEM coordinated experiments 1985–1986. *Progress in Oceanography*, 22(2), 125–170. [https://doi.org/10.1016/0079-6611\(89\)90004-9](https://doi.org/10.1016/0079-6611(89)90004-9)
- Özsoy, E., Hecht, A., Ünlüata, Ü., Brenner, S., Sur, H. I., Bishop, J., Latif, M. A., Rozentraub, Z., & Oğuz, T. (1993). A synthesis of the Levantine Basin circulation and hydrography, 1985–1990. *Deep Sea Research Part II: Topical Studies in Oceanography*, 40(6), 1075–1119. [https://doi.org/10.1016/0967-0645\(93\)90063-S](https://doi.org/10.1016/0967-0645(93)90063-S)
- Papadopoulos, A., Katsafados, P., & Kallos, G. (2001). Regional weather forecasting for marine application. *Global Atmos. Ocean Syst.*, 8(2-3), 219–237.
- Papandrea, E., Casadio, S., Castelli, E., Dinelli, B. M., & Miglietta, M. M. (2019). Lee wave detection over the Mediterranean Sea using the advanced infra-red water vapour estimator (AIRWAVE) total column water vapour (TCWV) dataset. *Atmospheric Measurement Techniques*, 12(12), 6683–6693. <https://doi.org/10.5194/amt-12-6683-2019>

- Pavlakakis, P., Tarchi, D., & Sieber, A. J. (2001). On the monitoring of illicit vessel discharges using spaceborne SAR remote sensing - a reconnaissance study in the Mediterranean Sea. *Annales Des Télécommunications*, 56(11-12), 700–718. <https://doi.org/10.1007/BF02995563>
- Pegliasco, C., Chaigneau, A., Morrow, R., & Dumas, F. (2021). Detection and tracking of mesoscale eddies in the Mediterranean Sea: A comparison between the sea level anomaly and the absolute dynamic topography fields. *Advances in Space Research*, 68(2), 401–419. <https://doi.org/10.1016/j.asr.2020.03.039>
- Pelinovksy, E., Talipova, T., & Ivanov, V. (1995). Estimations of the nonlinear properties of the internal wave field off the Israel coast. *Nonlinear Processes in Geophysics*, 2(2), 80–88. <https://doi.org/10.5194/npg-2-80-1995>
- Peterson, C. H. (2001). The “Exxon Valdez” oil spill in Alaska: Acute, indirect and chronic effects on the ecosystem. Elsevier. [https://doi.org/10.1016/S0065-2881\(01\)39008-9](https://doi.org/10.1016/S0065-2881(01)39008-9)
- Peterson, J. (2002). Environmental sensitivity index guidelines : Version 3.0. *NOAA technical memorandum NOS-OR&R 11*. Retrieved June 16, 2025, from <https://repository.library.noaa.gov/view/noaa/10263>
- Pinardi, N., Cessi, P., Borile, F., & Wolfe, C. L. P. (2019). The Mediterranean Sea overturning circulation. *Journal of Physical Oceanography*, 49(7), 1699–1721. <https://doi.org/10.1175/JPO-D-18-0254.1>
- Pinardi, N., Estournel, C., Cessi, P., Escudier, R., & Lyubartsev, V. (2023). Chapter 7 - Dense and deep water formation processes and Mediterranean overturning circulation. In K. Schroeder & J. Chiggiato (Eds.), *Oceanography of the Mediterranean Sea* (pp. 209–261). Elsevier. <https://doi.org/10.1016/B978-0-12-823692-5.00009-1>
- Pinardi, N., & Navarra, A. (1993). Baroclinic wind adjustment processes in the Mediterranean Sea. *Deep Sea Research Part II: Topical Studies in Oceanography*, 40(6), 1299–1326. [https://doi.org/10.1016/0967-0645\(93\)90071-T](https://doi.org/10.1016/0967-0645(93)90071-T)
- Pisano, A., Bignami, F., & Santoleri, R. (2015). Oil spill detection in glint-contaminated near-infrared MODIS imagery. *Remote Sensing*, 7(1), 1112–1134. <https://doi.org/10.3390/rs70101112>
- Pleskachevsky, A., Tings, B., Jacobsen, S., Wiehle, S., Schwarz, E., & Krause, D. (2024). A system for near-real-time monitoring of the sea state using SAR satellites. *IEEE Transactions on Geoscience and Remote Sensing*, 62, 1–18. <https://doi.org/10.1109/TGRS.2024.3419582>

- Polinov, S., Bookman, R., & Levin, N. (2021). Spatial and temporal assessment of oil spills in the Mediterranean Sea. *Marine Pollution Bulletin*, 167, 112338. <https://doi.org/10.1016/j.marpolbul.2021.112338>
- Potiris, M., Mamoutos, I. G., Tragou, E., Zervakis, V., Kassis, D., & Ballas, D. (2024). Dense water formation in the North–Central Aegean Sea during winter 2021–2022. *Journal of Marine Science and Engineering*, 12(2), 221. <https://doi.org/10.3390/jmse12020221>
- Poulain, P.-M., Menna, M., & Mauri, E. (2012). Surface geostrophic circulation of the Mediterranean Sea derived from drifter and satellite altimeter data. *Journal of Physical Oceanography*, 42(6), 973–990. <https://doi.org/10.1175/JPO-D-11-0159.1>
- Prince, R. C., McFarlin, K. M., Butler, J. D., Febbo, E. J., Wang, F. C. Y., & Nedwed, T. J. (2013). The primary biodegradation of dispersed crude oil in the sea. *Chemosphere*, 90(2), 521–526. <https://doi.org/10.1016/j.chemosphere.2012.08.020>
- Qi, Z., Sun, R., Yu, Y., Xiong, D., Li, W., Yu, X., & Fu, S. (2021). Performance of dispersed oil and suspended sediment during the oil-sediment aggregation process. *Marine pollution bulletin*, 168, 112455. <https://doi.org/10.1016/j.marpolbul.2021.112455>
- Reiche, S., Hübscher, C., Brenner, S., Betzler, C., & Hall, J. K. (2018). The role of internal waves in the late Quaternary evolution of the Israeli continental slope. *Marine Geology*, 406, 177–192. <https://doi.org/10.1016/j.margeo.2018.09.013>
- Robbe, N., & Hengstermann, T. (2006). Remote sensing of marine oil spills from airborne platforms using multi-sensor systems. In C. A. Brebbia & J. S. A. d. Carmo (Eds.), *Water pollution viii* (pp. 347–355). WIT. <https://doi.org/10.2495/WP060351>
- Roberts, G., & Peace, D. (2007). Hydrocarbon plays and prospectivity of the Levantine Basin, offshore Lebanon and Syria from modern seismic data. *GeoArabia*, 12(3), 99–124. <https://doi.org/10.2113/geoarabia120399>
- Robinson, I. S. (2004). *Measuring the oceans from space: The principles and methods of satellite oceanography*. Springer Science & Business Media.
- Robinson, I. S. (2010a). Mesoscale ocean features: Eddies. In I. S. Robinson (Ed.), *Discovering the ocean from space: The unique applications of satellite oceanography* (pp. 69–114). Springer Berlin Heidelberg. https://doi.org/10.1007/978-3-540-68322-3_3
- Robinson, I. S. (2010b). Ocean mesoscale features: Upwelling and other phenomena. In I. S. Robinson (Ed.), *Discovering the ocean from space: The unique applications*

- of satellite oceanography* (pp. 159–193). Springer Berlin Heidelberg. https://doi.org/10.1007/978-3-540-68322-3_5
- Robinson, I. S., & Fangohr, S. (2010). Fluxes through the air–sea interface. In I. S. Robinson (Ed.), *Discovering the ocean from space: The unique applications of satellite oceanography* (pp. 359–390). Springer Berlin Heidelberg. https://doi.org/10.1007/978-3-540-68322-3_10
- Rosentraub, Z., & Brenner, S. (2007). Circulation over the southeastern continental shelf and slope of the Mediterranean Sea: Direct current measurements, winds, and numerical model simulations. *Journal of Geophysical Research*, 112(C11). <https://doi.org/10.1029/2006JC003775>
- Saadoun, I. M. (2015). Impact of oil spills on marine life. In M. L. Larramendy & S. Soloneski (Eds.), *Emerging pollutants in the environment - current and further implications*. InTech. <https://doi.org/10.5772/60455>
- Saleh, N. M. (2004). *Automated oil spill detection with ship borne radar* [Master’s thesis]. University of Twente.
- Salisbury, J. W., D’Aria, D. M., & Sabins, F. F. (1993). Thermal infrared remote sensing of crude oil slicks. *Remote Sensing of Environment*, 45(2), 225–231. [https://doi.org/10.1016/0034-4257\(93\)90044-X](https://doi.org/10.1016/0034-4257(93)90044-X)
- Schmidt, O., Schwarz, E., & Krause, D. (Eds.). (2024). *Oil spill detection on Landsat-8/9 images based on deep learning methods: Zenodo*. <https://doi.org/10.5281/ZENODO.14214876>
- Schowengerdt, R. A. (2007). Chapter 1 - The nature of remote sensing. In R. A. Schowengerdt (Ed.), *Remote sensing* (pp. 1–44). Academic Press. <https://doi.org/10.1016/B978-012369407-2/50004-8>
- Schroeder, K., Tanhua, T., Chiggiato, J., Velaoras, D., Josey, S. A., Lafuente, J. G., & Vargas-Yáñez, M. (2023). Chapter 4 - The forcings of the Mediterranean Sea and the physical properties of its water masses. In K. Schroeder & J. Chiggiato (Eds.), *Oceanography of the Mediterranean Sea* (pp. 93–123). Elsevier. <https://doi.org/10.1016/B978-0-12-823692-5.00005-4>
- Seveso, D., Louis, Y. D., Montano, S., Galli, P., & Saliu, F. (2021). The Mauritius oil spill: What’s next? *Pollutants*, 1(1), 18–28. <https://doi.org/10.3390/pollutants1010003>
- Shaban, M., Salim, R., Abu Khalifeh, H., Khelifi, A., Shalaby, A., El-Mashad, S., Mahmoud, A., Ghazal, M., & El-Baz, A. (2021). A deep-learning framework for the detection of oil spills from SAR data. *Sensors (Basel, Switzerland)*, 21(7). <https://doi.org/10.3390/s21072351>

- Shanmukh, M. P., & Priya, S. B. (2024). Enhancing oil spill detection using synthetic aperture radar with dual attention U-Net model. *2024 15th International Conference on Computing Communication and Networking Technologies (ICCCNT)*, 1–6. <https://doi.org/10.1109/ICCCNT61001.2024.10724194>
- Shi, Z., Yu, L., Cao, D., Wu, Q., Yu, X., & Lin, G. (2015). Airborne ultraviolet imaging system for oil slick surveillance: Oil-seawater contrast, imaging concept, signal-to-noise ratio, optical design, and optomechanical model. *Applied optics*, *54*(25), 7648–7655. <https://doi.org/10.1364/AO.54.007648>
- Singha, S., Bellerby, T. J., & Trieschmann, O. (2013). Satellite oil spill detection using artificial neural networks. *IEEE Journal of Selected Topics in Applied Earth Observations and Remote Sensing*, *6*(6), 2355–2363. <https://doi.org/10.1109/JSTARS.2013.2251864>
- Siokou-Frangou, I., Christaki, U., Mazzocchi, M. G., Montresor, M., Ribera d'Alcalá, M., Vaqué, D., & Zingone, A. (2010). Plankton in the open Mediterranean Sea: A review. *Biogeosciences*, *7*(5), 1543–1586. <https://doi.org/10.5194/bg-7-1543-2010>
- Skou, N. (1986). Microwave radiometry for oil pollution monitoring, measurements, and systems. *IEEE Transactions on Geoscience and Remote Sensing*, *GE-24*(3), 360–367. <https://doi.org/10.1109/TGRS.1986.289593>
- Solberg, A., Storvik, G., Solberg, R., & Volden, E. (1999). Automatic detection of oil spills in ERS SAR images. *IEEE Transactions on Geoscience and Remote Sensing*, *37*(4), 1916–1924. <https://doi.org/10.1109/36.774704>
- Sørensen, L., Melbye, A. G., & Booth, A. M. (2014). Oil droplet interaction with suspended sediment in the seawater column: Influence of physical parameters and chemical dispersants. *Marine pollution bulletin*, *78*(1-2), 146–152. <https://doi.org/10.1016/j.marpolbul.2013.10.049>
- Spaulding, M. L. (1988). A state-of-the-art review of oil spill trajectory and fate modeling. *Oil and Chemical Pollution*, *4*(1), 39–55. [https://doi.org/10.1016/S0269-8579\(88\)80009-1](https://doi.org/10.1016/S0269-8579(88)80009-1)
- Stevens, J. (2020). NASA earth observatory map. Retrieved September 8, 2020, from <https://visibleearth.nasa.gov/images/147190/explorer-base-map>
- Suez Canal Authority. (2025). The Green Canal. Retrieved July 28, 2025, from <https://www.suezcanal.gov.eg/English/About/SuezCanal/Pages/greencanal.aspx>
- Swinkels, C., Peters, H., & van Heesen, J. (2012). Analysis of current patterns in coastal areas using X-band radar images. *Coastal Engineering*, 1–10.
- Taillandier, V., D'Ortenzio, F., Prieur, L., Conan, P., Coppola, L., Cornec, M., Dumas, F., Durrieu de Madron, X., Fach, B., Fourier, M., Gentil, M., Hayes,

- D., Husrevoglu, S., Legoff, H., Le Ster, L., Örek, H., Ozer, T., Poulain, P. M., Pujo-Pay, M., . . . Wimart-Rousseau, C. (2022). Sources of the Levantine Intermediate Water in winter 2019. *Journal of Geophysical Research: Oceans*, 127(6). <https://doi.org/10.1029/2021JC017506>
- Tassy, A., Crouzy, E., Gorini, C., Rubino, J.-L., Bouroullec, J.-L., & Sapin, F. (2015). Egyptian tethyan margin in the mesozoic: Evolution of a mixed carbonate-siliciclastic shelf edge (from western desert to sinai). *Marine and Petroleum Geology*, 68, 565–581. <https://doi.org/10.1016/j.marpetgeo.2015.10.011>
- Tennyson, E. J. (1988). Shipboard navigational radar as an oil spill tracking tool—a preliminary assessment. *OCEANS '88. 'A Partnership of Marine Interests' Proceedings*, 857–859 vol.3. <https://doi.org/10.1109/OCEANS.1988.23623>
- Teruzzi, A., Aydogdu, A., Amadio, C., Clementi, E., Colella, S., Di Biagio, V., Drudi, M., Fanelli, C., Feudale, L., Grandi, A., Miraglio, P., Pisano, A., Pistoia, J., Reale, M., Salon, S., Volpe, G., & Cossarini, G. (2024). Anomalous 2022 deep-water formation and intense phytoplankton bloom in the Cretan area. *State of the Planet*, 4-osr8, 1–15. <https://doi.org/10.5194/sp-4-osr8-15-2024>
- Theocharis, A., Nittis, K., Kontoyiannis, H., Papageorgiou, E., & Balopoulos, E. (1999). Climatic changes in the Aegean Sea influence the Eastern Mediterranean thermohaline circulation (1986–1997). *Geophysical Research Letters*, 26(11), 1617–1620. <https://doi.org/10.1029/1999GL900320>
- Theophilopoulos, N. A., Efstathiadis, S. G., & Petropoulos, Y. (1996). ENVISYS environmental monitoring warning and emergency management system. *Spill Science & Technology Bulletin*, 3(1-2), 19–24. [https://doi.org/10.1016/S1353-2561\(96\)00023-0](https://doi.org/10.1016/S1353-2561(96)00023-0)
- Topouzelis, K. N. (2008). Oil spill detection by SAR images: Dark formation detection, feature extraction and classification algorithms. *Sensors (Basel, Switzerland)*, 8(10), 6642–6659. <https://doi.org/10.3390/s8106642>
- Topouzelis, K. N., Karathanassi, V., Pavlakis, P., & Rokos, D. (2007). Detection and discrimination between oil spills and look-alike phenomena through neural networks. *ISPRS Journal of Photogrammetry and Remote Sensing*, 62(4), 264–270. <https://doi.org/10.1016/j.isprsjprs.2007.05.003>
- True, M., Shuchman, R. A., Kletzli, J. W., Johannessen, J. A., Digranes, G., Berg, S., & Dalland, K. (1994). Thickness characterisation of oil spills using active microwave sensors. In J. A. Johannessen & T. H. Guymer (Eds.), *Oceanic remote sensing and sea ice monitoring* (pp. 92–103). SPIE. <https://doi.org/10.1117/12.197270>

- Trujillo-Acatitla, R., Tuxpan-Vargas, J., Ovando-Vázquez, C., & Monterrubio-Martínez, E. (2024). Marine oil spill detection and segmentation in SAR data with two steps deep learning framework. *Marine pollution bulletin*, 204, 116549. <https://doi.org/10.1016/j.marpolbul.2024.116549>
- UNEP/MAP. (2012). *State of the Mediterranean marine and coastal environment*. UNEP/MAP – Barcelona Convention, Athens.
- Uribe-Martínez, A., Espinoza-Tenorio, A., Cruz-Pech, J. B., Cupido-Santamaría, D. G., Trujillo-Córdova, J. A., García-Nava, H., Flores-Vidal, X., Gudiño-Elizondo, N., Herguera, J. C., Appendini, C. M., & Cuevas, E. (2024). An affordable operational oil spill monitoring system in action: A diachronic multiplatform analysis of recent incidents in the southern Gulf of Mexico. *Environmental monitoring and assessment*, 196(11), 1069. <https://doi.org/10.1007/s10661-024-13161-5>
- van Gils, A. (2014). *Validation of X-band radar derived hydrodynamic phenomena* [Master's thesis]. TU Delft.
- Vankayalapati, K., Dasari, H. P., Langodan, S., El Mohtar, S., Sanikommu, S., Asfahani, K., Desamsetti, S., & Hoteit, I. (2023). Multi-mission satellite detection and tracking of October 2019 Sabiti oil spill in the Red Sea. *Remote Sensing*, 15(1), 38. <https://doi.org/10.3390/rs15010038>
- Velaoras, D., Krokos, G., Nittis, K., & Theocharis, A. (2014). Dense intermediate water outflow from the Cretan Sea: A salinity driven, recurrent phenomenon, connected to thermohaline circulation changes. *Journal of Geophysical Research: Oceans*, 119(8), 4797–4820. <https://doi.org/10.1002/2014JC009937>
- Velegrakis, A., Oikonomou, E., Theocharis, A., Collins, M., Kontoyiannis, H., Papadopoulos, V., Voulgaris, G., Wells, T., & Balopoulos, E. (1999). Internal waves revealed by synthetic aperture radar (SAR) imagery in the vicinity of the eastern Cretan Arc Straits (Eastern Mediterranean). *Progress in Oceanography*, 44(4), 553–572. [https://doi.org/10.1016/S0079-6611\(99\)00046-4](https://doi.org/10.1016/S0079-6611(99)00046-4)
- Walker, A. H. (2017). Chapter 1 - Oil spills and risk perceptions. In M. Fingas (Ed.), *Oil spill science and technology* (pp. 1–70). Gulf Professional Publishing. <https://doi.org/10.1016/B978-0-12-809413-6.00001-1>
- Wan, J., & Cheng, Y. (2013). Remote sensing monitoring of Gulf of Mexico oil spill using Envisat ASAR images. *2013 21st International Conference on Geoinformatics*, 1–5. <https://doi.org/10.1109/Geoinformatics.2013.6626165>
- Wang, Z., Fingas, M., Yang, C., & Christensen, J. H. (1964). 16 - Crude oil and refined product fingerprinting: Principles. In R. D. Morrison & B. L. Murphy (Eds.), *Environmental forensics* (pp. 339–407). Academic Press. <https://doi.org/10.1016/B978-012507751-4/50038-0>

- Watts, P. D., Allen, M. R., & Nightingale, T. J. (1996). Wind speed effects on sea surface emission and reflection for the along track scanning radiometer. *Journal of Atmospheric and Oceanic Technology*, 13(1), 126–141. [https://doi.org/10.1175/1520-0426\(1996\)013<0126:WSEOSS>2.0.CO;2](https://doi.org/10.1175/1520-0426(1996)013<0126:WSEOSS>2.0.CO;2)
- Werle, D., Tittley, B., Theriault, E., & Whitehouse, B. (1997). Using RADARSAT-1 SAR imagery to monitor the recovery of the 'irving whale' barge. *International symposium on geomatics in the era of RADARSAT*.
- Wessel, P., & Smith, W. H. F. (1996). A global, self-consistent, hierarchical, high-resolution shoreline database. *Journal of Geophysical Research: Solid Earth*, 101(B4), 8741–8743. <https://doi.org/10.1029/96JB00104>
- Westerholm, D. A., & Rauch III, S. D. (2016). Deepwater Horizon oil spill : Final programmatic damage assessment and restoration plan and final programmatic environmental impact statement. Retrieved June 22, 2025, from <https://repository.library.noaa.gov/view/noaa/18084>
- Wiehle, S., Mandapati, S., Günzel, D., Breit, H., & Balss, U. (2022). Synthetic aperture radar image formation and processing on an MPSoC. *IEEE Transactions on Geoscience and Remote Sensing*, 60, 1–14. <https://doi.org/10.1109/TGRS.2022.3167724>
- Wolfe, D. A., Hameed, M. J., Galt, J. A., Watabayashi, G., Short, J., O'Claire, C., Rice, S., Michel, J., Payne, J. R., Braddock, J., Hanna, S., & Sale, D. (1994). The fate of the oil spilled from the Exxon Valdez. *Environmental Science & Technology*, 28(13), 560A–568A. <https://doi.org/10.1021/es00062a712>
- Wong, S. F., Lim, J. S., & Dol, S. S. (2015). Crude oil emulsion: A review on formation, classification and stability of water-in-oil emulsions. *Journal of Petroleum Science and Engineering*, 135, 498–504. <https://doi.org/10.1016/j.petrol.2015.10.006>
- Wotherspoon, P., Marks, D., Solsberg, L., & West, M. (1997). Development of environmental sensitivity maps for oil spill planning and response. *ARPEL*. Retrieved June 16, 2025, from https://arpel.org/hubfs/%5BSitio%202024%5D%20-%20Publicaciones/aeg16_development_of_environmental_sensitivity_maps.pdf
- Wu, W., Wong, M. S., Yu, X., Shi, G., Kwok, C. Y. T., & Zou, K. (2024). Compositional oil spill detection based on object detector and adapted Segment Anything Model from SAR images. *IEEE Geoscience and Remote Sensing Letters*, 21, 1–5. <https://doi.org/10.1109/LGRS.2024.3382970>

- Xu, J., Cui, C., Feng, H., You, D., Wang, H., & Li, B. (2019). Marine radar oil-spill monitoring through local adaptive thresholding. *Environmental Forensics*, 20(2), 196–209. <https://doi.org/10.1080/15275922.2019.1597781>
- Xu, J., Pan, X., Wu, X., Jia, B., Fei, J., Wang, H., Li, B., & Cui, C. (2021). Oil spill discrimination of multi-time-domain shipborne radar images using active contour model. *Geoscience Letters*, 8(1), 7. <https://doi.org/10.1186/s40562-021-00178-8>
- Yamagishi, S., Hitomi, K., & Yamanouchi, H. (1999). Detection and classification of an oil spill using a compact imaging Lidar system. *International Oil Spill Conference Proceedings*, 1999(1), 781–785. <https://doi.org/10.7901/2169-3358-1999-1-781>
- Yamagishi, S., Hitomi, K., Yamanouchi, H., & Yamaguchi, Y. (2001). Determination of a Lidar signal from images of backscattered natural light on water surface. *International Oil Spill Conference Proceedings*, 2001(2), 929–933. <https://doi.org/10.7901/2169-3358-2001-2-929>
- Yang, Y.-J., & Schnupfhagn, C. (2024). A near real-time automated oil spill surveillance system using SAR and its application to a new study area. *EUSAR 2024; 15th European Conference on Synthetic Aperture Radar*, 447–452.
- Yang, Y.-J., & Schnupfhagn, C. (2025). A near real-time automated oil spill monitoring system using SAR imagery from the European Copernicus mission. In R. J. Frouin, H. Murakami, J.-K. Choi, & K.-H. Tseng (Eds.), *Active and passive remote sensing of oceans, seas, and lakes* (132640G, Vol. 13264). SPIE. <https://doi.org/10.1117/12.3040472>
- Yekeen, S. T., & Balogun, A.-L. (2020). Automated marine oil spill detection using deep learning instance segmentation model. *The International Archives of the Photogrammetry, Remote Sensing and Spatial Information Sciences*, XLIII-B3-2020, 1271–1276. <https://doi.org/10.5194/isprs-archives-XLIII-B3-2020-1271-2020>
- Yekeen, S. T., Balogun, A.-L., & Wan Yusof, K. B. (2020). A novel deep learning instance segmentation model for automated marine oil spill detection. *ISPRS Journal of Photogrammetry and Remote Sensing*, 167, 190–200. <https://doi.org/10.1016/j.isprsjprs.2020.07.011>
- Zakzouk, M., El-Magd, I. A., Ali, E. M., Abdulaziz, A. M., Rehman, A., & Saba, T. (2024). Novel oil spill indices for Sentinel-2 imagery: A case study of natural seepage in Qaruh Island, Kuwait. *MethodsX*, 12, 102520. <https://doi.org/10.1016/j.mex.2023.102520>

- Zhang, B., Matchinski, E. J., Chen, B., Ye, X., Jing, L., & Lee, K. (2019). Chapter 21 - Marine oil spills—oil pollution, sources and effects. In C. Sheppard (Ed.), *World seas: An environmental evaluation* (pp. 391–406). Academic Press. <https://doi.org/10.1016/B978-0-12-805052-1.00024-3>
- Zhu, X., Li, Y., Feng, H., Liu, B., & Xu, J. (2015). Oil spill detection method using X-band marine radar imagery. *Journal of Applied Remote Sensing*, 9(1), 095985. <https://doi.org/10.1117/1.JRS.9.095985>

Acknowledgements

First of all, I would like to express my great appreciation to my supervisor, Florian. So far, I've only thanked him in a light-hearted way, but I'm really grateful to him for making it possible for me to complete my PhD. Although it wasn't a long time, the encouragement I received from him during our regular meetings (and the stress I got just because there was a meeting ahead) motivated me to complete my writing. Equally importantly, I would like to thank my DLR supervisor, Suman, for his guidance, always being available to discuss research (while he was in our group), and the unforgettable nice time we shared together: examining oil slicks in thousands of SAR images.

I would like to extend my thanks to members of the DARTIS project. Prof. Mayerle for his guidance during the early stages of my doctoral research. He also encouraged me to broaden my focus from remote sensing to oceanography. I would also like to thank Ron from IOLR for all our collaborative work and publications.

I am very grateful to my DLR colleagues for helping me overcome research difficulties, supporting me over the course of the Covid pandemic, and assisting me with issues relating to life in Germany. (I believe some of you might still remember the waiting music when calling the Migrationsamt.) Here, I would especially like to thank the colleagues who took their time to read this thesis and provided valuable comments: Stefan W., Christoph S., Dominik, Christoph P., and Karl.

My research voyage began in Taiwan. Therefore, I would like to take this opportunity to express my sincere gratitude to all those who supported, encouraged, and inspired me to pursue a PhD. This includes (but is not limited to) the invaluable support from my master's supervisor, Prof. Cheinway Hwang, as well as my research buddies, Wei-Ji, Wan-Hsin :'), and Jui-Chi. I would also like to thank Chia-Jui for his great attitude, passion, and patience in research (and music), all of which have influenced me deeply.

In the end, I want to give my big thank you to my family and my best friend Ju Wang, who have always been there for me despite the time difference, as well as Dominik and the family Günzel for supporting me as my family do. I treasure all the people I have crossed paths with throughout my life, whether it was on sports tracks, in badminton courts, at university or through music and faith.

Declaration

I hereby declare that my dissertation entitled, “*Automated Oil Spill Detection System Using Spaceborne Synthetic Aperture Radar with Deep Learning-Based Algorithm*” , apart from the supervisor’s guidance, the content and design of the thesis is all my own work. The thesis has been submitted neither partially nor wholly as part of a doctoral degree to another examining body, and no academic degree has ever been withdrawn. It has neither been published nor submitted for publication. I also assure that the thesis has been prepared subject to the Rules of Good Scientific Practice of the German Research Foundation.

Kiel, 2025-12-04

(Yi-Jie Yang)